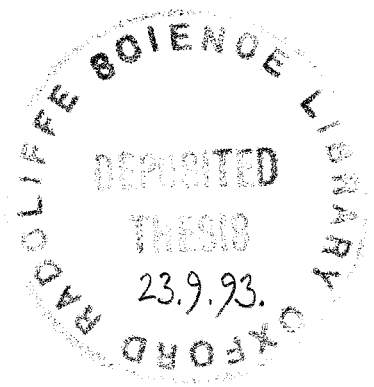
A Structural Study of an Arcuate Thrust Belt, Prebetic Zone, Southern Spain.

Clare Rosalind Meeson Mandeville, M.A. (Cantab.)

St. Edmund Hall and

Department of Earth Sciences,

University of Oxford.



Thesis submitted for the degree of

Doctor of Philosophy, Trinity 1993.

" Thought, I love thought.
But not the jiggling and twisting of already existent ideas..
..Thought is gazing on to the face of life, and reading what can be read.."

Extract from "Thought" by D.H. Lawrence.

A Structural Study of an Arcuate Thrust Belt, Prebetic Zone, Southern Spain.

Clare Rosalind Meeson Mandeville, M.A. (Cantab.),
St. Edmund Hall & Department of Earth Sciences, University of Oxford.

Thesis submitted for the Degree of Doctor of Philosophy, Trinity 1993.

Short Abstract

The Prebetic Zone, the most external zone of the Betic Cordillera of southern Spain, is a thin-skinned thrust belt of Mesozoic and Tertiary rocks formed on the southern margin of Iberia and exhibits an arcuate geometry in plan view. Deformation in the Prebetic Zone was initiated during the late Burdigalian-early Seravallian and propagated NNW/NW towards the foreland in a wave of deformation which became more WNW directed with time. Formation of the dextral Socovos wrench fault and strain partitioning across it strongly influenced the development of the arc.

Tectonic subsidence curves indicate a stretched continental margin in the Mesozoic. Some of these curves also show a rapid subsidence in the Miocene, represented by intramontane basins, in response to loading of thrust slices.

Gravity modelling indicates a shallowing of the Moho to the east, a decrease in the depth to basement to the east and wedging of the Internal Zones beneath the Subbetic Zone.

Three balanced cross-sections across the Prebetic orogen indicate a decrease in the shortening strain from 69% to 54% to 21%, with a calculated error of ±7%. Sequential 3-D reconstructions of the External Prebetics, constructed by restoring the three balanced cross-sections over four discrete time steps, show that the initial geometry of the External Prebetics was arcuate in plan view. The overall reduction of the restored area, in the horizontal plane, was 45%, with 45-53 km of dextral strike slip along the Socovos Fault. The rate of deformation varied during the Miocene; generally increasing from the Seravallian to the Messinian with a decrease in the Tortonian.

The results of this study are consistent with a model of Betic-Rif evolution in which there is syn-orogenic extensional collapse of an overthickened collisional ridge in the Alboran region.

A Structural Study of an Arcuate Thrust Belt, Prebetic Zone, Southern Spain.

Clare Rosalind Meeson Mandeville, M.A. (Cantab.),
St. Edmund Hall & Department of Earth Sciences, University of Oxford.

Thesis submitted for the Degree of Doctor of Philosophy, Trinity 1993.

Extended Abstract

The Prebetic Zone, the most external zone of the Betic Cordillera of southern Spain, is a thin-skinned thrust belt of Mesozoic and Tertiary rocks formed on the southern margin of Iberia. It exhibits an arcuate geometry in plan view where the strike of major features can be shown to vary by >90°. A comprehensive structural study of this area was undertaken to attain a greater understanding of the mechanism of formation of this arcuate thrust belt and to assess the significance of the results with respect to the general formation of arcuate orogens and the wider problem of the evolution of the Betic-Rif orogen. The aims of the structural study were to document the style and variation of deformation around the arc, both at the surface and at depth, to detail its deformational history through time, to define and account for episodes of extension and compression and to provide a valid 3-D reconstruction of its original geometry. A variety of structural and geophysical techniques were applied which included field mapping and kinematic data analysis, backstripping of stratigraphic sections to produce tectonic subsidence curves, gravity profiling and modelling, construction of balanced cross-sections and 3-D areal balancing.

The deformation in the Prebetic Zone was initiated during the late Burdigalian-early Seravallian and propagated towards the foreland from the Subbetic Front to the NNW/NW by frontal accretion of new material onto a deforming thrust wedge in a wave of deformation that became more WNW directed with time. Deformation also nucleated around, and propagated outwards from, the dextral Socovos wrench fault. The differential displacement and the partitioning of strain across the Socovos fault, into strike-slip motion parallel to the fault and orthogonal NE-SW thrusting/backthrusting, caused the formation of firstly, the Cenajo Syntaxis and NW Trending Limb and, with progressive deformation, the Alcaraz Antitaxis and the NE Trending Limb. The Cenajo Syntaxis

underwent convergent displacement with NW thrusting in the east and NE thrusting in the west arising as a result of strain partitioning across the Socovos Fault. Superposition of these trends of deformation was due to the tightening of the hinge area with time. The Alcaraz Antitaxis underwent divergent displacement as extension in the outer arc was accommodated The hinge angle was tightened as deformation continued and interference with obstacles in the foreland occurred. The anticlockwise swing in the displacement trend of the NE Trending Limb, from NW to WNW, was facilitated by movement along WNW-ESE oriented tear faults.

In the Internal Prebetics, deformation occurred from the late Burdigalian to the Tortonian.

For the External Prebetics, in the late Burdigalian-early Seravallian, deformation occurred predominantly in the NW Trending Limb and along the Socovos Fault. In the mid-late Seravallian, deformation occurred in both the middle part of the NW Trending Limb, along the Socovos Fault and in the hinterland part of the area to the east. In the Tortonian, deformation occurred predominantly in the hinterland region of the NE Trending Limb and the Alcaraz Antitaxis, and the foreland region of the NW Trending Limb. In the Messinian, deformation occurred in the NE Trending Limb and the Alcaraz Antitaxis.

The mechanism for the formation of the Prebetic Arc, obtained from analysis of the variation in the style of deformation, both spatially and temporally, was found to be predominantly due to movement along, and the differential shortening across the Socovos Wrench Fault. The presence of obstacles in the foreland had a minor affect on tightening the hinge of the Alcaraz Antitaxis, and the slightly arcuate original form of the External Prebetics also had a minor contributory role in the formation of the arc and may have had an influence on the location of the Socovos Fault. This mechanism of formation of the Prebetic Arc could not have been predicted from relative plate motion vectors or previous models for the formation of the Betic-Rif Orogen. Local body forces associated with shear faults and obstacles, and the partitioning of strain all exerted a strong influence on the strain pattern, although the change in the overall tectonic transport direction from NNW to NW to WNW may have resulted from changes in the relative plate motions. A change to a more WNW direction in the relative motion vector of Africa with respect to Europe at 9 Ma is documented by Helman (1989) and Dewey et al. (1989).

Backstripping of a series of stratigraphic sections compiled from different locations around the arc produces a set of basement and tectonic subsidence curves, which allow a more detailed study of the timing and duration of the different extensional and compressional events that have occurred in the Prebetic area.

The tectonic subsidence curves indicate an initial subsidence in the Triassic, which then decayed exponentially in the Jurassic, Cretaceous and early Tertiary. This is indicative of a stretched continental margin exhibiting a phase of gentle subsidence followed by thermal relaxation. Theoretical subsidence curves, generated by the uniform stretching model, were fitted to these tectonic subsidence curves allowing the stretching factor, ß, to be estimated. There is a gradual increase in ß from the western to the eastern External Prebetics, which may have given rise to an irregular continental margin and associated distribution of the sedimentary facies. There is also a notable increase in ß, basinward, from the External Prebetics through the Internal Prebetics to the Subbetic Zone. Extension was accommodated differently in the western and eastern Prebetic Zone; in the west, deformation was concentrated on a few, large-displacement faults; whereas in the east, it was more pervasive and accommodated by many small-displacement faults.

Some of the more internal sections show a marked increase in subsidence within the Cretaceous, which was probably due to local pulses of extension. In the Internal Prebetics two exclusive periods of increased subsidence are observed in certain sections, at the Jurassic/Cretaceous boundary and within the Albian.

Tertiary deposits, which are absent in the NE trending limb, increase in distribution around the arc and into the Internal Prebetics and the Subbetic Zone. The sections from the Alcaraz Antitaxis and the NW Trending Limb show only very minor amounts of subsidence in the Miocene whereas the section from the Cenajo Syntaxis shows a marked increase in subsidence rate during this time. The four sections in the Internal Prebetics all show rapid subsidence in the Miocene. The subsidence curves show a variation in the timing of the initial deviation from the exponentially decreasing subsidence path to that of increased subsidence in both the east and the west. In the east, initial basin formation varies from 30-25 Ma (Oligo-Aquitanian) for the Internal Prebetics to about 20-15 Ma (Burdigalian/Langhian/early Seravallian) for

the Cenajo Syntaxis to 15-10 Ma (mid-late Seravallian/early Tortonian) for the area located close to the undeformed foreland. Whereas, in the west, the initial basin formation varies from 23-20 Ma (Aquitanian/Burdigalian) in the Internal Prebetics close to the present Subbetic Front to about 15-10 Ma (mid-late Seravallian/early Tortonian). This compares well with the timing of the initiation of deformation around the arc, compiled from structural and sedimentological data, rather than that of the main deformation.

This deviation in Miocene subsidence rates from the theoretical curve was probably due to local loading caused by the emplacement of the Prebetic/Subbetic thrust piles from the SE. The basins formed by flexural response to this loading were carried towards the foreland in a passive, piggy-back style and received a sediment supply from both hinterland and foreland thrust slices.

The gravity anomalies over five hypothetical cross-sections across the eastern Betic Cordillera were modelled and compared with the observed anomalies. Analysis of these results suggests that the regional structure shows a marked lateral change across the eastern Betic Cordillera. The most westerly section indicates the presence of a small crustal root under the Internal Zones which becomes reduced in the profiles to the east where the Moho becomes shallower and its gradient decreases. This occurs landward of the coast indicating that the transition between stretched and unstretched crust is narrow and located beneath onshore regions. The most easterly section shows an increase in Moho gradient and thinning of the Iberian crust which may be related to stretching in the Valencia trough.

Analysis of the upper crustal structure shows a decreasing gradient of the basement/Prebetic-Subbetic thrust pile interface from west to east, which may be due to the greater amount of shortening that occurred in the west. The frontal nose of the Internal Zone, which wedges beneath the Subbetic Zone, becomes less well defined and more complex towards the east. The non-alignment of the contours on the map of the basement elevation with the Socovos fault indicate that it is a thin-skinned feature across which there is no significant change in the basement structure. The very short wavelength negative anomalies are due to the presence of low density Tertiary and Quaternary basins.

Construction of a series of three balanced cross-sections, located at intervals from west to east, parallel to the observed tectonic transport directions, allowed the amount of shortening across the Prebetic orogen to be estimated whilst also providing useful controls on the structure at depth and the correlation of décollement horizons. Two methods for calculating the amount of shortening of section, bed length balancing and cumulative displacement-distance analysis, were applied to the three balanced sections. The results of these calculations show a west to east decrease in shortening strain from 69% to 54% to 21%, with a calculated error of ±7%. The decrease from 69% to 54% across the major Socovos wrench fault indicates that there is no dramatic decrease in the amount of deformation to the east of this fault. The component of deformation to the NW (sub-parallel to the movement along the Socovos Fault), however, does decrease significantly across the Socovos Fault with most deformation occurring in the orientation of the other component of partitioned deformation, i.e. approximately perpendicular to the Socovos Fault. The amount of NW strain exhibited in the Elche section was obtained using the graphical method of Cooper (1983) applied to an oblique section oriented at 120-130° and gave values which varied between 5% and 18% shortening.

The most north-westerly segment of the Cazorla section shows a decrease in bulk strain to below the average for that section due to the influence of the Palaeozoic Massif. The strain for the Jumilla and Elche sections show an increase towards the foreland where there is a basin of Mesozoic sediments.

'Areal balancing' of the External Prebetics was attempted to provide a viable 3-D reconstruction This was completed by restoring the known amounts of deformation obtained by the construction of three balanced cross-sections at various locations around the Prebetic Arc over four discrete time steps. The initial geometry of the External Prebetics can then be shown to be arcuate in plan view with a marked increase in the thickness of the stratigraphic sequence from west to east. This increase, which becomes greater basinward, appears to be fairly abrupt in nature and the presence of a pre-existing heterogeneity is invoked.

Sequential restoration of the dextral strike-slip of the Socovos Fault results in a graphical estimation of a minimum displacement along the Socovos Fault in the External Prebetics of 45-53 km. Strike-slip motion was probably initiated preferentially in the area where the boundary was

oriented approximately NW-SE. With continued differential deformation across the Socovos Fault, the initial arcuate feature became exaggerated and the hinge angles of the antitaxis and syntaxis decreased.

An overall reduction in the horizontal plane of 45% was determined graphically from scaled drawings of the area of the External Prebetics between the Cazorla and Jumilla sections. The rate of deformation varied during this Miocene deformation. In the Seravallian there was a gradual increase in the rate of deformation, which decreased in the Tortonian, possibly associated with the formation of the 'Tranco Zone' where deformed Triassic is exposed at the erosional surface. A two-fold increase in the rate of deformation occurred in the Messinian, where the deformation was located predominantly in the NE Trending Limb and the Alcaraz Antitaxis, and coincides with the final ramping up of the basal décollement from within the Triassic to the Triassic/Jurassic interface.

The results of the structural analysis, the predicted model of formation of the Prebetic Arc and the 3-D reconstruction cannot be wholly applied to any other arcuate orogen at whatever scale although aspects may apply in individual cases.

The model of formation of the Prebetic Arc and the overall tectonic transport directions and style of deformation documented for the Prebetic Zone cannot be extended to apply to the more hinterland parts of the orogen i.e. the Subbetic Zone and the Internal Zones. These results, which arise from an important area at the boundary of the region of intracontinental deformation and the stable Iberian margin, can provide new evidence to support or discount existing models for the evolution of the Betic-Rif orogen. No conclusive evidence for the gravitational sliding of nappes from a high located in the Alboran Sea, oroclinal bending of an initially linear orogenic belt, westward emplacement of a Alboran microplate or the formation of a broad zone of dextral transpression between the Iberian and African plates has resulted from this study and the details of structural analysis, timing, palaeomagnetic and kinematic analysis all contradict the predictions of these models. However, the model of extensional collapse of an overthickened collisional ridge in the Alboran region is consistent with the results of this study. Syn-orogenic rather than post-orogenic extensional collapse is the mechanism indicated by the detailed analysis of timing relationships.

ACKNOWLEDGEMENTS

The foremost person I must thank is Dr J.P.Platt who has operated a most enlightened non-interventionist style of supervision. The other Beticophiles who aided, abetted, provoked and encouraged this thesis on until it was cowed into submission were Simon Allerton, Tom Argles, Andy Kirker, Lidia Lonergan, Miguel Mora and Ellen Platzman.

The instigator of brief forays into the world of gravity modelling was Professor A.B.Watts, whilst the practicalities were revealed to me by Cath Marr. The work on subsidence histories was carried out with the invaluable assistance and enthusiasm of Dr N.White and Lidia Lonergan.

Technical advice and assistance was provided by Steve Baker, Andy Clark, Roy Goodwin, Richard McAvoy and Derek Preston. Smoothing of the bureaucratic waves remains the province of John O'Sullivan, Carol Coggins, Karen Crause, Trish McNiff, Mary Marsland, Diana Relton and Sally Thompson and essential library services were provided by Dorothy Haigh and Helen Elder.

The people who will always remain firmly entwined in my memory with the gradual formulation of this are my supportive housemates at Domestic Bliss: Simon Davey, Malcolm Dransfield, Pamela Sansom and laterly Julian Bessa and Audrey Willet.

An experience which was only possible with the backing of the Oxford department was that of the Oxford Expedition to the Northern Andes 1990. My comrades on that jaunt were Jon Bass, Sarah Crampton, Jaumé Dinares, Steve Hart, Roxby Hartley, Sean Hodges, Miguel Mora, Karen Ogden, Jane Scarrow and Andy Whittingham.

Other department members who I want to thank for entertaining me, often in many unbelievable ways, are Pete Burgess, Sian Davies, Jon Hinchey, Jon Kennedy, Jo Lihou, Maria Mange, Tom Martel, Elaine Scott, Ed Thorogood, Sara Vickery, Gavin Wall and Halcyon Wills.

My family, well, I wouldn't be here now without their unfailing support and encouragement.

And finally....to Steve, he promised me the world and we've been travelling it ever since!

CONTENTS

Short Abstract i
Extended Abstract ii
Acknowledgements viii
Contents ix
Figure list xi

CHAPTER 1
INTRODUCTION
1.1. Tectonic setting of the Betic-Rif Orogen 1
1.2. Existing models of the tectonic evolution of the Betic-Rif Orogen 5
1.3. Discussion of arcuate orogens 10
1.4. Objectives of the thesis 16
1.5. Working methods 16
1.5.1. Collection of field data 16
1.5.2. Computer analysis 17
1.5.3. Laboratory analysis 17

CHAPTER 2
DEFORMATIONAL VARIATION AROUND THE ARC
2.1. Introduction 18
2.2. Description of deformation around the arc 21
2.2.1. The External Prebetics 21
2.2.1.1. The NE Trending Limb 21
2.2.1.2. The Alcaraz Antitaxis 24
2.2.1.3. The NW Trending limb 25
2.2.1.4. The Cenajo Syntaxis 26
2.2.2. The Internal Prebetics 28
2.3. Timing of the deformation 29
2.3.1. Late Burdigalian-early Seravallian 30
2.3.2. Middle-late Seravallian 32
2.3.3. Tortonian 34
2.3.4. Messinian 35
2.4. Palaeomagnetic studies and the presence of rotations around a vertical axis 36
2.5. Summary of the formation of the Prebetic Arc 39

CHAPTER 3
SUBSIDENCE AND BASIN FORMATION IN THE PREBETIC ZONE
3.1. Introduction 43
3.2. Tectonic subsidence 45
3.2.1. Comparison of Mesozoic subsidence 48
3.2.2. Cretaceous extension 51
3.2.3. Tertiary basin formation 52
3.3. The lack of a foreland basin in the Eastern Betic Cordillera 55

CHAPTER 4
INTERPRETATION OF GRAVITY DATA
4.1. Introduction 61
4.2. Gravity modelling 62
4.3. Interpretation of the regional structure 65
4.4. Interpretation of the upper crustal structure 66
4.5. Summary of results 69

CHAPTER 5
ESTIMATES OF SHORTENING ACROSS THE PREBETIC OROGEN
5.1. Introduction 71
5.2. Balanced sections in 2-D 74
5.2.1. The Cazorla section 76
5.2.2. The Elche section 78
5.2.3. The Jumilla section 80
5.2.4. Correlation of décollement horizons 82
5.3. Estimates of shortening 84
5.3.1. Method 84
5.3.1.1. Bed length balancing 84
5.3.1.2. Cumulative displacement-distance diagram 85
5.3.1.3. Errors in calculation 86
5.3.2. The Cazorla section 87
5.3.3. The Elche section 91
5.3.4. The Jumilla section 93
5.4. Discussion of results 95

CHAPTER 6
3-D RECONSTRUCTION OF THE PREBETIC ARC
6.1. Introduction 99
6.2. Restoring the Prebetic Arc 101
6.3. Calculation of the deformation 105
6.4. Original shelf geometry 107
6.5. Summary and comparison with previous reconstruction 110

CHAPTER 7
INTEGRATED SYNTHESIS AND CONCLUSIONS
7.1. Summary of results of the structural study of the Prebetic Arc 112
7.2. The model of the formation of the Prebetic Arc in regional context 121
7.3. Future work to extend this study of the Prebetic Arc 127

REFERENCES

APPENDICES
Appendix 1. Compilation of kinematic data of the Prebetic Zone
Appendix 2. Co-ordinates of the gravity models used in Chapter 4

FIGURE LIST

CHAPTER 1
INTRODUCTION
Fig 1.1.1. Structural map of the Betic-Rif Orogen.
Fig 1.1.2. a) Correlation chart showing the general direction of Africa's motion with respect to Europe after Dewey et al. (1989).
Fig 1.1.2. b) Motion of three points on Africa with respect to Europe from 92 Ma to the present (Dewey et al. 1989).
Table 1.2. Summary of the models of tectonic evolution for the Betic-Rif Orogen.
Fig 1.2.1. Nappe model after Durand-Delga (1966).
Fig 1.2.2. Independent Alboran microplate model after LeBlanc & Olivier (1984).
Fig 1.2.3. Broad zone of distributed dextral shear model after Osete (1989).
Fig 1.2.4. Extensional collapse model after Platt & Vissers (1989).
Fig 1.2.5. Oblique relative convergence model after Platzman (1992).
Fig 1.3.1. A map of the Mediterranean area showing the five main orogenic arcs and associated variation in tectonic transport direction.
Fig 1.3.2. Summary of the models which can account for the formation of arcuate orogens.

CHAPTER 2
DEFORMATIONAL VARIATION AROUND THE ARC
Fig 2.1.1. Summary map of the western Prebetic Zone showing the division into the External Prebetics and the Internal Prebetics.
Fig 2.1.2. Gently dipping Messinian lacustrine marls and limestones unconformably overlying folded Cenomanian dolomite.
Fig 2.1.3. Satellite image of the Prebetic Arc clearly showing the change in structural trend across the Alcaraz Antitaxis and Cenajo Syntaxis of the External Prebetics.
Fig 2.1.4.a). Comparison of representative stratigraphic sequences around the Prebetic Arc.
Fig 2.1.4.b). Key for stratigraphic columns shown in Fig 2.1.4.a).
Fig 2.1.5. Brittle shear zone showing the development of a gouge fabric, R_1 and R_2 Riedel shears and a low-angle P-shear used in shear sense analysis.
Fig 2.1.6. Fault gouge developed in a mud layer in the Lower Jurassic.
Fig 2.1.7.a) Riedel shear plane (R_1) developed within Lower Jurassic dolomite.
Fig 2.1.7.b) Low angle Riedel shear planes (R_1) developed within a shear zone of Aquitanian sandstone and mudstone showing an small normal offsets.
Fig 2.1.8. Small-scale thrust fault in Lower Jurassic dolomite.
Fig 2.2. Summary map of the variation in tectonic transport directions around the Prebetic Arc.
Fig 2.2.1.1. Four imbricate slices, thrust approximately to the NNW, with subsequent backsteepening of earlier, more hinterland slices.
Fig 2.2.1.2. Variation in tectonic transport directions in the Tranco area.

Fig 2.2.1.3. Stereoplots of locations from the Tranco area.
Fig 2.2.1.4. Variation in tectonic transport directions in the Orcera area.
Fig 2.2.1.5.a) A section through Albian Utrillas facies sandstone, mudstone and marl and Cenomanian dolomite showing two phases of deformation.
Fig 2.2.1.5.b) Drawing of photomontage, Fig 2.2.1.5a), in the Orcera area.
Fig 2.2.1.5.c) Detail of deformation located in Fig 2.2.1.5.b). Original extension in Albian sandstone is reactivated by backthrusting .
Fig 2.2.1.6. Stereoplots of locations from the Orcera area.
Fig 2.2.1.7. Messinian marls incorporated in the frontal thrust sheets of Jurassic.
Fig 2.2.1.8.a) Passive-roof duplex developed in NE Trending Limb.
Fig 2.2.1.8.b) The development of a hinterland dipping duplex.
Fig 2.2.1.8.c) Out-of-sequence thrusting in gently tilted Lower Jurassic dolomite of the duplex roof thrust.
Fig 2.2.1.9. Detailed structural map of the passive-roof duplex formed in the Tranco area.
Fig 2.2.1.10. Subvertical tear fault developed in Lower Jurassic dolomite showing the development of wear grooves and a Riedel shear plane.
Fig 2.2.1.11. Distribution of the WNW-ESE tear faults within the Tranco area.
Fig 2.2.1.12. Intrusive contact between the remobilised Adamellite and Palaeozoic metamorphosed rock.
Fig 2.2.1.13. Cross-bedded upper Tortonian/lower Messinian calcarenites incorporated into the thrust slices of Jurassic close to the Prebetic Front.
Fig 2.2.1.14. Red Triassic sandstone overthrusting Jurassic units causing the formation of recumbent folds in the footwall.
Fig 2.2.1.15a) E-W crystal lineations on a gypsum shear zone within the Triassic sandstone.
Fig 2.2.1.15b) Cross-section of the gypsum shear zone showing a dextral shear foliation.
Fig 2.2.1.16. Stereoplot of deformed gypsum veins within the Triassic of the Riopar area.
Fig 2.2.1.17. Distribution of the dextral NW-SE and sinistral NE-SW strike slip faults within the Alcaraz Antitaxis.
Fig 2.2.1.18. Variation in tectonic transport directions in the Riopar area.
Fig 2.2.1.19. Oblique backthrust duplex cross-cutting earlier forethrusts.
Fig 2.2.1.20. Stereoplots of locations from the Riopar area.
Fig 2.2.1.21. Variation in tectonic transport directions in the Elche area.
Fig 2.2.1.22. Stereoplots of locations from the Elche area.
Fig 2.2.1.23. Original extensional faults within Jurassic limestone.
Fig 2.2.1.24. Contoured stereoplots of distribution of fault lineations associated with the dextral Socovos Fault.
Fig 2.2.1.25. Variation in tectonic transport directions in the Isso area.
Fig 2.2.1.26. Stereoplots of locations from the Isso area.
Fig. 2.2.1.27. Two sets of crystal lineations on a fault plane .
Fig 2.2.1.28. Two trends of deformation.

Fig 2.2.1.29. Schematic diagram of the formation of the Cenajo Syntaxis after Jerez Mir (1973).
Fig 2.2.1.30. Thrust fault within Messinian marl and limestone.
Fig 2.2.2.1. Stereoplot of SSE backthrust duplex with associated NNW thrusting, from the Internal Prebetics, SW of the Socovos Fault.
Fig 2.2.2.2. Listric extensional faults within Cretaceous marl and mudstone of the Internal Prebetics.
Fig 2.3.1.a) Deformation in the late Burdigalian-early Seravallian.
Fig 2.3.1.b) Deformation in the middle-late Seravallian.
Fig 2.3.1.c) Deformation in the Tortonian.
Fig 2.3.1.d) Deformation in the Messinian.
Fig 2.3.2. Slumps within upper Burdigalian to lower Seravallian limestone and marl.
Fig 2.3.3. Stereoplot of the slumps associated with the Socovos Fault
Fig 2.3.4. Intra-formational unconformity.
Fig 2.3.5. Diagram of the propagation of the main wave of deformation in the External and Internal Prebetics showing an anticlockwise swing in the trend of the deformation.
Table 2.4. Results of palaeomagnetic studies.
Fig 2.4.1. Location map of palaeomagnetic sites in the western Prebetics.
Fig 2.4.2. Zijderveld plot for sample CRM5-5 in Jurassic limestone.
Fig 2.4.3. i) Stereoplot showing the palaeomagnetic vectors for sample B49-6 in Jurassic limestone ii) Zijderveld plot for sample B49-6.

CHAPTER 3
SUBSIDENCE AND BASIN FORMATION IN THE PREBETIC ZONE
Fig 3.1.1. a) Subsidence curve for the Sierra del Carche, Internal Prebetics, after Kenter et al. (1990).
Fig 3.1.1. b) Subsidence curve for the Sierra Caramucel-E, Subbetic Zone, after Kenter et al. (1990).
Fig 3.2.1. Locations of compiled sections or well-logs in the Prebetic Zone and northern Subbetic Zone for which basement and tectonic subsidence curves were generated.
Table 3.2 Values of parameters used in backstripping program
Fig 3.2.2.a). Examples of stratigraphic sections from around the Prebetic Arc which have been used to compile basement and tectonic subsidence curves.(12 sections)
Fig 3.2.2.b). Key for stratigraphic columns shown in Fig 3.2.2.a).
Fig 3.2.3.a). Basement subsidence curve for the section CM1 of the External Prebetics.
Fig 3.2.3.b). Water-loaded, tectonic subsidence curve for the section CM1.
Fig 3.2.4.a). Basement subsidence curve for the section CM2 of the External Prebetics.
Fig 3.2.4.b). Water-loaded, tectonic subsidence curve for the section CM2.
Fig 3.2.5.a). Basement subsidence curve for the section CM3 of the External Prebetics.
Fig 3.2.5.b). Water-loaded, tectonic subsidence curve for the section CM3.
Fig 3.2.6.a). Basement subsidence curve for the section CM4 of the External Prebetics.

Fig 3.2.6.b). Water-loaded, tectonic subsidence curve for the section CM4.
Fig 3.2.7.a). Basement subsidence curve for the section CM9 of the External Prebetics.
Fig 3.2.7.b). Water-loaded, tectonic subsidence curve for the section CM9.
Fig 3.2.8.a). Basement subsidence curve for the section CM6 of the External Prebetics.
Fig 3.2.8.b). Water-loaded, tectonic subsidence curve for the section CM6.
Fig 3.2.9.a). Basement subsidence curve for the section CM7 of the External Prebetics.
Fig 3.2.9.b). Water-loaded, tectonic subsidence curve for the section CM7.
Fig 3.2.10.a). Basement subsidence curve for the section CM5 of the Internal Prebetics.
Fig 3.2.10.b). Water-loaded, tectonic subsidence curve for the section CM5.
Fig 3.2.11.a). Basement subsidence curve for the section BP1 of the Internal Prebetics.
Fig 3.2.11.b). Water-loaded, tectonic subsidence curve for the section BP1.
Fig 3.2.12.a). Basement subsidence curve for the section BP2 of the Internal Prebetics.
Fig 3.2.12.b). Water-loaded, tectonic subsidence curve for the section BP2.
Fig 3.2.13.a). Basement subsidence curve for the section CM10 of the Internal Prebetics.
Fig 3.2.13.b). Water-loaded, tectonic subsidence curve for the section CM10.
Fig 3.2.14.a). Basement subsidence curve for the section N. SUBBETIC of the Subbetic Zone.
Fig 3.2.14.b). Water-loaded, tectonic subsidence curve for the section N.
Fig 3.2.15. Map of the Prebetic Zone and the northern Subbetic Zone showing the spatial variation in the value of ß.
Fig 3.2.16. Graph showing the distribution in duration of the initial Mesozoic rifting.
Fig 3.2.17.a) Structural cross-section showing the locations of CM1 and CM5.
Fig 3.2.17.b) Structural cross-section showing the locations of CM2, CM3, CM4 and CM10.
Fig 3.2.18. Variation in timing of the deviation of the subsidence curve from the theoretical curve in the Tertiary due to local basin formation.
Fig 3.2.19. Drainage pattern shown in the Tertiary deposits in the Alcaraz Antitaxis.
Fig 3.2.20. Wedge of late Tortonian/early Messinian calcarenites derived from uplifted Mesozoic units to the foreland, indicating the intramontane style of basin formation.

CHAPTER 4
INTERPRETATION OF GRAVITY DATA
Fig 4.1.1. Summary map of the Betic Cordillera showing the locations of profiles along which gravity models and/or seismic interpretation, referenced in this work, have been constructed.
Fig 4.1.2. Contour map of the Bouger gravity anomaly for the eastern Betic Cordillera showing the strong NE-SW regional trend.
Table 4.2. Summary of density values and sources.

Fig 4.2.1. a) Comparison of the observed and predicted Bouger gravity anomalies for the Cazorla section. b) Density distribution model for the Cazorla section used to generate the predicted gravity anomaly shown in a). c) Geological model for the Cazorla section.
Fig 4.2.2. a) Comparison of the observed and predicted Bouger gravity anomalies for the Orcera section. b) Density distribution model for the Orcera section used to generate the predicted gravity anomaly shown in a). c) Geological model for the Orcera section.
Fig 4.2.3. a) Comparison of the observed and predicted Bouger gravity anomalies for the Isso section. b) Density distribution model for the Isso section used to generate the predicted gravity anomaly shown in a). c) Geological model for the Isso section.
Fig 4.2.4. a) Comparison of the observed and predicted Bouger gravity anomalies for the Jumilla section. b) Density distribution model for the Jumilla section used to generate the predicted gravity anomaly shown in a). c) Geological model for the Jumilla section.
Fig 4.2.5. a) Comparison of the observed and predicted Bouger gravity anomalies for the Elche section. b) Density distribution model for the Elche section used to generate the predicted gravity anomaly shown in a). c) Geological model for the Elche section.
Fig 4.2.6. a) Density distribution model for the Cazorla section showing the alterations in the thickness of the Prebetic/Subbetic nappe pile. b) Observed and predicted Bouger gravity anomalies for the density distribution model shown in a).
Fig 4.2.7. a) Density distribution model for the Cazorla section showing the alterations in the gradient of the Moho as it shallows to the SE. b) Observed and predicted Bouger gravity anomalies for the density distribution model shown in a).
Fig 4.3.1. Contour plot of the depth of the Moho obtained from gravity modelling across the five profiles shown in Figs 4.2.1c)-5c).
Fig 4.4.1. Contour plot of the basement elevation obtained from gravity modelling across the five profiles shown in Figs 4.2.1c)-5c).
Fig 4.4.2. Contour plot of the thickness of the Prebetic/Subbetic nappe pile obtained from gravity modelling across the five profiles shown in Figs 4.2.1c)-5c).
Fig 4.4.3. a) Density distribution model for the Cazorla section showing the alterations in the position of the nose of the Internal Zone wedge. b) Observed and predicted Bouger gravity anomalies for the density distribution model shown in a).
Fig 4.4.4. a) Density distribution model for the Cazorla section showing the alterations in the depth and geometry of a Tertiary basin. b) Observed and predicted Bouger gravity anomalies for the density distribution model shown in a).
Fig 4.4.5. Contour map of the Bouger gravity anomaly for the eastern Betic Cordillera after filtering of the longer wavelength (>80km) features.

CHAPTER 5
ESTIMATES OF SHORTENING ACROSS THE PREBETIC OROGEN
Fig 5.1.1. Locations of previously balanced or 'semi-balanced' cross-sections in the western Prebetics.
Fig 5.2.1.1. The Cazorla balanced section. and location map
Fig 5.2.1.2. The Cazorla restored section.
Fig 5.2.1.3. Cartoon of the sequence of deformation resulting in the formation of the Cazorla passive-roof duplex (PRD).
Fig 5.2.2.1. The Elche balanced section. and location map
Fig 5.2.2.2. The Elche restored section.
Fig 5.2.2.3. Cartoon of the sequence of deformation resulting in the formation of the Elche section.
Fig 5.2.3.1. The Jumilla balanced section. and location map
Fig 5.2.3.2. The Jumilla restored section.
Fig 5.2.4.1a). The correlation of décollement horizons for five representative stratigraphic sections for the three balanced sections.
Fig 5.2.4.1b). Key for stratigraphic columns shown in Fig 5.2.4.1a).
Fig 5.2.4.2. Locations of the five stratigraphic sections shown in Fig 5.2.4.1.
Fig 5.2.4.3. Possible linking of the last ramping of the basal décollement through the Triassic.
Fig 5.3.1.1. Diagram of the cumulative displacement-distance method of analysis after Chapman & Williams (1984).
Fig 5.3.2.1. Division of the Cazorla section into three segments which have experienced slightly different trends of deformation.
Fig 5.3.2.2. The cumulative displacement-distance diagram for the Cazorla section.
Fig 5.3.3.1. The cumulative displacement-distance diagram for the Elche section.
Fig 5.3.4.1. The cumulative displacement-distance diagram for the Jumilla section.
Fig 5.4.1. Graphical method to attain e' from e for obliquely oriented sections after Cooper (1983).

CHAPTER 6
3-D RECONSTRUCTION OF THE PREBETIC ARC
Fig 6.2.1.a) Reconstruction of Messinian deformation.
Fig 6.2.1.b) Reconstruction of Tortonian deformation.
Fig 6.2.1.c) Reconstruction of middle-late Seravallian deformation.
Fig 6.2.1.d) Reconstruction of late Burdigalian-early Seravallian deformation.
Fig 6.3.1. The amount of areal reduction of the External Prebetics through time.
Fig 6.3.2. Variation in rate of deformation during the four time divisions.
Fig 6.4.1. Restoration of representative post-Triassic stratigraphic sequences to their original pre-deformational locations along translation paths obtained from the area restoration.
Fig 6.4.2. Contour plot of the post-Triassic thickness of the original shelf sequence of the External Prebetics.

Fig 6.4.3.a) Geometrical division of the External Prebetics used to calculate the post-deformational volume.
Fig 6.4.3.b) Geometrical division of the External Prebetics used to calculate the pre-deformational volume.
Fig 6.4.4. Geometrical approximation for volume calculations.
Fig 6.5.1. Previous reconstruction of Garcia-Hernandez et al. (1980).

CHAPTER 7
INTEGRATED SYNTHESIS AND CONCLUSIONS
Table 7.1. Summary of results of the structural study of the Prebetic Arc.
Table 7.2. Summary of new evidence from this study towards the existing models of formation of the Betic-Rif orogen.
Fig. 7.2.1. Cartoon of the tectonic setting of the Prebetic Zone with respect to the extending Alboran Domain at 19 Ma.

Chapter 1

CHAPTER 1

INTRODUCTION

1.1. Tectonic setting of the Betic-Rif Orogen

The tightly curved Betic-Rif orogenic system is the westernmost expression of the destructive margin originating from the convergence of the Eurasian and African plates and the concomitant closure of the Tethys Ocean (Fig 1.1.1). This extensive plate boundary, which stretches from the Mid-Atlantic Ridge to the Himalayas, shows a variation in the width of its deforming zone. From the narrow Azores-Gibraltar fracture zone it broadens markedly when continental crust becomes involved, from a width of approx 400km between the stable Iberian and African margins to over 2,000km between the Indian and Eurasian margins (England & Jackson 1989).

Reconstructions of the palaeogeographical location and the relative motion of Africa with respect to Europe indicate convergent motion since the late Cretaceous (92 Ma?), originally to the NE and then becoming N or NNE directed since the early Eocene (52 Ma). From the Messinian (9 Ma) to the present, northwesterly motion of Africa with respect to Europe occurred which caused dextrally oblique displacement in the Betic Cordillera (Fig 1.1.2). This analysis indicates that about 200 km of N-S convergence has occurred since anomaly 13 (38 Ma) and that about 50 km of oblique, NW directed convergence has occurred since anomaly 5 (9 Ma) (Dewey et al. 1973, Helman 1989, Dewey et al. 1989). Therefore, a compressional regime has existed during the entire Betic orogenic event.

Present-day seismic events in this region usually have shallow depths of focus and magnitudes of less than 4. There appears to be no evidence of an active N-dipping subduction zone, but two deep-focus events, centred at approx 600 km below Grenada, indicate possible detached lithosphere. Seismic tomography of the upper mantle also suggests the

presence of a N-dipping detached slab beneath the Alboran Sea (Spakman 1986, Wortel & Spakman 1991, Blanco & Spakman, in press).

The Betic Cordillera has a predominantly ENE-WSW structural trend which apparently varies to a more N-S orientation around the Gibraltar arc, becoming more E-W in orientation through the Rif and the Tell mountains. The Betic Cordillera and the Rif mountains of Morocco have been traditionally divided into Internal and External Zones based on original palaeogeographic and structural criteria (Fig 1.1.1).

The External Zone of the Betic Cordillera is a thin-skinned foreland fold and thrust belt with its décollement within the evaporitic Keuper horizon, and consists of the unmetamorphosed Mesozoic and Tertiary sediments of the southern Iberian passive margin (Paquet 1969, Garcia-Hernandez et al. 1980). The main compressional phases of deformation occurred in the early and late middle Miocene (Garcia-Hernandez et al. 1980, Jerez Mir 1981, Kenter et al. 1990). The tectonic division of the External Zones is into the parautochthonous Prebetic Zone and the allochthonous Subbetic Zone.

The extension of the passive margin began in the Pliensbachian (Dercourt et al. 1984), allowing Mesozoic and Paleogene sediments to be deposited in subparallel SW-NE trending facies belts on the SE sloping continental margin. There is a clear division of these sediments into the shelf facies Prebetic and the deep water/offshore platform facies Subbetic. Between these zones lie the Intermediate Units comprising deep water basinal marls. This unit is overthrust by the Subbetic units and although it is observable at the surface in the central Betic Cordillera it is only exposed locally in the eastern Betic Cordillera (Banks & Warburton 1991).

The Guadalquivir Basin, with Neogene sedimentary fill, forms an extensive foreland basin to the central and western Betic Cordillera but extends eastwards only as far as the Prebetic Arc. Along its southern margin sediments of Messinian age are incorporated into Subbetic thrust sheets.

The Internal/External Zone boundary has been suggested to be a major dextral strike-slip fault, but recent work (Lonergan et al., in press) demonstrates that in the eastern Betic Cordillera this boundary is a S to SE directed backthrust.

The Internal Zone of the Betic Cordillera has undergone metamorphism and penetrative deformation in an Alpine (late Cretaceous to mid Miocene) event and is composed of Permo-Triassic, with occasionally a more complete cover sequence, lying above Precambrian to Palaeozoic basement. There is a further division of the Internal Zones into three tectonic complexes by the degree of metamorphism and structural position in the thrust stack. The lowest unit, the Nevado-Filabride Complex, has undergone high pressure (up to 10 kbar or more)/low temperature metamorphism and the metabasites and eclogites found within the Mulhacen nappe have been considered to be originally an ophiolite sequence (Puga et al. 1991). The middle structural unit, the Alpujarride Complex, has undergone low-medium grade metamorphism but also shows locally high grade metamorphism. High temperature peridotite massifs have been emplaced into this complex around the Gibraltar arc. The highest unit, the Malaguide Complex, remains unmetamorphosed and only this Complex contains dated post-Triassic sediments. The polarity of the convergence of this thrust stack along sub-

horizontal faults is not clear and the kinematic data collected may only represent later deformation (Platt & Vissers 1989).

Overprinting this compressional deformation are low-angle extensional detachment fault systems which have produced the Basin and Range type topography of the Internal Zone Sierras and their associated fault-bounded Neogene basins (Platt & Vissers 1989, García-Dueñas & Balanyá 1991). This late extensional phase was probably initiated in the latest Oligocene or earliest Miocene (Platt & Vissers 1989).

The Alboran Basin, lying at the westernmost end of the Mediterranean is surrounded to the north, west and south by the Betic, Rif and Tell orogens and bounded to the east by the Balearic Basin. It is underlain by a thin continental crust, 13-20 km, of metamorphosed units very similar to that of the on-shore Internal Zone and by anomalously low velocity upper mantle (Banda et al. 1983). The presence in the Alboran Basin of east-west trending horst and graben structures (Dillon et al. 1980), intrusive rocks indicated by magnetic anomalies (Galdeano et al. 1974), and widespread Neogene volcanics as on-shore, indicate a phase of extensional rifting. This extension began within the basin coevally with that in the Internal Zone and the compression within the External Zone (Watts et al., in press).

1.2. Existing models of the tectonic evolution of the Betic-Rif Orogen

There have been numerous models proposed for the tectonic evolution of the western Mediterranean area over the last 60-70 years, some of which obviously pre-date plate tectonic theory.
The models under consideration fall into five categories:

1) Gravitational sliding of nappes from a high located in the Alboran Sea.
2) Oroclinal bending of an initially linear orogenic belt.
3) Westward emplacement of an Alboran microplate with associated zones of dextral and sinistral strike slip to the north and south respectively.
4) Formation of a broad zone of dextral transpression between the Iberian and African plates.
5) Syn- or post-orogenic extensional collapse of an overthickened collisional ridge in the Alboran region.

To consider the validity of the existing models it is necessary to review their ability to account for, or incorporate, several salient features.

i) The symmetry of the tectonic zones around the Betic Cordillera, the Gibraltar Arc and the Rif and the Tell mountains.
ii) The formation of the Gibraltar Arc.
iii) The presence of a Neogene extensional basin floored by thinned continental crust centrally located within the Betic-Rif orogen.
iv) The approximately radial thrusting around the Betic-Rif orogen. Kinematic evidence indicates a variation of shortening direction from NW in the Betic Cordillera (Banks and Warburton 1991), to W in the Gibraltar

arc region (Balanyá & García-Dueñas 1987, 1988) to WSW in the Rif (Frizon de Lamotte 1987).

v) The extensional detachments and the exhumation of high temperature and pressure metamorphic core complexes and upper mantle peridotites within the Internal Zone.

vi) The coeval occurrence of extension in the Alboran basin and the Internal Zones and compression in the External Zones in an overall compressive regime.

vii) The pattern of palaeomagnetic rotations about a vertical axis which shows a predominantly clockwise rotation in the Betic Cordillera compared with a predominantly anticlockwise rotation in the Rif Mountains (Platzman 1992).

A review of the current models with respect to the above seven points is shown in Table 1.2.

The first models proposed for the evolution of the orogen involve the formation of nappes of the various Internal Zone complexes which were believed to be derived from separate domains (e.g. Blumenthal 1927, Fallot 1948, Durand-Delga 1966, Egeler & Simon 1969) (Fig 1.2.1). The later nappe models incorporate gravity sliding driven by locally developed body forces related to the development of a high. This was postulated to have developed due to either crustal thickening in the centre of the orogen or doming due to a thermal anomaly or diapir (Van Bemmelen 1969, Loomis 1975, Mäkel 1985, Weijermars 1985, Torres-Roldan 1979). Although this model can account for the symmetry of the tectonic zones around the arc and some extension at the centre of the orogen it cannot predict the exhumation of the high temperature/high pressure metamorphic

complexes and upper mantle peridotites, and the observed pattern of palaeomagnetic rotation.

Oroclinal bending of an originally linear mountain belt, formed earlier in the Betic-Rif deformation, has been postulated for the Betic-Rif orogen (Carey 1958, Didon 1969, Tubía & Cuevas 1987). However a problem arises as it is necessary to place this deformation post-late Miocene, when the initial deformation was still occurring in the External Zones. The extension that would result from oroclinal bending would occur to the convex (westerly) side of the arc, where there is no evidence for this, rather than at the centre of the orogen. Also the pattern of magnetic declination rotations predicted from this model should vary smoothly around the arc which is not observed (Platzman 1992).

The traditionally popular model invokes plastic indentation tectonics (Molnar & Tapponier 1975). It proposes westward displacement of an independent Alboran microplate, comprising the Internal Zones of the Betic and Rif and the Alboran Basin. This displacement predicts the formation of zones of dextral and sinistral transpression along the north and south margins of the microplate respectively (Andrieux et al. 1971, de Smet 1984, Boullin et al. 1986, Sanz de Galdeano 1990) (Fig 1.2.2). LeBlanc & Olivier (1984) define the boundaries of this microplate as the Internal /External Zone boundary of southern Spain (the North Betic Fault) and the Jebha fault, which extends from Morocco into the Mediterranean Sea. They extend the earlier models, implying that `locking' of these faults will occur as the displacement progresses in Burdigalian times, causing the main boundary faults to become more external. They advocate the Crevillente and Nekor faults, initiated in the mid to late Miocene, as being the later

microplate boundaries. The main drawback of this model is that it fails to account for the non-rigid behaviour i.e. pervasive compressional and extensional deformation, within the Internal Zones. Also, this model does not predict palaeomagnetic rotations at the tip of an indentor as are observed in the Northern Rif Mountains.

Frizon de Lamotte et al. (1989) regard the Internal Zones as a double pile of nappes. The upper pile (Upper Apujarride and Malaguide complexes) exhibit structures consistent with an earlier mean northward transport direction. The lower pile (Lower Alpujarride and Nevado-Filabride complexes) exhibit pervasive deformation consistent with a later westward transport direction. In this model the Internal/External Zone boundary, with northward overturning of the Alpujarride complex, is inferred to be a lateral structure related to drag affects. They explain the exposure of the high P/T Nevado-Filabride complex as due to culminations in the imbricate nappe pile as a result of hangingwall stacking, and propose a morpho-tectonic relationship between these culminations and the development of adjacent Miocene basins which they believe are controlled by `the swelling and thinning of the westward flowing nappe pile.'

This postulated westward displacement of a microplate requires a driving mechanism. Opening of the Algerian-Provençal Basin in the early to middle Miocene has been invoked by Sanz de Galdeano (1990) as a possible mechanism. The presence of a N-S subduction zone to the west has been theorized but there is no geophysical evidence to support this.

The significant palaeomagnetic rotations which occur in the Betic Cordillera have been accounted for by Osete (1989) as having developed in a broad zone of distributed dextral strike slip (Fig 1.2.3). This however,

would only produce clockwise rotations and does not in any way account for the anticlockwise rotations observed in the Rif mountains.

All the models described above do not adequately account for the presence of the Alboran Basin and the underlying thinned crust, and low velocity mantle (Banda et al. 1983) or provide a viable mechanism for exhuming the high P/T rocks of the metamorphic core complexes. Radial syn- or post-orogenic collapse of an overthickened collisional ridge situated in the Alboran region, during a period of slow Africa/Europe convergence, has been invoked (Doblas & Oyarzun 1989, Platt & Vissers 1989) (Fig 1.2.4). Doblas & Oyarzun (1989) propose a post-orogenic extensional collapse model in which they believe compressional and extensional events to be well-differentiated and relate all Neogene phenomena to be a product of the extension and associated aethenospheric upwelling. The model of Platt & Vissers (1989) implies delamination of cold and gravitationally unstable lithosphere from beneath the collisional ridge, in the late Oligocene to early Miocene, which causes an increase in the surface elevation and gravitational potential energy of the ridge (England & Houseman 1988). When the increased vertical stresses exceed the horizontal stresses arising from plate convergence, extension will occur in the central region with associated compression in the external regions to accommodate this.

This model has been extended by Platzman (1992), who proposed oblique relative convergence along the margin of the Alboran domain to account for the observed palaeomagnetic rotations (Fig 1.2.5). This obliquity was calculated by combining the motion of the Alboran margin relative to its centre of mass, generated by the extensional collapse, and the relative motions of Eurasia with respect to the Alboran domain and

Africa. Dextral shear and therefore clockwise rotations would be produced in the External Zones of the Betic Cordillera with concomitant sinistral shear and anticlockwise rotations in the External Zones of the Rif. As this proposes a collapse of an ENE-WSW ridge, a greater amount of elongation will occur E-W than N-S resulting in an overall displacement of the Alboran domain to the west.

It is quite apparent that the model of formation of the Betic-Rif orogen, with its broad and varied zone of deformation cannot be predicted from the relative plate motions alone.

1.3. Discussion of arcuate orogens

The majority of the orogenic belts around the world exhibit curvature of their regional structural trend in plan view. The Alpine - Himalayan orogenic belt shows a number of separate arcuate mountain belts within its broad zone of deformation which is only to be expected from the complex interactions of the varying rheologies and structural styles, and the presence of coherent blocks within such a wide area of compressive deformation (England & Jackson 1989). The arcuate belts of the Mediterranean region reflect these interactions by exhibiting a wide range in orientation of their tectonic displacement vectors (Fig 1.3.1). Most models of wedge dynamics fail to describe this 3-D phenomenon adequately and hence many workers use scaled models to investigate the mechanisms behind arc formation e.g. Marshak (1988).

Historically there have been many theories to account for the origin of arcuate belts. The grounding work, pre plate-tectonics, was by Carey (1955, 1958) who divided arcuate orogens into primary bends, which were initiated with their present form, and secondary bends or oroclines, which resulted from the impression of a later strain on a previously straight orogenic belt. This definition of oroclines was extended by Eldredge et al. (1985) to include belts that were previously less curved and not necessarily linear. Subsequent overusage of the term orocline has now led it to be merely a descriptive term meaning any arcuate orogen regardless of its primary or secondary nature. Recent work by Marshak (1988) reclassifies oroclines or rotational arcs, as bent orogens in which segments of the orogen change strike during the evolution of the bend, not necessarily at a distinct, later stage, and primary bends or nonrotational arcs, as bent orogens in which segments of the orogen do not change strike during development of the bend.

Arcuate orogens may vary greatly in their dimensions and symmetry. Their geometry may be described with reference to the direction of tectonic vergence. An antitaxis is an arc which is convex towards the foreland, whereas a syntaxis is an arc which is concave towards the foreland in plan view.

A distinction is made between bends in a thick-skinned or thin-skinned orogen. The kinematic evolution of the latter can be described in terms of the following three parameters and hence its rotational or nonrotational nature may be established:

i) The displacement path trajectories followed by points along the strike of the orogen.

ii) The magnitude and distribution of tangential extension along the strike of the orogen.

iii) The change in position of the endpoints of the orogen with respect to a reference line.

The strain pattern, and its variation both spatially and temporally around an arc may be ascertained by detailed structural analysis and palaeomagnetic studies. Structural analysis should involve collection of kinematic data, location of major shear zones, establishment of the presence of extension and how it is accommodated together with the timing and evolution of all the above. Palaeomagnetic studies may elucidate whether any significant systematic rotations around a vertical axis have occurred, as predicted in the formation of rotational arcs. This rotation cannot be further classified into either block rotation or rotation of individual thrust sheets by palaeomagnetic studies alone. Declination variations have been shown to exist in some but not all arcuate orogens (Grubbs & Van der Voo 1976, Van der Voo & Channell 1980, Eldredge et al. 1985).

The models which have been proposed in recent literature to account for the formation of arcuate orogens may be divided into seven different mechanisms which are summarized below and in Fig 1.3.2:

i) Later noncoaxial deformation.
ii) Movement along wrench faults and within shear zones.
iii) The generation of local body forces.
iv) The presence of an originally irregular continental margin and hence facies distribution.
v) The action of a rigid indentor against the deforming margin.
vi) The presence of one or several obstacles in the foreland.

vii) Formation of independent thrust corridors.

Four of the above mechanisms, iii), iv), v), and vii), are more likely to produce nonrotational arcs, but it is possible for all of them to produce rotational arcs. The difference between nonrotational and rotational arcs in these cases, which show only slight variation in their displacement paths, is of no major tectonic significance. The causal mechanism behind the arc formation is, however, important.

i) Later noncoaxial deformation was the original mechanism invoked by Carey (1955, 1958) to account for the formation of several arcuate orogens and Ries & Shackleton (1976) to explain the Iberian arc. Superposition of a second deformational phase on a segment of an earlier formed orogen may cause oblique reactivation of existing faults and a continuous change in structural trend from an unaffected segment into that which has been reactivated and rotated. An example of this occurs in the Appalachian fold and thrust belt near Kingston, New York (Alterman 1984, Marshak et al. 1985). This model is also proposed for the Pamir-Himalaya arc (Sarwar & De Jong 1979).

ii) Movement along wrench faults can result in the reorientation of structures in a fold and thrust belt as it is strained by simple shear in plan view. This may occur adjacent to a major shear zone, for example the left-lateral Chaman fault of SW Pakistan (Sarwar & De Jong 1979, Platt et al. 1988) or in a zone of shear involving several wrench faults (Van der Voo & Zijderveld 1969, Ricou & Siddans 1985). Graham (1978) suggested that formation of arcuate belts within the cover sequence of the western Alps

may result from strike slip faults within the basement in conjunction with a detachment zone at the base of the cover.

iii) An arcuate pattern of thrusts may be produced by locally generated body forces within a thickened thrust wedge in an area of oblique convergence. The gravitational pressure gradients generated act in the direction of greatest surface slope and produce an arc-normal pattern of motion. This has been proposed as an important factor in the formation of the western Alps (Platt et al. 1989a, Platt et al. 1989b).

iv) An irregular continental margin may be formed by a number of processes during its passive rifting stage; for example the geometry of triple junctions during the initial stages of rifting and the position of transform faults or differential extension during the rifting. The shape of the margin and its bathymetry will determine the distribution of the stratigraphic units and hence décollement horizons which would have a strong control on the initiation and geometry of the thrusts (Davis & Engelder 1985). This may produce thrusts that were initiated with a curved plan view (Marshak 1988). This mechanism has been proposed for the Roberts Mountains, western Nevada (Oldow 1984), the Jura Mountains (Eldredge et al. 1985), the Idaho-Wyoming Overthrust Belt (Grubbs & Van der Voo 1976) and possibly the Pennsylvania salient, although this is still under debate (Schwartz & Van der Voo 1983, Miller & Kent 1986).

v) The action of an indentor, a relatively rigid crustal block which impinges on a continental margin, can cause a variation in the stress field along strike and hence an arcuate strain pattern. An indentor may be described as a microplate colliding with a convergent margin or a

promontory of a continental margin against which a wedge is deforming. Sand wedge modelling of this indicates such a mechanism would result in the likely formation of nonrotational arcs as the faults formed showed an initial arcuate trace and did not bow out to the foreland with progressive deformation. Instead the faults became inactive and with progressive deformation new faults developed towards the foreland (Marshak 1988). This mechanism has been proposed for the Sicilian-Calabrian arc, involving the rigid Calabria-Peloritani block colliding with the southern Tethyan margin of Sicily and Italy (Eldredge et al. 1985) and the Himalayan arc, invoking the Indian subcontinent as the indentor with the added complexity of the indentor itself being underthrust (Tapponier & Molnar 1977).

vi) The presence of one or several obstacles in the foreland may impede the movement of the thrust wedge and cause significant bending. A variety of geological phenomena may act as obstacles, for example, a basement massif on an underthrust plate or a stratigraphic pinch out of a décollement horizon e.g. the Sulaiman Range of Pakistan (Sarwar & De Jong 1979, Jaumé & Lillie 1988). Pinning of a segment of the wedge by an obstacle may cause the formation of a coupled arc i.e. a genetically related syntaxis and antitaxis.

vii) The formation of independent thrust corridors has been proposed as a mechanism for producing an arcuate structural trend in plan view. These may be active synchronously or to some extent serially and have been proposed for the western Alps (Cobbold et al. 1985, Vialon 1987).

None of the above mechanisms are mutually exclusive and within an individual arcuate orogen a combination of any number of these mechanisms may have contributed towards formation of the arc.

1.4. Objectives of the thesis

The Prebetic Zone, being the most external zone of the Betic Cordillera, has tended to be overlooked as an interesting and informative study areas in favour of the more obvious attractions of the Internal Zones and the Gibraltar Arc.

The main objectives of this thesis were to compile a comprehensive structural study of the arcuate Prebetic thrust belt and to reconstruct its deformational history. Presently, there is a wealth of models proposed for the formation of the Betic-Rif orogen in the literature. The results of this study were intended to be used to test the validity of these models and also to assist a more detailed understanding of the factors contributing to, and the mechanisms employed in, the formation of small-scale arcs within an orogenic belt.

1.5. Working methods

1.5.1. Collection of field data

Within the Prebetic thrust belt, data relating to the fault geometries was collected and their displacement sense ascertained using analysis of crystal fibres, Reidel shear planes, fault gouges and fold asymmetry.

Representative sections were logged and attempts were made to provide tighter constraints on the correlation and dating of the Tertiary units present. Collection of the above data facilitated the construction of several balanced cross-sections.

1.5.2. Computer analysis

The sub-surface structure of the eastern Betic Cordillera was constructed using gravity modelling techniques on existing gravity data.

Basement and tectonic subsidence curves were constructed by backstripping various sections compiled from around the Prebetic Arc using the program devised by Dr. N. White, Cambridge University.

1.5.3. Laboratory analysis

Demagnetisation of palaeomagnetic cores from several sites was undertaken. Unfortunately the lithologies present within the Prebetic Zone were not suitable for extensive palaeomagnetic studies.

CHAPTER 1

FIGURES

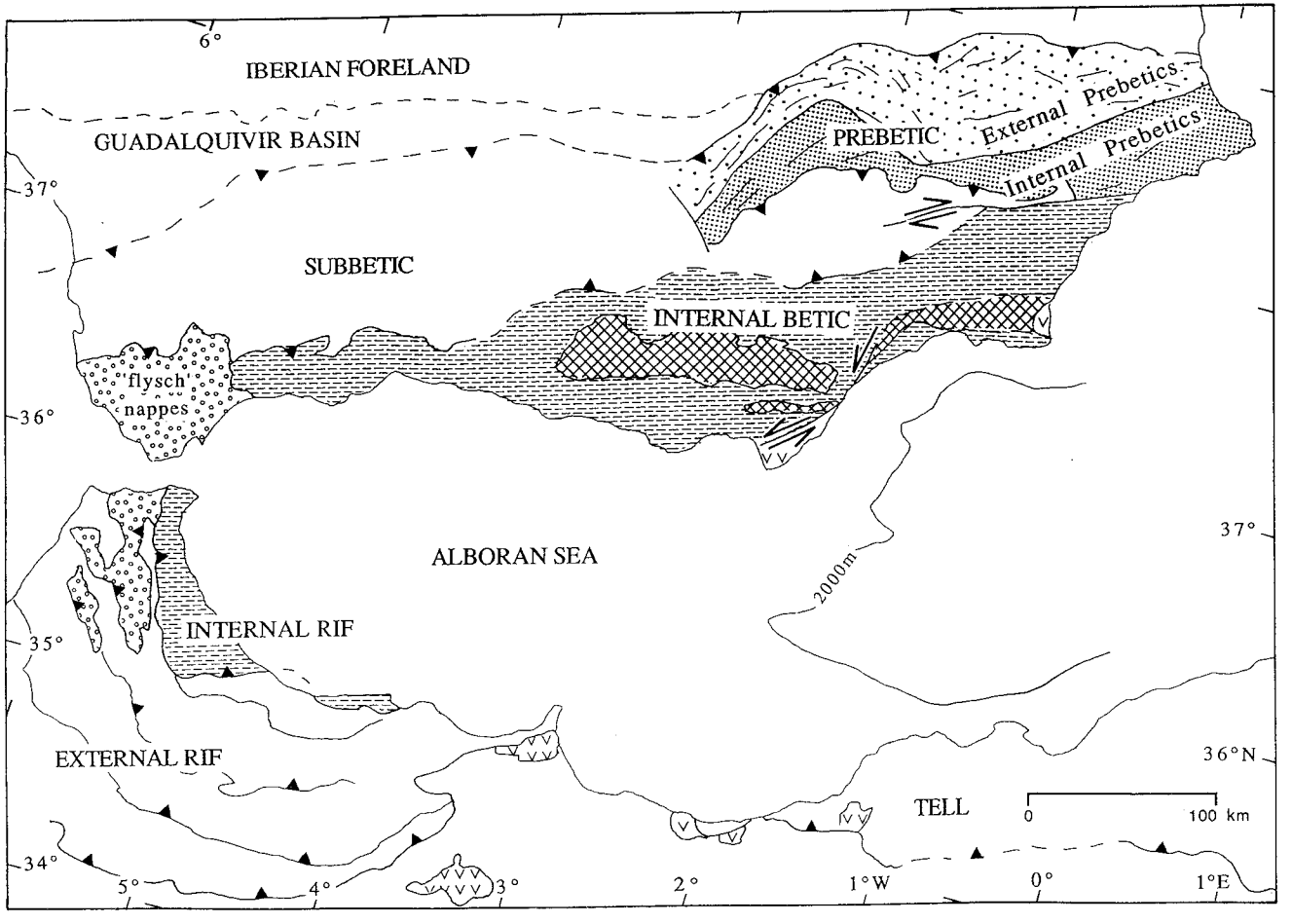


Fig 1.1.1. Structural map of the Betic-Rif Orogen. Dashed area represents low P/T Alpujarride and Malaguide Complexes. Cross-hatched area represents the high P/T Nevado-Filabride Complex. V-Neogene volcanics.

a)

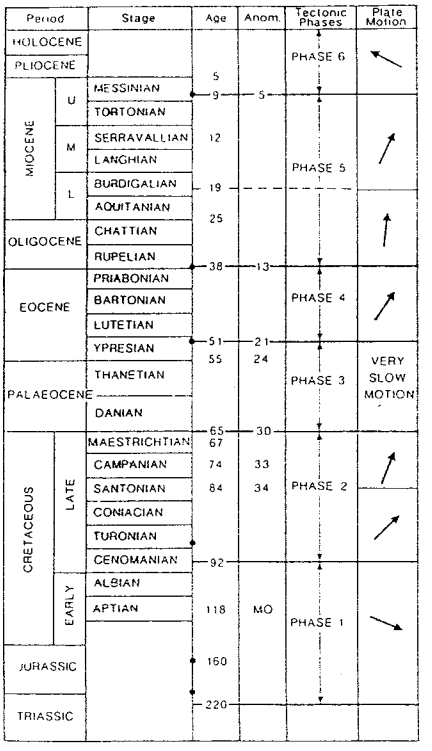


Fig 1.1.2. a) Correlation chart showing the general direction of Africa's motion with respect to Europe after Dewey et al. (1989).

b)

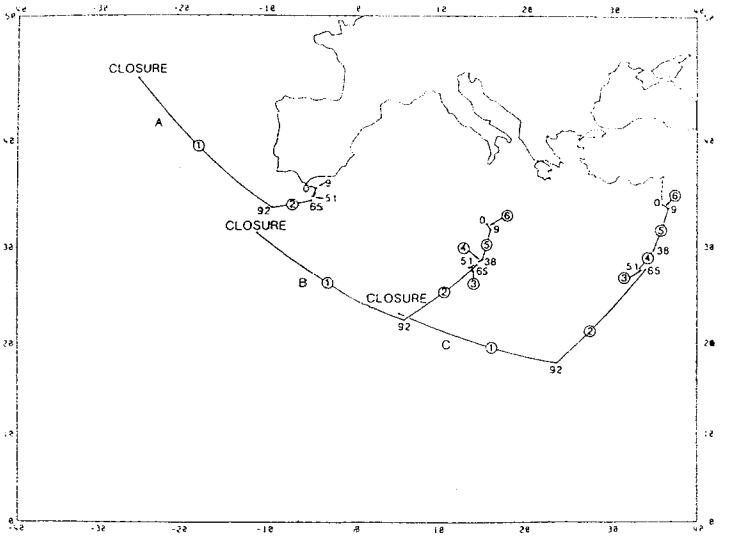


Fig 1.1.2. b) Motion of three points on Africa with respect to Europe from 92 Ma to the present after the translation paths have been smoothed and simplified into six stages (Dewey et al. 1989).

	Gravity sliding of nappes	Oroclinal bending	Microplate (plastic indentation)	Strike slip - dextral shear zone	Extensional collapse
i) symmetry of tectonic zones around the arc	Yes	Yes	No	No	Yes
ii) formation of Gibraltar Arc	Yes	Yes	Yes	? possibly by small block rotation	Yes
iii) extensional basin in centre of orogen	Extension by gravity sliding - from thickened crust or thermal doming	No - extension only predicted on convex side of arc	No ? to the east (Algerian- Provançal Basin)	No	Yes
iv) radial thrusting around the arc	Yes	Possibly	No	No	Yes
v) extensional detachments, meta complexes and mantle peridotite	No	No	Traditionally No - partly explained by Frizon de Lamotte 1989	No	Yes
vi) coeval extension and compression	Yes	Yes	Traditionally No - explained by Frizon de Lamotte 1989	No	Yes
vii) pattern of palaeomag rotation	No - does not produce a systematic pattern	No - would expect a smooth variation around the arc	Only agrees with rotations to the N and S, not to the W	No - expect consistent clockwise rotation	No Yes if modified by oblique convergence (Platzman 1991)

Table 1.2. Summary of the models of tectonic evolution for the Betic-Rif Orogen.

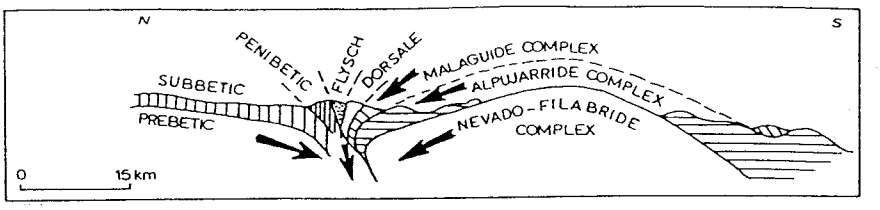


Fig 1.2.1. Nappe model after Durand-Delga (1966).

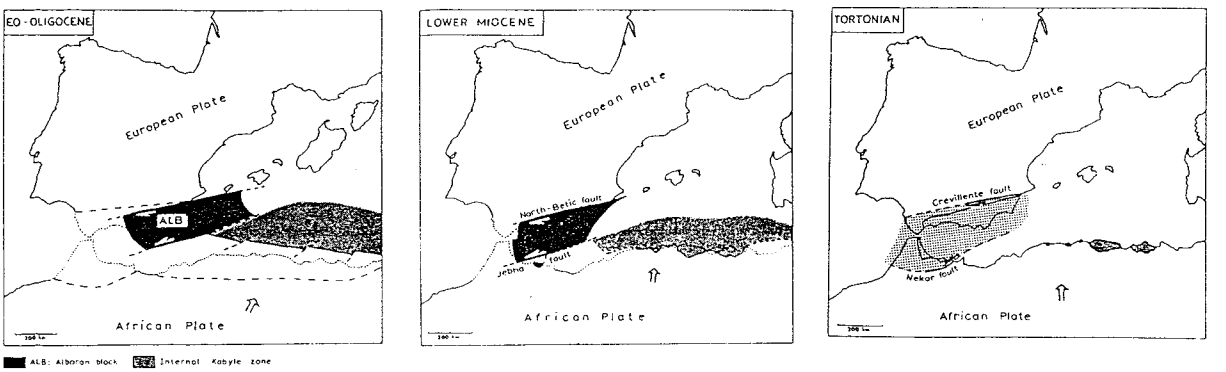


Fig 1.2.2. Independent Alboran microplate model after LeBlanc & Olivier (1984). The westward displacement of the Alboran microplate with boundaries defined as the dextral North-Betic Fault (External/Internal Zone boundary) and the sinistral Jebha Fault is shown. Later locking of the faults causes the main boundary faults to switch to the more external Crevillente and Nekor Faults.

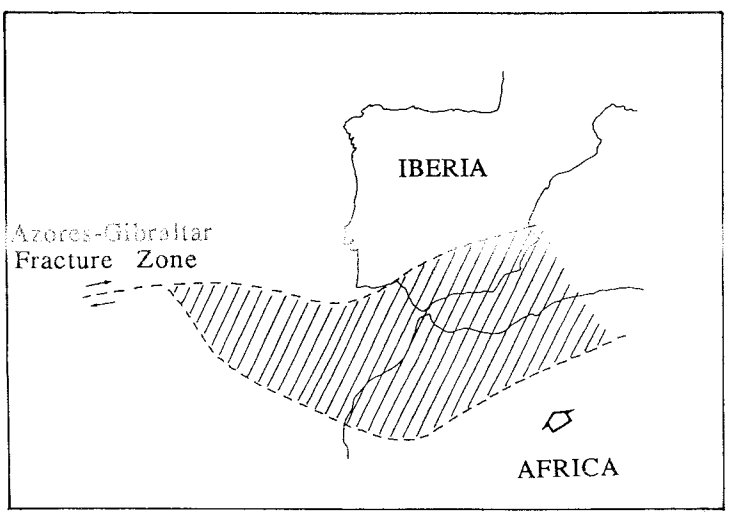


Fig 1.2.3. Broad zone of distributed dextral shear model after Osete (1989). Geodynamic setting for the middle Tortonian-Present for the zone of deformation between Iberia and Africa.

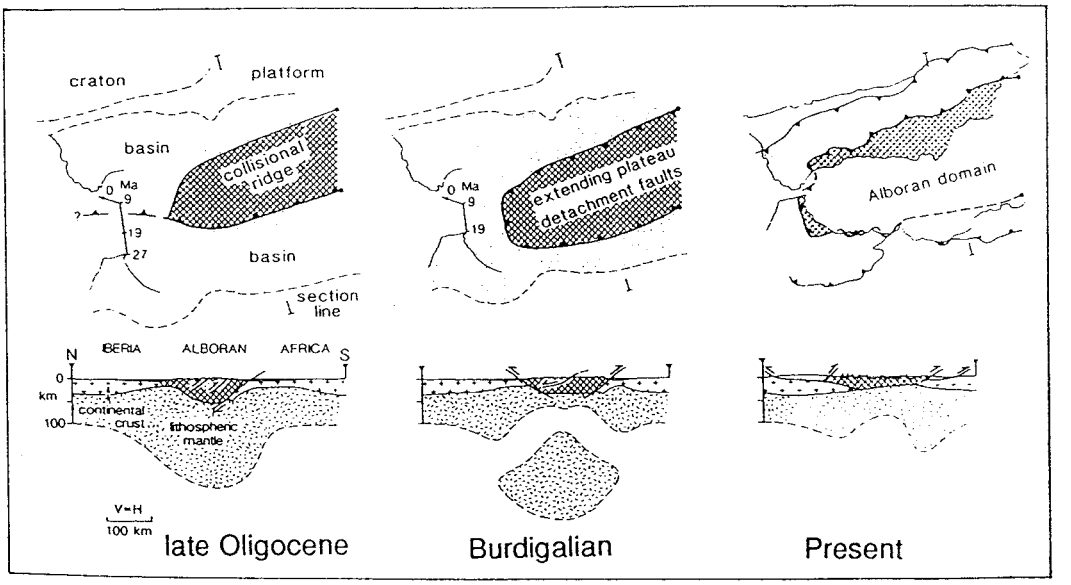


Fig 1.2.4. Extensional collapse model after Platt & Vissers (1989). Radial syn- or post-orogenic collapse of the overthickened ridge in the Alboran domain is initiated in the late Oligocene to early Miocene due to delamination of unstable lithosphere.

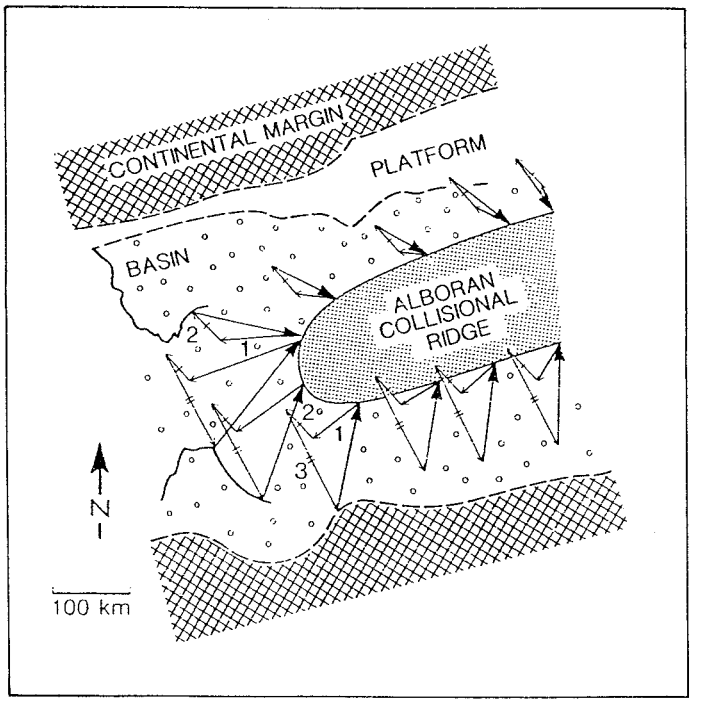


Fig 1.2.5. Oblique relative convergence model after Platzman (1992). The time-averaged motion of Eurasia and Africa relative to the margin of the Alboran domain from 27 Ma to the present. Along the northern margin, relative motion between Eurasia and the Alboran margin is derived from (1) motion of margin relative to centre of mass of extending Alboran domain and (2) motion of centre of mass of Alboran domain relative to Eurasia. Along the southern margin, relative motion between Africa and the Alboran margin is derived from (1) and (2) above and (3) motion of Eurasia relative to Africa.

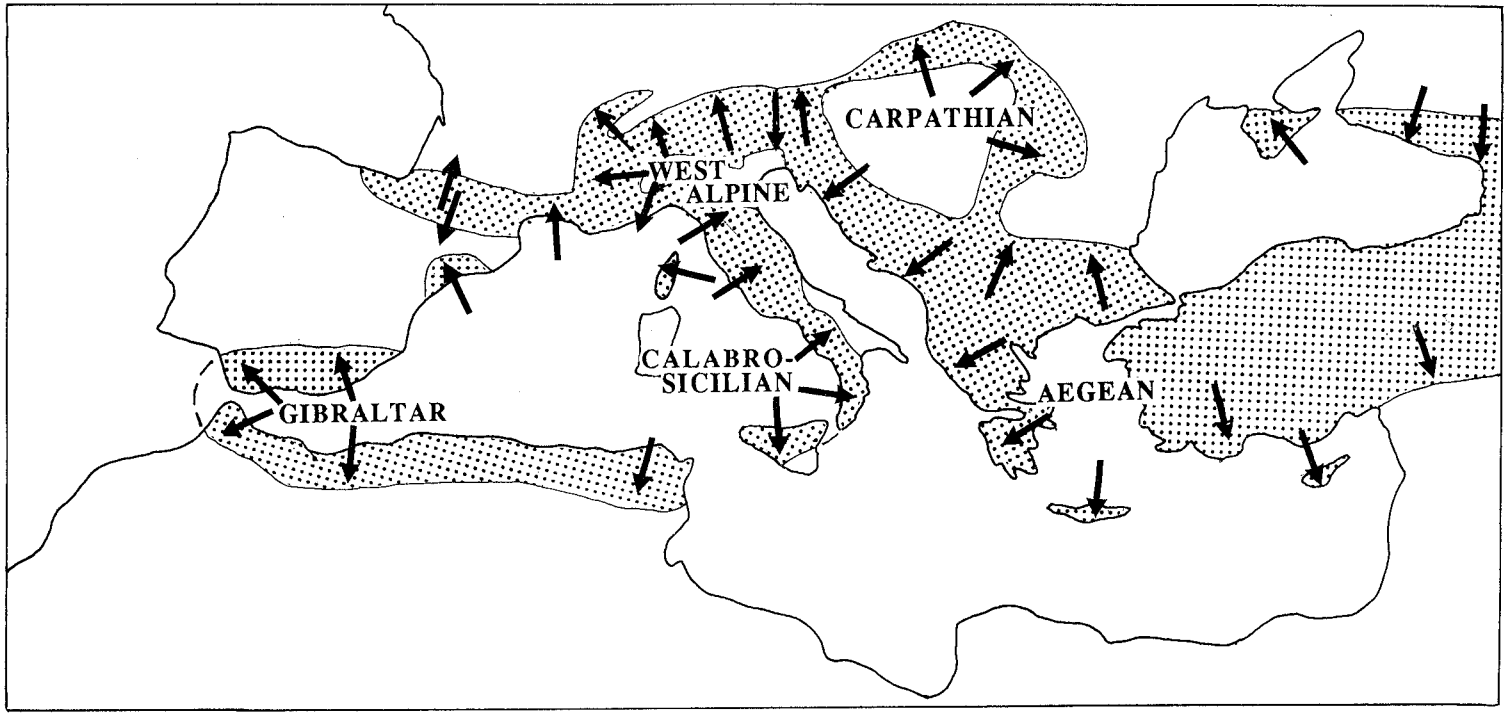


Fig 1.3.1. A map of the Mediterranean area showing the five main orogenic arcs and associated variation in tectonic transport direction.

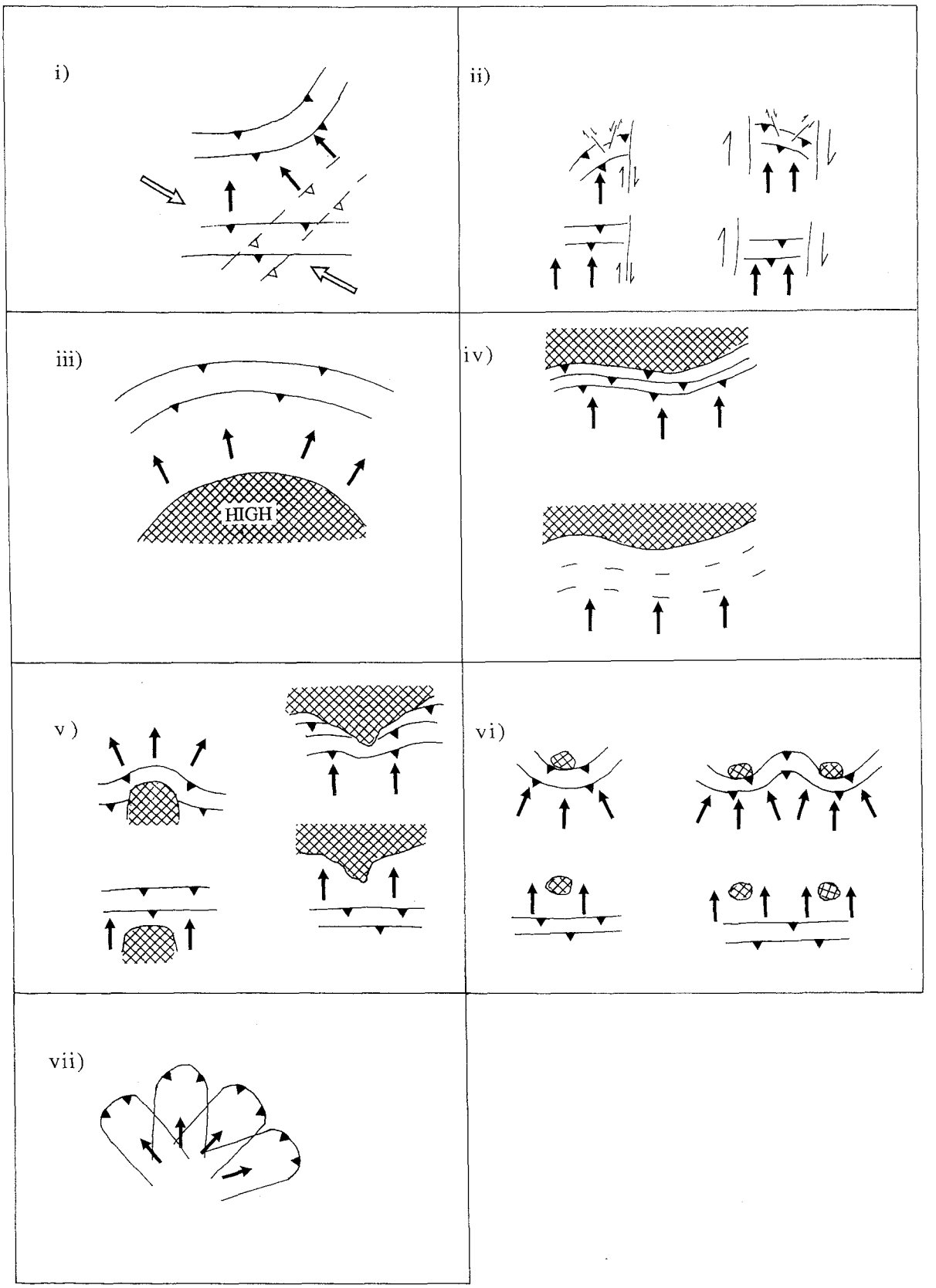


Fig 1.3.2. Summary of the models which can account for the formation of arcuate orogens. i) Later noncoaxial deformation (shown by open arrows). ii) Movement along wrench faults and within shear zones. iii) The generation of local body forces. iv) The presence of an originally irregular continental margin and facies distribution. Dashed lines schematically represent the facies boundaries. v) The action of a rigid indentor against a deforming margin. The indentor may be translated towards a previously linear orogen or the linear orogen may be translated towards a stable indentor. vi) The presence of one or several obstacles in the foreland. Note that syntaxes and antitaxes are both formed when several obstacles are in the foreland. vii) The formation of independent thrust corridors.

Chapter 2

CHAPTER 2

DEFORMATIONAL VARIATION AROUND THE ARC

2.1. Introduction

The Prebetic Zone, the most external zone of the Betic Cordillera, is exposed predominantly in the eastern Betics. It has been inferred to continue westwards to some extent, beneath the Guadalquivir Basin and the Subbetic nappes from seismic and borehole data (Hermes 1978).

Differentiation of the Prebetic Zone into two palaeogeographic subdivisions by the variation exhibited in the stratigraphic sequence, is well accepted (Jerez Mir 1973, Hermes 1978, Garcia-Hernandez et al. 1980) (Fig 2.1.1). The External Prebetics are characterised by a thin Mesozoic cover sequence with notable stratigraphic gaps in the Jurassic and early Cretaceous. The Triassic near the margin of the stable Meseta is predominantly clastic in origin whereas towards the interior of the basin carbonate of Muschelkalk facies is found. The Lower Jurassic is represented by dolostone with an increasing upward proportion of marl and clay interbeds. The Middle Jurassic is, again, predominantly dolostone capped locally with limestone whilst the Upper Jurassic sediments are typically nodular limestone in the Middle-Upper Oxfordian, and marl and marly limestone in the Lower Kimmeridgian, and contain abundant ammonite fauna. The thin Upper Cretaceous sequence consists of Cenomanian dolostone and Senonian lagoonal deposits. The External Prebetics became emergent during the Paleogene causing the Miocene units to transgressively overlie the Mesozoic rocks (Fig 2.1.2).

The Internal Prebetics possess a thicker Mesozoic sequence with fewer stratigraphic gaps, which, when present, are located around marginal areas or associated with diapiric structures in the Triassic rocks. The units of the Internal Prebetics began to differ significantly from those of the External Prebetics in Upper Jurassic times, which is represented by a

more developed sequence in Purbeck facies. The Early Cretaceous shows a wide range of facies which become more pelagic to the SSE, the interior of the basin. In the Aptian - Albian, shallow water carbonate Urgonian facies are developed which are overlain by the sands and clays of the Utrillas Formation, which contain a continentally derived component. The Upper Cretaceous dolomite and limestone are undoubtedly pelagic. The Internal Prebetics differ markedly from the External Prebetics in that they possesses a well developed Paleogene shallow marine sequence with coastal and continental episodes, especially in the southernmost region. The Miocene may unconformably overlie Cretaceous or Paleogene units.

As can be seen from satellite images, the structural trend of the External Prebetic Zone exhibits a sigmoidal geometry in plan view where an antitaxial and a syntaxial arc (as defined in section 1.3) are coupled together (Fig 2.1.3). The deformational style and kinematic movement vectors can be shown to vary substantially around the arc of the External Prebetics, which has therefore been divided up, using these criteria, to facilitate detailed study. Fig 2.1.1 shows the locations of these four sub-areas: the NE Trending Limb, the Alcaraz Antitaxis, the NW Trending Limb and the Cenajo Syntaxis, and the positions of the two important strike slip faults, the Socovos and the Tiscar Faults, which affect the western eastern Prebetic Zone. A comparison of their representative stratigraphic sequences is shown in Fig 2.1.4.

The Prebetic arcuate orogen has been relatively less studied compared to some other Mediterranean arcs, which are on a larger scale, such as the Western Alpine Arc and the Gibraltar Arc. Hermes (1978) suggested that the whole Prebetic Zone had been laterally displaced as a

coherent crustal block to the ENE, forming the Guadalquivir depression in its wake. This rather extreme hypothesis appears unlikely as there is no obvious driving mechanism for the displacement and no evidence of the large scale shear zones invoked at the margins of the Prebetic Zone. To the north the Mesozoic of the Prebetic Zone continues undisturbed onto the Meseta, whilst the southern margin, the Prebetic/Subbetic boundary is a NW directed thrust contact (Platt & Allerton, pers. comm.). Banks and Warburton (1991) describe the Prebetic Zone as a foreland fold and thrust belt formed by oblique restacking of a stretched continental margin due to compression but do not account for the arcuate geometry. Guezou et al (1991) present results of kinematic analysis in the NE Trending Limb of the Prebetic Zone, which indicate a bulk translation to the WNW. They cite this as evidence to support the model of Betic-Rif formation of Frizon De Lamotte et al (1989) in which there is westward translation of the Alboran Domain with displacement trajectories which are independent of strike and subparallel all along the belt. More detailed kinematic and timing relations studies, however, show that this WNW translation does not apply to all sub-areas of the Prebetic Zone, nor is it consistent through time.

To determine the mechanism of formation of the Prebetic Arc it is necessary to describe the strain pattern, spatially and temporally around the arc and the magnitude and distribution of any tangential extension (section 1.3). To elucidate the strain pattern, kinematic data in the form of the orientations of wear grooves, and crystal fibres was collected systematically from meso-scale faults around the arc. The meso-faults are concentrated in 1-10m zones at the base of the thrust sheets. Fig 2.1.5. shows the kind of features which develop within a brittle shear zone. The

sense of shear was inferred by fault gouge (Fig 2.1.6) and Reidel shear plane analysis (Fig 2.1.7a/b and stereoplot 2.2.1.26 j), the direction of growth of crystals along the fault plane (Fig 2.2.1.27) and the geometry of the thrusts and their cut-offs (Fig 2.1.8) (Hancock 1985, Rutter 1986, Petit 1987). In areas where the stratigraphic sequence is dominated by limestone and/or dolomite, fault planes and associated Reidel shear planes are well developed; in areas where the stratigraphic sequence comprises a significant marl and mud content, fault planes and associated Reidel shear planes are ~~commonly~~ less developed and fault gouges were more commonly found within the shear zones.

2.2. Description of the deformation around the arc

A summary of the variations in tectonic transport directions around the Prebetic Arc is shown in Fig 2.2. (values shown in Appendix 1). A description of the deformation experienced by each of the four sub-areas, using the thrust tectonic terminology of Boyer & Elliott (1982) and McClay (1991), is detailed below:

2.2.1. The External Prebetics

2.2.1.1. The NE Trending Limb

The shortening in this limb is characterised by sub-parallel NE-SW trending, hinterland dipping thrust faults which are laterally continuous for tens of kilometres. The thickness of these thrust slices varies in scale from hundreds of metres to kilometres depending on the thickness of the original sedimentary sequence and the position of the thrust slice within

the deforming wedge. Original continental-margin extensional faults are preserved locally. Backsteepening of earlier thrust sheets is accommodated by backthrusting and normal faulting (Figs 2.2.1.1-3) and results from the propagation of the thrusts towards the foreland in a piggy-back manner. A gradual change in transport direction from NW to more WNW with progressive deformation towards the foreland is observed across the Tranco area (Fig 2.2.1.2) and across the Orcera area (Fig 2.2.1.4). Concomitant ESE backthrusting also occurs, associated with the later WNW thrusting and cross-cutting more hinterland structures (Figs 2.2.1.4-6).

Towards the boundary with the Internal Prebetics is a zone [the Tranco Zone of Banks & Warburton (1991)] in which Triassic rocks are exposed at the surface (Fig 2.1.1). This indicates a ramping of the sole thrust, from a décollement horizon within the Triassic to one at the base of the Jurassic, at a location further to the SE. The Prebetic Front or sole thrust is weakly emergent at the erosional surface (classification of Morley 1986) and Messinian marls are incorporated into the most frontal thrust slices (Fig 2.2.1.7). Passive roof duplexes, in which the roof thrust has a backthrust sense and the roof sequence remains relatively stationary during foreland propagation, have developed at various positions across the belt (Figs 2.2.1.8a/b/c). These duplexes may represent locations of temporary sticking points of the orogenic front when it would possess, transiently, a foreland dipping frontal slice (Banks & Warburton 1986, Baby et al. 1992). Comparison of the tectonic transport vectors of the roof slice, the duplex horses and the more foreland and hinterland thrust slices indicate a possible small local variation in the tectonic transport vector of the roof slice (Fig 2.2.1.9). This is probably caused by later translation of the roof slice of the culmination as the duplex formed.

Dextral tear faults, orientated approximately WNW-ESE, cross cut the main thrust faults (Fig 2.2.1.10). These lateral structures facilitate the WNW shortening accommodated by the thrust stack and may divide areas which show an along-strike variation in structural style e.g. a different number of thrust slices or thrust slices with different dimensions or geometry. Analysis of these tear faults indicate the presence of only one family of faults (Fig 2.2.1.11). To the SW of the limb is a major dextral wrench fault, the Tiscar Fault (Foucault 1971) which contains the leading branch point of the Prebetic Front and the Subbetic Front (Guezou et al. 1991).

A balanced section has been constructed across the NE Trending Limb which is described in detail in section 5.2.1. Restoration of this cross-section indicates that the area has undergone 69% shortening to the NW in the Tortonian and Messinian.

To the northeast, in the Puerta de Segura - Puente Génave area, are several outcrops of porphoritic adamellite which contain quartz, plagioclase, biotite, zircon and opaques with secondary chlorite and sericite. They are attributed to the metasomatic remobilisation of Hercynian granites which were then emplaced into the upper Palaeozoic basement and Triassic in this part of the NE Trending Limb during the Tertiary deformation (IGME Memoir no. 865 Siles). The adamellite appears to have intruded along pre-existing planes of weakness i.e. the cleavage planes of the Hercynian basement, causing the development of planar contacts with the Palaeozoic metamorphic rock (Fig 2.2.1.12).

2.2.1.2. The Alcaraz Antitaxis

The structural trend around this part of the arc varies from NE-SW, through E-W, to NW-SE. The Prebetic Front is emergent around the antitaxis and cross-bedded Miocene bioclastics are incorporated into the frontal thrust sheets (Fig 2.2.1.13). The Tranco Zone which contains Triassic rocks at the surface is also present and the Triassic units can be shown to overthrust Jurassic units causing the formation of recumbent folds in the footwall (Fig 2.2.1.14). Shear zones within these Triassic units yield evidence for the subsequent remobilisation of gypsum (Figs 2.2.1.15a/b and stereoplot shown in Fig 2.2.1.16). Most of the shortening is accommodated by foreland propagating thrusts which are less laterally continuous than in the NE Trending Limb. The formation of the antitaxis due to differential shortening and strain partitioning across the Socovos fault causes a general divergent translation around the antitaxis and the development of conjugate strike slip faults (NE-SW sinistral, NW-SE dextral) which accommodate tangential extension predominantly in the outer region of the arc (also shown by Marshak (1988) to occur in other arcuate orogens) and can be shown to cross-cut earlier deformation (Figs 2.2 and 2.2.1.17).

From kinematic analysis, later deformation in the hinge area is characterised by oblique backthrusting giving rise to small fault bounded blocks which are locally complex (Figs 2.2.1.18-20). This later deformation may be associated with a change in the local stress regime of the frontal part of the thrust wedge as it interacts with obstacles in the foreland, i.e. the buttress of the Palaeozoic Massif and the stratigraphic pinch-out of the décollement horizon against it. This gives rise to oblique backthrusting to accommodate the tightening of the hinge angle with progressive deformation.

2.2.1.3. The NW Trending Limb

The strain exhibited by this limb is partitioned into dextral displacement along the near-vertical Socovos wrench fault and a series of NW-SE trending thrusts and backthrusts (Figs 2.2.1.21/22), which may reactivate original continental margin extensional faults (Fig 2.2.1.23). The Prebetic Front, from this sub-area eastward, becomes a blind thrust as the deformation of the Prebetic Zone and the Iberian Chain overlap (Fig 2.1.1). There is a greater amount of folding within these thrust slices compared with those of the NE Trending Limb. This is probably facilitated by the increased limestone and marl content of the stratigraphic sequence. The coaxial thrust/backthrust deformation progresses towards the NE with episodes of thrusting and foreland propagating backthrusting which may cross-cut earlier structures. The backthrusts, formed at the thrust front, cause the development of a blind front geometry (Price 1981, Vann et al 1986) and the formation of a passive-roof duplex (Banks & Warburton 1986). Where there is convergence of the differing polarities of thrusting a triangle zone is formed, between two thrusts with the same basal detachment and with opposing vergence (McClay 1991) and where there is a divergence of the thrusting directions, there is a jacking-up of a thrust slice (section 5.2.2). Rapid frontal accretion of material onto this limb is facilitated by the lack of basement massifs in the foreland.

The Socovos fault shows evidence for major NW-SE dextral motion with subsidiary minor NE-SW sinistral motion (Fig 2.2.1.24). Oblique overthrusting to the N/NNE occurs locally on faults within contractional strike slip duplexes (Woodcock & Fischer 1986). The pattern of kinematic vectors, which show an increased alignment of vectors towards the Socovos fault, indicate possible minor block rotations associated with progressive displacement along this fault (Fig 2.2.1.21).

Common in this limb, and further to the east, are Miocene syn- to post- deformational basins (Fig 2.1.1), which may exhibit intra-formational unconformities (Fig 2.3.4), and are translated towards the foreland by piggy-back thrusting.

A balanced section has been constructed across the NW Trending Limb which is described in detail in section 5.2.3. Restoration of this cross-section indicates that the area has undergone 54% shortening to the NNE in the Seravallian.

2.2.1.4. The Cenajo Syntaxis

The structural trend of this part of the Prebetic Zone varies around an arc from NW-SE to NE-SW, with the hinge of the syntaxis showing both E-W and N-S intermediate structural trends.

The pattern of tectonic transport vectors shows converging NE, N and NW directed thrusts with a decreasing amount of coaxial backthrusting to the east (Figs 2.2, 2.2.1.21 and 2.2.1.25/26). This convergent pattern arises due to the NW thrusting in the east of the syntaxis, transferred from more hinterland zones, the NE thrusting caused by the strain partitioning across the Socovos Fault in the west of the syntaxis and their interaction within the hinge zone. This distribution of deformation and the subsequent tightening of the hinge zone with progressive deformation cause the superposition of transport directions, facilitated by the reactivation of existing faults which produces an oblique secondary lineation overprinting the pre-existing lineations. Figs 2.2.1.27 and 2.2.1.26 c) and d) indicate an initial phase of NNE-SSW thrusting/backthrusting by primary wear grooves, and an overprinting crystal lineation indicates superposed WNW-ESE thrusting/backthrusting. Figs 2.2.1.21 and 2.2.1.28

show two distinct trends of deformation, indicated by the pattern of the thrusts and confirmed by dating of syn-deformational basin unconformities. The earlier trend of NE-SW tectonic transport, shown to the west of Fig 2.2.1.21, was syn-orogenic with the Burdigalian, Langhian and early Seravallian deposits which are subvertical, but pre-dates the flat-lying middle Seravallian deposits. The later trend of NW-SE tectonic transport, to the east of Fig 2.2.1.21, post-dates the middle Seravallian deposits which are subvertical. In the centre of the area, more complex patterns of kinematic data are found due to the interference of the two phases of deformation.

Jerez Mir (1973) accounts for the formation of the Cenajo Syntaxis by substantial strike slip movement along dextral NE-SW and sinistral NW-SE faults (Fig 2.2.1.29). However, this block movement appears to cause space problems and is inconsistent with the pattern of tectonic transport vectors for the Cenajo area. The syntaxis was formed by convergent thrusting of overlapping sheets. Subsequent tightening of the hinge angle caused superposition of deformation and oblique reactivation of the thrust sheets (Figs 2.2.1.21 and 2.2.1.25).

Only minor ESE directed deformation is exhibited in the Messinian marls of the syntaxis, again, indicating that WNW-ESE directed translation is the younger phase of deformation (Figs 2.2.1.30 and 2.2.1.26.a). This deformation may be associated locally with diapirism as subsurface Triassic evaporite-cored anticlines became gravitationally unstable, due to their relatively low density, and the evaporite migrated towards the surface.

The distribution of the Tertiary basins in this area increases to the east, the direction of marine influence.

A balanced section has been constructed to the east of the Cenajo Syntaxis which is described in detail in section 5.2.3. Restoration of this cross-section indicates that the area has undergone 21% shortening to the NW in the Seravallian and Tortonian.

2.2.2. The Internal Prebetics

The Internal Prebetics differ from the External Prebetics in that their structural trend does not describe an arcuate pattern in plan view (Fig 2.1.3). The shortening across this zone, comprising a more complete Cretaceous and Paleogene sequence, is exhibited by NW-SE thrusting and backthrusting with a greater amount of gentle folding than the External Prebetics (Fig 2.2.2.1). The tectonic transport directions appear to become more WNW-ESE with progressive deformation towards the foreland (Fig 2.2). Original listric extensional faults are observed in outcrop and on seismic section causing a thickening of the sequence in the downthrown block (Banks & Warburton 1991) (Fig 2.2.2.2).

The northern boundary of the Internal Prebetics, with the External Prebetics, varies widely in its nature around the arc. In the area of the NE Trending Limb, the boundary was an original extensional fault across which there is a marked change in thickness of the Mesozoic sequence. Subsequently this was reactivated as a NW-directed thrust with the main phase of compressional deformation, and then locally exhibits a backthrust nature as back-steepening occurred with continued, piggy-back thrusting and thickening of the thrust wedge. The nature of this boundary is shown clearly in the Cazorla balanced cross-section (Fig 5.2.1.1). A similar style and history of deformation is found towards the hinge of the Alcaraz Antitaxis except that the later, local backthrusting is of a more oblique,

southerly nature. As the trend of the Alcaraz Antitaxis becomes more NW-SE into the NW Trending Limb, the Internal/External Prebetic boundary becomes a dextral strike-slip fault, acting as a lateral ramp for the shortening in the Internal Prebetics. The original palaeogeographic boundary between the External and Internal Prebetics becomes less distinct in the NW Trending Limb and to the east and its relationship to the current tectonic boundary between the External and Internal Prebetics is unclear. To the SE, the Socovos fault transfers its displacement onto the Subbetic Front causing the generation of Miocene pull-apart basins, e.g. the Abarán Basin (Van der Straaten 1990).

The southern boundary of the Internal Prebetics with the Subbetic Zone, the Subbetic Front is a package of two major sub-horizontal overthrusts, with Intermediate Units between these overthrusts, and a minimum cumulative displacement of 40 km, estimated from the highly indented map pattern and seismic data (Banks & Warburton 1991). The direction of displacement on the western part of the Internal Prebetic/Subbetic boundary is to the NW (Platt & Allerton, pers. comm.). To the east, the Socovos fault transfers its displacement onto the Subbetic Front, causing it to change in nature to a E-W trending dextral fault.

2.3. Timing of the deformation

The Prebetic Zone exhibits a complex pattern of tectonic transport directions around the arc (Fig 2.2). It is essential, however, to constrain the timing of these movements as accurately as possible before any valid mechanism of arc formation may be proposed. Overall, the distribution of the vectors indicates radial translation but on detailed study it becomes

clear that the deformation around the arc is not synchronous and different areas experience deformation at different times.

Evidence for the dating of the deformation around the arc was compiled from field data, e.g. cross-cutting relationships, locations of intra-basinal unconformities and facies analysis, the I.G.M.E. 1:50,000 geological maps and previously published literature. The accuracy of the dating of Miocene units varies widely around the Prebetic Zone due to the poorly preserved or inadequate faunal assemblages present. Some units are assigned a wide-ranging age e.g. late Burdigalian-early Seravallian or mid-late Miocene if there is an ambiguity. In the areas where this is the case, the widest possible range of timing of deformation is assumed. The deformation has been divided into four time periods for clarity of data presentation: i) late Burdigalian-early Seravallian, ii) middle-late Seravallian, iii) Tortonian and iv) Messinian. In the early Miocene, pre-deformation, much of the External Prebetics was emergent and experienced continental sedimentation. Small discontinuous marine basins were formed from the late Burdigalian-Seravallian due to marine transgression (Jerez Mir 1973, Croese 1982).

Figs 2.3.1a)-d). present summaries of the location and displacement direction of the main deformation during each of these time periods.

2.3.1. Late Burdigalian-early Seravallian (Fig 2.3.1a)

The deformation in the Prebetic Zone was initiated during this time and was associated with the Subbetic Front which was then located further to the SE, and also nucleated around, and propagated outwards from, the Socovos Fault.

Location 1. Syn-tectonic slumping is observed in upper Burdigalian-lower Seravallian limestone and marl within a section of the Socovos Fault Zone at GR 75074157 near Socovos (Figs 2.3.2/3). This section of the fault is overlain by gently-dipping middle Seravallian massive limestone.

Location 2. NW thrusting is exhibited in the Internal Prebetics. Upper Burdigalian-lower Seravallian units have been incorporated into the thrust sheets which are overlain by gently-dipping middle Seravallian units (GR 74904092 on the road from Socovos to Benizar).

The NW Trending Limb exhibited a partitioning of strain into strike-slip motion parallel to the Socovos fault and into orthogonal NE-SW folding and thrusting/backthrusting .

Location 3. Fig 2.3.4 shows an intra-formational unconformity at GR 74794240 on the Elche de la Sierra to Socovos road. Syn-orogenic upper Burdigalian-lower Seravallian bioclastic limestone with 5-40% quartz impurities, have been steepened to sub-vertical and then subsequently overlain by gently-dipping middle Seravallian bioclastic limestone. A polygenic conglomerate is locally present at the base of the middle Seravallian unit and is predominantly composed of clasts of Cenomanian-Turonian dolomite eroded from the emergent thrust stack (Jerez Mir 1973). See also Fig 2.2.1.21.

Location 4. An unconformity is present at the base of the middle Seravallian which cuts down through a syncline, cored by upper Burdigalian-lower Seravallian units, to the Cretaceous (GR 76534125 near El Chopillo).

The Subbetic Front was presumably active as a thrust at this time but was located further to the SE.

2.3.2. Middle-late Seravallian (Fig 2.3.1b)

The deformation during this time showed a marked progression towards the foreland. Thrusting in the Internal Prebetics continued in a NW direction.

Location 1. Upper Burdigalian-lower Seravallian and middle Seravallian units which are folded and cut by minor faults are overlain unconformably by flat-lying late Miocene (Tortonian?) deposits at GR 72954146 on the road from Yetas de Abajo to Letur.

Location 2. Seravallian mass flow deposits, which indicate a close proximity to tectonic activity, are present, for example, on the south side of the Sierra del Carche. The late Seravallian-early Tortonian is represented by pelagic marls and only shows minor faulting, which probably occurred after the main phase of deformation (Croese 1982, Kenter et al. 1990).

The NW Trending Limb continued to exhibit partitioning of strain into strike-slip motion parallel to the Socovos fault and into orthogonal NE-SW thrusting/backthrusting giving rise to an overall NNW tectonic transport direction.

Around the Cenajo Syntaxis, deformation was exhibited by convergent NE, N, and NW translations, which caused overprinting of kinematic vectors formed closely in time (section 2.2.1.4)

Location 3. A Seravallian intra-formational unconformity is present at GR 78054335 off the Hellín to Cieza road. The units are poorly dated and the pre-unconformity unit is referred to as Burdigalian on the IGME map but dating by other workers shows that at this locality continental conditions were present during the Burdigalian and only fissure fill deposited (Nobel, pers. comm. 1991).

Location 4. Seravallian-early Tortonian bioclastic limestone is both folded and overlying the main thrusts and also incorporated into the thrust sheets within a small area (GR 806440-807441 near Fuente del Pino).

The Socovos Fault was only active along certain segments.

Location 5. Upper Burdigalian-lower Seravallian bioclastic limestone is incorporated into the dextral Socovos Fault Zone whilst middle Seravallian unconformably overlies the strike slip zone indicating inactivity of this section in the middle-late Seravallian at GR 73534252 northeast of Peñarrubia. The displacement on the more foreland segments of the Socovos Fault may be transferred onto other branches of the fault, in the Peñarrubia area, whose timing of deformation movement is not easily inferred. Further to the NW the Socovos Fault was active as deformation occurred laterally on Internal Prebetic thrusts (Location 1).

The SE segment and adjacent areas became active in response to the out-of-sequence motion of the Subbetic frontal thrust during this time.

Location 6. Seravallian-early Tortonian conglomerates are overturned and unconformably overlain by flat-lying Tortonian marls north of Calasparra at GR 77434097.

Location 7. The out-of-sequence nature of the Subbetic frontal thrust is displayed where it is shown to cut down through the middle Seravallian to the Oligocene on the southern flank of the Muela anticline (GR 75434064 and GR 74604003, NW and W of Moratalla) (Banks 1985).

Location 8. Seravallian units adjacent to the Subbetic Front are overturned at 78054052 east of Calasparra.

2.3.3. Tortonian (Fig 2.3.1c)

The Internal Prebetics show a slight swing in tectonic transport direction from NW to more WNW as the deformation progressed towards the foreland (Fig 2.2).

Location 1. Tortonian marl and limestone is folded and cross-cut by minor faults (GR 69683922, west of Santiago de la Espada).

The most NW segment of the Socovos Fault which facilitates the shortening across the Internal Prebetic thrusts was active.

The more foreland parts of the NW Trending limb and the Cenajo Syntaxis also experienced deformation at this time.

Location 2. Late Miocene (Tortonian?) units are cross-cut by minor faults but are not incorporated into the thrust sheets at GR 74794359 north of Elche de la Sierra.

Location 3. Seravallian-early Tortonian limestone is incorporated into the thrust sheets which are overlain by gently-dipping upper Tortonian-Messinian marls (Gr 79234375 on the road from Jumilla to Albatana).

Location 4. The Subbetic Front was still active to some extent, with a dextral strike slip sense of movement transferred from the Socovos Fault, in the region east of Calasparra. Tortonian sediments of the Abarán Basin (centred around GR 800403) are offset by, and incorporated into, the Subbetic fault zone (Van der Straaten 1990).

The deformation in the Alcaraz Antitaxis and the NE Trending Limb was probably initiated in the Tortonian.

2.3.4. Messinian (Fig 2.3.1d)

The Socovos Fault became inactive and the shortening accommodated by it was transferred onto the E-W and NE-SW trending thrusts of the NE Trending Limb and the Alcaraz Antitaxis, the most external parts of the arc. There was a gradual change in transport direction in the NE Trending Limb, from NW to more WNW, with progression towards the foreland.

Location 1. The Prebetic rocks of the Sierra de Quesada (GR 656355) which is associated with the dextral Tiscar fault zone are faulted against upper Miocene (Messinian?) sediments (Guezou et al 1991).

Location 2. Messinian marls are folded and overthrust (GR 66423818, west of Chilluévar).

Location 3. The Prebetic Front can be seen to be emergent and overthrust and incorporate Messinian sediments at GR 66253975 on the road from Villanueve del Arzobispo to Tranco (Fig 2.2.1.7).

Location 4. Upper Tortonian bioclastic limestone is incorporated into the thrust sheets of the Alcaraz Antitaxis and is presently elevated and found capping some mountains (GR 72954422, west of Bogarra).

Location 5. Upper Tortonian-lower Messinian sediments are overthrust by the Prebetic Front at GR 70424470 on the road from Alcaraz to Riopar (Fig 2.2.1.13).

Location 6. Minor deformation was exhibited in the Cenajo Syntaxis and may be associated with local diapirism as subsurface Triassic evaporite-cored anticlines became gravitationally unstable, due to their relatively low density, and the evaporite migrated towards the surface (Gr 76514223 on the Hellín to Cenajo road) (section 2.2.1.4).

Combining the data from Figs 2.3.1a-d allows investigation of propagation of the main wave of deformation, both spatially and temporally. Fig 2.3.5 shows a wave of deformation progressing from SE to NW, with a swing in its trend in the External Prebetics from ENE-WSW to more NNE-SSW with time with overall tectonic transport vectors also showing a swing from NNW to NW to WNW. This anticlockwise swing in deformation may be facilitated by movement along the NW-SE oriented sub-vertical dextral faults, both on the scale of the Socovos and Tiscar wrench faults and the smaller tear faults in the NE Trending Limb (Fig 2.2.1.11). The change in tectonic transport direction, especially in the late Miocene, may result from changes in external factors such as the overall stress field dictated by the relative plate motions. Helman (1989) and Dewey et al. (1989) document a change to a more WNW direction in the relative motion vector of Africa with respect to Europe at 9 Ma (Fig 1.1.2).

The localities of deformation on either side of the Socovos fault in its early stages of slip which are now juxtaposed were initially spaced apart and hence the analysis of the wave of deformation for the southwesterly Internal Prebetics and the External Prebetics are separated.

The progression of the deformation of the out-of-sequence Subbetic Front to the NW can also be clearly seen.

2.4. Palaeomagnetic studies and the presence of rotations around a vertical axis

Many previous palaeomagnetic studies have been carried out in the Betic-Rif orogen which demonstrate the presence of rotations around a

vertical axis (e.g. Osete et al. 1989, Platzman 1992, Allerton et al. submitted). Although much attention has been focused on the mechanism of formation of the Gibraltar Arc and its associated palaeomagnetic rotations, no comprehensive palaeomagnetic study of the Prebetic Zone has so far been completed.

Initially, a detailed palaeomagnetic study of the Prebetic Zone, with the aim of identifying the presence of rotations around a vertical axis and the manner in which they occurred, was planned. Unfortunately, after an initial field season, this was found to be unfeasible in the External Prebetics, where the arc is exhibited, due to the absence of sufficient lithological units which:

i) are continuous around the arc.

ii) yield a stable original magnetization.

Fig 2.4.1. shows the locations of the sites sampled for palaeomagnetic data and Table 2.4. lists the results of the preliminary work which shows the magnetisation, especially in the ubiquitous Lower Jurassic dolomite, to be either too weak (see NRM values) or to result from an overprinting of the present day field, carried by a low-temperature goethite component. In the Alcaraz Antitaxis, initial demagnetisation from two sites, CRM5 (Fig 2.4.2) and B07, hint at possible anticlockwise rotations whilst results from site B08 in Messinian marl, show an original reverse component of magnetisation and indicate that no rotation of this site relative to stable Iberia has occurred since the Messinian (Fig 2.4.1). These results, however, do not represent site means and are not statistically valid.

In the Internal Prebetics, only one site produced reliable evidence for the presence of an original magnetic signature. This indicated that the Internal Prebetics have not rotated significantly relative to stable Iberia (Allerton et al. submitted) (Figs 2.4.1 and 2.4.3). This site was drilled in Upper Jurassic *ammonitico rosso* facies limestone which has been successfully sampled in previous studies of External Zone deformation (Platzman 1992, Allerton et al. submitted).

Further to the south, in the eastern Subbetic Zone, palaeomagnetic declinations indicate large rotations of tectonic blocks, with internally consistent rotation vectors, during their emplacement by thrusting (Allerton et al. submitted).

From analysis of the kinematic vectors and the deformation variation around the arc, prediction of the presence of local, moderately-sized rotations throughout the arc may be made. These rotations may be facilitated by rotation on a décollement during thrust emplacement, the predominant mechanism proposed for rotations in the limbs of the arc, or by rotation of small fault-bounded blocks, the predominant mechanism proposed for rotations local to the Socovos fault and for the hinges of the arc where superimposed deformation is present. This may be due to the progression of divergent translation and oblique backthrusting in the Alcaraz Antitaxis or the progression of convergent deformation in the Cenajo Syntaxis.

Large-scale rotation of the Prebetics Arc as a block may be ruled out due to:

i) The absence of a candidate for a wrench fault in the foreland required for this to occur.

ii) The continuity of the geological structure and the smooth variation of the orientation of kinematic vectors.

iii) The short amount of time i.e. since the Messinian, in which this would have to take place. Site B08 hints that post-Messinian rotations are absent.

iv) The indication from site B49, that the Internal Prebetics have not rotated significantly relative to stable Iberia.

2.5. Summary of the formation of the Prebetic Arc

Satellite images of the Prebetics clearly show the coupled arcuate nature of the structural trend of the External Prebetics and its absence in the Internal Prebetics. The structural style and kinematic displacement vectors, and hence deformation history, vary markedly around the arc.

The mechanism of formation of the Prebetic Arc was determined by detailed study of the variation in the style of deformation, spatially and temporally around the arc and the magnitude and distribution of tangential extension. The strain pattern was ascertained by detailed structural analysis, construction of several balanced cross-sections and preliminary palaeomagnetic studies. The structural analysis involved collection of kinematic data, location of major shear zones and establishment of the presence and distribution of extension, together with the timing and evolutionary history of these phenomena. The palaeomagnetic studies were to ascertain whether any significant systematic rotations around a vertical axis had occurred, as predicted in the formation of rotational arcs.

The deformation in the Prebetic Zone was initiated during the late Burdigalian-early Seravallian and propagated towards the foreland from the Subbetic Front to the NNW/NW by frontal accretion of new material onto a deforming thrust wedge in a wave of deformation shown to become more WNW with time. Deformation also nucleated around, and propagated outwards from, the dextral Socovos wrench fault. The differential displacement and the partitioning of strain across this Socovos fault, into strike-slip motion parallel to the fault and orthogonal NE-SW thrusting/backthrusting, caused the formation of firstly, the Cenajo Syntaxis and NW Trending Limb and with progressive deformation the Alcaraz Antitaxis and the NE Trending Limb. The Cenajo Syntaxis underwent convergent displacement with NW thrusting in the east and NE thrusting in the west arising as a result of strain partitioning across the Socovos Fault. Superposition of these trends of deformation was due to the tightening of the hinge area with time. The Alcaraz Antitaxis underwent divergent displacement as extension in the outer arc was accommodated and a tightening of the hinge with continued deformation and the added interference of obstacles in the foreland. The anticlockwise swing in the displacement trend of the NE Trending Limb, from NW to WNW, is facilitated by movement along WNW-ESE oriented tear faults.

The models which have been proposed in recent literature to account for the formation of arcuate orogens may be divided into seven different mechanisms which are summarized in section 1.3 (Fig 1.3.2) and below:

i) Later noncoaxial deformation.

ii) Movement along wrench faults and within shear zones.

iii) The generation of local body forces.

iv) The presence of an originally irregular continental margin and hence facies distribution.

v) The action of a rigid indentor against the deforming margin.

vi) The presence of one or several obstacles in the foreland.

vii) Formation of independent thrust corridors.

Therefore, from detailed study of the deformation exhibited in the Prebetic Arc, the formation of the arc was inferred to be due, predominantly, to movement along, and the differential shortening across, a wrench fault i.e. the Socovos Fault (model ii). The presence of obstacles in the foreland had a minor affect on tightening the hinge of the Alcaraz Antitaxis (model vi). The External Prebetics originally possessed a slightly arcuate form due to the strong control of an irregular continental margin on deposition of sedimentary facies (sections 3.2.1 and 6.4). This also had a minor contributory role in the formation of the arc and may have had an influence on the location of the Socovos Fault (model iv).

Oroclinal bending (model i) may be ruled out as the deformation of the Prebetic Arc occurred in just one wave of deformation. Gravity gliding caused by local body forces (model iii) does not seem applicable as there was no synchronous radial pattern of displacement around the arc and both the limbs. The action of a rigid indentor (model v) may also be discarded as the Prebetic deformation resulted from propagation of an internally deforming wedge from SE to NW. The final model, the formation of independent thrust corridors, (model vii) cannot have occurred as the deformation is shown to propagate in a NE-SW trending wave and not in a serial manner around the arc.

Previously proposed models for the formation of the Prebetic Arc may now be re-examined. Hermes (1978) suggested that the whole Prebetic zone has been laterally displaced as a coherent crustal block to the ENE, forming the Guadalquivir depression in its wake. There is no obvious driving mechanism for the displacement and no evidence of the large scale shear zones invoked at the margins of the Prebetics. The tectonic transport vectors displayed by the Prebetics indicate a predominant NW/WNW displacement contrary to that predicted in the model.

Guezou et al (1991) present results of kinematic analysis in the NE Trending Limb of the Prebetics, which indicate a bulk translation to the WNW. They cite this as evidence to support the model of Betic-Rif formation of Frizon De Lamotte et al (1989) in which there is westward translation of the Alboran Domain with displacement trajectories which are independent of strike and subparallel all along the belt. After detailed study of kinematic and timing relations it is clear that this WNW translation does not apply to all sub-areas of the Prebetics, nor is it consistent through time.

To conclude, the style of deformation exhibited in the Prebetic Arc and the mechanism for its formation cannot be predicted from relative plate motion vectors (Shackleton & Ries 1984, Baird & Dewey 1986) or previous models for the formation of the Betic-Rif Orogen. Local body forces associated with shear faults and obstacles, and the partitioning of strain, all exert a strong influence on the strain pattern. The change in the overall tectonic transport direction from NNW to NW to WNW may result from changes in the relative plate motions. A change to a more WNW direction in the relative motion vector of Africa with respect to Europe at 9 Ma is documented by Helman (1989) and Dewey et al. (1989).

CHAPTER 2

FIGURES

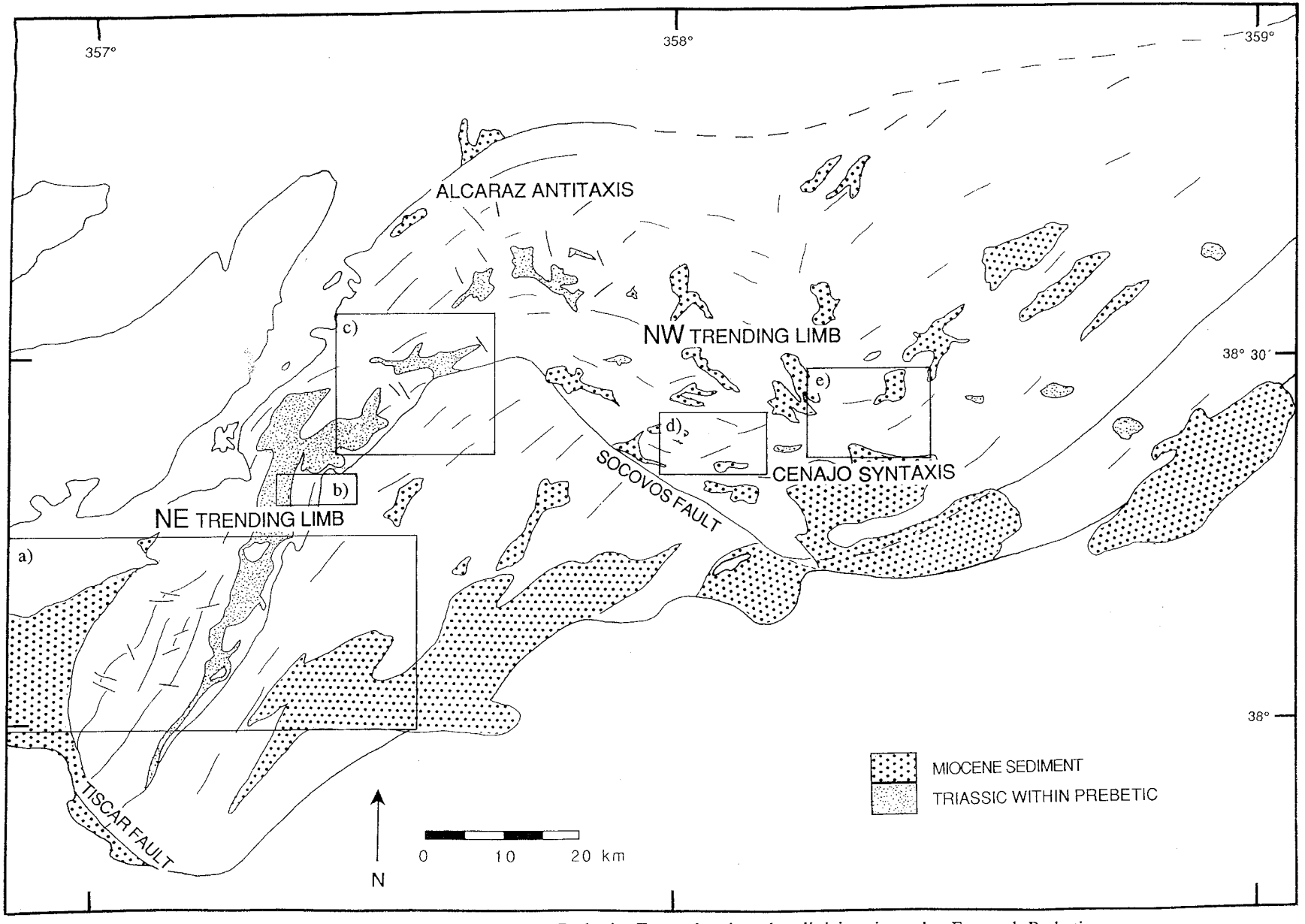


Fig 2.1.1. Summary map of the western Prebetic Zone showing the division into the External Prebetics and the Internal Prebetics. There is further structural subdivision of the External Prebetics into the NE Trending Limb, the Alcaraz Antitaxis, the NW Trending Limb and the Cenajo Syntaxis. The inset boxes give the locations of a) the Tranco area (Fig 2.2.1.2) b) the Orcera area (Fig 2.2.1.4) c) the Riopar area (Fig 2.2.1.18) d) the Elche area (Fig 2.2.1.21) e) the Isso area (Fig 2.2.1.25).

A structural and stratigraphic map of the western Prebetic Zone

Fig 2.1.1. (continued)

Compiled from I.G.M.E 1:50,000 geological maps

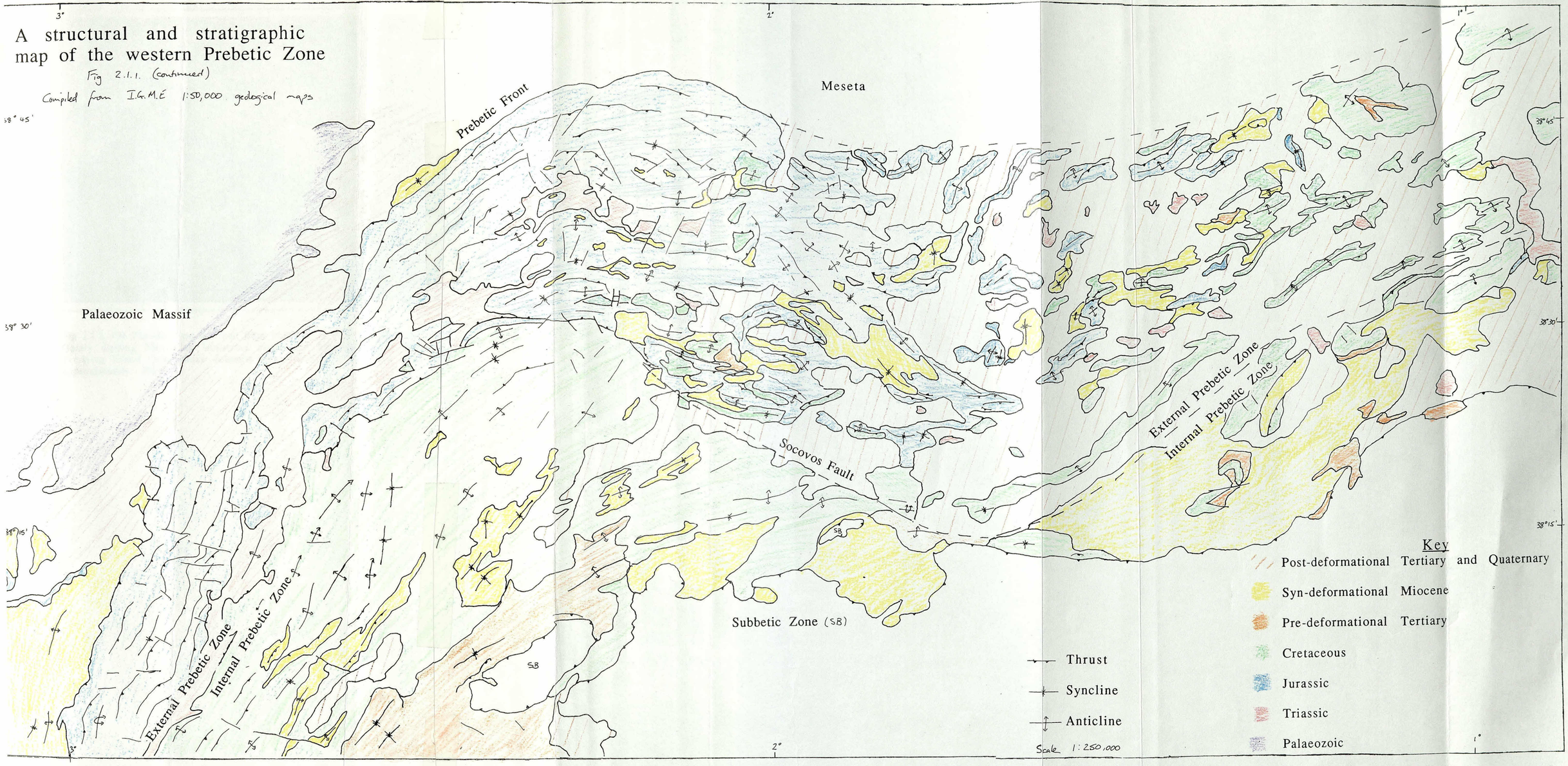




Fig 2.1.2. GR 74684261 on the road from Elche de la Sierra to Socovos. Looking N. Gently dipping Messinian lacustrine marls and limestones (M) unconformably overlying folded Cenomanian dolomite (C). Relief of cliff above river is approximately 20m.

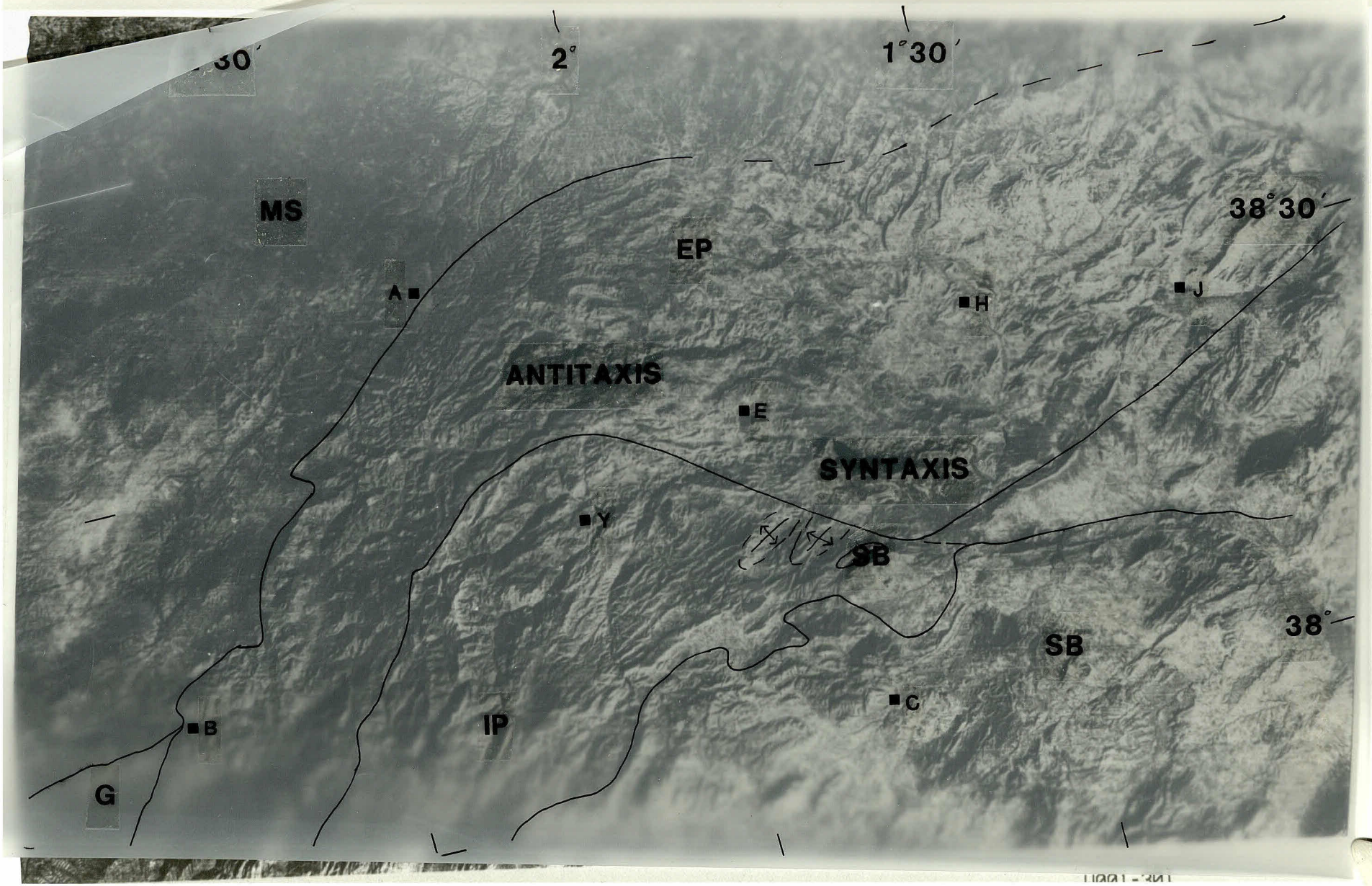


Fig 2.1.3. Satellite image of the Prebetic Arc clearly showing the change in structural trend across the Alcaraz Antitaxis and Cenajo Syntaxis of the External Prebetics which is absent in the Internal Prebetics. Compare with Fig 2.1.2. EP-External Prebetics, IP-Internal Prebetics, SB-Subbetic Zone, MS-Meseta, G-Miocene sediments of the Guadalquivir basin. A-Alcaraz, B-Beas de Segura, C-Caravaca, E-Elche de la Sierra, H-Hellin, J-Jumilla, Y-Yeste.

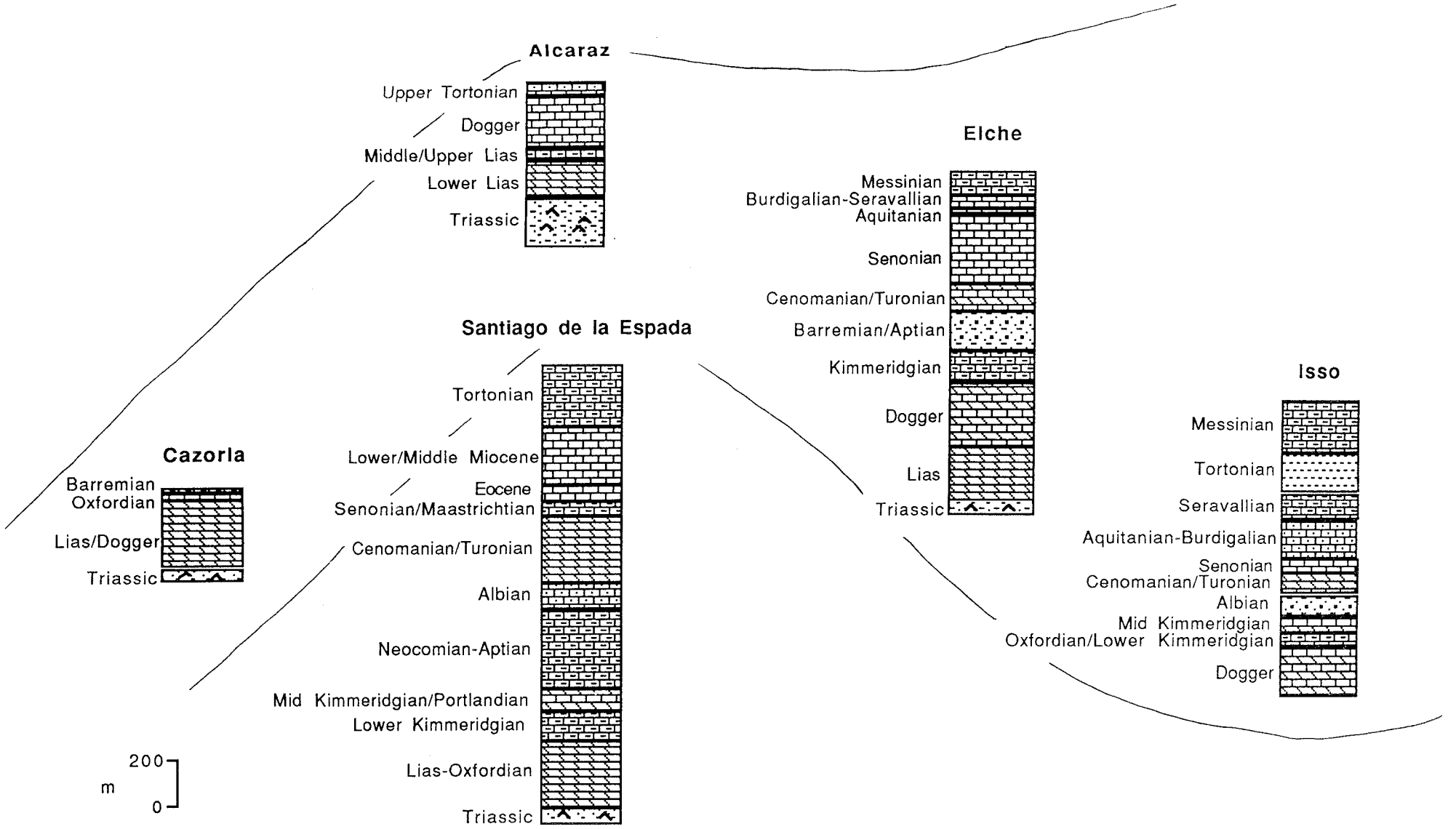


Fig 2.1.4.a). Comparison of representative stratigraphic sequences around the Prebetic Arc. The NE Trending limb is represented by the **Cazorla** section, the Alcaraz Antitaxis by the **Alcaraz** section, the NW Trending Limb by the **Elche** section, the Cenajo Syntaxis by the **Isso** section and the Internal Prebetics by the **Santiago de Espada** section. Compiled from I.G.M.E. 1:50,000 Geological maps. Key for stratigraphic columns shown in Fig 2.1.4.b).

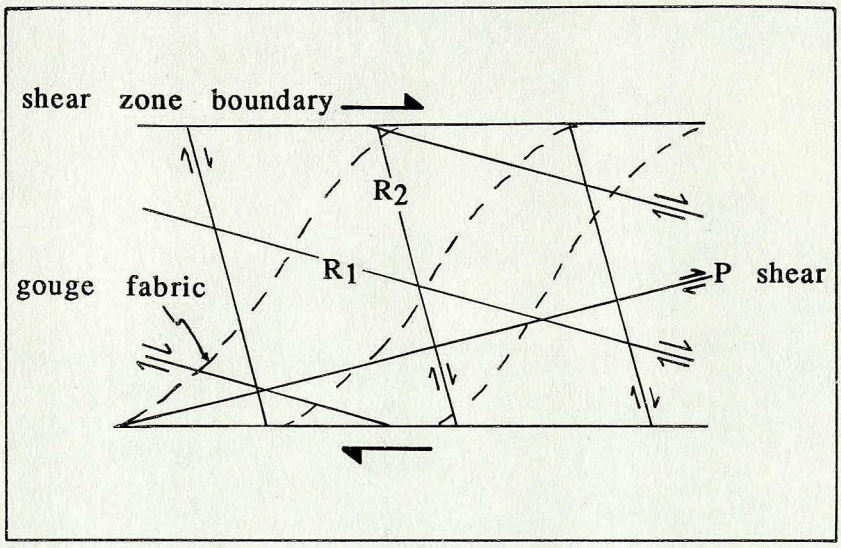


Fig 2.1.5. Brittle shear zone showing the development of a gouge fabric, R_1 and R_2 Riedel shears and a low-angle P-shear used in shear sense analysis.



Fig 2.1.6. GR 67403973 on the road from Tranco to Cazorla. Looking SW. Fault gouge (G) developed in a mud layer in the Lower Jurassic and aligned parallel to the pencil within a shear zone aligned parallel to the compass. Shear sense inferred from the fault gouge is top to right of photo.

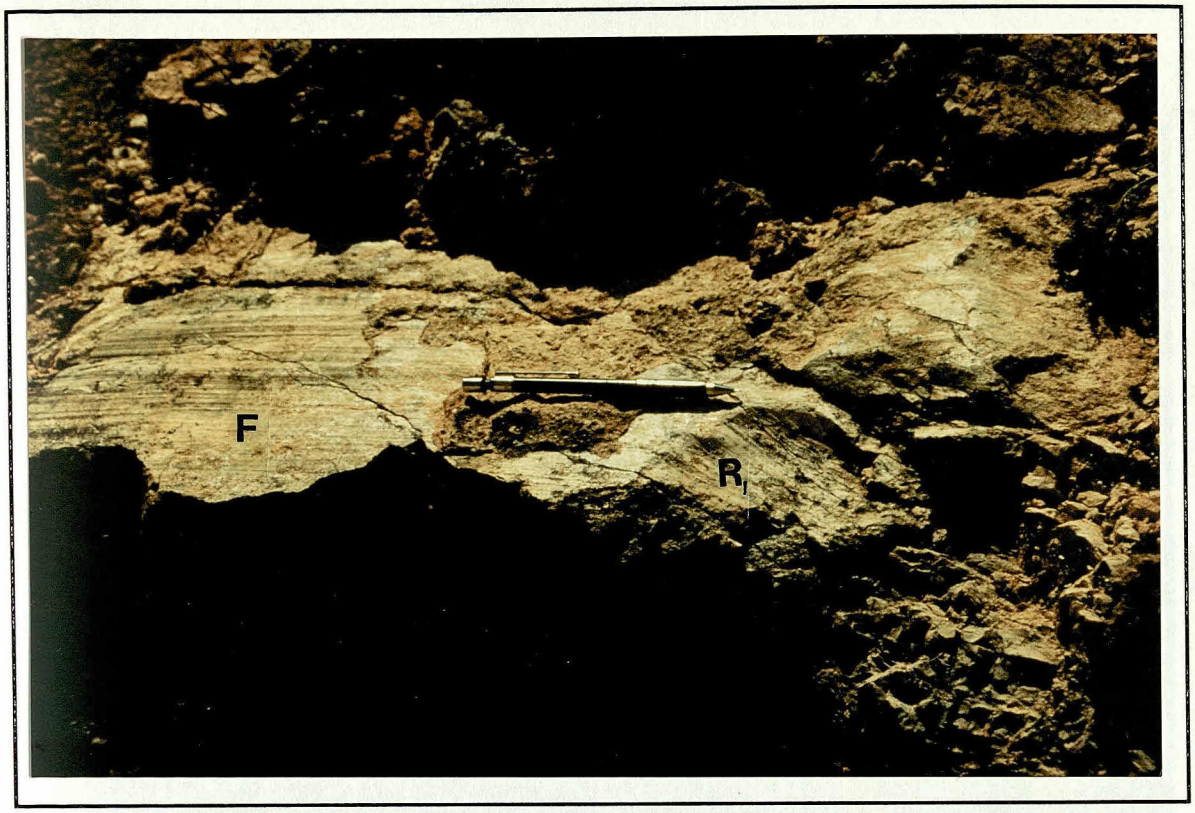


Fig 2.1.7.a) GR 71884481 near Paterna del Madera. Looking SW. Riedel shear plane (R1) developed within Lower Jurassic dolomite. Wear grooves are well developed along both the fault plane (F) (32/062) (parallel to the pencil) and the Riedel shear plane (40/042). Shear sense inferred from the Reidel shear plane is top to right of photo.



Fig 2.1.7.b) GR 76734206 below the Cenajo dam. Looking NNE. Low angle Riedel shear planes (R1) developed within a shear zone of Aquitanian sandstone and mudstone showing an small normal offsets. Shear sense inferred from the Riedel shear planes is top to left of photo.



Fig 2.1.8. GR 72724513 on the road from Peñascosa to Fuenlabrada. Looking SE. Small-scale thrust fault (F) in Lower Jurassic dolomite (defined by the hammer). The shear sense is inferred to be top to right of the photo by the presence of a hanging wall anticline and cut-off (HC) and a footwall syncline and cut-off (FC). Hammer=30cm.

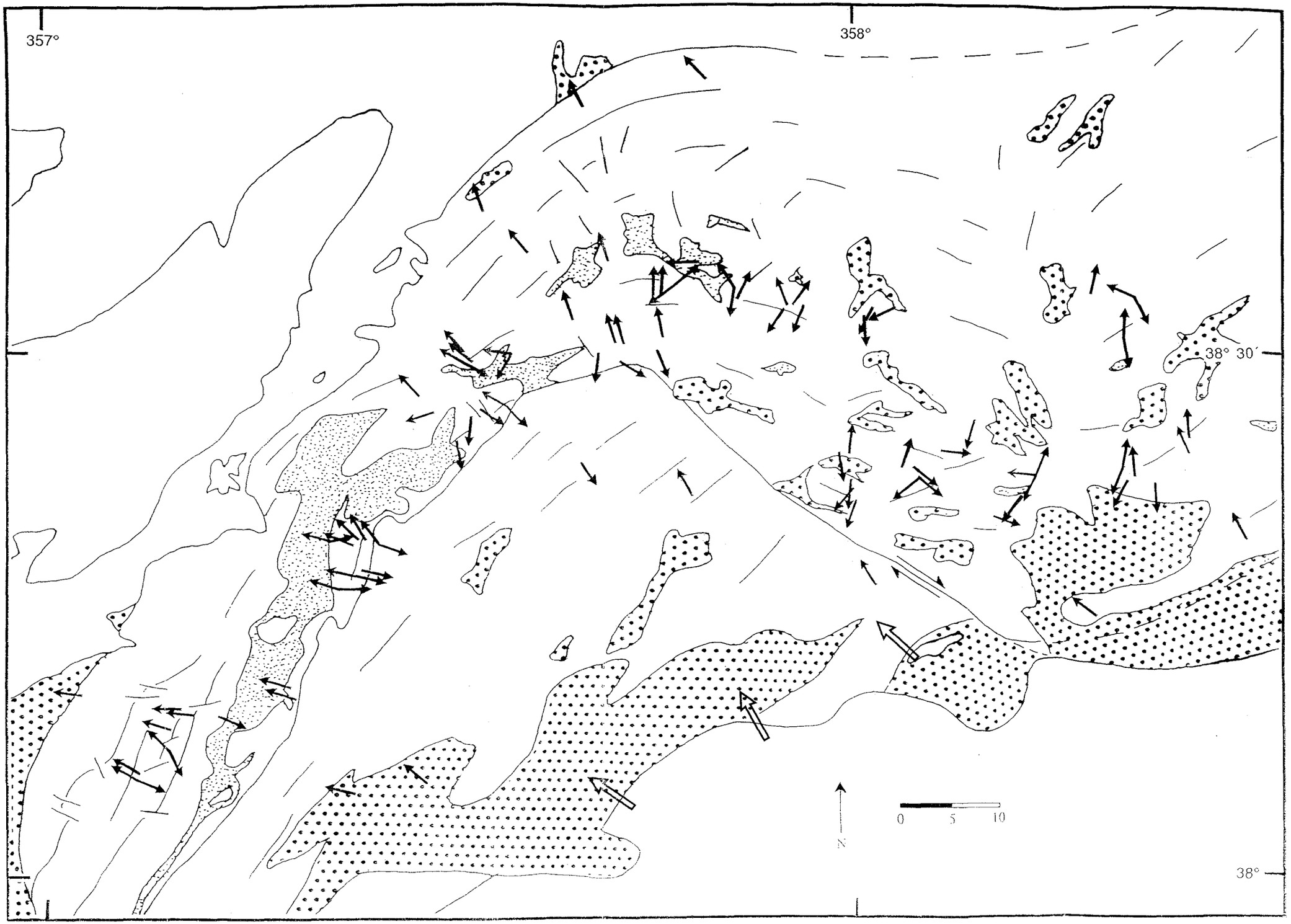


Fig 2.2. Summary map of the variation in tectonic transport directions around the Prebetic Arc. Values shown in Appendix 1. Closed arrows-this study, open arrows-Platt & Allerton, pers. comm.



Fig 2.2.1.1. GR 67403973 on the road from Tranco to Cazorla. Looking northward. Four imbricate slices, thrust approximately to the NNW, with subsequent backsteepening of earlier, more hinterland slices. A strike perpendicular tear fault (tr) is present in the middle ground. Thrust - T. Field of view approximately 3km.

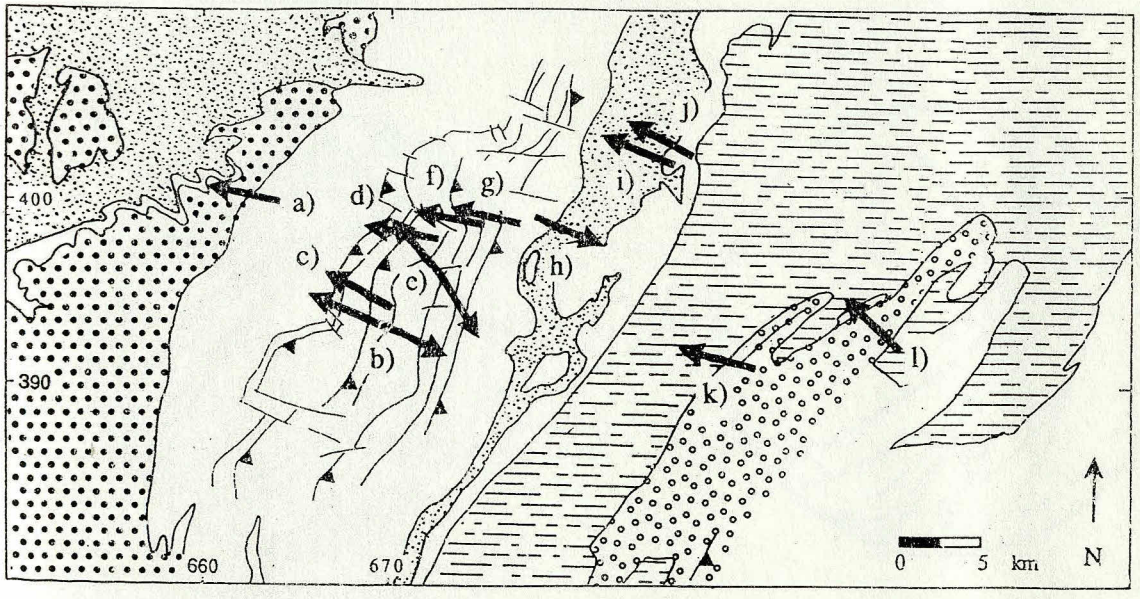


Fig 2.2.1.2. Variation in tectonic transport directions in the Tranco area (located in Fig 2.1.1). There is a gradual change in transport direction from l) to a) with progression of deformation. b) to g) shown in more detail in Fig 2.2.1.9. Stipple-Triassic, unshaded-Jurassic, dashed-Cretaceous, open dots-lower Miocene, closed dots-upper Miocene.

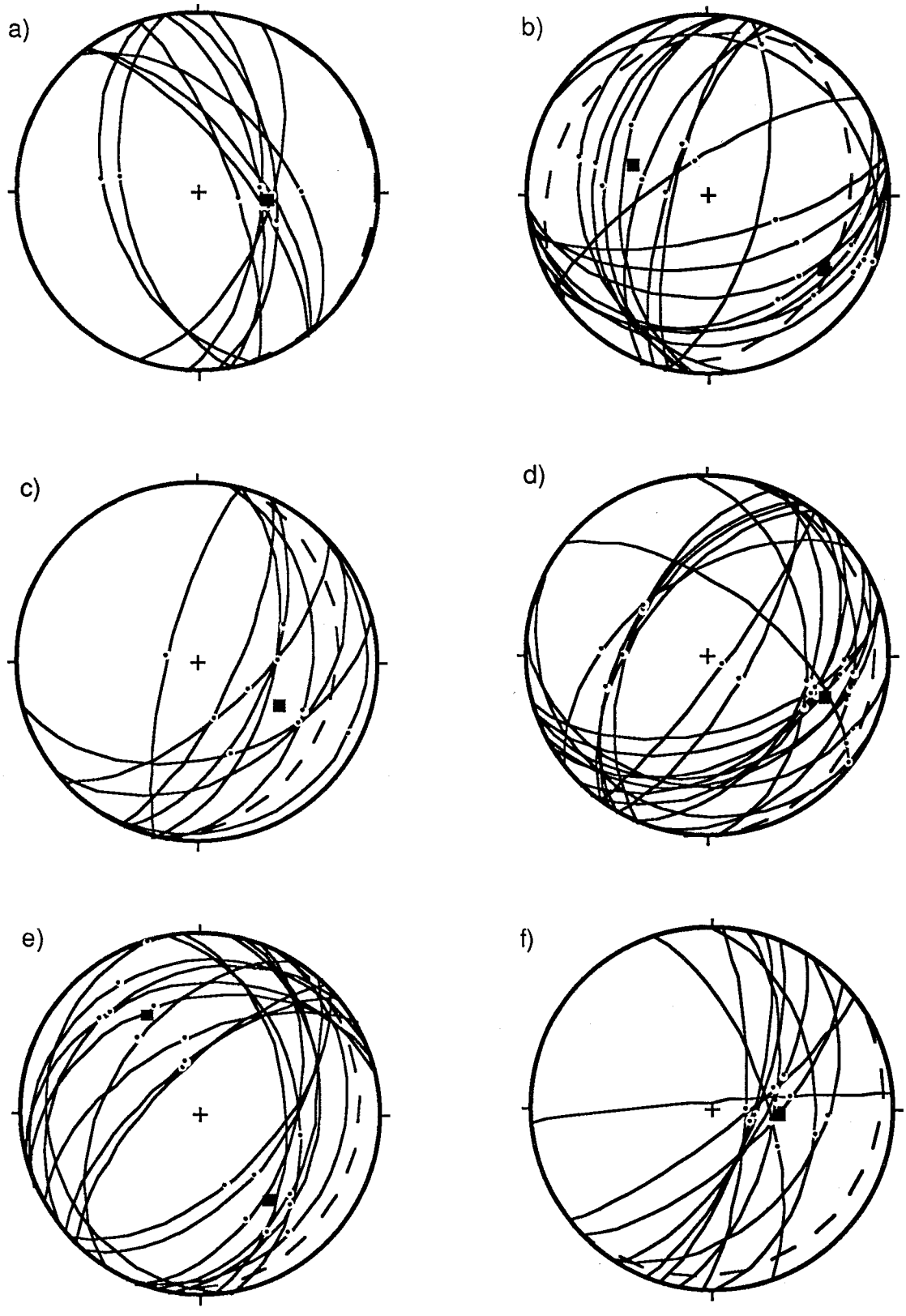


Fig 2.2.1.3. Stereoplots of locations a) to f) from the Tranco area (Fig 2.2.1.2).
a) W thrusting with minor backthrusting (N=8, Mean=58/098)
b) WNW thrusting (N=8, Mean=25/122) and backthrusting (N=8, Mean=54/294)
c) WNW thrusting (N=8, Mean=48/117)
d) WNW thrusting (N=16, Mean=32/110) and backthrusting
e) NW thrusting (N=8, Mean=38/139) and backthrusting (N=9, Mean=39/331)
f) W thrusting (N=11, Mean=59/092)
Solid line-fault plane, dashed line-bedding plane, dot-fault lineation, square-mean vector, N-number of lineations included in calculation of mean vector.

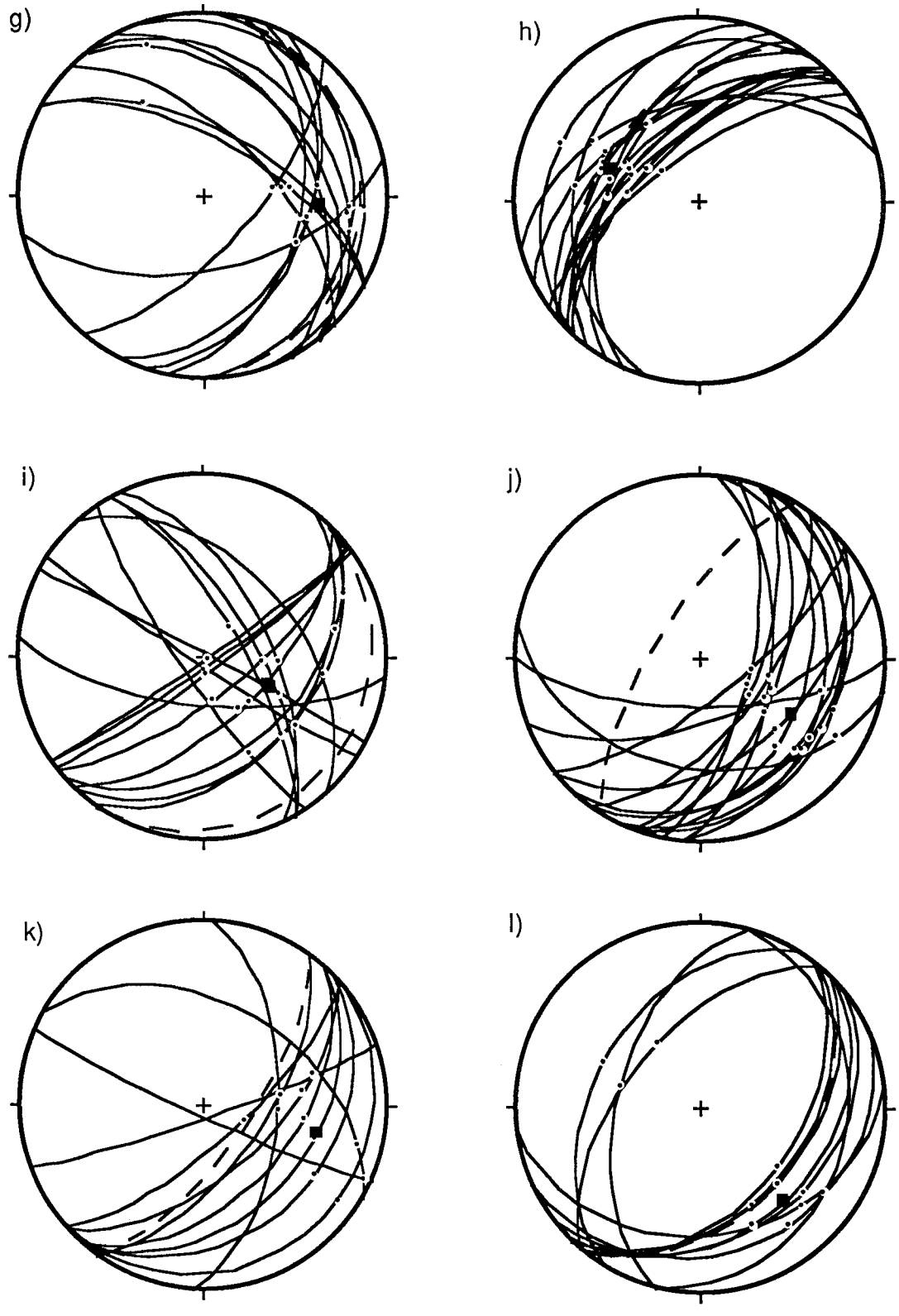


Fig 2.2.1.3. (cont'd) Stereoplots of locations g) to l) from the Tranco area (Fig 2.2.1.2).
g) W thrusting with minor backthrusting (N=12, Mean=38/095)
h) ESE backthrusting (N=13, Mean=50/293)
i) WNW thrusting (N=16, Mean=61/112) with WNW-ESE tear faulting
j) NW thrusting (N=16, Mean=43/122)
k) WNW thrusting (N=10, Mean=38/103) with WNW-ESE tear faulting
l) NW thrusting (N=8, Mean=33/137) with minor backthrusting
Solid line-fault plane, dashed line-bedding plane, dot-fault lineation, square-mean vector, N-number of lineations included in calculation of mean vector.

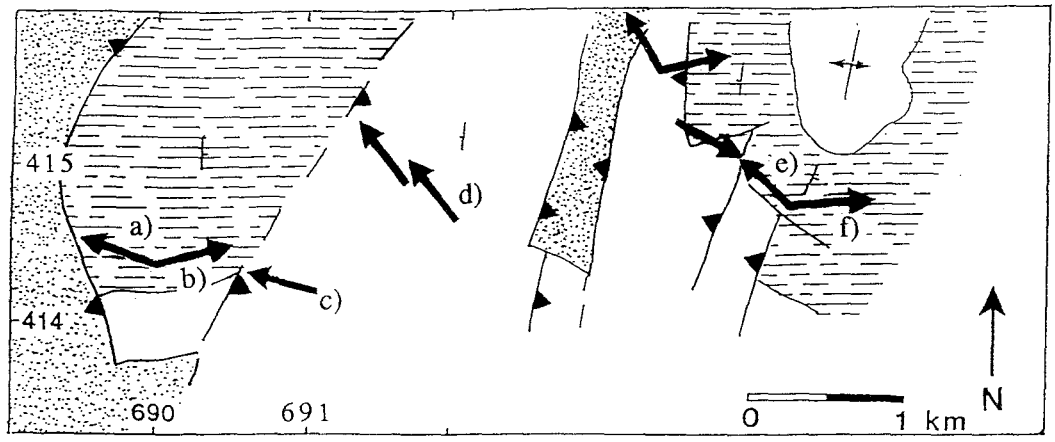


Fig 2.2.1.4. Variation in tectonic transport directions in the Orcera area (located in Fig 2.1.1). There is a gradual change in transport direction from f) to a) with progression of deformation and later more eastward backthrusting. Stipple-Triassic, unshaded-Jurassic, dashed-Cretaceous.



Fig 2.2.1.5.a) GR 68954144 on the track north of Orcera. Looking northward. A section through Albian Utrillas facies sandstone, mudstone and marl (A) and Cenomanian dolomite (C) showing two phases of deformation. An earlier westerly forethrusting (1) reactivates original extensional faults and is cross-cut by a later easterly backthrust deformation (2). This is shown in more detail in Fig 2.2.1.5.b). Stereoplots shown in Fig 2.2.1.6 a) and b).

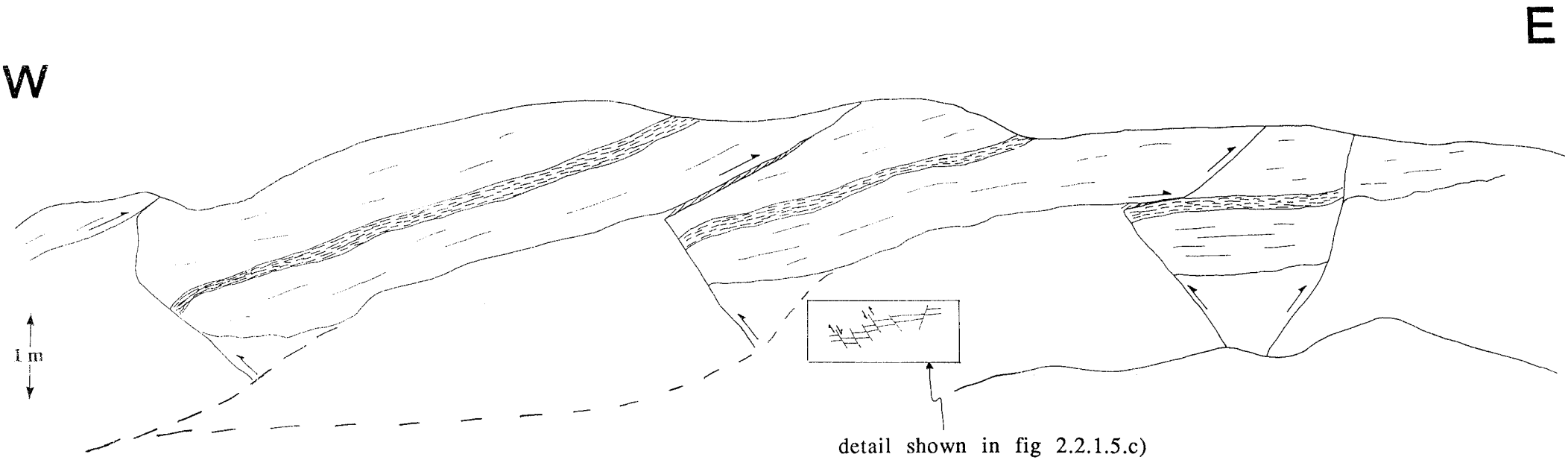


Fig 2.2.1.5.b) Drawing of photomontage, Fig 2.2.1.5a), in the Orcera area. Initial WNW thrusting is cross-cut by later eastward backthrusting which forms flats which preferentially follow original bedding planes. Dashed lines indicate the location and linking of the backthrusts within the Albian sands. Small scale original extensional faulting and later thrust reactivation within the Albian Utrillas Facies is shown above and in detail in Fig 2.2.1.5c).



Fig 2.2.1.5.c) Detail of deformation located in Fig 2.2.1.5.b). Original extension (E) in Albian sandstone is reactivated by backthrusting (T).

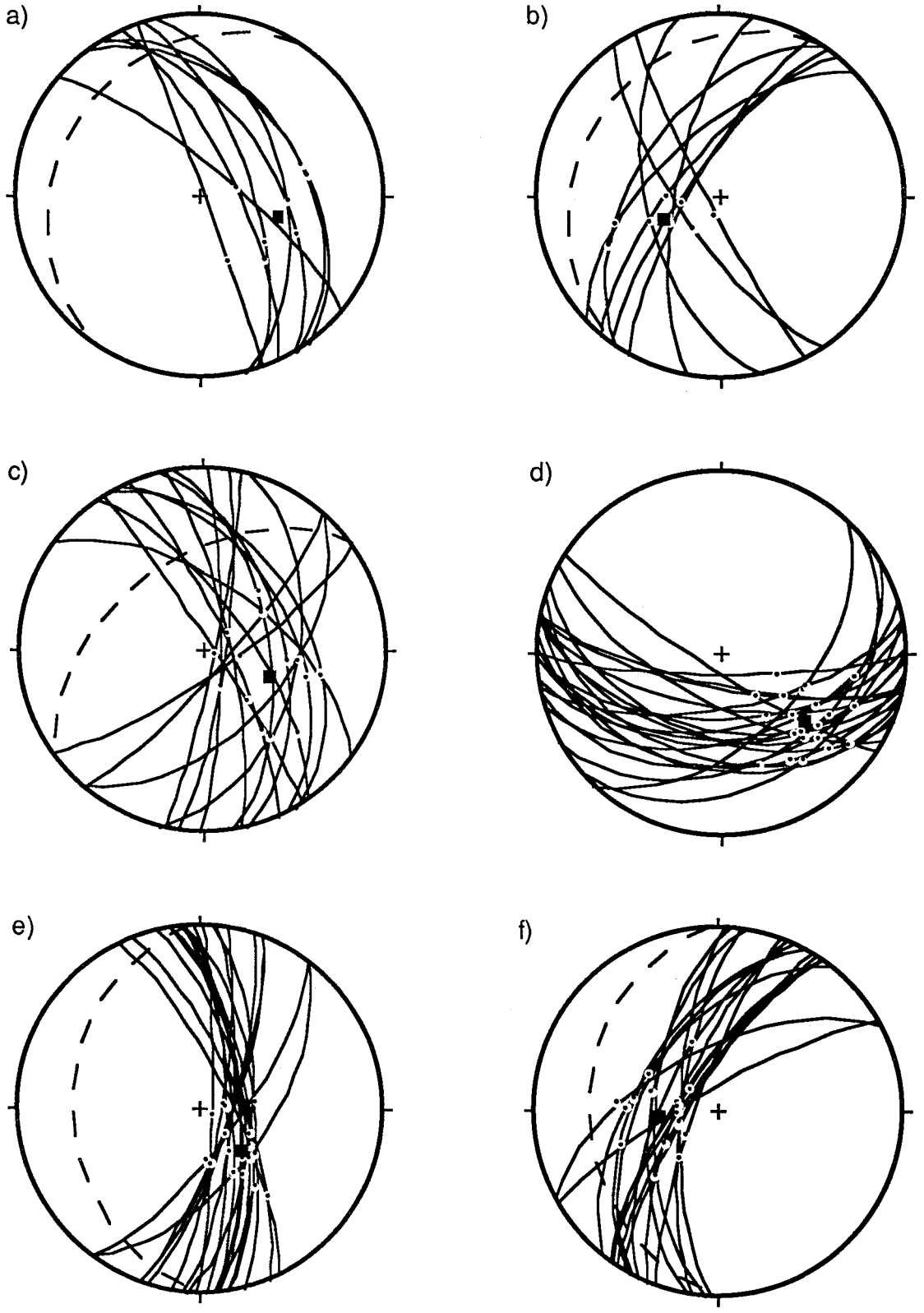


Fig 2.2.1.6. Stereoplots of locations a) to f) from the Orcera area (Fig 2.2.1.4).
a) WNW thrusting (N=8, Mean=55/106) and b) ESE backthrusting (N=9, Mean=62/247)
c) WNW thrusting (N=16, Mean=59/110)
d) NW thrusting (N=20, Mean=41/129)
e) NW thrusting (N=17, Mean=65/139) and f) E backthrusting (N=15, Mean=65/267)
Solid line-fault plane, dashed line-bedding plane, dot-fault lineation, square-mean vector, N-number of lineations included in calculation of mean vector.



Fig 2.2.1.7. GR 66253975 on the road from Villanueve del Arzobispo to Tranco. Looking SSW. Messinian marls (M) incorporated in the frontal thrust sheets of Jurassic (J). Thrusts-T. Maximum relief=200m.



Fig 2.2.1.8.a) GR 67123930 on the road from Tranco to Cazorla. Looking SE. Passive-roof duplex developed in NE Trending Limb. The main thrust slice of the duplex is seen to become foreland dipping and then become repeated due to the development of a hinterland dipping duplex. Roof thrust-RT, duplex thrust-DT. Maximum relief 300m. Stereoplots shown in Fig 2.2.1.3.b).



Fig 2.2.1.8.b) GR 67123930 on the road from Tranco to Cazorla. Looking SE. The development of a hinterland dipping duplex. Maximum relief 300m. Stereoplots shown in Fig 2.2.1.3.b).

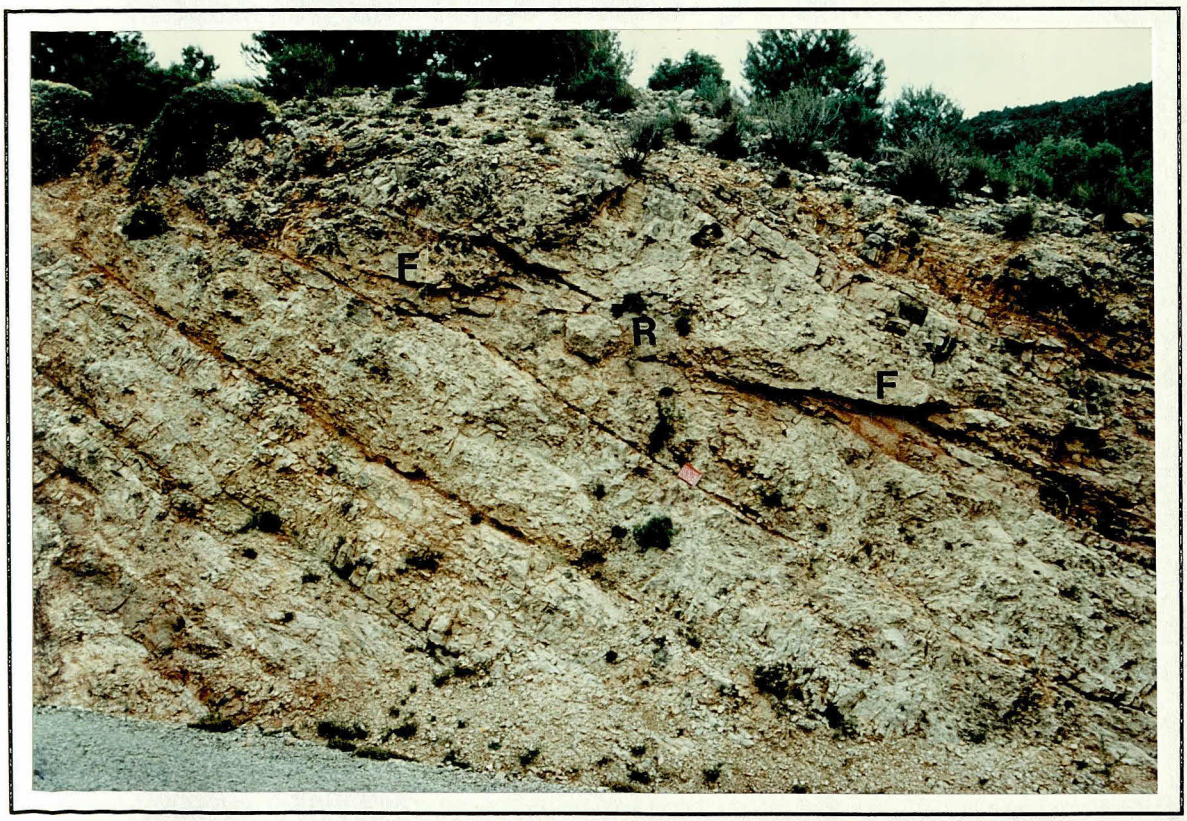


Fig 2.2.1.8.c) GR 67103932 on the road from Tranco to Cazorla. Looking northward. Out-of-sequence thrusting (F) in gently tilted Lower Jurassic dolomite of the duplex roof thrust. The thrusts frequently develop ramps (R) along bedding planes if they are preferentially oriented.

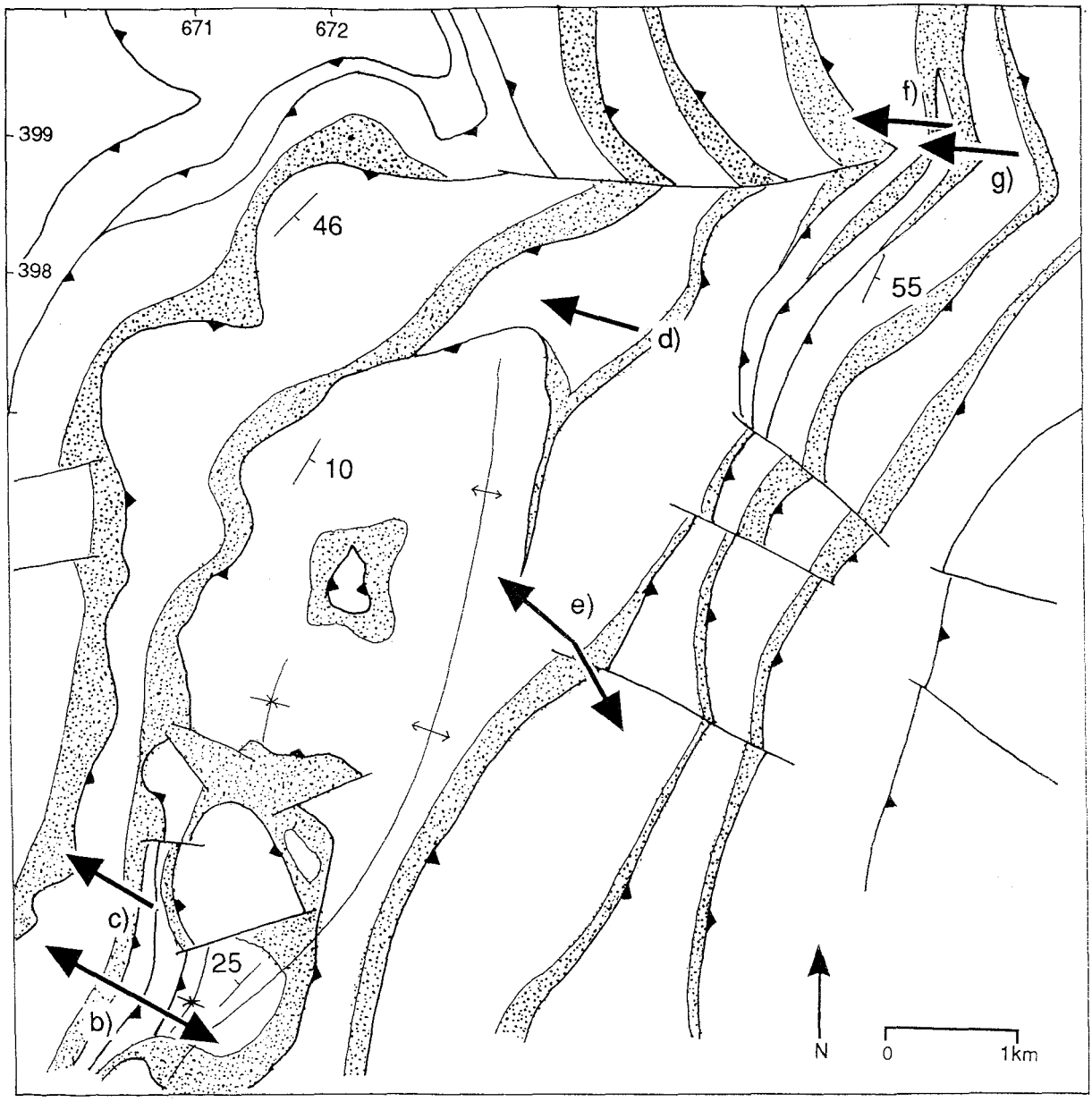


Fig 2.2.1.9. Detailed structural map of the passive-roof duplex formed in the Tranco area (Fig 2.2.1.2). Stereoplots b) - g) are shown in Fig 2.2.1.3. The local affect of duplex development by WNW-ESE thrusting and backthrusting [b) and c)] causes out-of-sequence translation of the roof thrust slice and associated development of NW thrusting and SSE backthrusting [e)]. Laterally to the NE, the duplex is undeveloped and the thrust slices below and above the duplex roof slice show the more common WNW sense of thrusting [d) and f),g) respectively].



Fig 2.2.1.10. GR 67304000 on the road from Villanueve del Arzobispo to Tranco. Looking NE. Subvertical tear fault developed in Lower Jurassic dolomite showing the development of wear grooves and a Riedel shear plane (R) which indicates a dextral shear sense. Book=18cm.

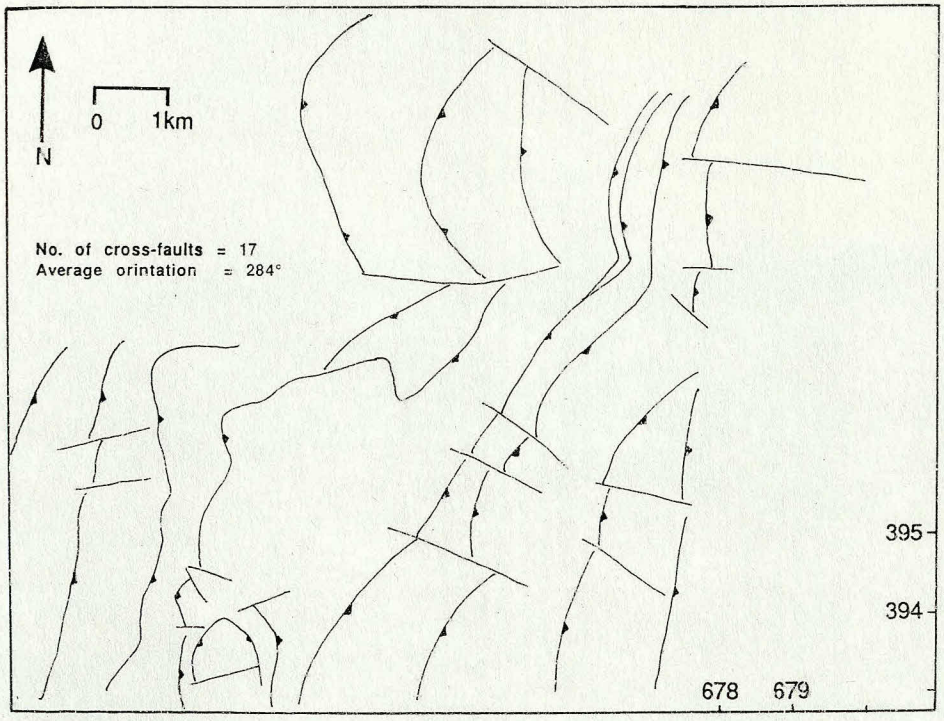


Fig 2.2.1.11. Distribution of the WNW-ESE tear faults within the Tranco area. Only one population of subvertical faults are identified which subparallel the tectonic transport direction of the area.



Fig 2.2.1.12. GR 67974216 near Siles. Looking downwards. Intrusive contact between the remobilised Adamellite (Ad) and Palaeozoic metamorphosed rock (P). The Adamellite appears to intrude preferentially along the cleavage and fracture planes.



Fig 2.2.1.13. GR 70424470 on the road from Alcaraz to Riopar. Looking NE. Cross-bedded upper Tortonian/lower Messinian calcarenites (M) incorporated into the thrust slices of Jurassic (J) close to the Prebetic Front. Thrust faults-T. Relief of outcrop by road=3m.



Fig 2.2.1.14. GR 71924476 near Paterna del Madera. Looking E. Red Triassic sandstone (Tr) overthrusting (T) Jurassic units (J) causing the formation of recumbent folds in the footwall. Hinge of fold-H.



Fig 2.2.1.15a) GR 72384478 north of the Bogarra to Paterna del Madera road. Looking W. E-W crystal lineations on a gypsum shear zone within the Triassic sandstone. Stereoplot shown in Fig 2.2.1.16.



Fig 2.2.1.15b) GR 72384478 north of the Bogarra to Paterna del Madera road. Looking downwards. Cross-section of the gypsum shear zone of Fig 2.2.1.15. showing a dextral shear foliation (F).

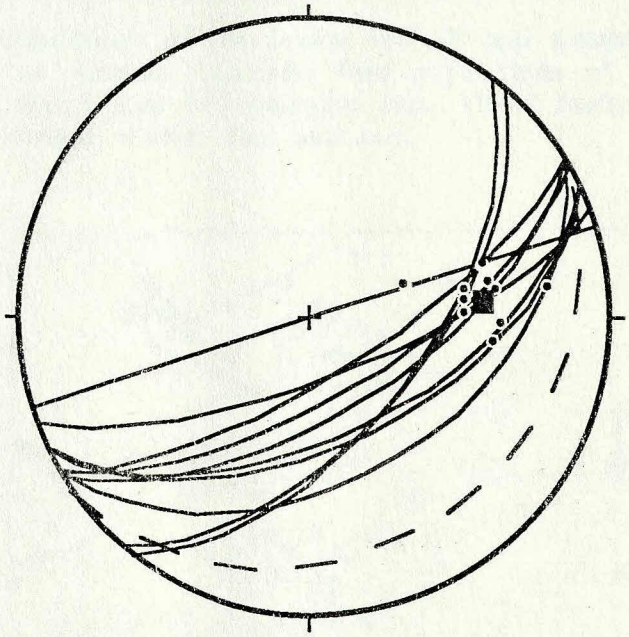


Fig 2.2.1.16. Stereoplot of deformed gypsum veins within the Triassic of the Riopar area (see photo 2.2.1.15). Oblique westward thrusting is exhibited (N=10). Solid line-fault plane, dashed line-bedding plane, dot-fault lineation, square-mean vector, N-number of lineations included in calculation of mean vector.

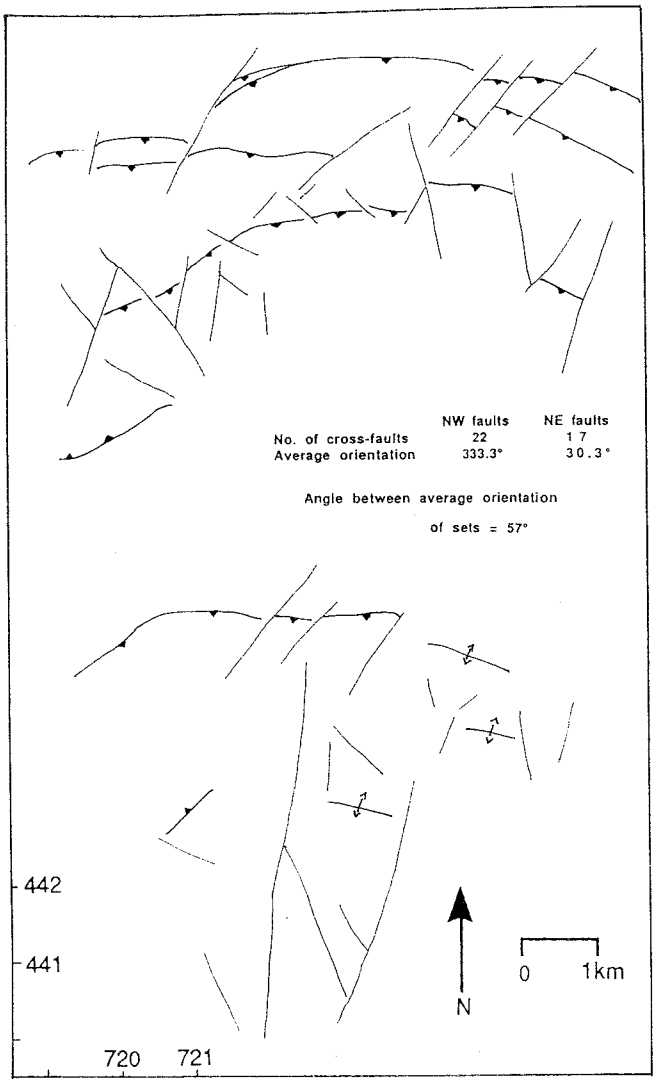


Fig 2.2.1.17. Distribution of the dextral NW-SE and sinistral NE-SW strike slip faults within the Alcaraz Antitaxis. Two populations of subvertical faults are identified which may be conjugate sets. These faults may accommodate tangential extension within the antitaxis.

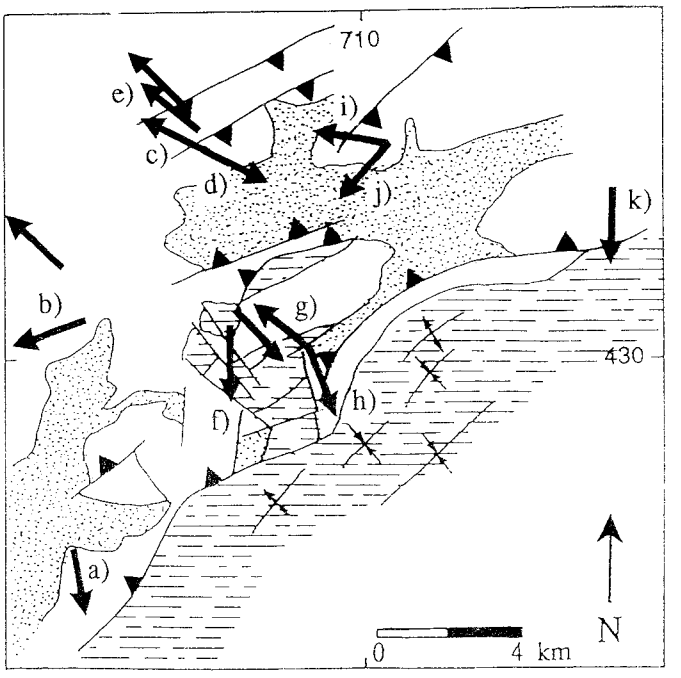


Fig 2.2.1.18. Variation in tectonic transport directions in the Riopar area (located in Fig 2.1.1). NW and WNW thrusting predominates with minor WSW thrusting. Later oblique SSE backthrusting occurs in some locations, causing the development of small fault-bounded blocks. Stipple-Triassic, unshaded-Jurassic, dashed-Cretaceous.



Fig 2.2.1.19. GR 70864300 near the Nacimiento del Rio Mundo. Looking SW. Oblique backthrust duplex (D) is shown to cross-cut (2) earlier forethrusts (1). Stereoplots shown in Fig 2.2.1.20 g) and h). Book=18cm.

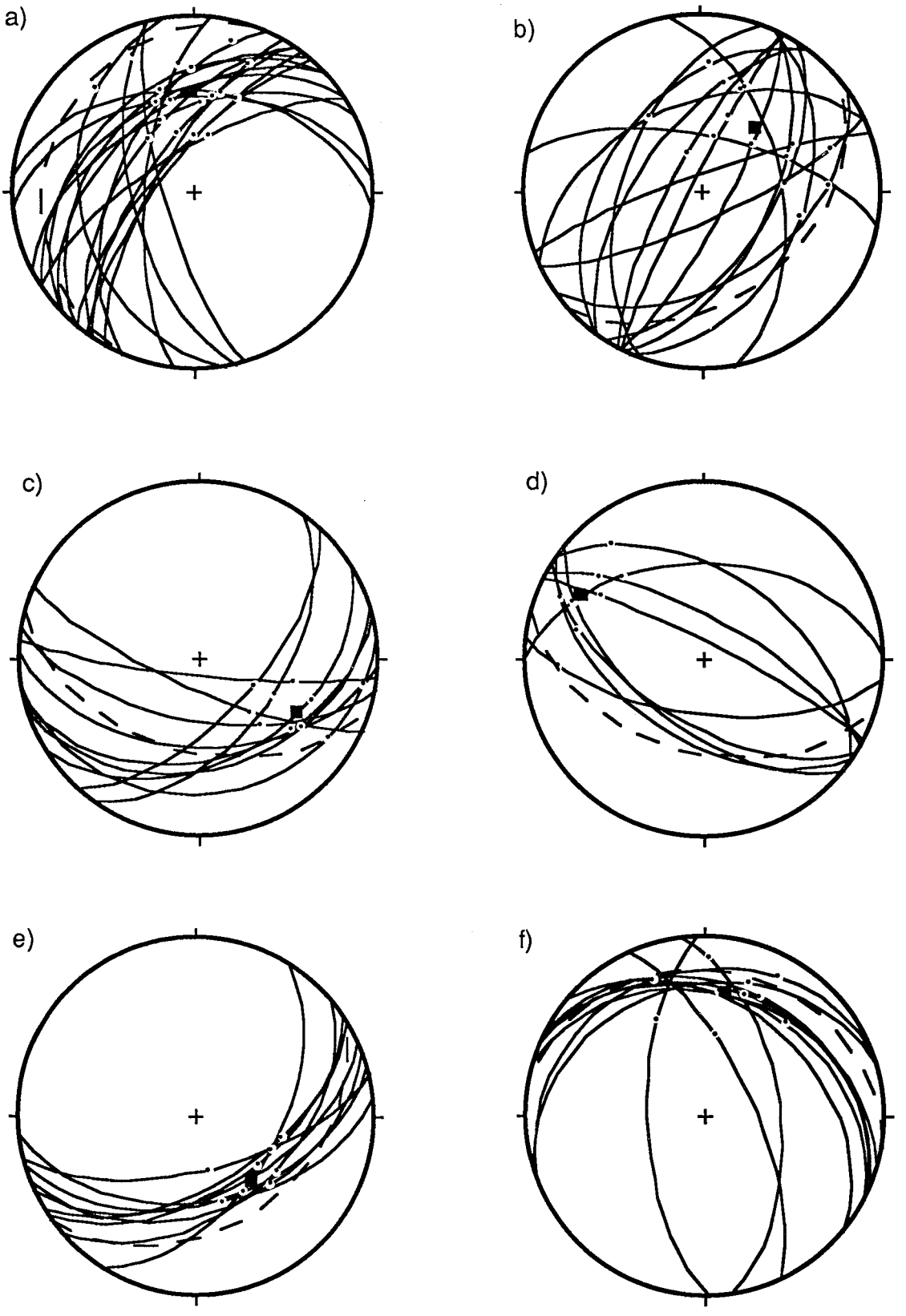


Fig 2.2.1.20. Stereoplots of locations a) to f) from the Riopar area (Fig 2.2.1.18).
a) S thrusting (N=18, Mean=43/355)
b) SW oblique thrusting (N=15, Mean=44/070)
c) WNW thrusting (N=9, Mean=40/118) and d) ESE oblique backthrusting/strike slip (N=8, Mean=26/298)
e) NW thrusting (N=9, Mean=52/134)
f) S thrusting and minor strike slip faulting (N=10, Mean=30/010)
Solid line-fault plane, dashed line-bedding plane, dot-fault lineation, square-mean vector, N-number of lineations included in calculation of mean vector.

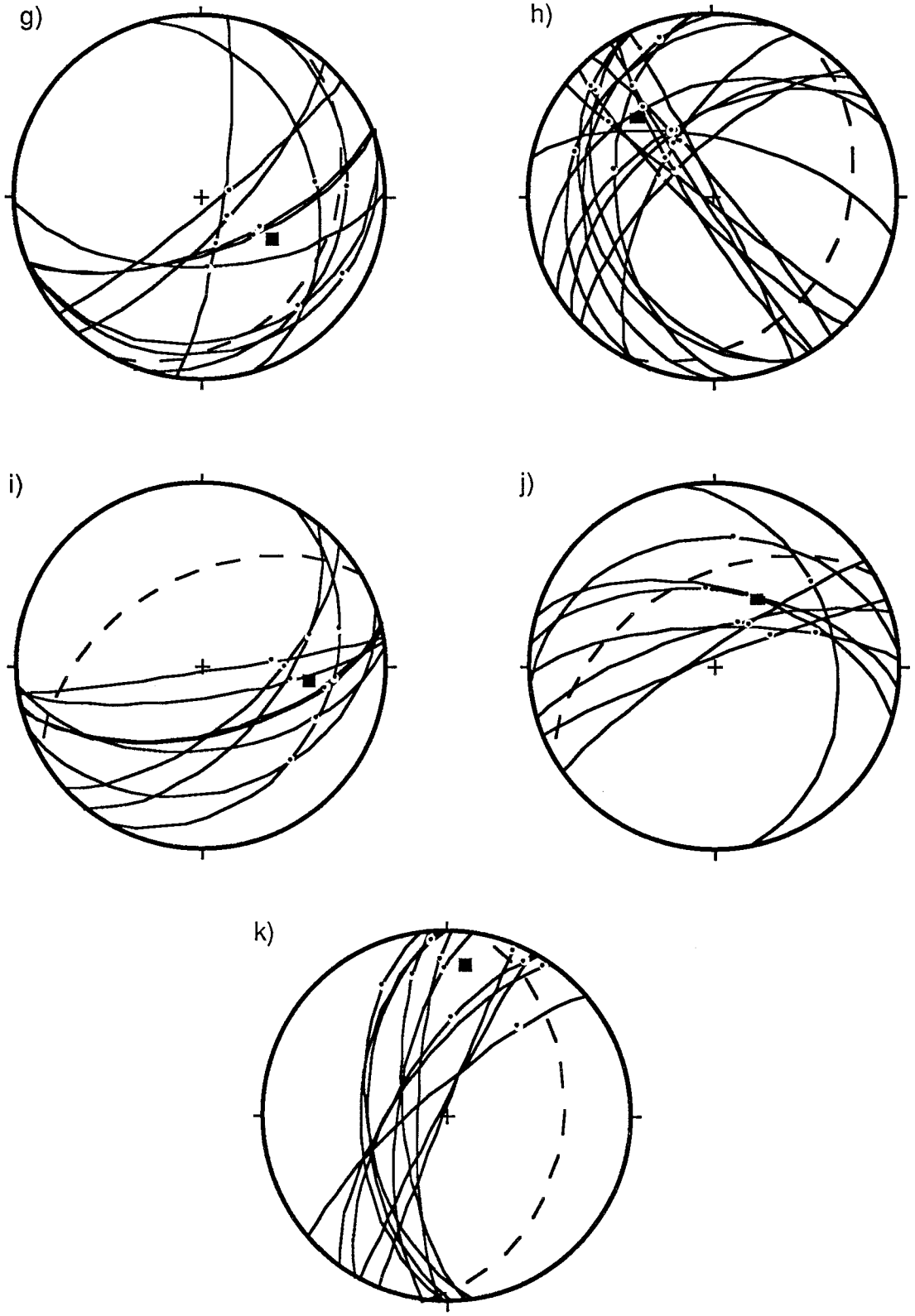


Fig 2.2.1.20. (cont'd) Stereoplots of locations g) to l) from the Riopar area (Fig 2.2.1.18).
g) NW thrusting (N=10, Mean=54/119) and h) SE backthrusting (N=18, Mean=43/317) with strike slip faulting
i) W thrusting (N=9, Mean=41/097)
j) SW thrusting (N=9, Mean=54/034) and k) SSW oblique thrusting/strike slip (N=10, Mean=19/006)
Solid line-fault plane, dashed line-bedding plane, dot-fault lineation, square-mean vector, N-number of lineations included in calculation of mean vector.

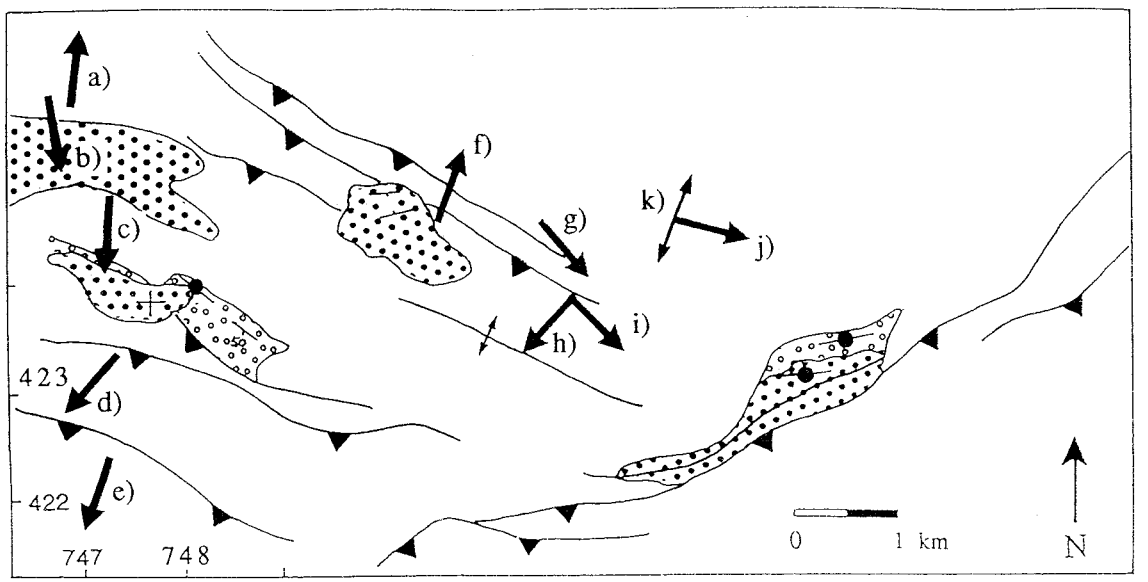


Fig 2.2.1.21. Variation in tectonic transport directions in the Elche area (located in Fig 2.1.1). In the west of the area, there is N/NNE and S/SSW thrusting and backthrusting [a) to e)].
In the east, there are two distinct trends of deformation, an earlier trend of NE-SW tectonic transport and a later trend of NW-SE tectonic transport (see photo 2.2.1.28). This superposition of structural trends is due to the continuing progression of convergent tectonic transport directions in the syntaxis (Fig 2.2). Unshaded-Jurassic, open dots-Burdigalian to early Seravallian, closed dots-middle Seravallian.

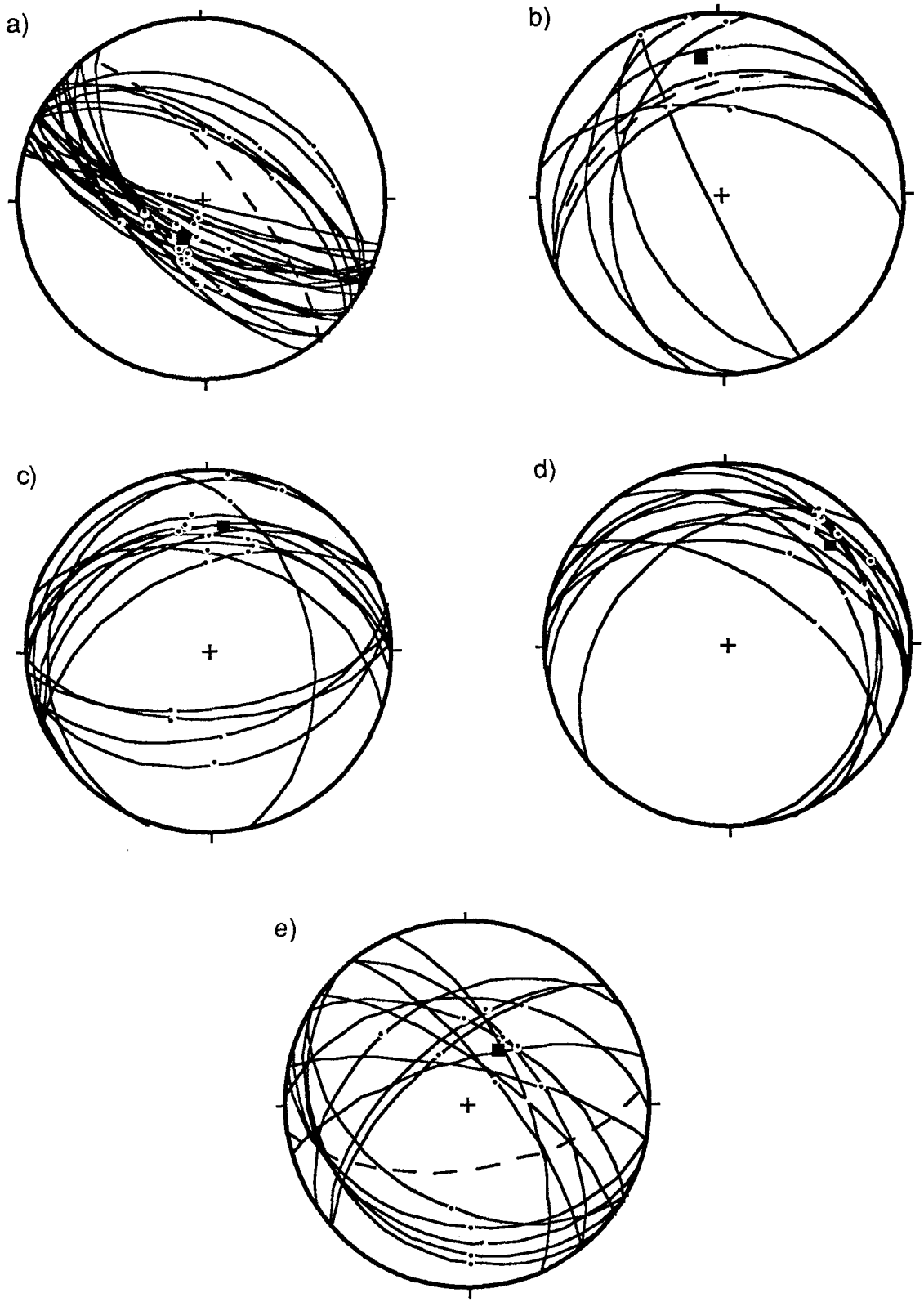


Fig 2.2.1.22. Stereoplots of locations a) to e) from the Elche area (Fig 2.2.1.21).
a) NNE thrusting (N=19, Mean=70/208) with minor backthrusting
b) S backthrusting (N=8, Mean=26/353)
c) SSW backthrusting (N=10, Mean=31/007) with minor thrusting. Rotated around bedding 22/340
d) SW backthrusting(N=11, Mean=23/047). Rotated around bedding 88/040
e) SSW backthrusting (N=11, Mean=62/028) and NNE thrusting
Solid line-fault plane, dashed line-bedding plane, dot-fault lineation, square-mean vector, N-number of lineations included in calculation of mean vector.

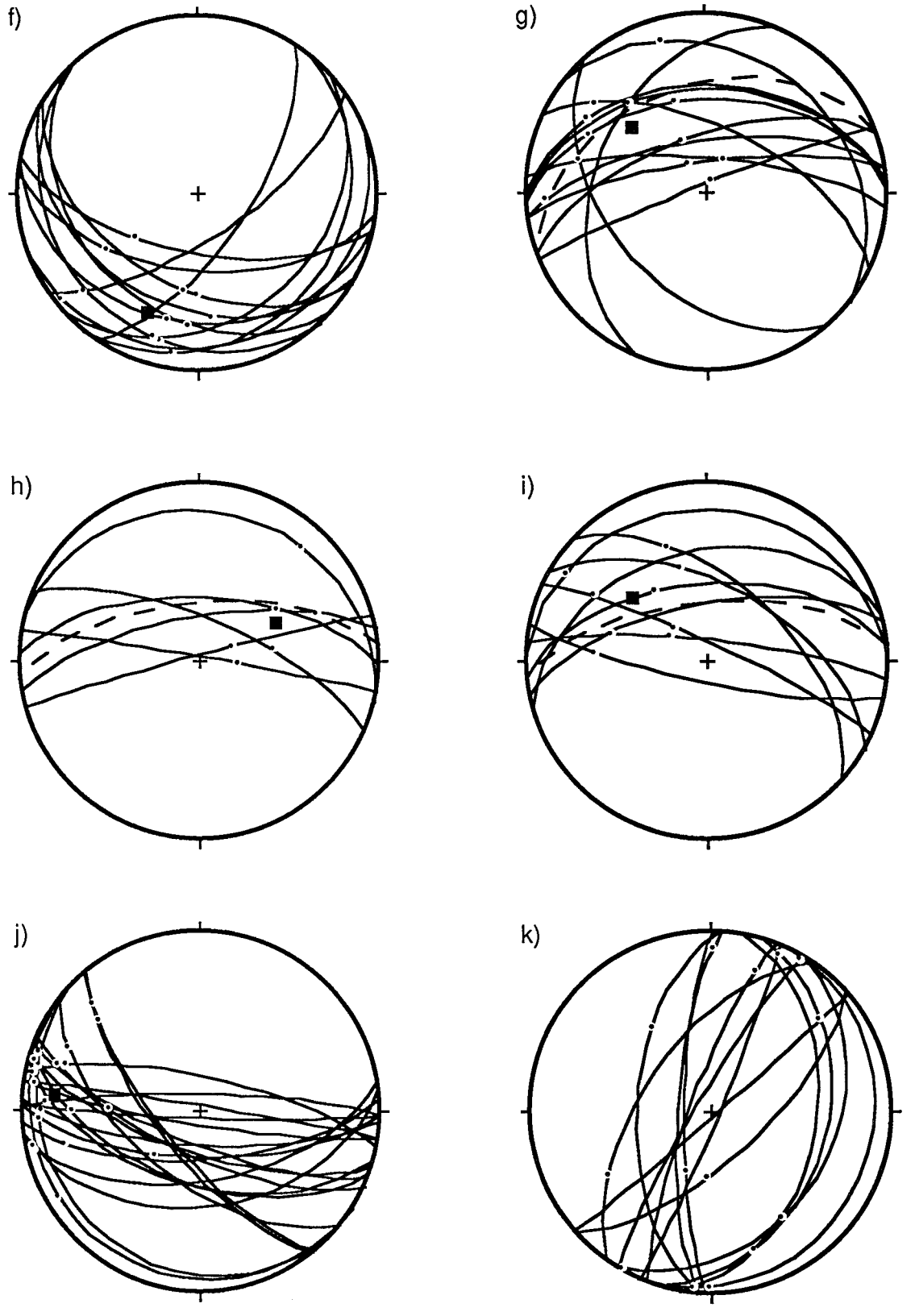


Fig 2.2.1.22. (cont'd) Stereoplots of locations f) to k) from the Elche area (Fig 2.2.1.20).
f) NNE thrusting (N=12, Mean=29/202). Rotated around bedding 84/205
g) SE backthrusting (N=12, Mean=45/313) with minor strike slip faulting
h) WSW backthrusting (N=6, Mean=61/053) and i) SE backthrusting (N=9, Mean=45/309)
j) ESE backthrusting (N=20, Mean=18/277). Rotated around bedding 28/230 and k) NNE-SSE oblique thrusting/backthrusting/strike slip. Rotated around bedding 28/230
Solid line-fault plane, dashed line-bedding plane, dot-fault lineation, square-mean vector, N-number of lineations included in calculation of mean vector.



Fig 2.2.1.23. GR 74704250 on the road from Elche de la Sierra to Socovos. Looking W. Original extensional faults (E) within Jurassic limestone. Thrust (T) ramps (r) may preferentially reactivate these original extensional structures. Thrust flats may sub-parallel bedding (f). Stereoplot shown in Fig 2.2.1.22 c). Hammer=25cm.

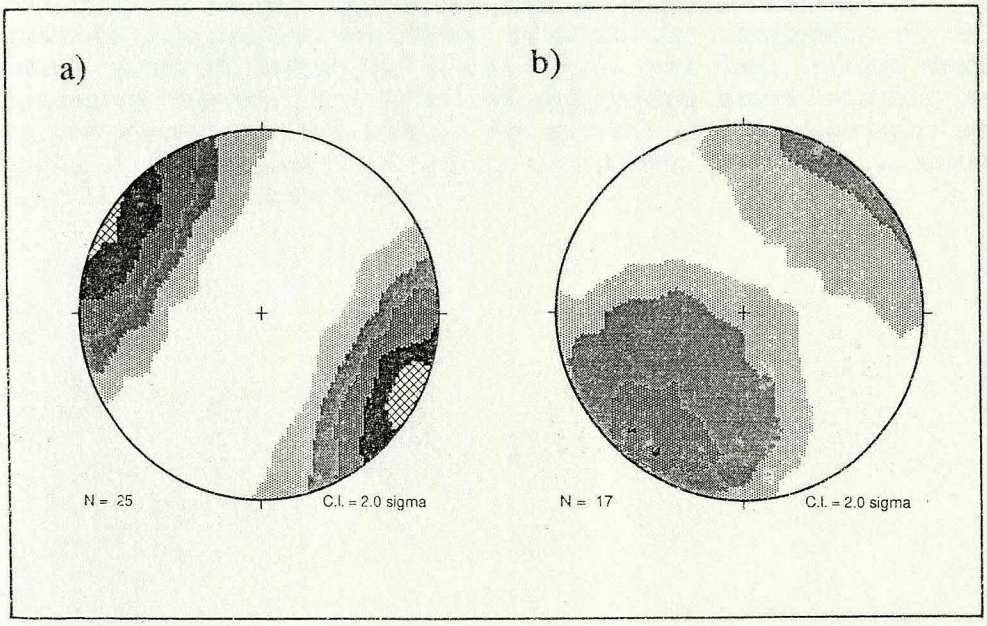


Fig 2.2.1.24. Contoured stereoplots of distribution of fault lineations associated with the dextral Socovos Fault. a) dextral strike slip faults trending at 117°. b) sinistral strike slip faults trending at 41°.

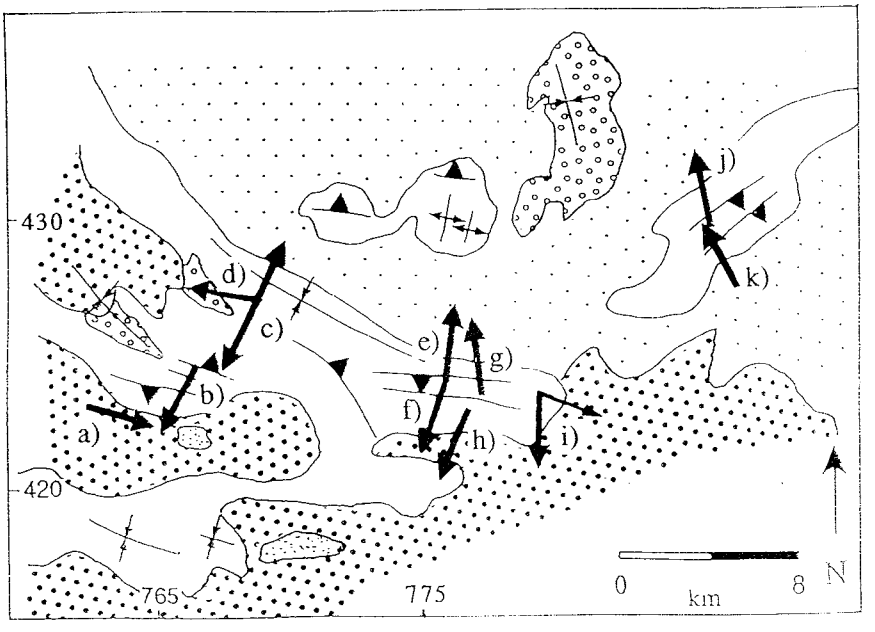


Fig 2.2.1.25. Variation in tectonic transport directions in the Isso area (located in Fig 2.1.1). NW thrusting predominates in the east of the area and the tectonic transport direction in the west of the area is predominantly NE-SW thrusting and backthrusting representing the strike perpendicular component of strain partitioning exhibited across the Socovos Fault with later oblique reactivation. The interaction between these trends of deformation causes complex patterns of folding and thrusting in the core of the syntaxis. Unshaded-Jurassic, open dots-Burdigalian to early Seravallian, closed dots-middle Seravallian to Messinian, spaced dots-Pliocene/Quaternary.

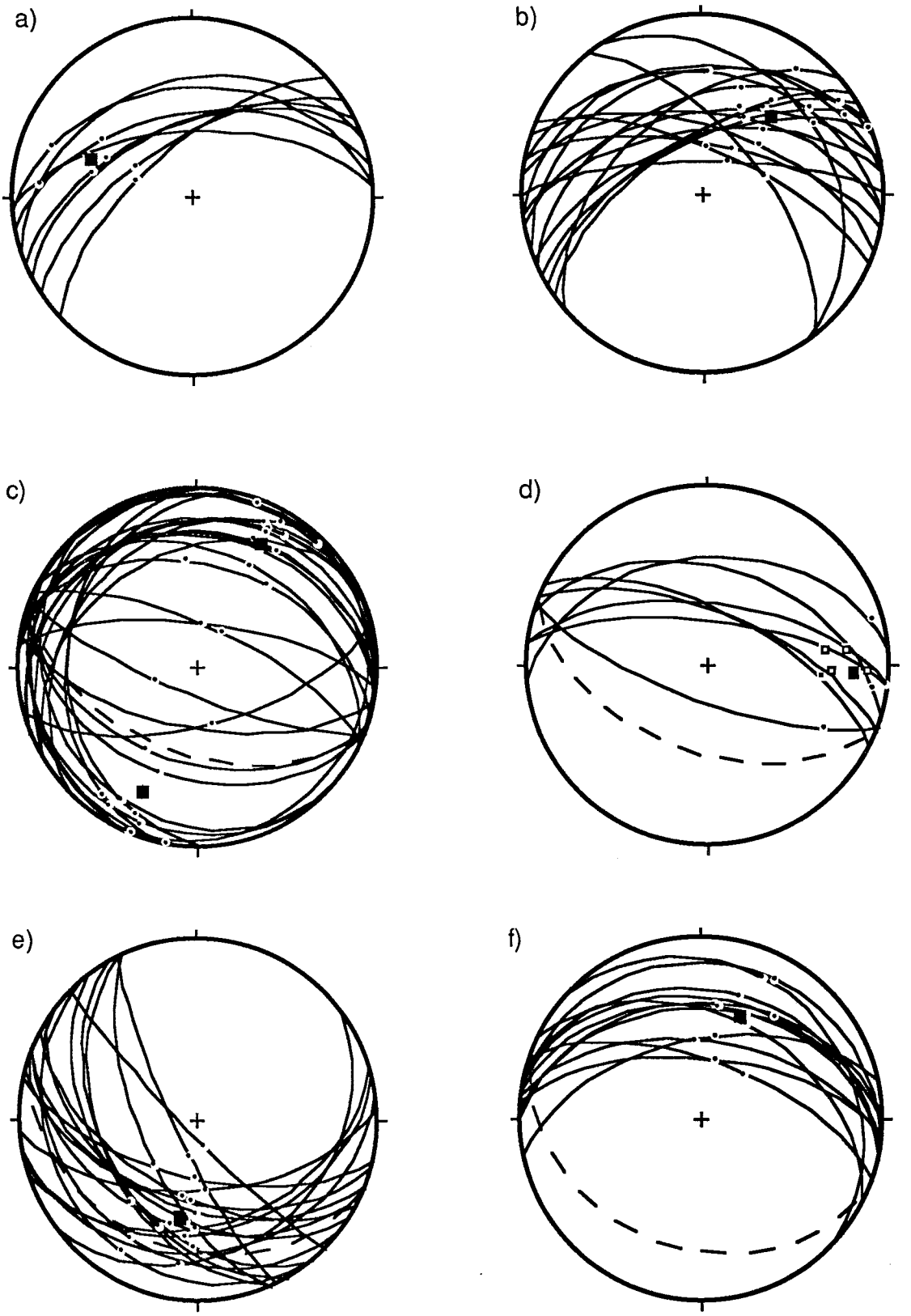


Fig 2.2.1.26. Stereoplots of locations a) to f) from the Isso area (Fig 2.2.1.25).
a) later ESE backthrusting (N=8, Mean=41/290). Rotated around bedding 11/092
b) SW backthrusting (N=18, Mean=41/042). Rotated around bedding 25/010
c) NNE/SSW thrusting (N=10, Mean=25/026)/backthrusting (N=14, Mean=28/205) and
d) later oblique westward reactivation and strike slip faulting (N=8, Mean=21/094), open boxes represent secondary reactivation lineations
e) NNE thrusting (N=17, Mean=46/192) and f) SSW backthrusting (N=12, Mean=41/020)
Solid line-fault plane, dashed line-bedding plane, dot-fault lineation, square-mean vector, N-number of lineations included in calculation of mean vector.

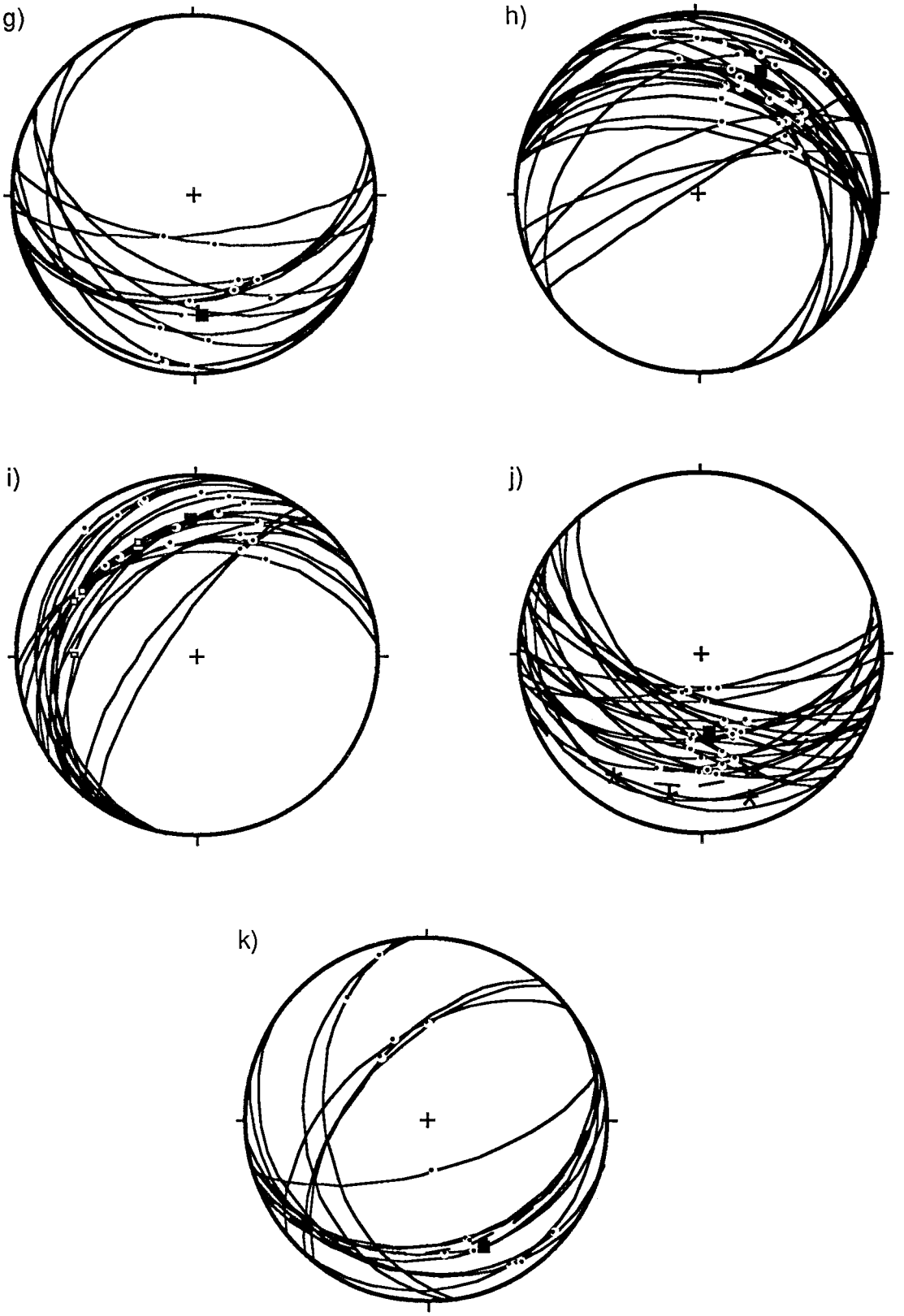


Fig 2.2.1.26. (cont'd) Stereoplots of locations g) to k) from the Isso area (Fig 2.2.1.25).
g) N thrusting (N=13, Mean=35/175). Rotated around bedding 30/200
h) SSW backthrusting (N=26, Mean=31/030). Rotated around bedding 30/112
i) S backthrusting (N=21, Mean=24/357), open boxes represent secondary reactivation lineations. Rotated around bedding 50/055
j) N thrusting (N=25, Mean=50/175), stars represent low-angle (R1) Reidel shear lineations
k) NNW thrusting (N=8, Mean=27/155) with minor backthrusting
Solid line-fault plane, dashed line-bedding plane, dot-fault lineation, square-mean vector, N-number of lineations included in calculation of mean vector.



Fig. 2.2.1.27. GR 76754244 on the road from Hellín to Cenajo. Looking N. Two sets of crystal lineations on a fault plane (65/027). Earlier lineation (L1), oriented at 62/353; second lineation (L2), oriented at 37/091. Stereoplots shown in Fig 2.2.1.26 c) and d).



Fig 2.2.1.28. GR 75284247 from the viewpoint on the Hellín to Cenajo road. Looking 140°SE. Two trends of deformation. A NW-SE trending thrust slice (1) is present in the foreground. NE-SW trending thrust slices (2), which incorporate middle Seravallian calcarenites, are seen in the background. Relief of foreground thrust slice=150m.

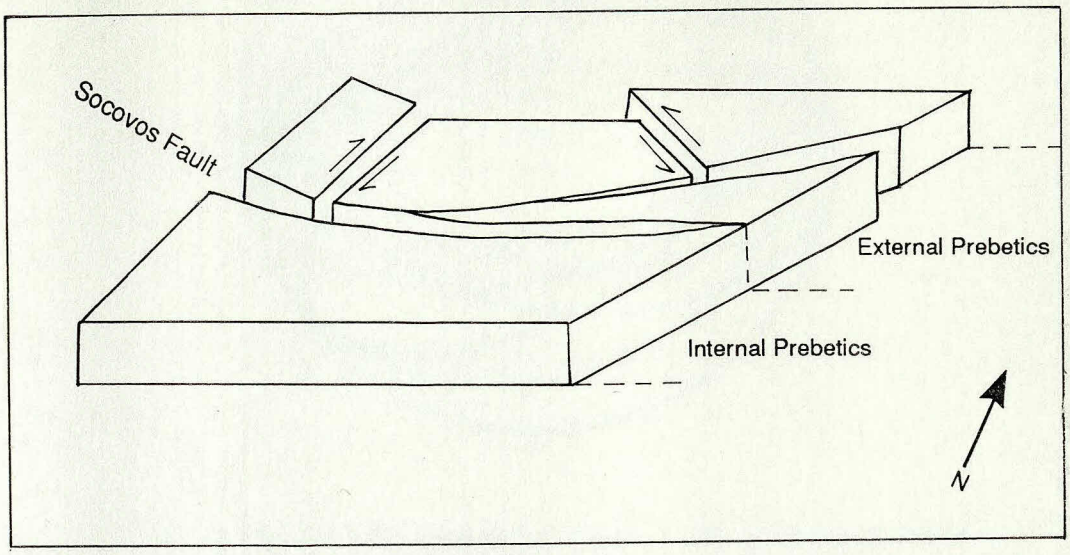


Fig 2.2.1.29. Schematic diagram of the formation of the Cenajo Syntaxis after Jerez Mir (1973).



Fig 2.2.1.30. GR 76554223 on the road from Hellín to Cenajo. Looking NE. Thrust fault (F) within Messinian marl and limestone. Stereoplot shown in Fig 2.2.1.26.a).

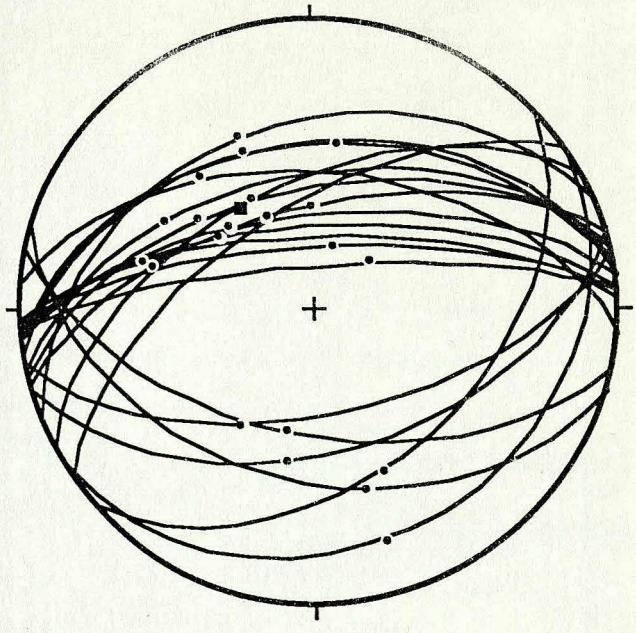


Fig 2.2.2.1. Stereoplot of SSE backthrust duplex with associated NNW thrusting, from the Internal Prebetics, SW of the Socovos Fault. (N=15). Solid line-fault plane, dot-fault lineation, square-mean vector, N-number of lineations included in calculation of mean vector.



Fig 2.2.2.2. GR 72044207 near Yeste. Looking W. Listric extensional faults (L) within Cretaceous marl and mudstone of the Internal Prebetics. Relief of outcrop=15m.

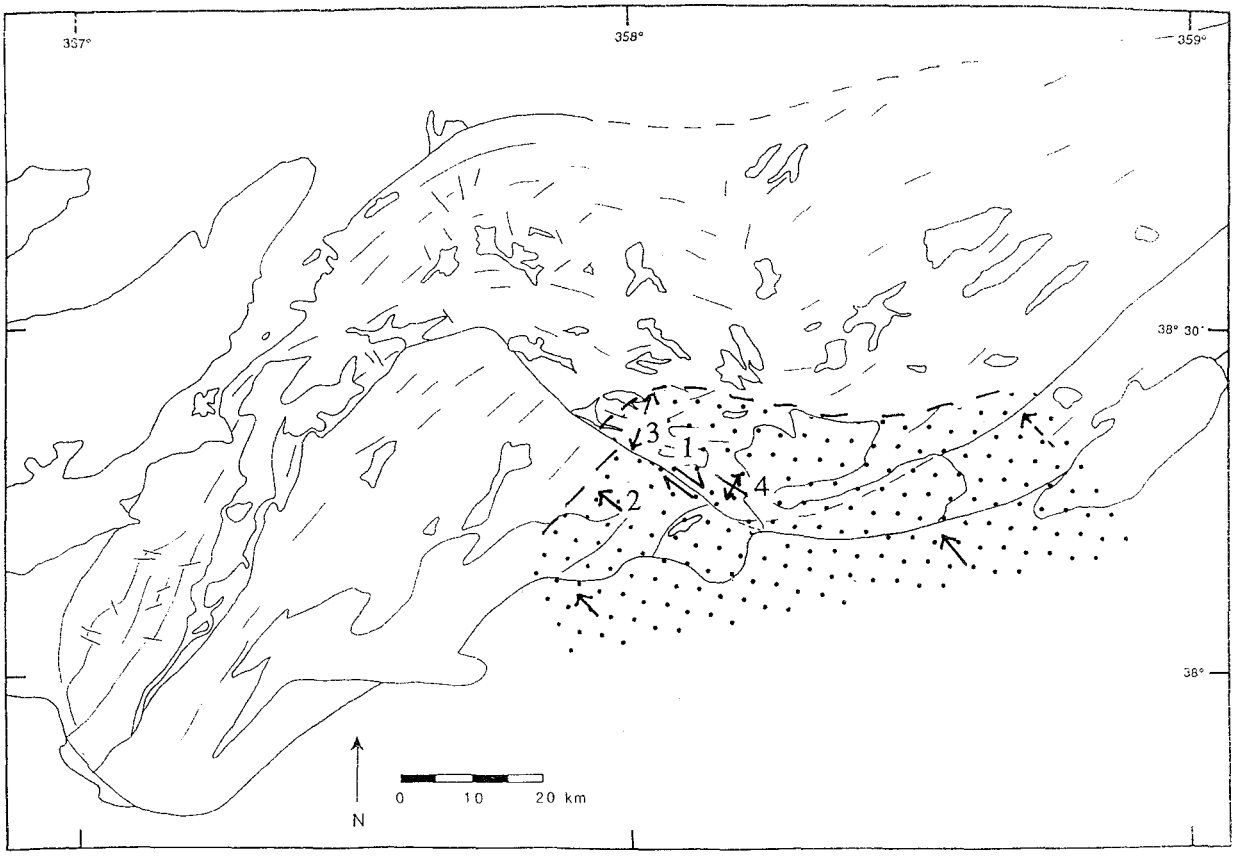


Fig 2.3.1.a) Deformation in the late Burdigalian-early Seravallian. The deformation was initiated during this time and nucleated around and propagated out from the Socovos Fault. The Subbetic Front was active as a thrust at a location further to the SE. Shaded area-active, closed arrows-tectonic transport direction in active areas, open arrows-tectonic transport direction in possibly active areas. Location numbers-see text.

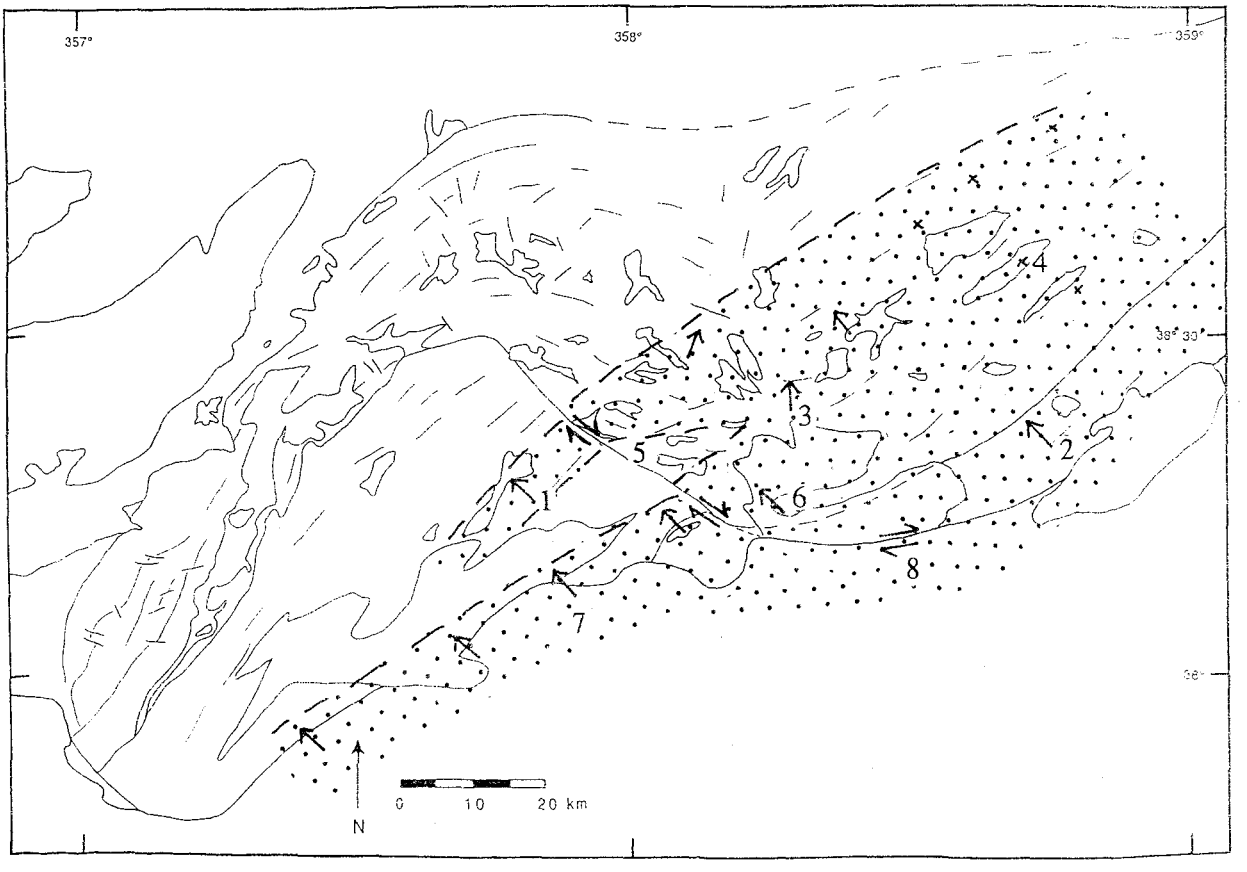


Fig 2.3.1.b) Deformation in the middle-late Seravallian. There is a marked progression of deformation towards the foreland. The Socovos Fault zone is active in segments, the SE segment and adjacent areas were active in response to the out-of-sequence nature of the Subbetic frontal thrust.

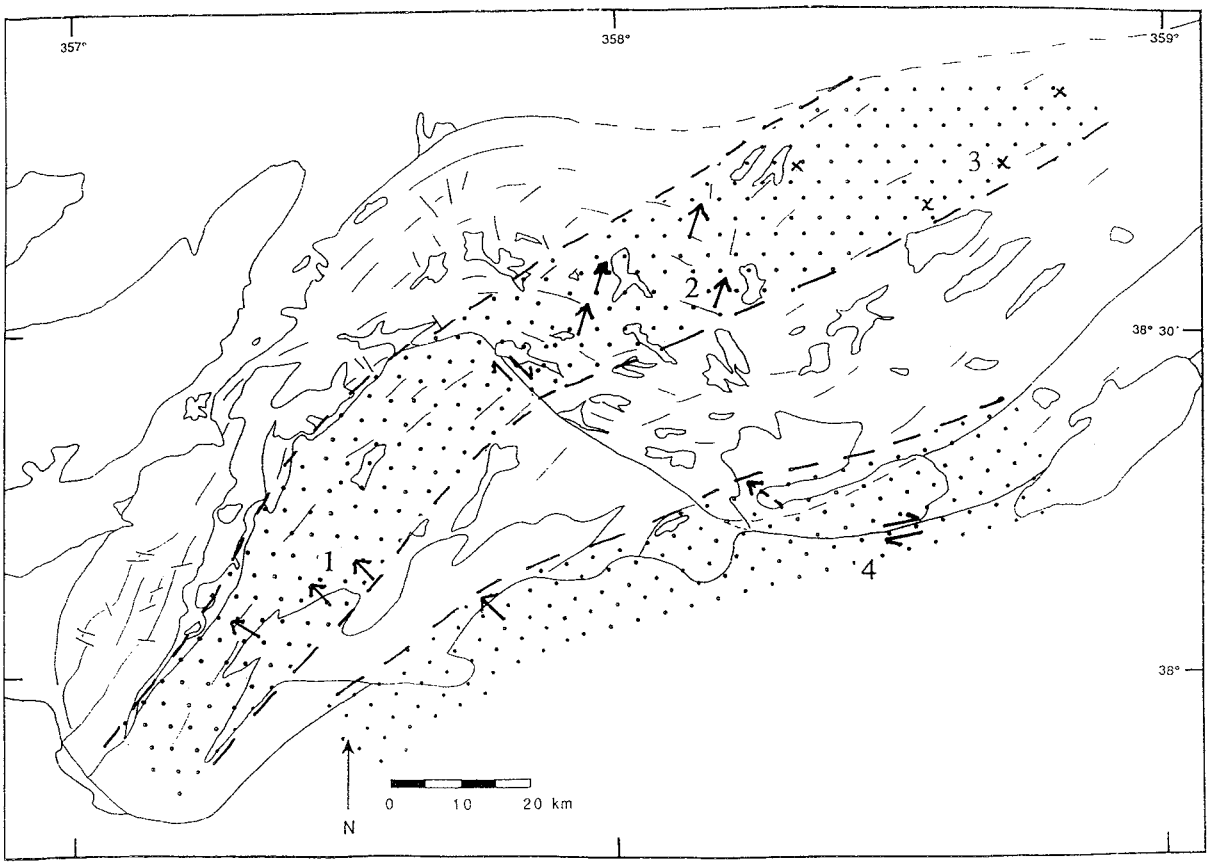


Fig 2.3.1.c) Deformation in the Tortonian. The Internal Prebetics shows a slight swing in tectonic transport direction from NW to more WNW as deformation progresses towards the foreland. Only the NW segment of the Socovos Fault is active. The more foreland parts of the NW Trending Limb and Cenajo Syntaxis also experienced deformation at this time. The Subbetic frontal thrust remains active to some extent.

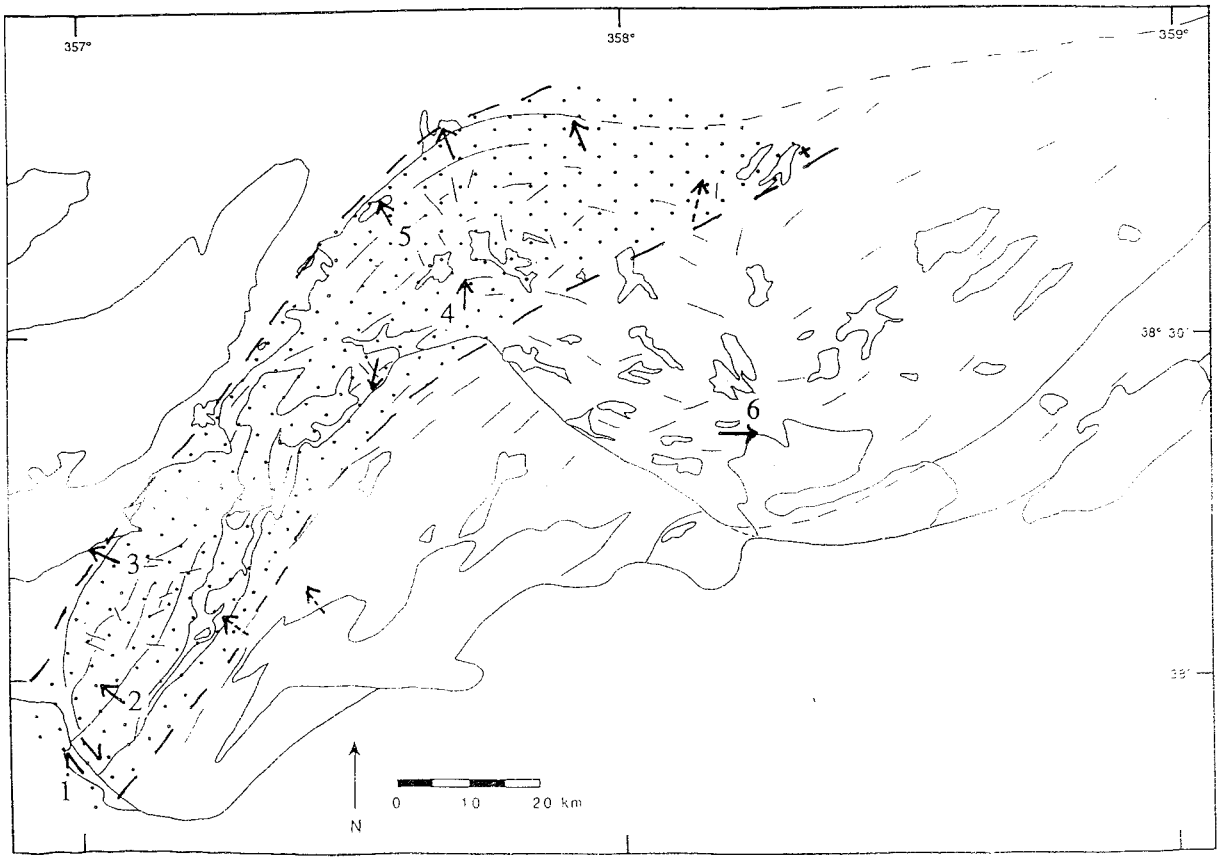


Fig 2.3.1.d) Deformation in the Messinian. The Socovos Fault became inactive and the shortening accommodated by it was transferred onto the E-W and NE-SW trending thrusts of the NE Trending Limb and the Alcaraz Antitaxis. There was a gradual change in transport direction in the NE Trending Limb, from NW to more WNW, with progression towards the foreland. Minor deformation was exhibited in the Cenajo Syntaxis which may be associated with local diapirism of subsurface Triassic.



Fig 2.3.2. GR 75074157 near Socovos. Looking SE. Slumps within upper Burdigalian to lower Seravallian limestone and marl. Slump hinges-H. Stereoplot shown in Fig 2.3.3.

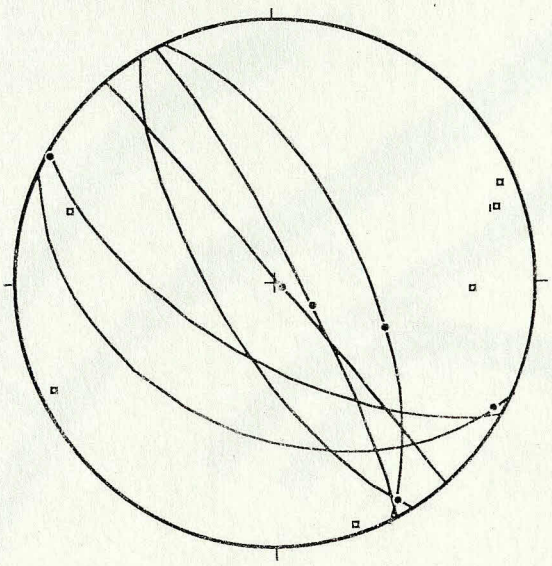


Fig 2.3.3. Stereoplot of the slumps associated with the Socovos Fault (see photo 2.3.2). Solid line-fault plane, dot-fault lineation, square-slump fold hinge line.



Fig 2.3.4. GR 74594240 on the road from Elche de la Sierra to Socovos. Looking ESE. Intra-formational unconformity (U). Syn-orogenic upper Burdigalian to lower Seravallian bioclastic limestone (1) has been steepened to sub-vertical and then overlain by shallowly-dipping middle Seravallian bioclastic limestone (2). Maximum relief approximately 60m.

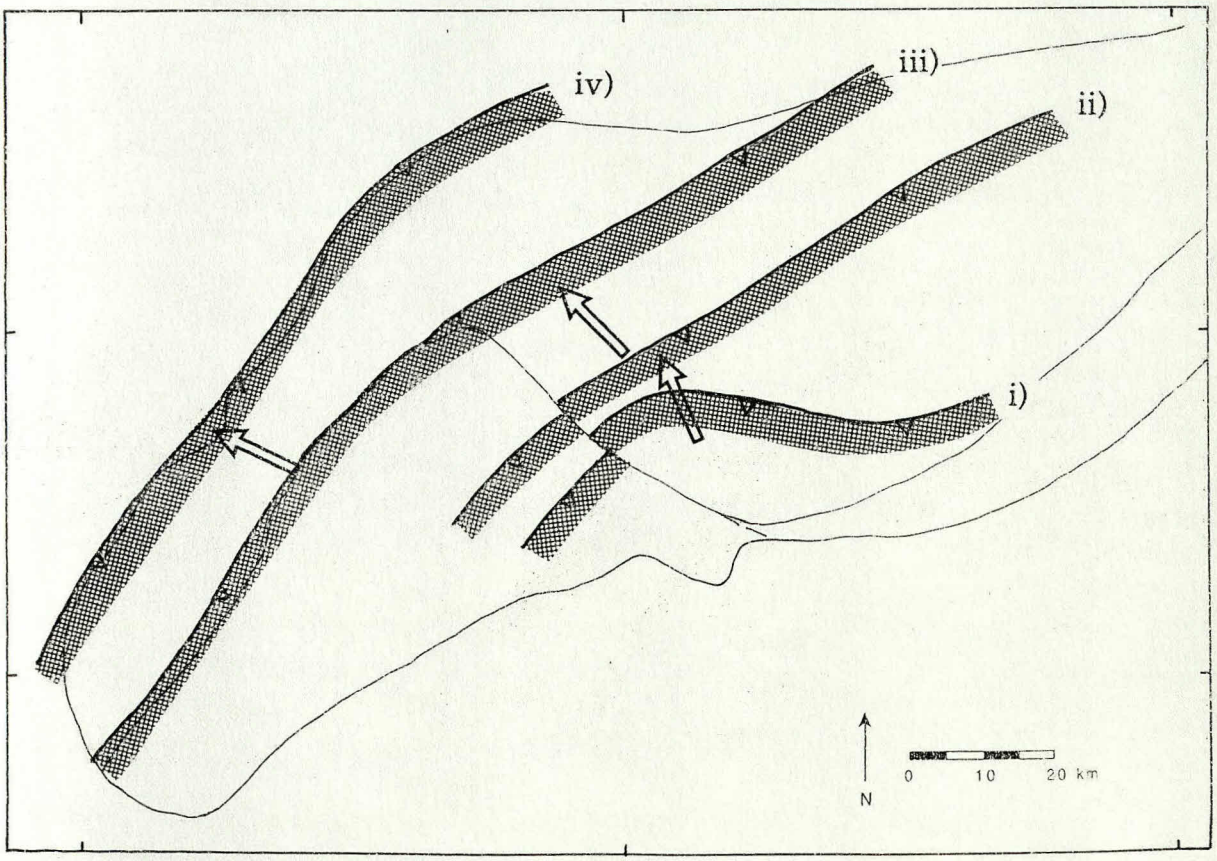


Fig 2.3.5. Diagram of the propagation of the main wave of deformation in the External and Internal Prebetics showing an anticlockwise swing in the trend of the deformation. Open arrows - overall tectonic transport direction vector.

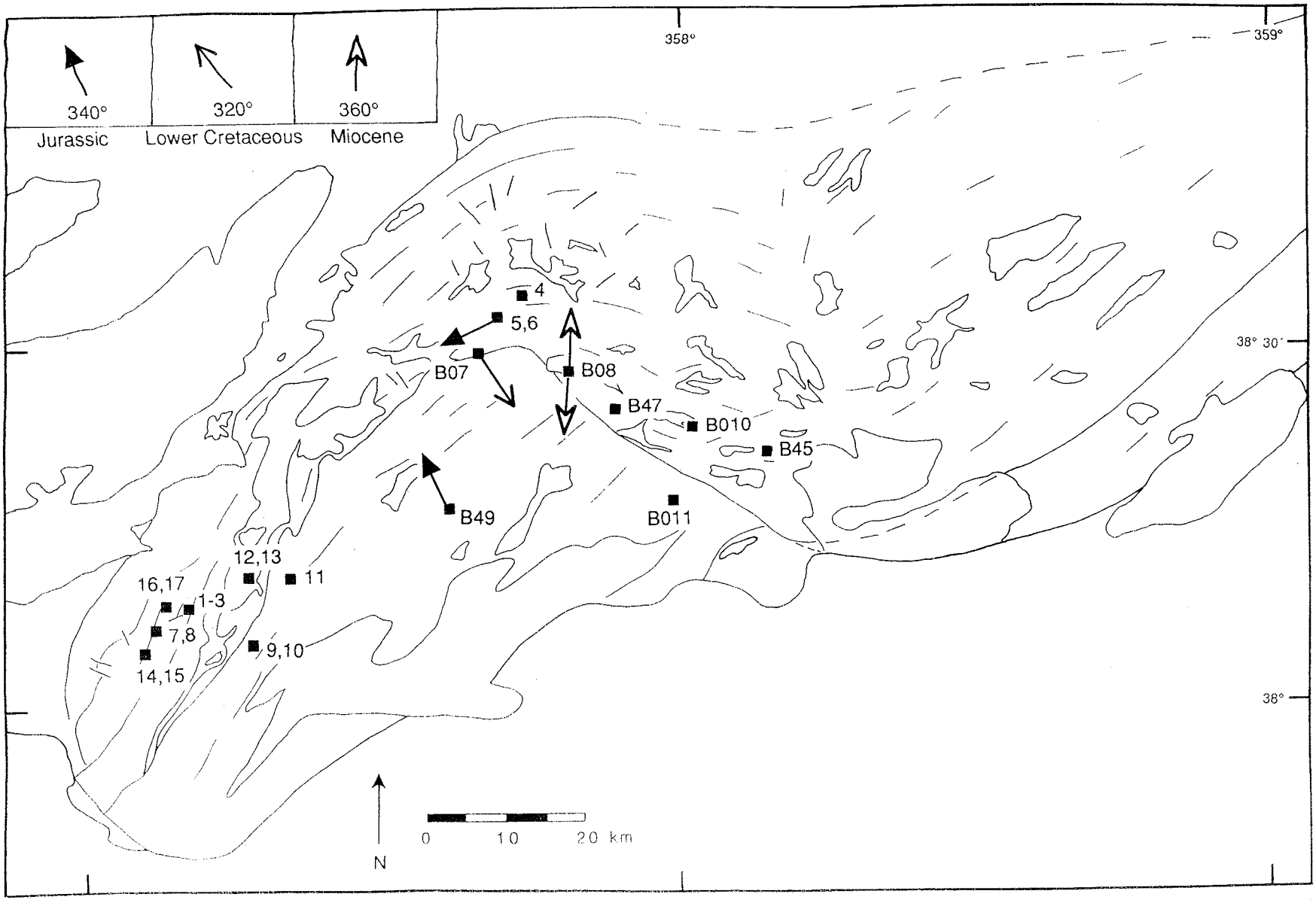


Fig 2.4.1. Location map of palaeomagnetic sites in the western Prebetics (Table 2.4). Palaeomagnetic vectors and the reference directions for Jurassic, lower Cretaceous and Miocene are shown. Locations 5,6 and B07 suggest the presence of small block rotations in the hinge area of the Alcaraz Antitaxis. Location B49 indicates that the Internal Prebetics is unrotated. Location B08 indicates that no substantial rotation has occurred since the Miocene.

Sample No.	Age	Lithology	typical NRM	Declination/ Inclination	Bedding - dip/dip direct.	Bedding corrected Dec/Incl	Comments
Data from C.R.M.Mandeville							
CRM1.2	L. Jurassic	dolomite	0.07				unstable
CRM2.6	L. Jurassic	dolomite	0.07				unstable
CRM3.2	L. Jurassic	dolomite	0.07	310/40	13/042	320.8/39.2	present day field?
CRM4.3	L. Jurassic	dolomite	0.12				unstable
CRM5.5	L. Jurassic	dolomite	0.2	227/-2.9	80/353	252.4/34.7	approx 90° rot anticlockwise
CRM6.6	L. Jurassic	dolomite	0.2				unstable
CRM7.4	U. Jurassic	*Amm. Rosso*	0.1	020/45	55/282	335.3/29.1	
CRM7.7	U. Jurassic	*Amm. Rosso*	0.1	360/50	35/327	327/18.6	
CRM8.4	U. Jurassic	limestone	0.1	010/50	22/354	005.6/28.6	present day field?
CRM9.1	Cenomanian	limestone	0.8	350/50	49/274	316.5/22.7	
CRM9.2	Cenomanian	limestone	0.8	350/50	49/274	316.5/22.7	low temperature component
CRM10.1	Cenomanian	limestone	0.8	350/45	10/300	343.5/38.1	possibly goethite
CRM11.1	Aptian	limestone	0.2	340/70	39/262	289.4/43.3	
CRM11.8	Aptian	limestone	0.2	025/50	24/298	359.9/43.3	
CRM12.4	Triassic	sandstone	5				couldn't resolve high temperature
CRM13.3	Triassic	sandstone	5				component - much gypsum flow
CRM14.7	U. Jurassic	limestone	0.1	155/00	65/130	357.8/55.2	present day field?
CRM15.4	U. Jurassic	limestone	0.1				unstable
CRM16.2	L. Jurassic	dolomite	0.1				unstable
CRM17.3	L. Jurassic	dolomite	0.01				unstable
Data from S.Allerton							
B0701B	Aptian/Albian	limestone	-	162.9/42.6	-	135.7/40.5	possible clockwise rotation
B0801A	Messinian	marl/lmst	-	187/-55	-	183.9/-47.5	Miocene reversed component
							indicates no rotation
B010	U. Jurassic	limestone					unstable
B011	Albian	limestone					unstable
B45	U. Jurassic	limestone					weak NRM dominantly goethite
B47	U. Jurassic	limestone					"
B49	**U. Jurassic**	***Amm. Rosso***	**-**	**348/49**	**18/250**	**336/49**	**Site N=7 a95=13.7 k=20.4**

Table 2.4. Results of palaeomagnetic studies

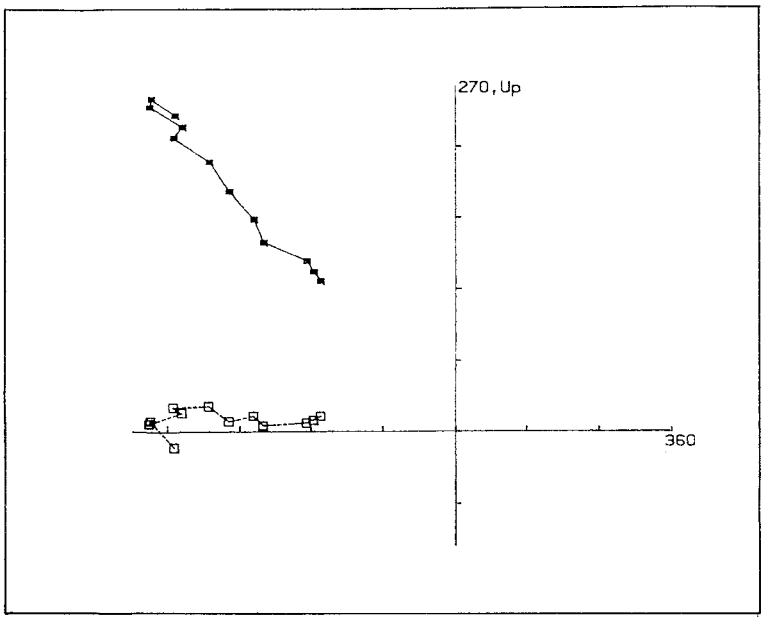


Fig 2.4.2. Zijderveld plot for sample CRM5-5 in Jurassic limestone. Closed squares-declination=230°, open squares-inclination=horizontal.

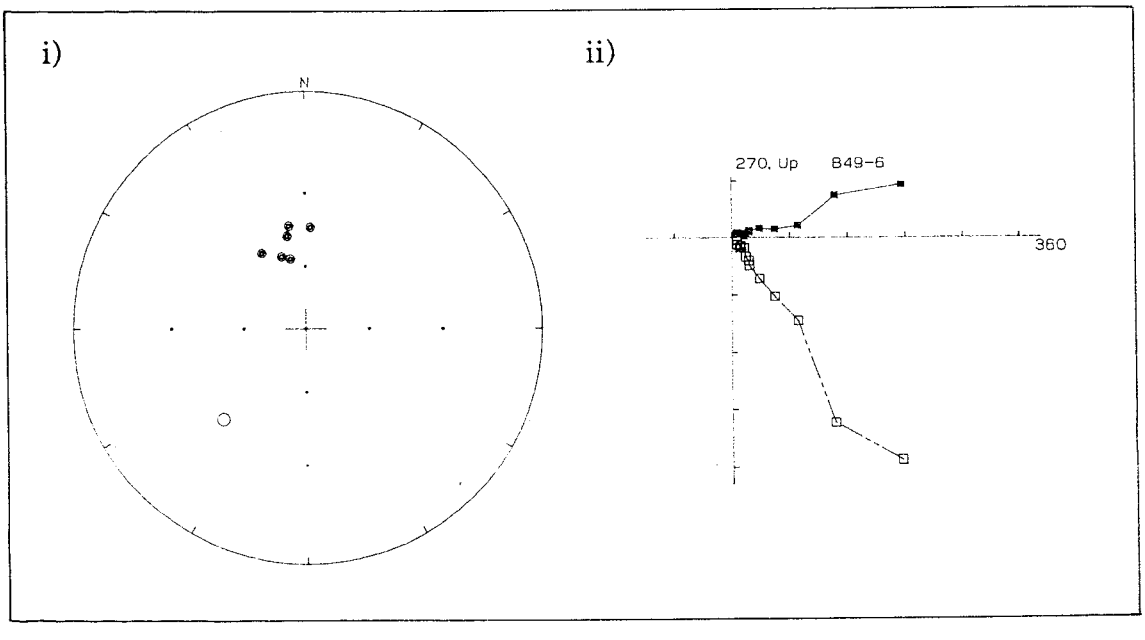


Fig 2.4.3. i) Stereoplot showing the palaeomagnetic vectors, for sample B49-6 in Jurassic limestone, of 7 cores, 6 showing a normal magnetic field and 1 showing a reversed magnetic field. declination=356°, inclination=49°, $\alpha 95$=13.7. ii) Zijderveld plot for sample B49-6. Closed squares-declination, open squares-inclination.

Chapter 3

CHAPTER 3

SUBSIDENCE AND BASIN FORMATION IN THE PREBETIC ZONE

3.1. Introduction

Stratigraphic and structural analysis indicate that the External Zones, including the Prebetic Zone, of the Betic Cordillera have experienced several episodes of deformation resulting from periods of different tectonic influence. Dercourt et al. (1984) postulate that the margin of stable Iberia underwent initial rifting in the Pliensbachian. However, the results of tectonic subsidence analysis of the Subbetic Zone by Peper & Cloetingh (1992) indicate initial rapid subsidence in the Middle Triassic with later phases of rapid subsidence in the Early Jurassic and Middle Jurassic-Early Cretaceous. Steady subsidence is observed from the Late Cretaceous onwards indicating a thermal control on subsidence (Peper & Cloetingh 1992) and the development of a passive continental margin (Garcia-Hernandez et al. 1980). Convergence between Africa and Iberia was initiated in the Late Cretaceous (Dewey et al. 1989) and caused compressive deformation to propagate through the Betic Cordillera overprinting the earlier extensional deformation. In the middle-late Miocene intramontane basins developed within the Prebetic Zone. Investigation of the tectonic subsidence curves calculated for various sections in the External and Internal Prebetics, can provide information on the nature and duration of the tectonic events experienced. Fitting of theoretical subsidence curves, generated by the uniform stretching model (McKenzie 1978, Jarvis & McKenzie 1980) to the water-loaded subsidence curves allows the magnitude and duration of stretching events to be quantified (e.g. Wooler et al. 1992).

Subsidence histories have been calculated previously for areas within the Internal Prebetics (Kenter et al. 1990, Peper & Cloetingh 1992) but the External Prebetics remains less studied. Within the Jumilla-Cieza

region, Kenter et al. (1990) have identified six distinct periods of deformation based on subsidence histories, sedimentary facies patterns and the presence of marked unconformities in the stratigraphic sequence. The three main phases of deformation of the southern Iberian margin as it progressed from a Mesozoic passive margin, through an extensional phase (40-20 Ma) to a fold and thrust belt (20 Ma to recent) are shown in the subsidence curves presented in Kenter et al. (1990) (Fig 3.1.1.). The first, rifting stage is characterised by steady-state subsidence, probably due to lithospheric cooling. De Ruig et al. (1991) conclude that changes in basin geometry of the southern Iberian margin in the Palaeocene may result from intraplate compression resulting from the Pyrenean collision. The second stage documents an erosive hiatus during which time the study area was emergent. This period of deformation is interpreted as being tensile and is linked to the development of the regional extensional tectonics in the western Mediterranean during the Oligocene-Early Miocene which influenced the development of the Valencia trough and the easternmost Betic Cordillera (Dercourt 1984, Dewey et al. 1989, Van der Beek & Cloetingh 1992, Watts & Torné 1992). The third phase is characterised by the change to a compressive regime and the inversion of the margin to form a fold and thrust belt. Peper & Cloetingh (1992) analysed subsidence curves from the Internal Prebetics and across the Subbetic Zone and concluded that the southern Iberian margin underwent three phases of stretching, at 220 Ma, 202 Ma and 160 Ma, during the Mesozoic rifting stage.

3.2. Tectonic subsidence

Quantitative analysis of the subsidence curves of the Prebetic sub-areas show the influence of the differing tectonic phases on the Prebetic Zone and the variation of this influence around the arc. Twelve representative sections were investigated, seven from the External Prebetics, four from the Internal Prebetics and one from the north Subbetic Zone (Figs 3.2.1/2). The lithologies, thicknesses and facies interpretations (and hence range of appropriate palaeowater depths) of the ten sections, CM1-7, CM9, CM10 and N. Subbetic, were compiled from a combination of outcrop logs published on the relevant I.G.M.E. 1:50,000 geological sheets, literature reviews (e.g. Garcia-Hernandez 1980, Banks 1985) and field observations. The two BP sections were compiled from well logs.

Determination of the water-loaded tectonic subsidence curves can reveal much about the style of deformation experienced by a region e.g. whether rifting and/or crustal loading has taken place. The stretching factor, ß, for rifting may then be determined by fitting theoretical subsidence curves, generated by the uniform stretching model, to the water-loaded, tectonic subsidence curves (Wooler et al. 1992). It is assumed that the stretching is of finite duration and that the strain rate during stretching is constant (McKenzie 1978, Jarvis & McKenzie 1980). The water-loaded, tectonic subsidence curves differ from the basement subsidence curves in that they have had the effect of the sediment loading removed. The method for producing the tectonic subsidence curves from the compiled sections is backstripping i.e. decompacting the sediment load at any time, converting it into a water load and adding the depth of water in which the sediment was deposited (Steckler & Watts 1978, Sclater & Christie 1980, Barton & Wood 1984, Wooler et al. 1992). Various

parameters are required for this operation: accurate dates and thicknesses of the section, palaeowater depths, porosity-depth variation of the sediment types and the response of the lithosphere to loading. Palaeowater depths are assigned by a comparison of the ancient sedimentary facies and faunal assemblages with that of the modern day. The decompaction of the sedimentary load requires a knowledge of the porosity-depth variation of the sections. For this, the initial porosity and compaction decay length for each lithological unit of the section are calculated from the percentage shale, limestone, chalk, dolomite, sandstone and evaporite component present in that unit (Sclater & Christie 1980). The eustatic variation in sea-level is not included in the backstripping calculation. The effects of four different sea-level curves from the literature (Haq et al. 1987, Pitman 1978, Watts & Steckler 1979 and Watts & Thorne 1984) on subsidence curves and β factors have been assessed by Wooler et al. (1992). Addition of this factor in the calculation introduced significant negative subsidence (uplift) for all four sea-level curves. As periods of uplift are usually only recorded as unconformities (zero subsidence) they concluded that the currently available sea-level curves were not of sufficient accuracy to be included in the calculation.

This 1-D method of backstripping assumes that the lithosphere experiences Airy isostasy as it subsides. If the lithosphere has flexural strength, (Te>0), the subsidence curves will be erroneous. If no significant syn-rift topography is present and the Te is very low, (Te<5), the tectonic subsidence curves will be a reasonably acceptable minimum value. If syn-rift topography is present and the value of the Te is significant, the ß factor is overestimated if the compiled section is on a basement high and underestimated if the section is in a basement low. Palaeogeographical reconstructions of the Prebetic Zone indicate that it was located at the basin

margin and sedimentation occurred at relatively shallow depths (<200m) (Garcia-Hernandez et al. 1980). Due to the differential subsidence of the External Zones, the Te of the basin margin (including the Prebetic Zone) is probably relatively higher than that of the more basinal region (e.g. the Subbetic Zone) (Stockmal et al. 1986). This relative difference in Te may effect the later crustal loading and Tertiary basin formation.

It is necessary to maintain an awareness of the errors inherent in the generation of water-loaded subsidence curves to aid the discrimination of the important tectonic features from induced artifacts. Inaccuracies of dating may arise from differing sedimentation rates over a short geological span. These errors are only in the order of 1-2 Ma and therefore do not greatly affect the subsidence curves (Wooler et al. 1992). The assigning of palaeowater depths are a major source of error as some facies and faunal assemblages may be present at a range of depths (Watts & Steckler 1979, Barton & Wood 1984, Bertram & Milton 1989). Therefore the error bars for this parameter are shown. The stratigraphic sections involved in this study predominantly represent shallow (0-50m) to outer shelf (50-150m) deposits for which palaeowater depths are more easily constrained in comparison with slope or abyssal facies (>150m) which show a wider and more ambiguous range of palaeowater depths. The assumption of Airy isostasy also introduces errors although the subsidence calculated will be a minimum estimate. The magnitude of the error depends on the Te: if the Te >10 km, there is a noticeable effect on the subsidence curve.

Figs 3.2.3-14 show the uncorrected and decompacted basement subsidence curves calculated for the twelve sections and their corresponding water-loaded, tectonic subsidence curves. Figs 3.2.3-9 represent sections from the External Prebetics, from west to east; Figs

3.2.10-13 represent sections from the Internal Prebetics, from west to east and Fig 3.2.14 represents the section from the northern Subbetic Zone.

3.2.1. Comparison of Mesozoic subsidence

The tectonic subsidence curves indicate an initial subsidence in the Triassic which then decayed exponentially during the Jurassic, Cretaceous and early Tertiary. This pattern is indicative of a stretched continental margin exhibiting a phase of rift-related subsidence followed by cooling and thermal subsidence. Theoretical subsidence curves, generated by the uniform stretching model, were fitted to these tectonic subsidence curves allowing the stretching factor, ß, to be estimated (Figs 3.2.3.b-14.b). The final curves fitted are modified to account for the later Cretaceous and Tertiary tectonic episodes (sections 3.2.2/3) and hence do not incorporate a constant strain rate. This, however, does not greatly alter the value of ß as the most important control when fitting the subsidence curve is the gradient of the syn-rift episode.

The uncertainties in the compilation of the sections allowed analysis of the effects of both a maximum and minimum estimate of the stratigraphic thickness of each section. Curves obtained from a section of maximum estimated stratigraphic thickness produced slightly greater values of ß than that obtained from a section of minimum estimated stratigraphic thickness (Fig 3.2.13.b). In the Prebetic Zone the greatest uncertainty in thickness is the Triassic units but although this alters the value of ß, the period of rifting should be basically unaltered. All the tectonic subsidence curves and ß values presented in this study are attained from analyses of sections of minimum estimated stratigraphic thicknesses and hence, the values calculated for ß are also a minimum.

ß factors only accurate to one decimal place

Fig 3.2.15 shows the systematic variation in the value of ß, from 1.031 to 1.324, in the Prebetic Zone and the most foreland part of the Subbetic Zone. There is a gradual increase in the ß factor around the arc of the External Prebetics, from ß = 1.031 in the west to ß = 1.122 in the east. This variation in ß value indicates differential stretching laterally, with an increased amount to the east, which may have given rise to an initially irregular continental margin and associated distribution of the sedimentary facies (section 1.3.iv and 6.4). Fig 3.2.16 indicates the range and frequency of the duration of this initial Mesozoic rifting obtained from the tectonic subsidence curves. The rifting in the more westerly sections, i.e. 1,2,4 and 5, is also of a shorter duration than that in the more easterly sections. There is a notable increase in the value of ß to the south-east e.g. in the west, ß = 1.031 in the External Prebetics; ß = 1.114 in the Internal Prebetics; ß = 1.324 in the northern Subbetic Zone. This indicates that the more basinward the zone, inferred from the palaeogeographic reconstructions of Garcia-Hernandez et al. (1980), the greater the amount of Mesozoic rifting. As the subsidence of the External Prebetics increases substantially from west to east, there is therefore, a greater contrast in the amount of subsidence occurring between the External and Internal Prebetics in the west e.g. between CM1 (ß = 1.031) and CM5 (ß = 1.114) than in the east e.g. between CM7 (ß = 1.122) and CM10 (ß = 1.132). This greater contrast is observed in the western Prebetic Zone by the dramatic contrast in the units and thicknesses of the stratigraphic sequences e.g. CM2 (External Prebetic) and CM5 (Internal Prebetic) compared with CM7 (External Prebetic) and CM10 (Internal Prebetic) of the eastern Prebetic Zone (Fig 3.2.2). Also the External/Internal Prebetic boundary itself in the west shows a significant change of stratigraphic sequence across it indicating that it was an important original palaeogeographical feature.

The External/Internal Prebetic boundary in the east shows a more gradual change of stratigraphic sequence across it. Subsidence was, therefore, probably accommodated differently in the western and eastern Prebetic Zone; in the west, extensional deformation was concentrated on a few, large-displacement faults, whereas in the east, extensional deformation was more pervasive and accommodated by many, small-displacement faults.

Previous authors have suggested that the extension of the passive margin, now comprising the External Zones, was initiated in the Pliensbachian (early Jurassic) (e.g. Dercourt et al. 1984). Garcia-Hernandez et al. (1980) conclude that the Mesozoic history of the External Zones of the Betic Cordillera may closely parallel that of other Mediterranean basins as described by Bernoulli & Jenkyns (1974) in which the main phase of rifting is assigned to the Liassic. The evidence from the subsidence curves described above indicate that the syn-rift stretching phase started earlier, at 235-245 Ma (early to middle Triassic), than previously attributed. Peper & Cloetingh (1992) present tectonic subsidence curves for the north and south Subbetic Zones which also show rapid subsidence in the middle Triassic. The durations of the initial stretching from the sections presented in this study are shown in Fig 3.2.16 but they may be slightly underestimated as the stratigraphic sections analysed were often incomplete.

There appears to be an inconsistency in the proposed timing of rift onset between that of previous authors, inferred from field work, and the results of subsidence studies, including this study and that of Peper & Cloetingh (1992). The substantial subsidence rates measured e.g. 70m/Ma for CM6 (Fig 3.2.8.b), during the early-middle Triassic is hard to ascribe to

anything other than the result of the syn-rift stage of the Mesozoic extension. Within the Triassic stratigraphic sequence, there are notable facies changes, such as the transition from the early Triassic continental Bundsandstein to the middle Triassic marine influenced Muschelkalk, and the occurrence of dolerite and other mafic intrusions which also provide evidence for a substantial amount of tectonic activity at this time. Previous field work may have been biased towards a later date for the syn-rift phase of extension as many of the extensional faults may have been growth faults, active over a significant amount of time, which may show most strongly their latest phase of activity but not preserve their early history so well due to their subsequent reactivation or being cross-cut by Tertiary thrust faults prevalent in the External Zones of the Betic Cordillera.

Restoration of the position of the section and its β factor can be used to enhance the gravity crustal model.

3.2.2. Cretaceous extension

Some of the more internal sections show a marked increase in subsidence within the Cretaceous which is probably due to local pulses of extension. This deviation from a uniform strain rate is accounted for in the fitting of the final tectonic subsidence curve. Increases are predominantly absent in all the sections in the External Prebetic although the sections CM7 and CM9 which are located in close proximity to the External/Internal Prebetic boundary, show slight increases in subsidence. The subsidence in section CM7 occurred between 100-90 Ma (Albian/Cenomanian) whilst the subsidence in section CM9 occurred between 140-120 Ma (Neocomian).

In the Internal Prebetics two exclusive periods of increased subsidence are observed but not within every section. This may depend

upon the differential deposition and preservation experienced by the compiled stratigraphic sequences. BP1 and CM10 show the steep gradient of subsidence curve at 100-90 Ma as seen in CM7. Section CM5 shows the increase in subsidence at approximately 100-90 Ma and also a slight increase at 155-145 Ma (Jurassic/Cretaceous boundary). BP2 shows a notable increase in subsidence at 150-140 Ma without any significant Albian extension. This large increase is probably due to the well being located in a thickened hangingwall sequence associated with the generation of listric extensional graben faults (Banks & Warburton 1991). Section N. SUBBETIC of the Subbetic Zone only exhibits the 150-140 Ma pulse of extension.

3.2.3. Tertiary basin formation

Tertiary deposits, which are absent in the NE trending limb, increase in distribution around the arc and into the Internal Prebetics and the Subbetic Zone. The sections CM2 and CM3, from the Alcaraz Antitaxis and the NW Trending Limb, show only very minor amounts of subsidence in the Miocene whereas section CM4 from the Cenajo Syntaxis, shows a marked increase in subsidence rate during this time. Further to the east, in sections CM6 and CM7, there is not such a notable increase in subsidence in the Tertiary. The four sections in the Internal Prebetics all show a certain amount of rapid subsidence in the Miocene. The stratigraphic sequence for section N. SUBBETIC from the Subbetic Zone, did not include Middle/Upper Tertiary sediments and therefore the presence or absence of this Miocene increase in subsidence cannot be resolved. This rapid Miocene subsidence is also observed in subsidence

curves for the Jumilla-Cieza region of the Internal Prebetic and Subbetic Zones (Kenter et al. 1990).

This Miocene increase deviates from the theoretical curve obtained from the uniform stretching model. This deviation from a uniform strain rate is incorporated into the final tectonic subsidence curve but does not represent a Mesozoic rift-related phenomena nor can a new phase of rifting be invoked as the subsidence rate appears to increase in time i.e. is convex in shape, and no thermal relaxation phase is present. This Tertiary profile is similar to the increased subsidence observed in backstripped sections from the Alps and the Internal Zones of the Betic Cordillera and attributed to foreland basin formation (Homewood et al. 1986, Lonergan & Mange, submitted). The areas which show this rapid Miocene subsidence were probably subject to a greater amount of loading locally, due to the emplacement of relatively thick Internal Prebetic/Subbetic thrust piles from the SE. The basement can be shown to be markedly depressed just to the SE of sections CM5 in the west and CM4 and CM10 in the east whereas this phenomena is not associated with the sections CM1-3 (Fig 3.2.17 and section 4.4).

More detailed investigation is carried out on the eastern and western regions separately due to the presence of the dextral Socovos Fault across which there is a variation in the onset of the main deformation. The subsidence curves show a variation in the timing of the initial deviation from the exponentially decreasing subsidence path to that of increased subsidence in both the east and the west (Fig 3.2.18). In the east, initial basin formation varies from 30-25 Ma (Oligo-Aquitanian) for the section CM10 of the Internal Prebetics to the section CM4, from the Cenajo Syntaxis which indicates initial basin formation at about 25-20 Ma (Aquitanian/early Burdigalian) to 15-10 Ma (Mid-late Seravallian/early

Tortonian) for the section CM6 which is located close to the undeformed foreland. Whereas, in the west, the initial basin formation varies from 23-20 Ma (Aquitanian/early Burdigalian) for the sections BP2 in the Internal Prebetics, close to the present Subbetic Front, to section CM5 which indicates a later age of basin formation at about 20-15 Ma (Burdigalian/Langhian).

This compares well with the timing of the initiation of deformation (rather than that of the main deformation) around the arc compiled from structural and sedimentological data (section 2.3). The result from CM4 also agrees with the results of Kenter et al. (1990) from the Internal Prebetics to the east of the Cenajo Syntaxis, which indicate initiation of the compressional tectonic phase at 20 Ma. Kenter et al. (1990) also indicate a deviation from the theoretical subsidence curve at 20 Ma for the Subbetic Zone. This age, which is later than the ages of some Internal Prebetic basin formation, may indicate the out-of-sequence nature of the Subbetic Thrust Front.

The basins, formed by a local flexural response to this loading, are not foreland basins sensu stricto, as with continued deformation towards the foreland the basins are carried towards the foreland in a passive, piggy-back style (Ori & Friend 1984). The basins may be termed subsiding intramontane basins as they receive their sediment supply from both hinterland and foreland thrust slices and their geometry in plan view may mirror the topography formed by the thrust slices. Figs 3.2.19/20 show the arcuate distribution of late Tortonian/early Messinian intramontane basins in the Alcaraz Antitaxis and a fan deposit from one of these basins showing sediment supply from foreland located thrust slices. Due to the piggy-back style deformation, some of the basins became elevated and,

after preferential erosion of the Mesozoic sequence, cap the present-day hills.

The subsidence curves do not rule out the possibility of these basins being formed in a transtensional strike-slip regime as the subsidence rates associated with strike-slip basins are generally very high (Dickinson et al. 1987). The loading of the sediments themselves within the available accommodation space, may cause the increasing subsidence rate and hence a convex subsidence curve although this is unlikely if the basins are small and the lithosphere has significant effective elastic thickness. The lack of basin margin strike slip faults observable in the field do not support to this basin formation mechanism for the Tertiary basins of the Prebetic Zone. Transgression, caused by the Seravallian eustatic sea-level rise, can be ruled out as a major contributor to the formation of the basins as this would not produce the observed trend of subsidence.

3.3. The lack of a foreland basin in the Eastern Betic Cordillera

The Guadalquivir basin, the foreland basin to the western Betic Cordillera, extends eastwards only as far 3° W, the very westerly part of the NE Trending Limb, and is therefore absent around the Alcaraz Antitaxis and further eastward (Fig 1.2).

The basin-fill in the easternmost part of the Guadalquivir Basin consists mainly of Tortonian conglomerates and calcareous sandstones overlain by Messinian marls, indicating a deepening of the basin and a change from alluvial to shallow marine facies. The Prebetic Front is emergent and overthrusts these Tertiary sediments incorporating them into the frontal thrust sheets. To the north of the

Alcaraz Antitaxis, late Tortonian conglomerates and calcarenites are present locally and are also incorporated into the thrust front. From their outcrop pattern and internal cross-bedded structure they are interpreted as channel-fill deposits, draining away from the Prebetic Zone. There is no substantial evidence to suggest they were joined together by a significant basin. Further east the Prebetic Front becomes a blind thrust as the undeformed Mesozoic cover to the foreland becomes thicker and Tertiary deposits found associated with the deformation front are absent.

The development of foreland basins s.s. is controlled by the interaction of the lithospheric response to loading and the geometry of the orogenic wedge (Beaumont 1981, Allen & Allen 1990, Watts, in press). The variation of these factors from the western to eastern Betic Cordillera has a strong influence on the location of the Guadalquivir Basin.

The lateral changes in flexural rigidity, due to varying rheologies, primarily caused by differing thermal histories, strongly control the wavelength and amplitude of the flexural response across an orogenic belt (Karner & Watts 1983, Watts, in press). This has been investigated in the Betic Cordillera, using flexural, gravity and rheology modelling, by Van der Beek & Cloetingh (1992) and Peper & Cloetingh (1992). The flexural response for four profiles, W-E, were modelled for varying elastic thicknesses of the lithosphere, from 5-20 km, and compared with the observed basement deflection. In the western Betic Cordillera the best fitting value for the elastic thickness is 10 km. This is comparable to the value of 0<Te>5 presented for the Pyrenean foreland basins in France and Spain by Brunet (1986) and for

the Ebro basin by Zoetemeijer (1990) but low compared to the value of 25 and 50 km derived for the western and eastern Alps respectively and other orogenic belts (Karner & Watts 1983, McNutt et al. 1988). The flexural rigidity may depend on whether the continental lithosphere has undergone previous stretching which would cause the inheritance of low values of Te (e.g. 10-20 km) or not which would give rise to higher values of Te (e.g. 80-90 km) (Watts & Torné 1992, Watts, in press). In the eastern Betic Cordillera flexural analysis is difficult to constrain due to the absence of a foreland basin, therefore Van der Beek & Cloetingh (1992) forward modelled the gravity anomalies associated with a) an elastic thickness of 10 km (similar to that which they attribute to the western Betic Cordillera) and for b) a model of local Airy isostatic response. They interpret the results of this modelling to support the existence of local isostasy in the eastern Betic Cordillera. They conclude that this difference in the lithospheric strength between the western and eastern Betic Cordillera is due to the development of the extensional regime in the western Mediterranean during the Oligocene-Early Miocene (Dercourt 1984, Dewey et al. 1989). This regional extension which influenced the formation of the Gulf of Valencia also effected the easternmost Betic Cordillera (Van der Beek & Cloetingh 1992, Watts & Torné 1992). Rheological strength profiles were also modelled by Van der Beek & Cloetingh (1992) to provide an additional constraint on the elastic thickness across the Betic Cordillera. However, these results are very dependent on the rheological and thermotectonic models used. Overall, the elastic thickness of the Betic lithosphere is interpreted by Van der Beek & Cloetingh (1992) to decrease from west to east. Hence the wavelength

of the foreland depression created in response to the loading of the Betic orogenic wedge will decrease from west to east.

The geometry of the orogenic wedge also has a significant control on the development of a foreland basin. In the Betic Cordillera, the main basal detachment is in the evaporite-rich Triassic which exhibits a low resistance to displacement [maximum of 300m of evaporite and 100m of salt in the External Zones (Garcia-Hernandez et al. 1980)]. This reduced basal shear causes the development of a broad orogenic wedge with a low angle of critical taper (Davis & Engelder 1985, Jaumé & Lillie 1988). Results from gravity modelling around the Prebetic Arc (section 4.4.) indicate a shallowing of the basement/wedge interface from the western to eastern Prebetic Zone. This may indicate an increased evaporitic content of the Triassic to the east. This may also account for the increased diapirism of the Triassic in the Cenajo Syntaxis and further to the east. In the case of an evaporite-rich basal detachment, a relatively long wavelength of the load i.e. the orogenic wedge, is developed. In the eastern Prebetic Zone, to the east of the Alcaraz Antitaxis, the low amounts of strain and small load documented (chapter 5) may also contribute to the low angle of taper and therefore a relatively long wavelength of the orogenic wedge.

In the western Betic Cordillera, where the Prebetic Zone is absent, the Subbetic Zone is the most frontal zone of the orogenic wedge and is relatively narrow with quite a high angle of taper.

The presence or absence of a foreland basin is dependent upon the relative wavelengths of the flexural depression and the imposed load. In the western Betic Cordillera, with its relatively greater lithospheric strength, the wavelength of the flexural depression is greater than the wavelength of the orogenic wedge. In the eastern

Betic Cordillera the wavelength of the flexural depression is less than the wavelength of the orogenic wedge and hence the foreland basin is absent. The small wavelength intramontane basins are formed by local compensation of thrust sheet loading on a lithosphere with a low flexural rigidity.

Howard & Kusznir (1991) present a scenario for foreland basin formation inferred from quantitative models of lithospheric shortening which incorporate a flexural response. They indicate that the thin-skinned thrusting in the External Zones of the eastern Betic Cordillera occurred rapidly and with an associated small load. Hence, the thrust wedge was implied to occupy its own depression.

A possible forebulge has been located to the NW of the Alcaraz Antitaxis to explain the relative uplift of the undeformed Mesozoic sequence (Banks & Warburton 1991).

The lack of a foreland basin to the eastern Betic Cordillera requires an alternative mechanism for storing the eroded sediment. Much of this sediment could be trapped in the intramontane basins described in section 3.2.3, which are common in the Internal Prebetics and in the External Prebetics, in the Alcaraz Antitaxis and further to the east, but are conspicuously absent in the NE Trending Limb where Guadalquivir foreland basin is present (Fig 2.1.1). The low angle of taper of the eastern Betic orogenic wedge due to its efficient evaporitic décollement horizon suggests also a low surface slope. This would increase the likelihood of sediment being trapped within small basins which are carried towards the foreland as part of the wedge rather than being transported to the foreland itself.

The carbonate lithologies, which predominate in this deformed shelf sequence, are readily dissolved during the weathering process and are then removed by the drainage systems to the north as indicated by the channels to the foreland of the Alcaraz Antitaxis, or to the SW/SE, the general directions of drainage for the western and eastern Prebetic Zone from the Miocene to the Present.

CHAPTER 3

FIGURES

a)

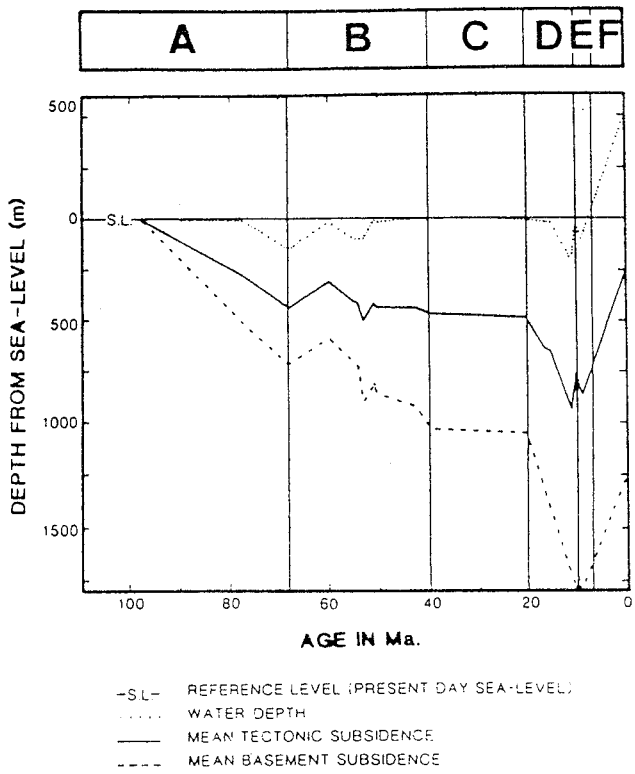


Fig 3.1.1.a) Subsidence curve for the Sierra del Carche, Internal Prebetics, after Kenter et al. (1990). Phases A and B represent the Iberian Mesozoic passive margin The curve then decays in phase C due to thermal relaxation from 40-20 Ma. Development of a fold and thrust belt, phases D-F, from 20 Ma to recent is also invoked. Kenter et al. interpret phase C to represent an extensional phase. However, major regional extension cannot be inferred from this very low gradient segment of the subsidence curve.

b)

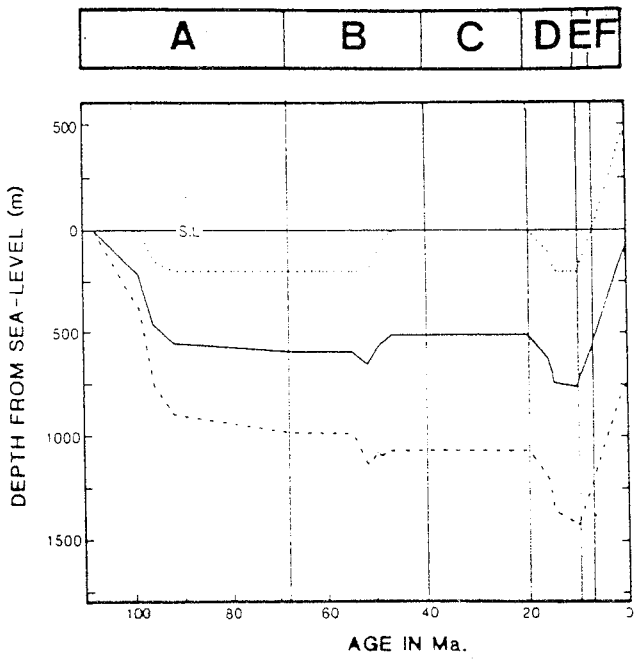


Fig 3.1.1.b) Subsidence curve for the Sierra Caramucel-E, Subbetic Zone, after Kenter et al. (1990). Phases A and B represent the Iberian Mesozoic passive margin The curve then decays in phase C due to thermal relaxation from 40-20 Ma. Development of a fold and thrust belt, phases D-F, from 20 Ma to recent is also invoked. Kenter et al. interpret phase C to represent an extensional phase. However, major regional extension cannot be inferred from this very low gradient segment of the subsidence curve.

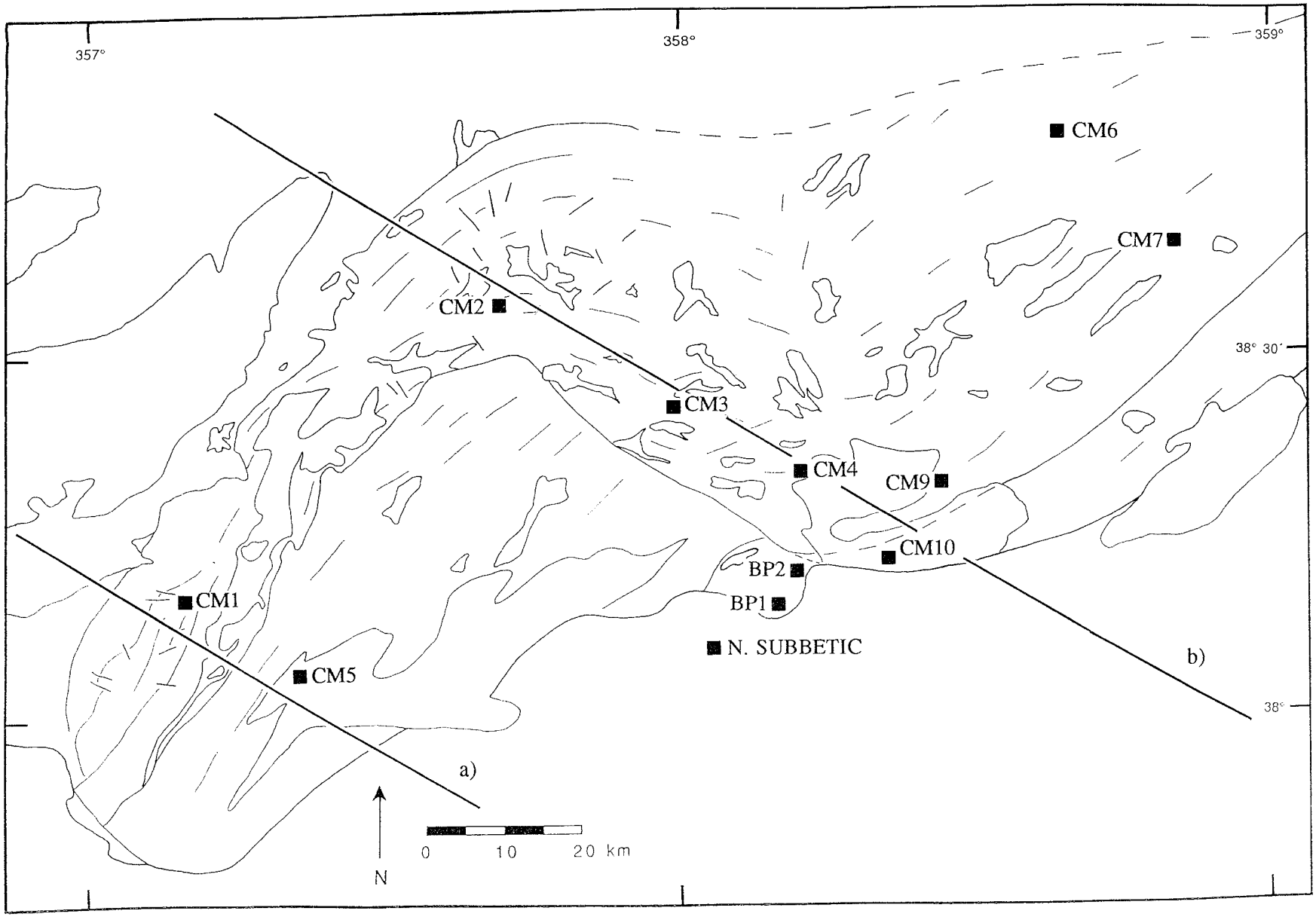


Fig 3.2.1. Locations of compiled sections or well-logs in the Prebetic Zone and northern Subbetic Zone for which basement and tectonic subsidence curves were generated.

lithospheric thickness	125 km
crustal thickness	30 km
sea water density	1.0 g cm^{-3}
crust density (at 0°C)	2.8 g cm^{-3}
mantle density (at 0°C)	3.33 g cm^{-3}
asthenosphere density (at 1333°C)	3.2 g cm^{-3}
asthenosphere temperature	1333°C
thermal expansion coefficient	3.28×10^{-5} $°C^{-1}$
thermal diffusivity	8×10^{-7} m^2 s^{-1}
decay time	62.8 Ma

Table 3.2. Values of the parameters used in the production of i) theoretical stretching curves and ii) subsidence curves from back-stripped stratigraphic sections, used in this thesis. (Porosity and compaction decay length are standard values [cf Sclater & Christie (1980)] and their precise values due not greatly affect the results).

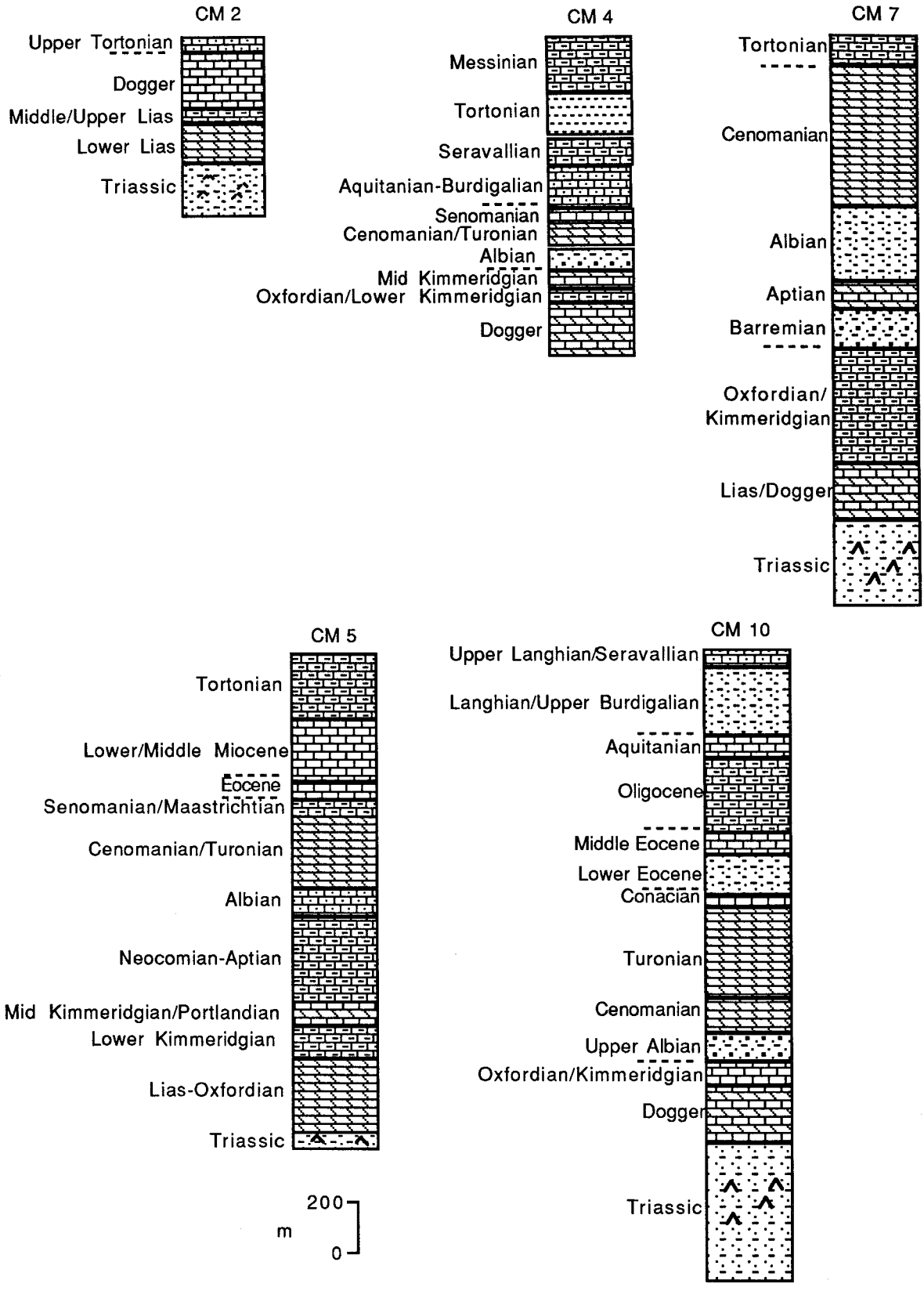


Fig 3.2.2.a) Examples of stratigraphic sections from around the Prebetic Arc which have been used to compile basement and tectonic subsidence curves. Sections CM2, CM4 and CM7 are from the External Prebetics whereas sections CM5 and CM10 are from the Internal Prebetics. Locations of these sections are shown in Fig 3.2.1. The key for the stratigraphic columns is shown in Fig 3.2.2.b).

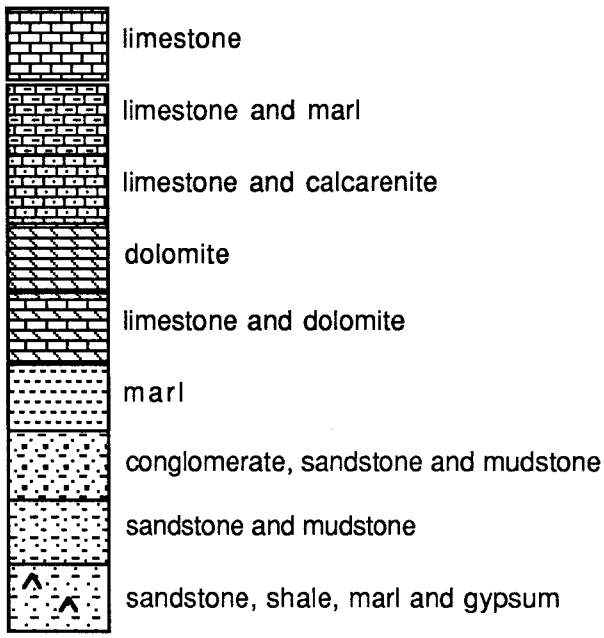


Fig 3.2.2.b). Key for stratigraphic columns shown in Fig 3.2.2.a).

Fig. 3.2.2 (continued)

Stratigraphic section - CM1

Grid ref - 667379 Compiled from- I.G.M.E 907 - Villacarrillo and logged sections

Section Minimum	cumulative Thickness min (m)	max	Age (Ma)	Lithology	Palaeowaterdepth min	max
	20	20	122 - 156 Ma - Kimmeridgian /	Marls 50% Muds 50%	30	100
	30	35	156 - 160 Ma - Upper Bajocian	Lmst 100%	30	100
	40	45	160 - 169 Ma - Lower Oxfordian	Lmst 100%	10	50
			169 - 213 Ma Lias / Dogger	Dolomite 90% Marls 10%	10	50
	290	295	213 → 231 Ma - Keuper	Marls/mud 60% Sandst 30% Gypsum 10%	0	50
	330	345	231 → 243 Ma - Muschelkalk	Lmst 100%	30	100
	350	355				

Scale 1cm = 100m

Stratigraphic section - CM 2

Grid ref - 724445 Compiled from- I.G.M.E. 841 - Alcaraz and logged section

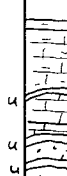
Section minimum	Cumulative Thickness min (m) max	Age (Ma)	Lithology	Palaeowaterdepth min	Palaeowaterdepth max
	5	1.5 → 6.5 Ma – Pliocene	Conglomerate 80% Marl 20%	30	50
u	55 (65)	6.5 → 8 Ma - Upper Tortonian	Lmst 100%	30	100
		163 – 188 Ma – Dogger	Lmst 90% Dolomite 10%	30	100
	265				
	310	188 → 203 Ma – Mid - upper Lias	Marls/Muds 60% Dolomite 40%	30	100
	485	203 → 213 Ma - Lower Lias	Lmst 40% Dolomite 60%	30	100
	585	213 → 231 Ma - Upper Triassic	Marl 50% Mud 40% Gypsum 10%	30	100
	615	231 → 243 Ma - Mid Triassic	Sandstone 50% Mud 30% Dolomite 20%	0	50
	690	243 – 248 Ma - Lower Triassic	Sandstone 50% Mudst 40% Dolomite 10%	30	100

Scale 1cm = 100m

10m added to section for unconformity

Stratigraphic section - CM3

Grid ref - 743429 Compiled from- I.G.M.E 867 - Elche de la Sierra and logged sections



Section	Cumulative Thickness (m) min	Age (Ma)	Lithology	Palaeowaterdepth min	Palaeowaterdepth max
	10	0 - 5·3 Ma - Recent/Pliocene	Mud 50% Sandst 30% Lmst 20%	0	30
	100	5·3 → 6·5 Ma - Messinian	Lmst 60% Marl 40%	0	50
u	(110)				
	140	12 → 13·5 Ma - Mid Serravallian	Lmst 100%	30	100
	160	13·5 → 19 Ma - Burd/Lang/Serav.	Lmst 100%	30	100
u	(170)				
	190	23 → 24·6 Ma - Lower Aquitanian	Lmst 30% Sandst 70%	0	30
u	(200)				
	475	65 → 88·5 Ma - Senonian	Lmst 100%	30	100
	555	88·5 → 91 Ma - Turonian	Dolomite 80% Lmst 20%	30	100
	585	91 → 97·5 Ma - Cenomanian	Dolomite 100%	30	100
	735	97·5 → 152 Ma - Lower Cret → Albian	Sandst 50% Congl 30% Mud 20%	30	100
	765	152 → 154 Ma - Mid Kimmeridgian	Dolomite 100%	30	100
	845	154 → 163 Ma - Upper Oxfordian → Mid Kimm.	Lmst 60% marl 40%	30	100
	1095	163 → 188 Ma - Dogger	Lmst 80% Dolomite 20%	30	100
	1115	188 → 200 Ma - Mid → Upper Lias	Dolomite 80% Mud/Marl 20%	30	100
	1280	200 → 213 Ma - Lower - Mid Lias	Dolomite 100%	30	100
	1330	213 - 235 Ma - Triassic	Mudst 80% Sandst 10% Gypsum 10%	0	50

Scale 1cm = 100m

10m added to section for an unconformity

Stratigraphic section - CM4

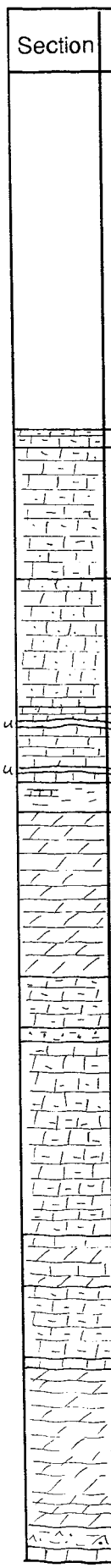
Grid ref - 770422 Compiled from- I.G.M.E 868 - Isso and logged sections

Section	Cumulative Thickness (m) min	Age (Ma)	Lithology	Palaeowaterdepth min	Palaeowaterdepth max
	200	5.5 → 6.5 Ma - Messinian	Marl 60% Lmst 40%	30	100
	350	6.5 → 10 Ma - Tortonian/Mess	Marl 100%	30	100
	450	10 → 15.1 Ma - Serravallian	Lmst 80% Marl 20%	30	100
	490	15.1 → 16 Ma - Upper Langhian	Lmst 60% Sandst 30% Mud 10%	30	100
	570	16 → 21.8 Ma - Burdigalian	Lmst 90% Sandst 10%	30	100
	600 (610)	21.8 → 23.7 Ma - Aquitanian	Sandst 90% Lmst 10%	0	50
	670	65 → 88.5 Ma - Senonian	Lmst 100%	30	100
	750	88.5 → 92.5 Ma - Cenomanian → Turonian	Dolomite 100%	30	100
	830 (840)	92.5 → 113 Ma - Albian	Mudst 30% Sandst 70%	0	50
	890	152 - 154 Ma - Mid Kimmeridgian	Lmst 70% Dolomite 30%	30	100
	940	154 - 163 Ma - Oxfordian → lower Kimmeridgian	Marl 60% Lmst 40%	30	100
	1040	163 - 181 Ma - Upper Dogger	Dolomite 70% Lmst 25% Sandst 5%	30	100
	1130	181 - 194 Ma - Upper Lias → Lower Dogger	Dolomite 60% Lmst 30% Marl 10%	30	100

Scale 1cm = 100m 10m added to section for an unconformity

Stratigraphic section - CM5

Grid ref - 690391 Compiled from- I.G.M.E. 908 - Santiago de la Espada and logged sections



Section	Cumulative Thickness (m) min	Age (Ma)	Lithology	Palaeowaterdepth min	Palaeowaterdepth max
	30	6.5 → 7.5 Ma - Upper Tortonian	Lmst 50% Marl 50%	30	100
	230	7.5 → 11.2 Ma - Lower/Mid Tortonian	Lmst 60% Marl 30% Sand 10%	30	100
	430	11.2 → 16.6 Ma - Mid Miocene	Lmst 70% Sandst 30%	30	100
	450	16.6 → 24.6 Ma - Lower Miocene	Lmst 100%	30	100
u	(460)				
	520	38 → 54 Ma - Eocene	Lmst 100%	30	100
u	(530)				
	540	65 → 73 Ma - Maastrichtian	Lmst 100%	50	300
	590	73 → 88.5 Ma - Lower Senonian	Marl 70% Lmst 30%	50	300
	840	88.5 → 94 Ma - Cenomanian/ Turonian	Dolomite 90% Marl 10%	50	300
	920	94 → 97.5 Ma - Lower Cenomanian Upper Albian	Lmst 50% Marl 50%	30	100
	940	97.5 → 113 Ma - Lower Albian	Sandst 50% Marl 30% Mud 20%	30	100
	1240	113 → 144 Ma - Neocomian - Aptian	Lmst 50% Marl 30% Sand 20%	50	300
	1320	144 → 153 Ma - Mid Kimmeridgian Portlandian	Dolomite 40% Lmst 40% Marl 20%	50	200
	1430	153 → 156 Ma - Lower Kimm.	Lmst 50% Marl 50%	30	100
	1440	156 → 163 Ma - Upper Oxfordian	Lmst 100%	30	100
	1690	163 → 213 Ma - Lias/Dogger	Dolomite 100%	30	100
	1720	213 → 231 Ma - Keuper	Mudst 60% Sand 30% Gypsm 10%	0	50
	1740	231 → 243 Ma - Muschelkalk	Lmst 100%	30	100

Scale 1cm = 100m 10m added to section for an unconformity

Stratigraphic section - CM6

Grid ref - 802462 Compiled from- I.G.M.E 818 - Montealegre Del Castillo

Section Minimum	Cumulative Thickness min (m) max	Age (Ma)	Lithology	Palaeowaterdepth min	Palaeowaterdepth max
	200 200	6.5 → 15.1 Ma - Serravallian/Tortonian	Lmst 70% Shale 20% Sandst 10%	0	30
U	(210) (210)				
	360 360	91 → 97.5 Ma - Cenomanian	Dolomite 80% Shale 20%	0	100
	560 560	97.5 → 113 Ma - Albian	Sandst 40% Shale 40% Lmst 20%	0	50
	810 810	113 → 124 Ma - Aptian/Barremian	Lmst 30% Dolomite 30% Shale 20% Sandst 20%	0	50
U	(820) (820)				
	1120 1120	152 → 163 Ma - Kimmeridgian → Oxfordian	Lmst 80% Shale 20%	30	100
	1320 1320	163 → 213 Ma - Lias/Rhaetian	Dolomite 80% Lmst 20%	0	50
	1720 1920	213 → 248 Ma - Triassic	Shale 40% Sandst 30% Lmst 20% Gypsum 10%	0	30

Scale 1cm = 100m

10m added to section for an unconformity

Stratigraphic section - CM7

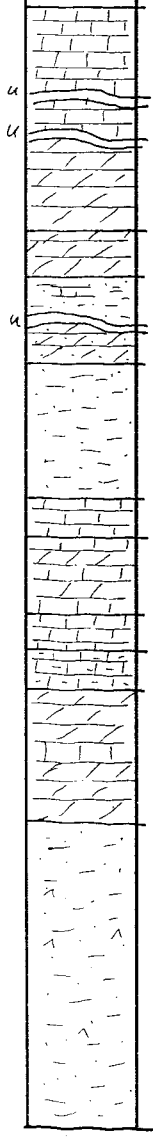
Grid ref - 829454 Compiled from- I.G.M.E maps 845-Yecla and 818 Montealegre del Castillo

Section minimum	Cumulative Thickness min	(m)	max	Age (Ma)	Lithology	Palaeowaterdepth min	max
u	20 (30)		100 (110)	6.5 → 11.2 Ma - Tortonian	Lmst 50% Shale 50%	0	50
	430		510	91 → 97.5 Ma - Cenomanian	Dolomite 100%	50	150
	680		760	97.5 → 113 Ma - Albian	Sandst 40% Shale 40% Lmst 20%	0	50
	930		1090	113 → 124 Ma - Aptian - Barremian	Lmst 30% Dolomite 30% Shale 20% Sandst 20%	0	50
u	(940)		(1020)				
	1340		1420	152 → 163 Ma - Kimmeridgian - Oxfordian	Lmst 80% Shale 20%	30	100
	1540		1620	163 → 213 Ma - Lias-Dogger	Dolomite 80% Lmst 20%	0	50
	1940		2320	213 → 248 Ma - Triassic	Shale 40% Sandst 30% Lmst 20% Gypsum 10%	0	30

Scale 1cm = 100m 10m added to section for an unconformity

Stratigraphic section - CM9

Grid ref - 805442 Compiled from- I.G.M.E Map 844 - Ostend



Section Minimum	Cumulative Thickness min (m) max		Age (Ma)	Lithology	Palaeowaterdepth min	Palaeowaterdepth max
	110	110	9 → 15.5 Ma - Mid Tortonian - Upper Langhian	Lmst 100%	0	30
u	(120)	(120)				
u	160	160	65 → 88.5 Ma - Senonian	Lmst 100%	0	100
	(170)	(170)				
	290	290	90 → 95 Ma - mid Turonian - mid Cenomanian	Dolomite 80% Lmst 20%	50	150
	350	350	95 → 97.5 Ma - lower Cenomanian	Dolomite 100%	50	150
	400	400	97.5 → 105 Ma - Upper Albian	Sst 40% Shale 40% Lmst 20%	0	50
u	(410)	(410)				
	460	460	113 → 119 Ma - Aptian	Dolomite 80% Shale 20%	30	50
	640	640	119 → 124 Ma - Barremian	Mud 60% Shale 30% Sst 10%	0	50
	690	690	124 → 144 Ma - Neocomian	Lmst 100%	0	30
	790	790	144 → 152 Ma - Portlandian - upper Kimm.	Lmst 60% Dolomite 40%	30	100
	840	840	152 → 154 Ma - Mid Kimm.	Lmst 100%	30	100
	890	890	154 → 163 Ma - Lower Kimm. - Oxfordian	Lmst 80% Shale 20%	30	100
	1070	1070	163 → 208 Ma - Lias/Dogger	Dolomite 80% Lmst 20%	0	50
	1470	1670	208 → 248 Ma - Triassic	Shale 40% Sst 30% Lmst 20% Gypsum 10%	0	30

Scale 1cm = 100m 10m added to section for an unconformity

Stratigraphic section - CM 10

Grid ref - 781406 Compiled from- I.G.M.E map 890 - Celasparra and logged section

Section	Cumulative Thickness min (m) max	Age (Ma)	Lithology	Palaeowaterdepth min	Palaeowaterdepth max
	50 50	11.2 → 15.8 Ma - Serravallian Upper Langhian	Lmst 50% Sst 50%	0	30
	300 300	15.8 → 17 Ma - Langhian Upper Burdigalian	Sandst 50% Shale 30% Lmst 20%	30	50
U	(310) (310)				
	385 385	21.8 → 23.7 Ma - Aquitanian	Lmst 100%	30	100
	535 535	23.7 → 30 Ma - Oligocene	Lmst 50% Shale 30% Sandst 20%	30	100
U	(545) (545)				
	595 595	43.6 → 52 Ma - Middle Eocene	Lmst 100%	30	100
	720 720	52 → 57.8 Ma - Lower Eocene	Shale 60% Lmst 20% Sandst 20%	0	50
U	(730) (730)				
	760 760	87.5 → 88.5 Ma - Coniacian	Lmst 100%	30	150
	1110 1110	88.5 → 91 Ma - Turonian	Dolomite 100%	30	150
	1260 1260	91 → 92.5 Ma - Cenomanian	Dolomite 100%	30	150
	1360 1360	97.5 → 105 Ma - Upper Albian	Sandst 50% Shale 30% Lmst 20%	0	50
U	(1370) (1370)				
	1420 1420	152 → 154 Ma - Mid Kimm.	Lmst 100%	30	100
	1470 1470	154 → 163 Ma - Lower Kimm Oxfordian	Lmst 80% Shale 20%	30	100
	1650 1650	163 → 208 Ma - Dogger	Lmst 20% Dolomite 80%	0	50
	2150 2250	208 → 248 Ma - Triassic	Shale 40% Sandst 30% Lmst 20% Gypsum 10%	0	30

Scale 1cm = 100m 10m added to section for an unconformity

Stratigraphic section - BP 1

Grid ref - 769399 Compiled from- BP log – Sierra de la Puerta - logged section

Section minimum	cumulative Thickness (m) min	Age (Ma)	Lithology	Palaeowaterdepth min	Palaeowaterdepth max
	200	14→16.3 Ma - Lower Serravallian Langhian	Marl 50% Lmst 50%	300	500
	265	16.3→23 Ma - Burdigalian Aquitanian	Lmst 100%	300	500
	300	23→35 Ma - Oligocene	Lmst 100%	0	100
	540	35→56 Ma - Eocene	Marl 50% Sandst 50%	50	300
	615	56→65 Ma - Palaeocene	Lmst 100%	0	300
	680	65→74 Ma - Maastrichtian	Lmst 100%	50	300
	750	74→88 Ma - Lower Senonian	Lmst 100%	50	300
	1150	88→97 Ma - Cenomanian	Marl 30% Lmst 70%	50	500
	1270	97→112 Ma - Albian	Lmst 100%	0	100

Scale 1cm = 100m

Stratigraphic section - BP 2

Grid ref - 76994015 Compiled from- BP Well Rio Segura 1 (and Socorro 2-74544124)

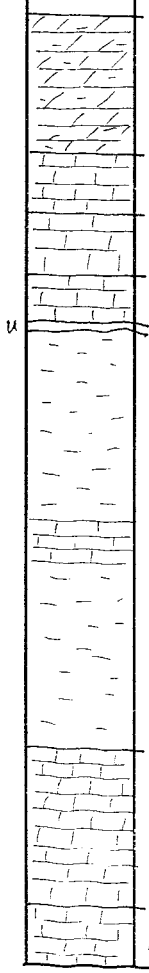
Section minimum	Cumulative Thickness (m) min	Age (Ma)	Lithology	Palaeowaterdepth min	Palaeowaterdepth max
	300	14 → 16.3 Ma - Lower Serravallian Langhian	Marl 50% Lmst 50%	300	1000
U	450 (460)	16.3 → 23 Ma - Burdigalian / Aquitanian	Lmst 100%	300	1000
	825	55 → 65 Ma - Palaeocene	Mud 50% Lmst 40% Sst 10%	50	300
	875	65 → 74 Ma - Maastrichtian	Mud 100%	0	100
	1000	74 → 97 Ma - Lower Senonian → Cenomanian	Lmst 100%	0	50
	1100	97 → 112 Ma - Albian	Lmst 60% Sst 30% Mud 10%	0	50
	1700	112 → 124 Ma - Aptian/Barremian	Lmst 60% Dolomite 40%	0	30
	2550	124 → 131 Ma - Mid Neocomian	Mud 60% Sst 20% Lmst 20%	20	100
	4850	131 → 145 Ma - Lower Neocomian	Mud 50% Lmst 40% Sst 10%	100	1000
	4950	145 → 152 Ma - Tithonian	Lmst 100%	100	1000
	6000	152 → 245 - Late Jurassic to Triassic	Lmst 50% Sst 30% Mud 20%	0	500

Scale 1cm = 500m

10m added to section for an unconformity

Stratigraphic section - N. SUBBETIC

Grid ref - 757391/760389 Compiled from- BP CSP/CS1 logged sections nr Cavavaca

Section	Cumulative Thickness (m) min	Age (Ma)	Lithology	Palaeowaterdepth min	Palaeowaterdepth max
	180	65->74 Ma - Maastrichtian	Dol 60% Mud 40%	0	50
	260	74->88 Ma - Lower Senonian	Lmst 100%	100	500
	340	88->97Ma - Cenomanian	Lmst 100%	100	500
	400 (410)	97->112 Ma - Albian	Lmst 100%	100	500
	955	124->145 Ma - Neocomian	Marl 90% Lmst 10%	50	500
	1155	145->157 Ma Upper Jurassic	Lmst 100%	0	50
	1235	157-178 Ma Oxfordian Dogger	Lmst 100%	0	50

Scale 1cm = 100m 10m added to section for an unconformity

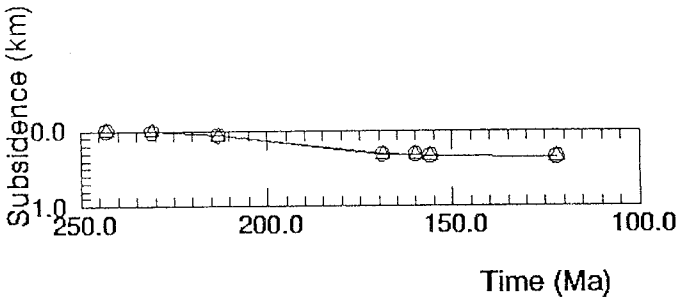


Fig 3.2.3.a). Basement subsidence curve for the section CM1 of the External Prebetics. Cirles-uncorrected subsidence, triangles-decompacted subsidence.

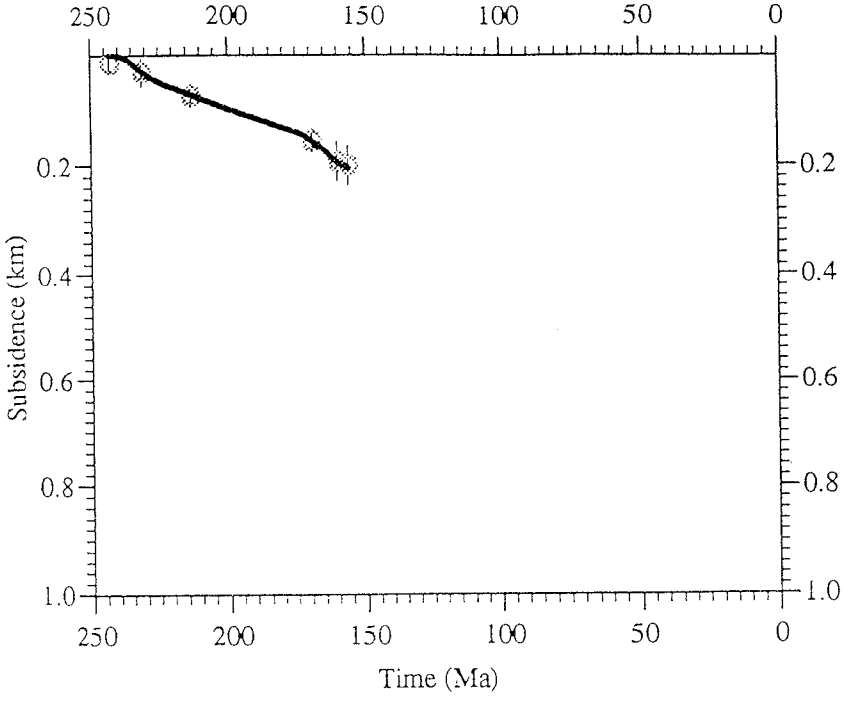


Fig 3.2.3.b). Water-loaded, tectonic subsidence curve for the section CM1. Bars on points-errors in subsidence values due to inaccuracy of palaeowater depths. Solid line-best-fit tectonic subsidence curve from which the ß value of **1.031** is attained.

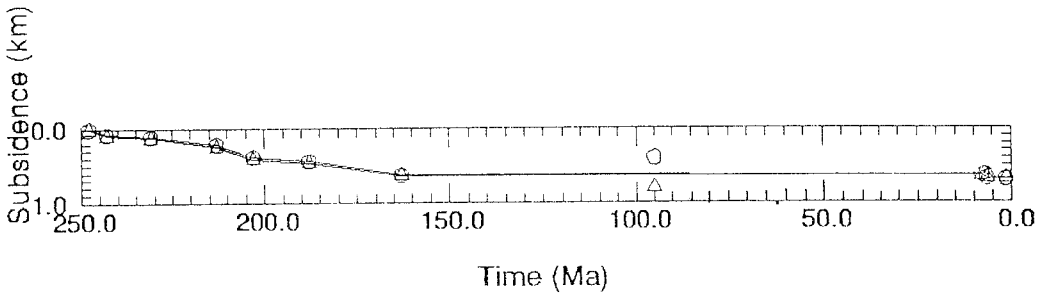


Fig 3.2.4.a). Basement subsidence curve for the section CM2 of the External Prebetics. Cirles-uncorrected subsidence, triangles-decompacted subsidence.

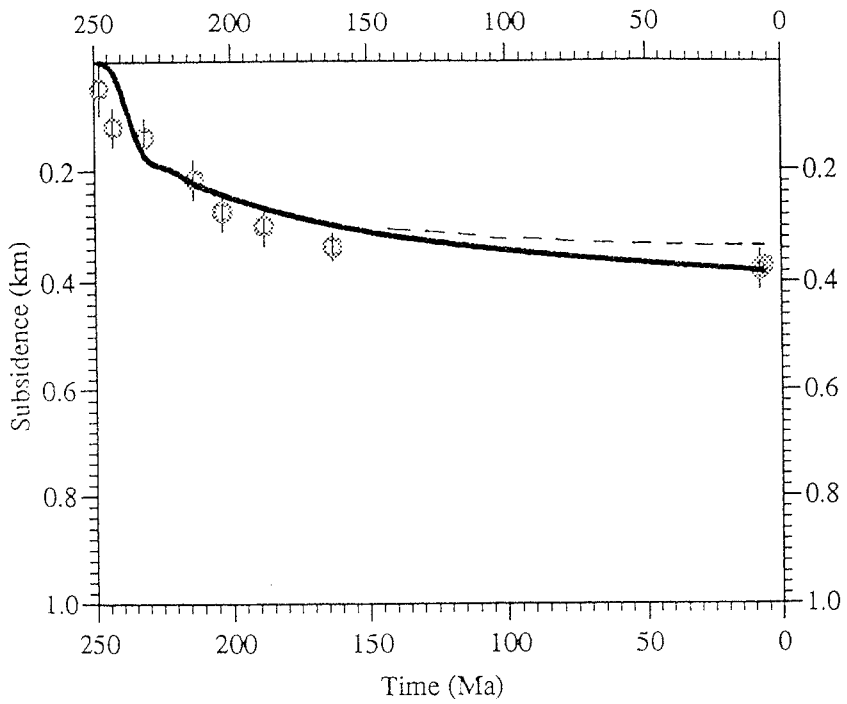


Fig 3.2.4.b). Water-loaded, tectonic subsidence curve for the section CM2. Bars on points-errors in subsidence values due to inaccuracy of palaeowater depths. Solid line-best-fit tectonic subsidence curve from which the ß value of **1.053** is attained. Dashed line-best-fit tectonic subsidence curve if events after 190 Ma are ignored.

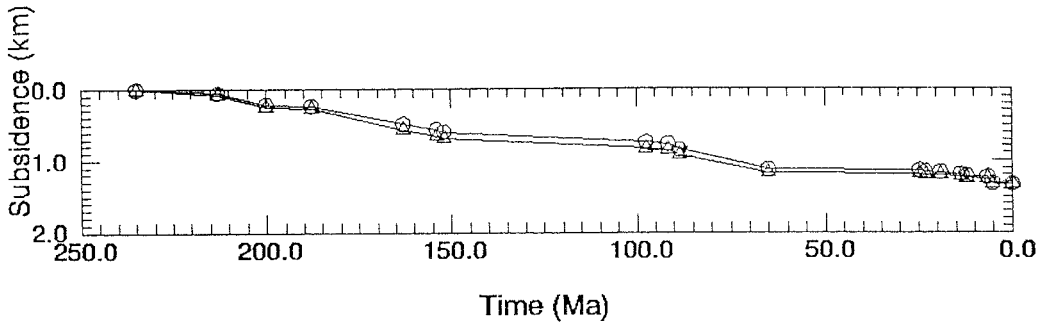


Fig 3.2.5.a). Basement subsidence curve for the section CM3 of the External Prebetics. Cirles-uncorrected subsidence, triangles-decompacted subsidence.

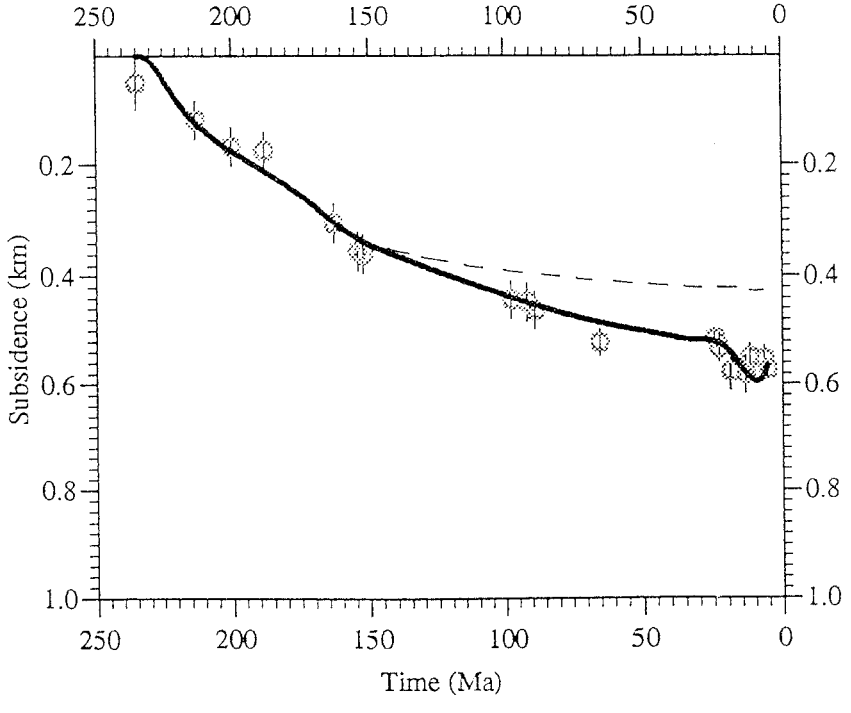


Fig 3.2.5.b). Water-loaded, tectonic subsidence curve for the section CM3. Bars on points-errors in subsidence values due to inaccuracy of palaeowater depths. Solid line-best-fit tectonic subsidence curve from which the ß value of **1.086** is attained. Dashed line-best-fit tectonic subsidence curve if events after 145 Ma are ignored.

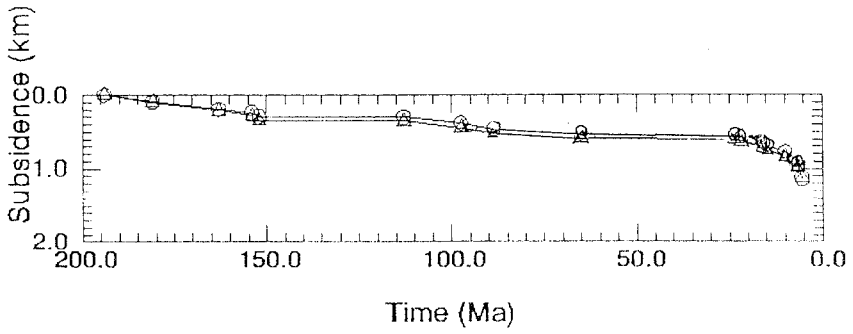


Fig 3.2.6.a). Basement subsidence curve for the section CM4 of the External Prebetics. Cirles-uncorrected subsidence, triangles-decompacted subsidence.

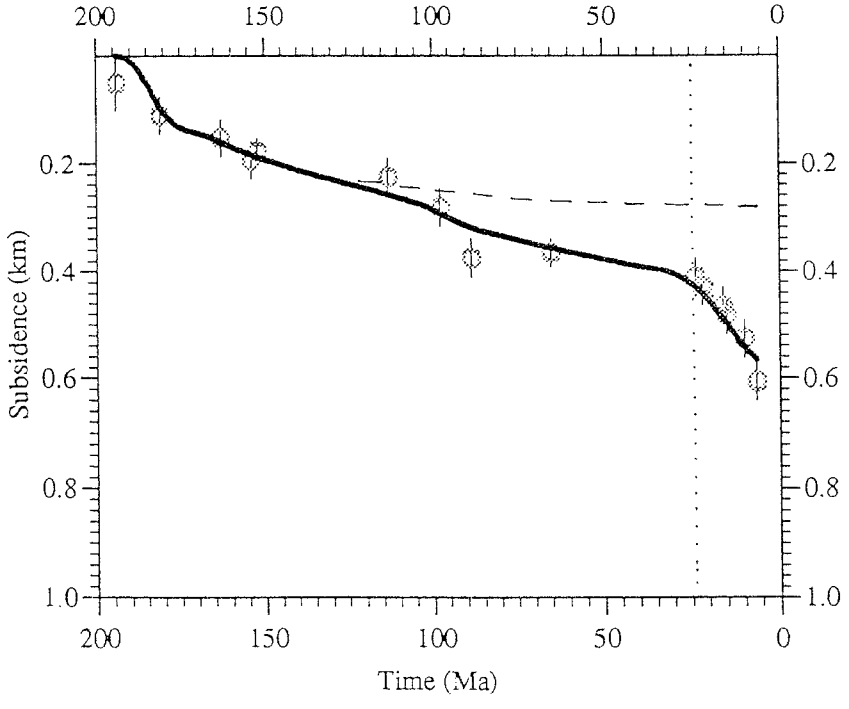


Fig 3.2.6.b). Water-loaded, tectonic subsidence curve for the section CM4. Bars on points-errors in subsidence values due to inaccuracy of palaeowater depths. Solid line-best-fit tectonic subsidence curve from which the ß value of **1.083** is attained. Dashed line-best-fit tectonic subsidence curve if events after 125 Ma are ignored. Dotted line-initiation of Tertiary increase in subsidence due to the loading of thrust slices at 25-20 Ma.

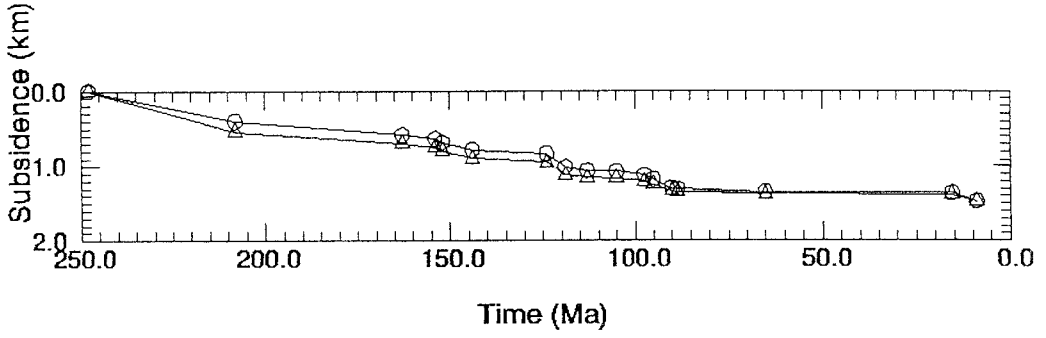


Fig 3.2.7.a). Basement subsidence curve for the section CM9 of the External Prebetics. Cirles-uncorrected subsidence, triangles-decompacted subsidence.

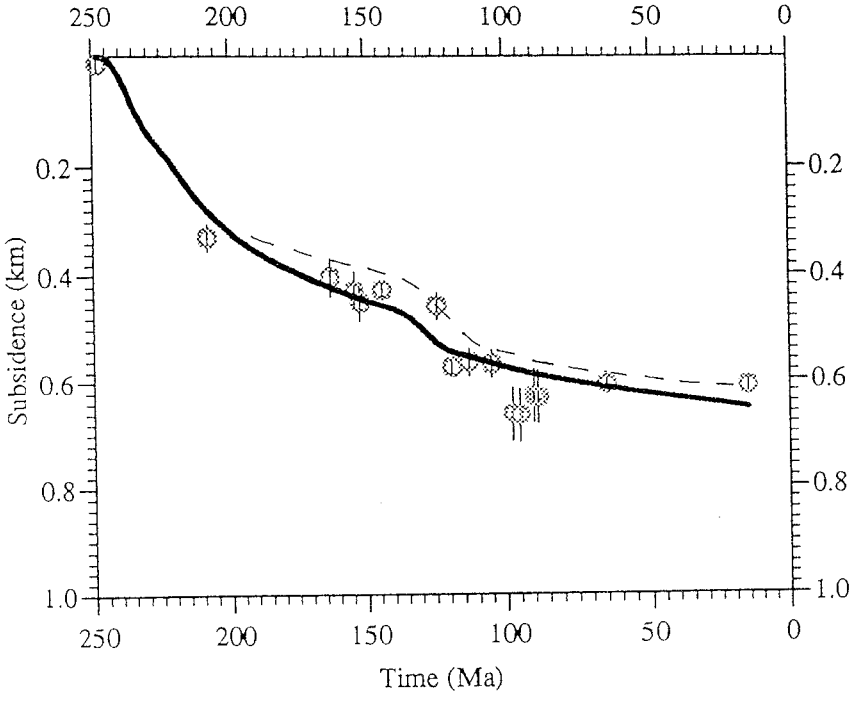


Fig 3.2.7.b). Water-loaded, tectonic subsidence curve for the section CM9. Bars on points-errors in subsidence values due to inaccuracy of palaeowater depths. Solid line-best-fit tectonic subsidence curve from which the ß value of **1.095** is attained. Dashed line-best-fit tectonic subsidence curve if events after 105 Ma are ignored.

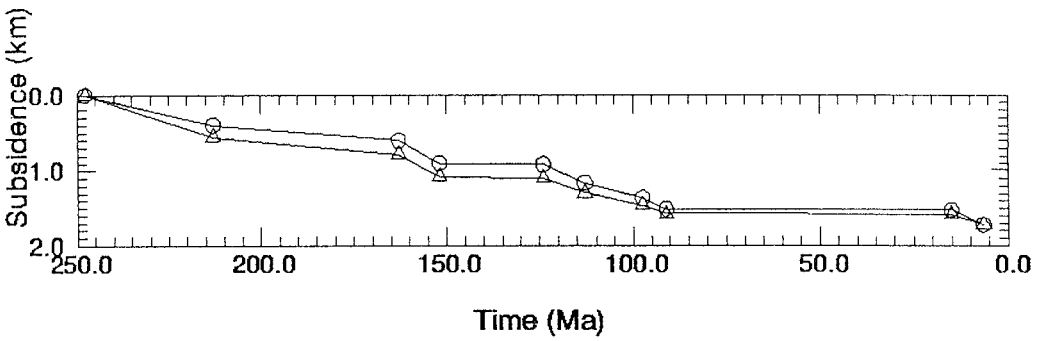


Fig 3.2.8.a). Basement subsidence curve for the section CM6 of the External Prebetics. Cirles-uncorrected subsidence, triangles-decompacted subsidence.

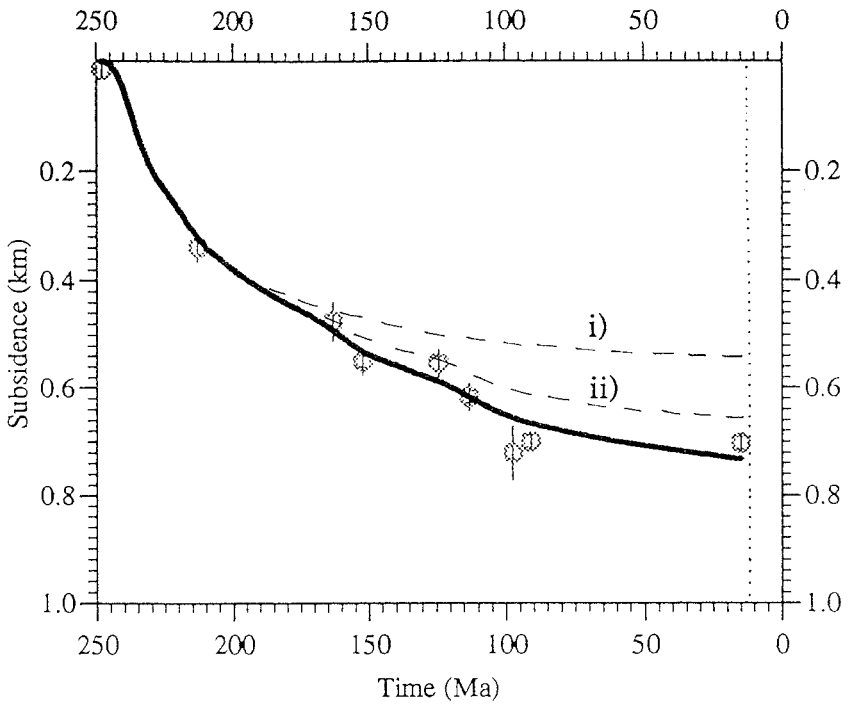


Fig 3.2.8.b). Water-loaded, tectonic subsidence curve for the section CM6. Bars on points-errors in subsidence values due to inaccuracy of palaeowater depths. Solid line-best-fit tectonic subsidence curve from which the ß value of **1.107** is attained. Dashed line-best-fit tectonic subsidence curve if events after i) 180 Ma and ii) 95 Ma are ignored. Dotted line-initiation of Tertiary increase in subsidence due to the loading of thrust slices at 15-10 Ma.

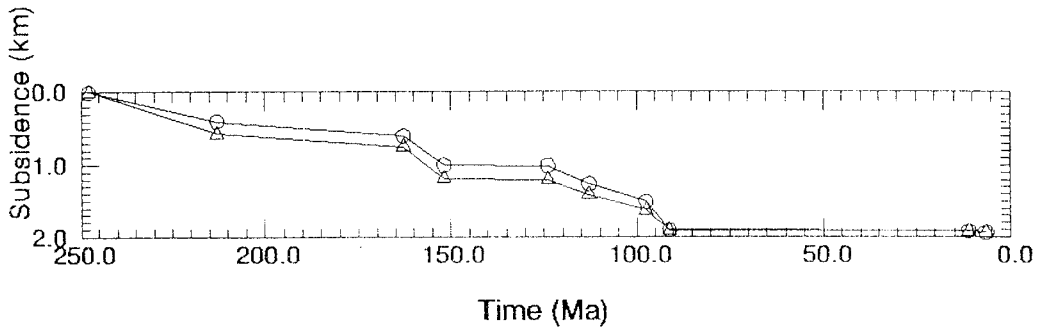


Fig 3.2.9.a). Basement subsidence curve for the section CM7 of the External Prebetics. Cirles-uncorrected subsidence, triangles-decompacted subsidence.

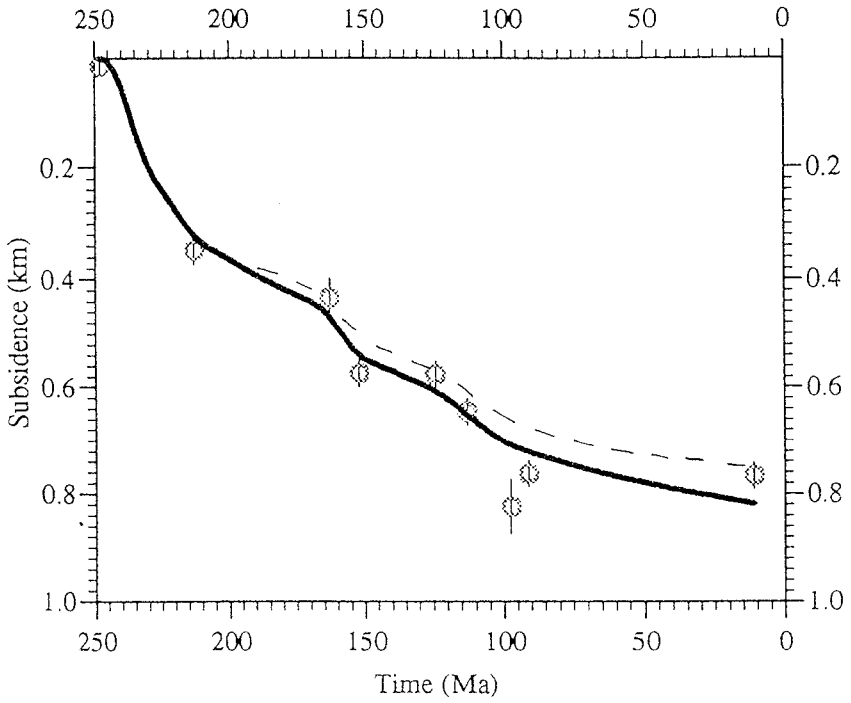


Fig 3.2.9.b). Water-loaded, tectonic subsidence curve for the section CM7. Bars on points-errors in subsidence values due to inaccuracy of palaeowater depths. Solid line-best-fit tectonic subsidence curve from which the ß value of **1.122** is attained. Dashed line-best-fit tectonic subsidence curve if events after 80 Ma are ignored.

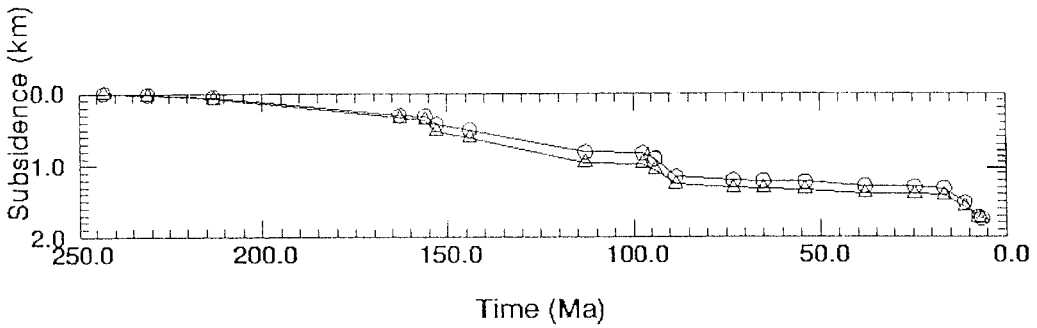


Fig 3.2.10.a). Basement subsidence curve for the section CM5 of the Internal Prebetics. Cirles-uncorrected subsidence, triangles-decompacted subsidence.

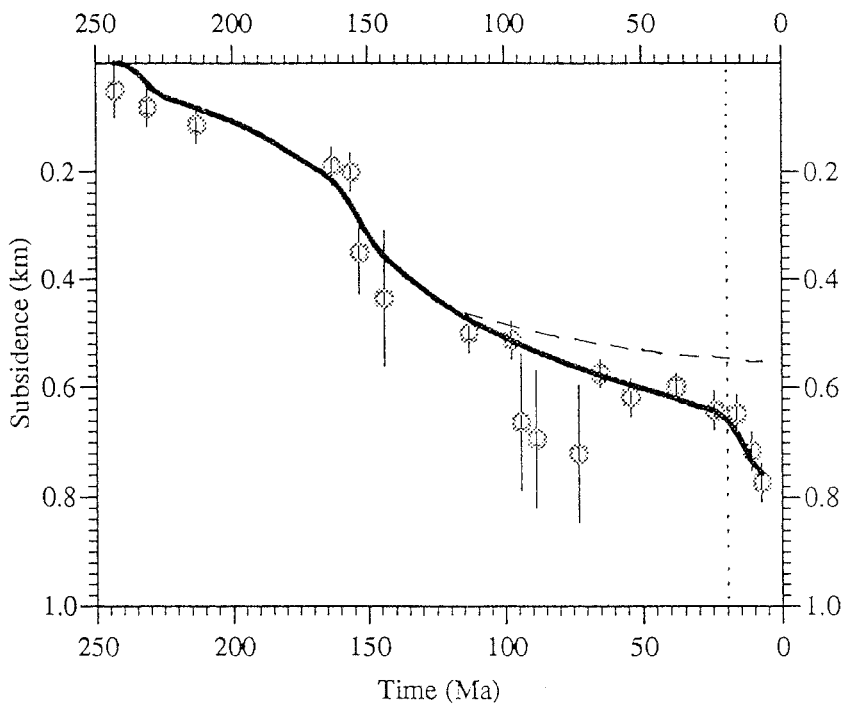


Fig 3.2.10.b). Water-loaded, tectonic subsidence curve for the section CM5. Bars on points-errors in subsidence values due to inaccuracy of palaeowater depths. Solid line-best-fit tectonic subsidence curve from which the ß value of **1.114** is attained. Dashed line-best-fit tectonic subsidence curve if events after 110 Ma are ignored. Dotted line-initiation of Tertiary increase in subsidence due to the loading of thrust slices at 20-15 Ma.

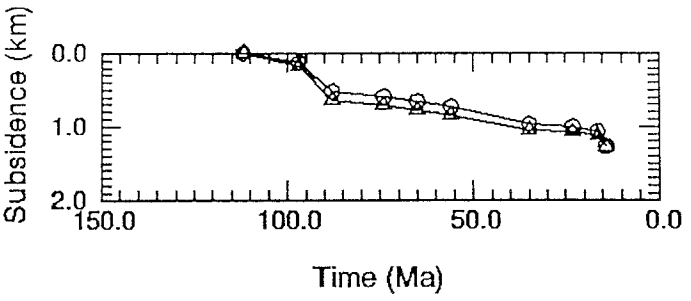


Fig 3.2.11.a). Basement subsidence curve for the section BP1 of the Internal Prebetics. Cirles-uncorrected subsidence, triangles-decompacted subsidence.

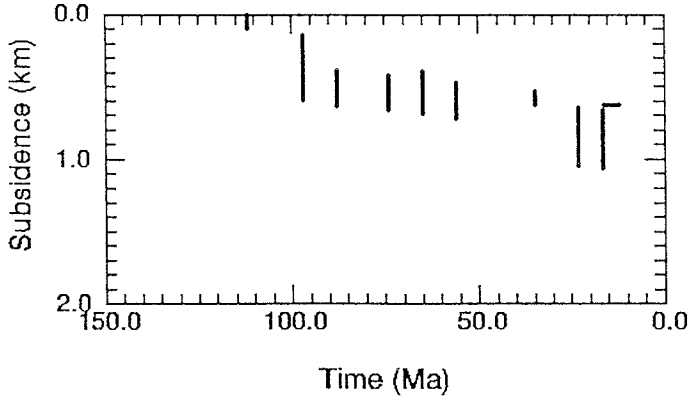


Fig 3.2.11.b). Water-loaded, tectonic subsidence curve for the section BP1. Bars-errors in subsidence values due to inaccuracy of palaeowater depths.

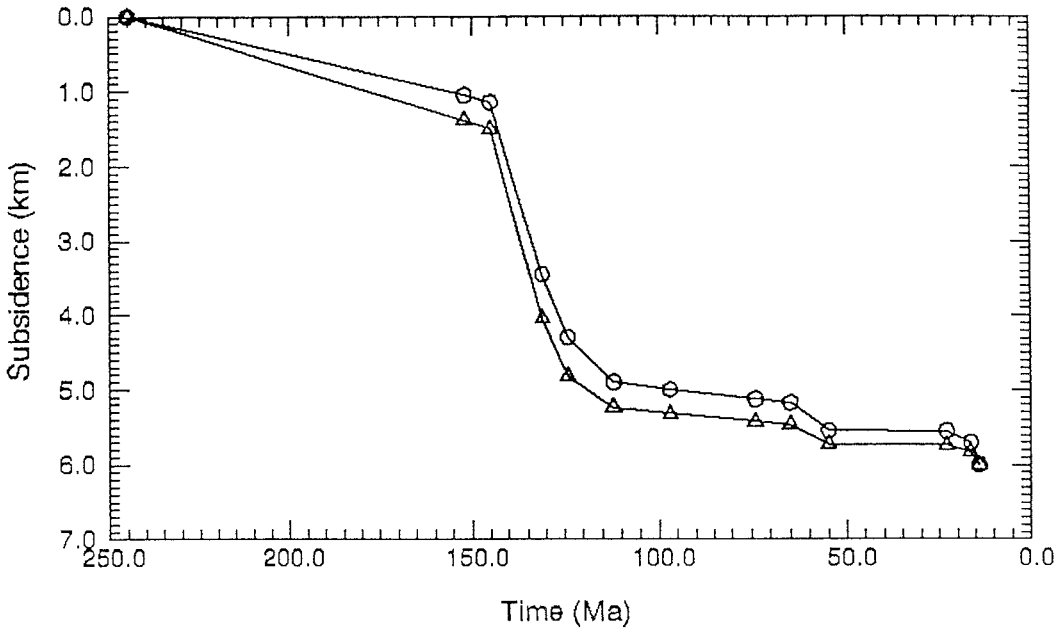


Fig 3.2.12.a). Basement subsidence curve for the section BP2 of the Internal Prebetics. Cirles-uncorrected subsidence, triangles-decompacted subsidence.

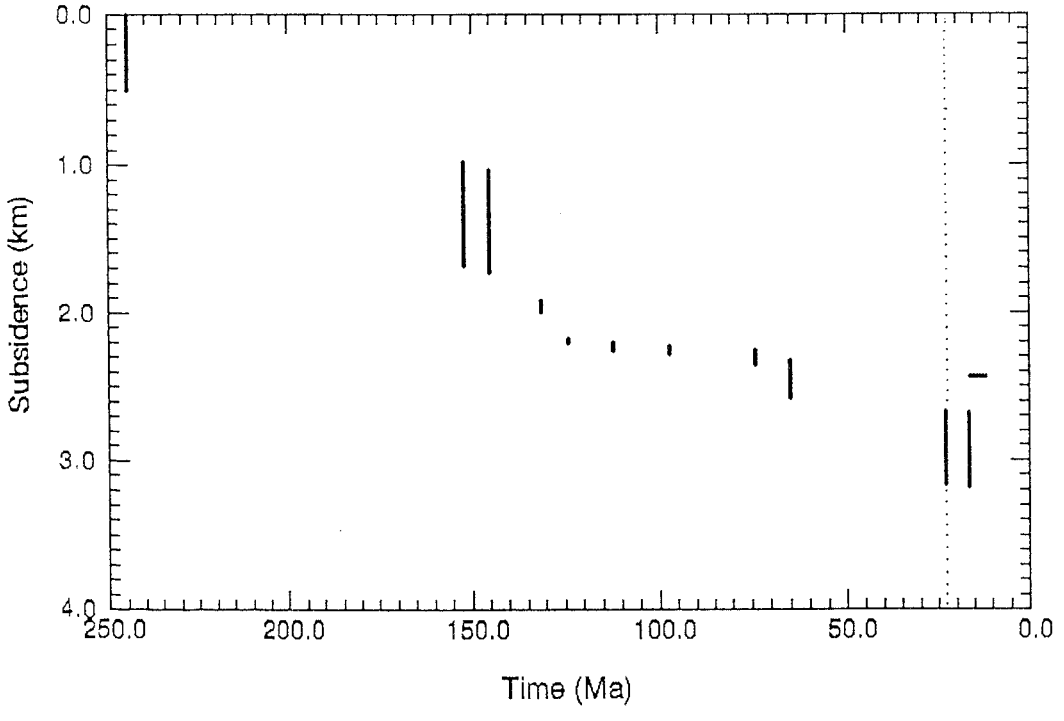


Fig 3.2.12.b). Water-loaded, tectonic subsidence curve for the section BP2. Bars-errors in subsidence values due to inaccuracy of palaeowater depths. Dotted line-initiation of Tertiary increase in subsidence due to the loading of thrust slices at 23-20 Ma.

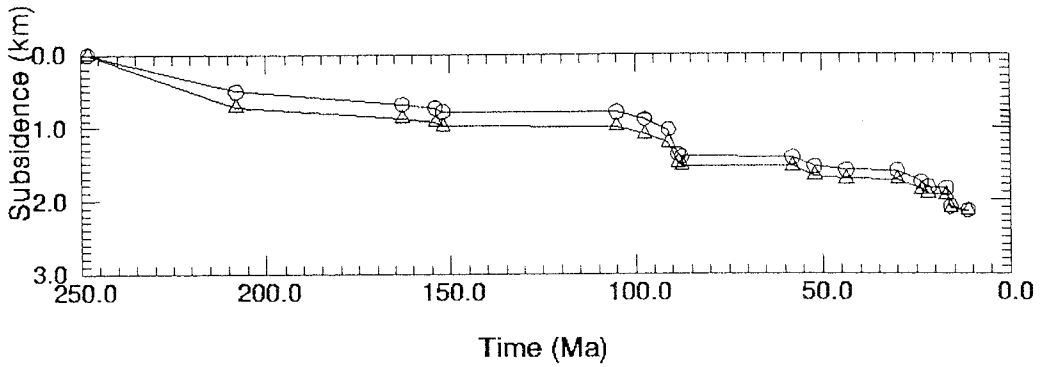


Fig 3.2.13.a). Basement subsidence curve for the section CM10 of the Internal Prebetics. Cirles-uncorrected subsidence, triangles-decompacted subsidence.

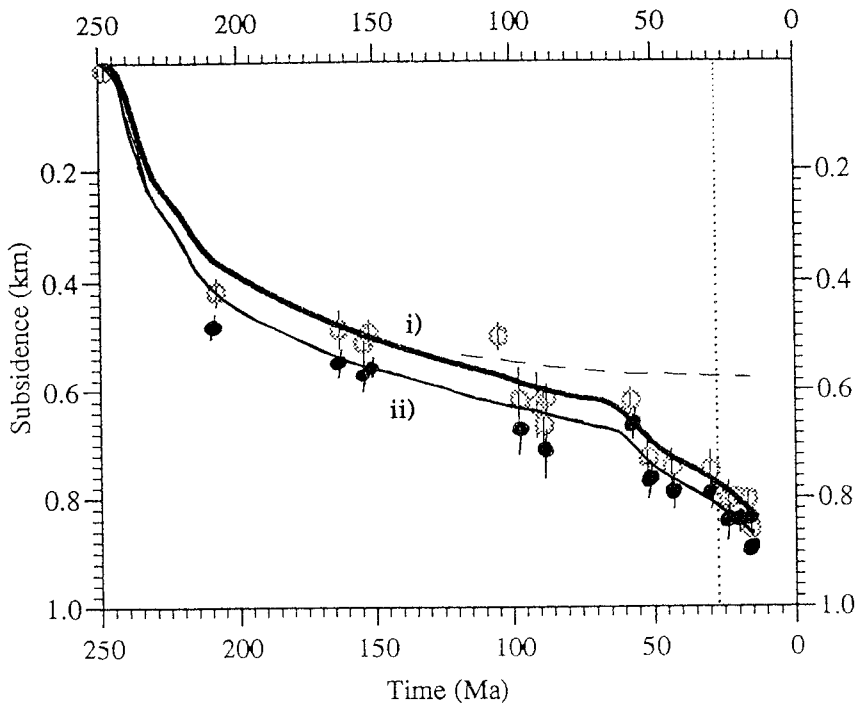


Fig 3.2.13.b). Water-loaded, tectonic subsidence curve for the section CM10. Open points-section of minimum stratigraphic thickness, closed points-section of maximum stratigraphic thickness. Bars on points-errors in subsidence values due to inaccuracy of palaeowater depths. Solid lines-best-fit tectonic subsidence curve for i) minimum thickness section from which the ß value of **1.132** is attained and for ii) maximum thickness section from which the ß value of **1.137** is attained. Dashed line-best-fit tectonic subsidence curve if events after 140 Ma are ignored. Dotted line-initiation of Tertiary increase in subsidence due to the loading of thrust slices at 30-25 Ma.

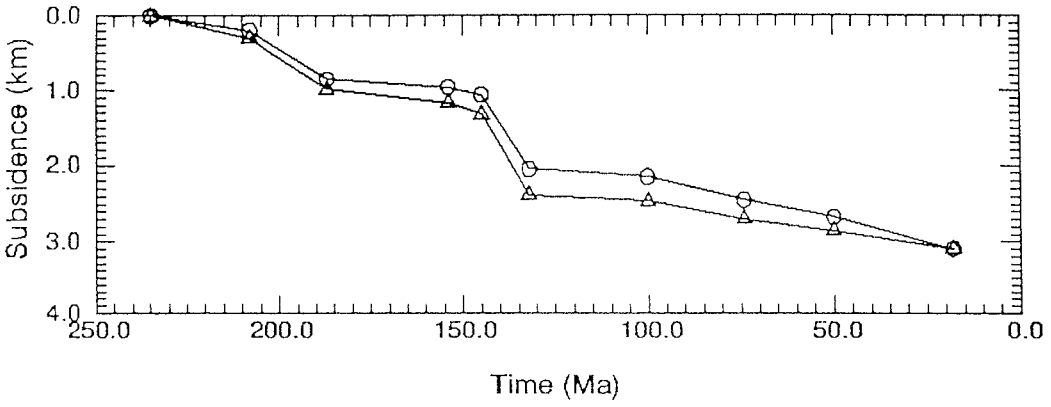


Fig 3.2.14.a). Basement subsidence curve for the section N. SUBBETIC of the Subbetic Zone. Cirles-uncorrected subsidence, triangles-decompacted subsidence.

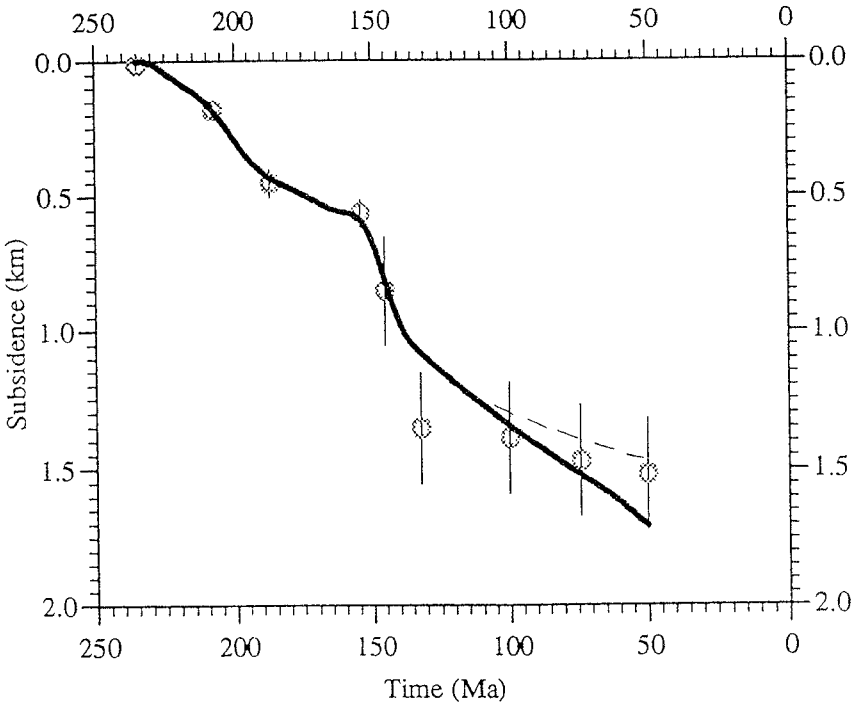


Fig 3.2.14.b). Water-loaded, tectonic subsidence curve for the section N. SUBBETIC. Bars on points-errors in subsidence values due to inaccuracy of palaeowater depths. Solid line-best-fit tectonic subsidence curve from which the ß value of **1.324** is attained. Dashed line-best-fit tectonic subsidence curve if events after 105 Ma are ignored.

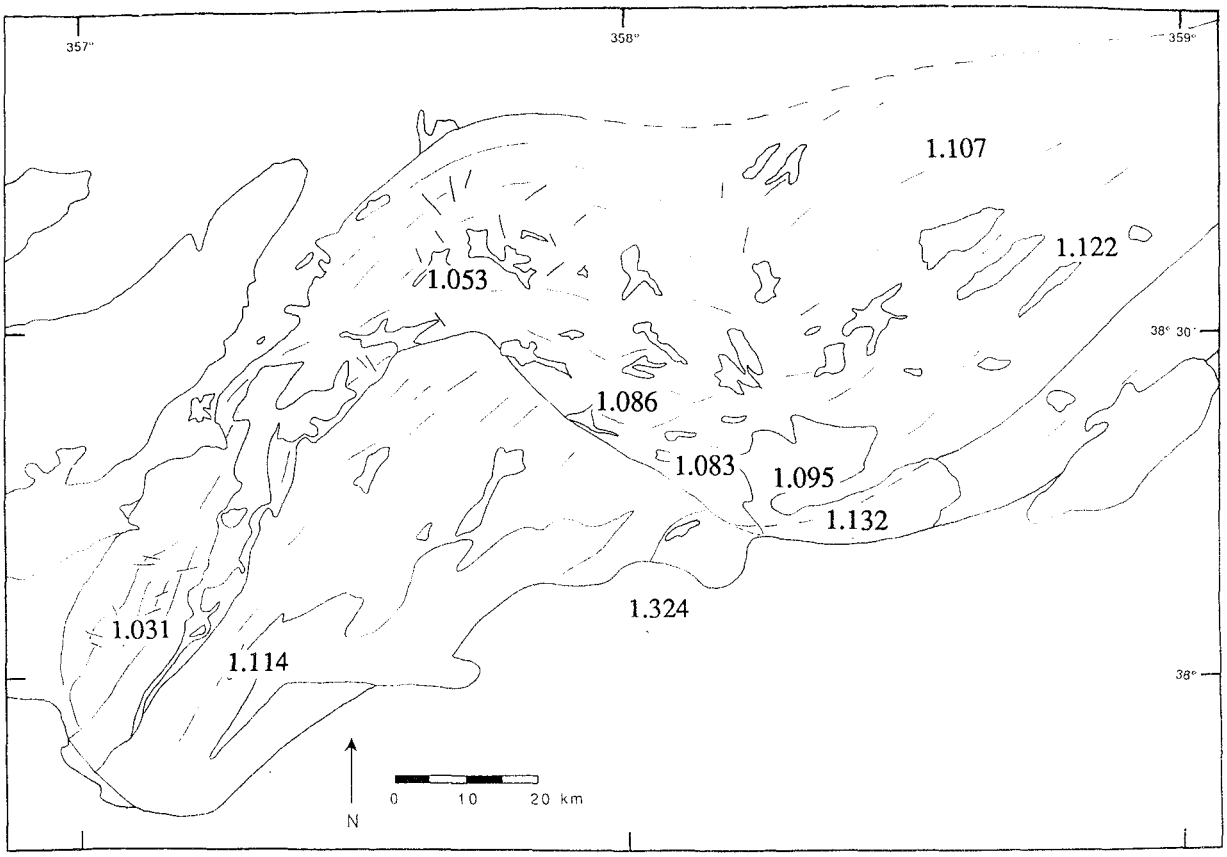


Fig 3.2.15. Map of the Prebetic Zone and the northern Subbetic Zone showing the spatial variation in the value of ß obtained from the tectonic subsidence curves shown in Figs 3.2.3-14.b). There is a notable increase in ß from west to east and from the most external areas basinward. ß factors only accurate to one decimal place.

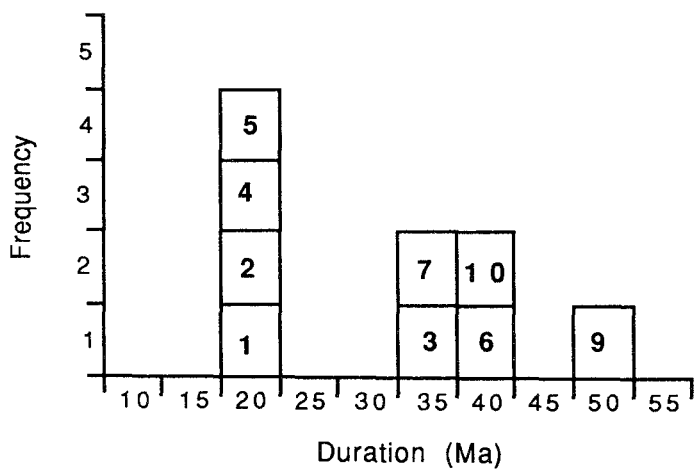


Fig 3.2.16. Graph showing the distribution in duration of the initial Mesozoic rifting obtained from the tectonic subsidence curves shown in Figs 3.2.3-14.b). The numbers in bold indicate the sections numbers (e.g. 1 = CM1). The rifting exhibited in the more westerly sections i.e. 1, 2, 4 and 5, is of a shorter duration than that of the more easterly sections.

a)

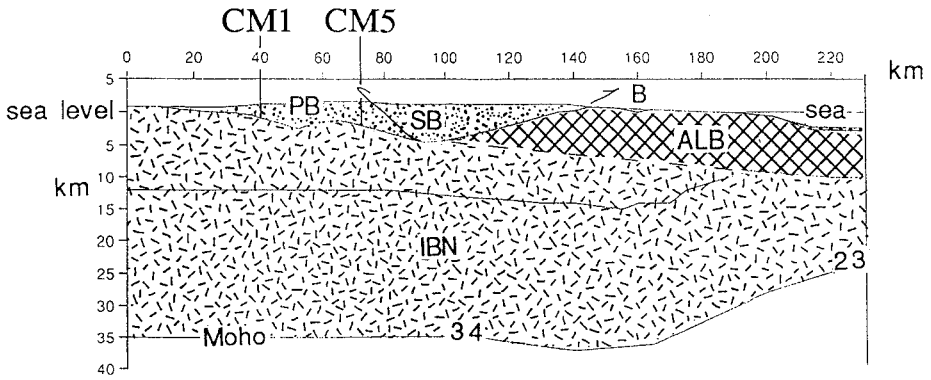


Fig 3.2.17.a) Structural cross-section showing the locations of CM1 and CM5. There is a marked increase in the thickness of the thrust pile and hence the amount of loading directly to the SE of CM5. PB - Prebetic Zone, SB - Subbetic Zone, B - Tertiary/Quaternary basin, ALB - Alboran crust, IBN - Iberian crust.

b)

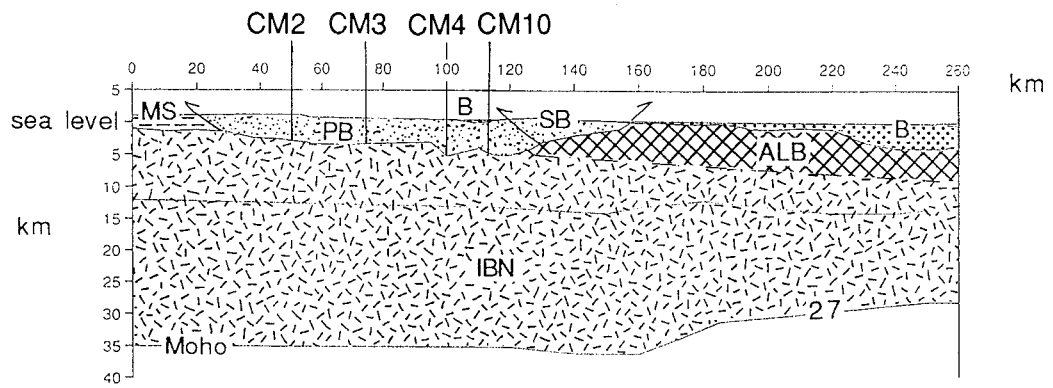


Fig 3.2.17.b) Structural cross-section showing the locations of CM2, CM3, CM4 and CM10. There is a marked increase in the thickness of the thrust pile and hence the amount of loading directly to the SE of CM4 and CM10. PB - Prebetic Zone, SB - Subbetic Zone, MS - Undeformed Mesozoic of the Meseta, B - Tertiary/Quaternary basin, ALB - Alboran crust, IBN - Iberian crust.

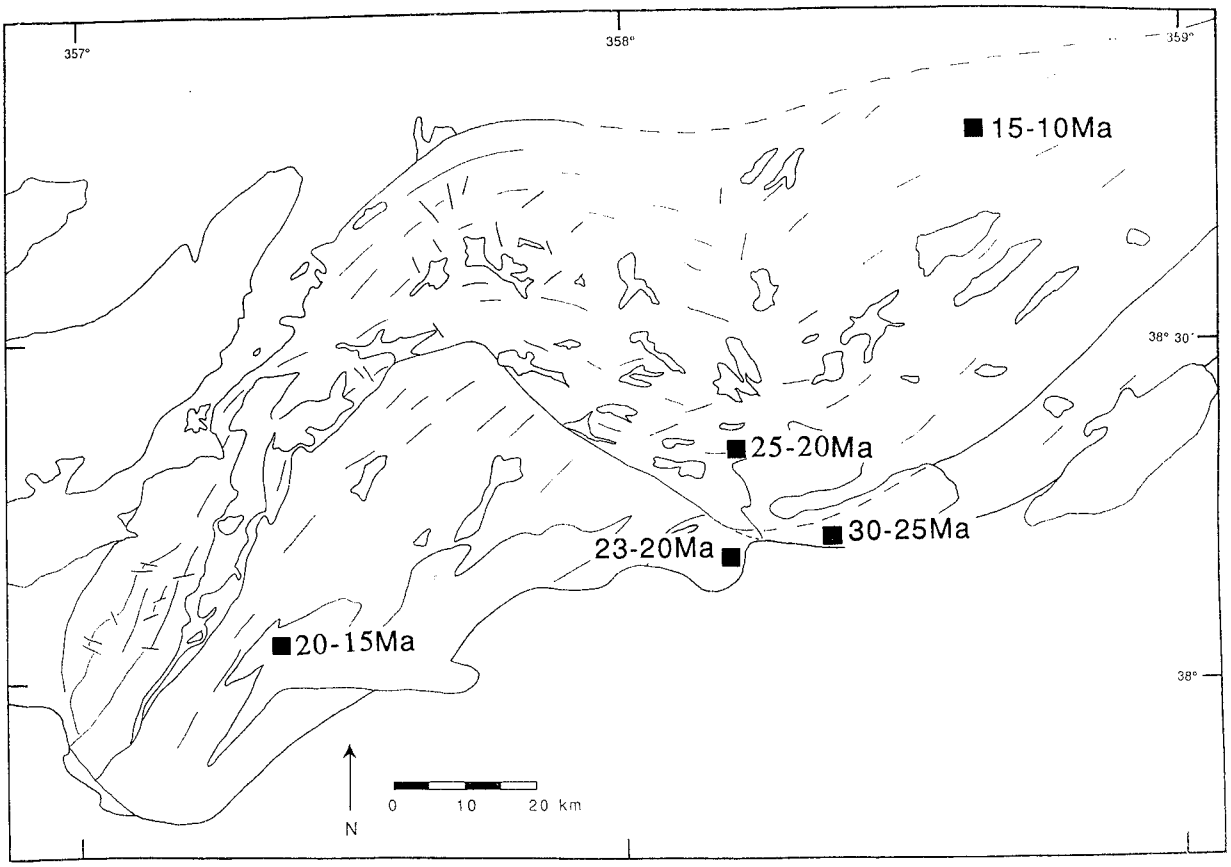


Fig 3.2.18. Variation in timing of the deviation of the subsidence curve from the theoretical curve in the Tertiary due to local basin formation. The timing is seen to become younger towards the foreland but not to correspond laterally across the Socovos Fault.

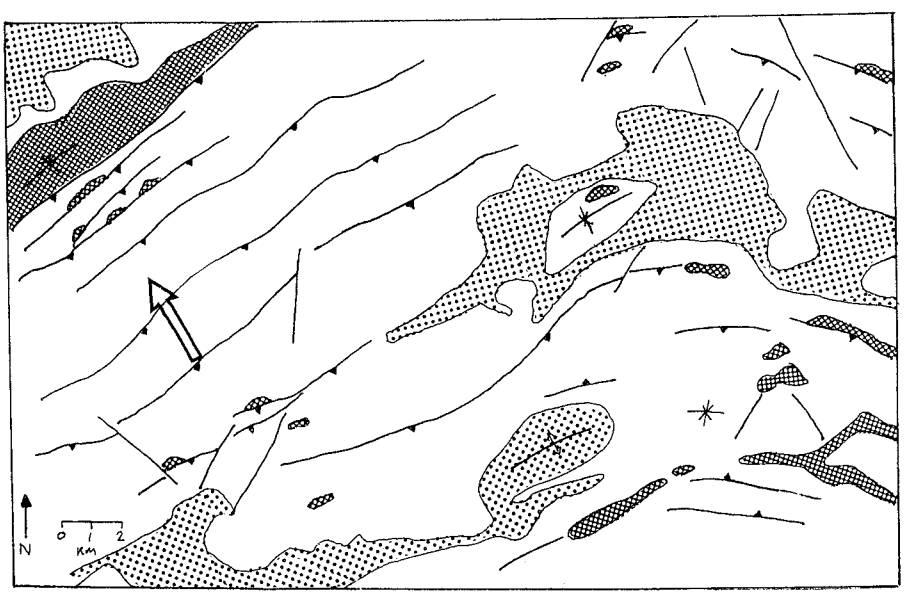


Fig 3.2.19. Drainage pattern shown in the Tertiary deposits in the Alcaraz Antitaxis. Pale stipple-Triassic, dark stipple-late Tortonian/early Messinian. The arcuate drainage pattern is shown in the SE of the area. Channels from the more internal parts of the orogen to the foreland may be indicated by the outcrop pattern of the overthrust late Tortonian/early Messinian sediments (open arrow).



Fig 3.2.20. GR 72434436 on the road from Bogarra to Vegallera. Looking E. Wedge of late Tortonian/early Messinian calcarenites derived from uplifted Mesozoic units to the foreland, indicating the intramontane style of basin formation. Relief of fan is approximately 5m.

Chapter 4

CHAPTER 4

INTERPRETATION OF GRAVITY DATA

4.1. Introduction

Gravity modelling can greatly increase our knowledge of subsurface structure and thereby contribute towards our understanding of the deformational style and history of the Betic Cordillera. The gravity anomaly over a hypothetical, but well constrained, 2-D crustal cross-section can be calculated using line-integral methods (e.g. Talwani et al. 1959) and compared with the observed gravity anomaly measured along that section. The input crustal model can then altered iteratively until a best fit with the observed gravity anomaly is obtained, which is in agreement with other geophysical and field data. There is an inherent ambiguity in gravity modelling but it provides useful constraints on tectonic models and the distribution of structural units.

A number of crustal cross-sections have been modelled across the Betic Cordillera and the Alboran Basin in previous gravity and seismic studies (Hatzfeld 1976, Banda & Ansorge 1980, Torné et al. 1992, Van der Beek & Cloetingh 1992, Banda et al. in press, Torné & Banda in press, Watts et al. submitted) (Fig 4.1.1.). These studies, however, do not cover the area of the Prebetic Arc comprehensively and are not in complete alignment with the general direction of tectonic transport in the eastern External Zone and therefore may not reveal the maximum gradients of their subsurface structures.

A Bouger anomaly gravity map, for the area 356°W-360°, 37°N-39°N, was compiled from B.G.I., Instituto Geográfico National, and available ship tracks. A reduction density of 2670 Kg/m^3 was used to correct the free air anomaly data for the area covering the Alboran Sea. The gravity anomaly gradient in this area of the eastern Betic Cordillera is approximately NW-SE although it can be shown to swing more NNW-

SSE to the west. This gradient which is absent over the Palaeozoic massif, increases notably towards the coast. The absolute values of the anomalies range from -140 mGal beneath the Tertiary Baza Basin to +200 mGal under the Alboran Sea (Fig 4.1.2).

Five profiles, four parallel and oriented NW-SE and one oriented NE-SW, were modelled across the eastern Betic Cordillera from the stable Iberian margin to the coast (Fig 4.1.2). The profiles were chosen to illustrate the change in crustal structure from west to east and were aligned sub-parallel to the tectonic transport direction and the gravity gradient. This allowed the results to be combined with section balancing techniques to provide an estimate of the amount of plane strain which has occurred along the profile (Chapter 5). The Elche section, orientated NE-SW, was completed mainly to provide a link between the other sections, but also to help construct a balanced section in an area of the NW Trending Limb where there is a NE-SW tectonic transport direction (section 2.2.1.3).

4.2. Gravity modelling

The vertical and horizontal density variations are not tightly constrained in this area and the values incorporated into the modelling in this study were taken from previously published work (e.g. Torné & Banda in press). The locations of the important structural boundaries of the sections for which the gravity anomaly was calculated have been constrained by the available seismic and well-log data and the results of field studies (e.g. Hatzfeld 1976, Banda & Ansorge 1980, Banks 1985, Torné et al. 1992, Banda et al. in press, Torné & Banda in press). (Table 4.2) Hence, the

External Zones and undeformed Mesozoic of the Meseta were allotted a density of 2450 Kg/m^3; the Internal Zones 2750 Kg/m^3; the Neogene and Quaternary sediments 2300 Kg/m^3; the upper crust 2750 Kg/m^3; the lower crust 2900 Kg/m^3 and the Iberian upper mantle 3330 Kg/m^3. Although some previous studies have incorporated lower upper mantle densities of 3200 Kg/m^3 beneath the Alboran Sea due to its anomalously low P-wave velocity (Hatzfeld 1976), recent models have used a density value of 3330 Kg/m^3 for the upper mantle beneath the Iberian crust (Van der Beek & Cloetingh 1992, Torné & Banda in press). The model of the distribution of the structural units has been further refined to include the backthrust nature of the Internal/External Zone boundary (Lonergan et al. in press). Due to the relatively low flexural rigidity of the eastern Betic lithosphere, a flexural response to the loading of the External Zone thrust sheets, with associated foreland basin formation, is greatly reduced (Van der Beek & Cloetingh 1992) (section 3.3). The structure of the input crustal section and hence its calculated gravity anomaly was corrected by iterative steps to provide a best fit to the observed gravity anomaly. The deeper, regional structure, which causes the longer wavelength anomalies, was altered first until an adequate match was made. Other structures, from deeper to shallower and hence shorter wavelength anomalies, were then varied until a best fit was reached. Edge effects on the predicted gravity anomaly were removed by using a cross-section compiled in such a way that each end was extended for 1000 km with the same structure as that of the actual end of the section. Subsequent sampling of the predicted anomaly only directly over the actual section removed any erroneous edge effects inherent in this type of modelling. For example the Cazorla section, 230 km long, was located at kilometres 1000 to 1230 of a compiled profile which stretched from 0 to 2230 km. The predicted gravity anomaly was

only sampled between 1000 and 1230 kms. The dynamics of the present day extension cause the presence of structural features which are not in isostatic equilibrium. Unfortunately these features cannot be identified in this modelling technique.

The crustal sections and their comparative calculated and observed anomalies produced from the gravity modelling are shown in Figs 4.2.1-5. (The co-ordinates of the gravity models are shown in Appendix 2). The maxima and minima of the observed gravity anomalies decrease in magnitude eastwards, from the Cazorla section to the Jumilla section. As the gravity anomaly along a profile represents the sum of the effects of a number of geological phenomena, which may be combined in a variety of ways, these crustal sections do not represent unique solutions but only ones which are possible. The varying effects of altering the geometry of geological structures such as the basement/External Zone thrust pile contact or the depth to the Moho discontinuity can also be modelled. (The co-ordinates of the alterations to the gravity model are shown in Appendix 2). Fig 4.2.6 illustrates how a 1km increase or decrease of the maximum depth of the External Zone thrust pile notably alters the value of the minima of the calculated anomaly. The gravity effect of this shallow feature is demonstrably relatively short in wavelength. Fig 4.2.7 illustrates the effect of increasing or decreasing the gradient of the Moho to the SE of the profile as the crust thins towards the Alboran Sea. This relatively deep feature effects a long wavelength anomaly, so most of the calculated anomaly is altered by an increasing amount towards the SE of the profile.

4.3. Interpretation of the regional structure

Analysis of the regional structure i.e. the longer wavelength features, such as the variation of crustal thickness and hence the location of the Moho discontinuity, shows a marked lateral change across the eastern Betic Cordillera (Fig 4.3.1). The most westerly section, the Cazorla section, indicates the presence of a small crustal root under the Internal Zones, inland from the coast. This structure, also modelled for profiles across the western Betic Cordillera by Van der Beek & Cloetingh (1992) (located on Fig 4.1.1), becomes very much reduced in the profiles to the east where the Moho becomes shallower. This shallowing of the Moho occurs landward of the coast indicating that the transition between stretched and unstretched crust is predominantly located beneath onshore regions. The gradient of the Moho shows a decrease from the Cazorla section to the Isso section illustrating the decreasing influence to the east of the extension which affected the Alboran Basin and adjacent Iberian crust from the Miocene onwards. The positive gradient of the gravity anomaly across the region where the Moho shallows varies from 1.8 mGal/km for the Cazorla section, 1.5 mGal/km for the Orcera section to 1.0 mGal/km for the Isso section with corresponding modelled Moho gradients of 0.18, 0.11 and 0.08 respectively (Figs 4.2.1-3). The gravitational effect of increasing or decreasing the Moho gradient is shown for the Cazorla section in Fig 4.2.7. A steeper or shallower Moho gradient causes a related increase or decrease in the gradient of the SE section of the gravity anomaly respectively. The most easterly section, the Jumilla section, however, displays an interesting increase in Moho gradient and thinning of the Iberian crust to the SE of the profile. The positive gradient of the Jumilla gravity anomaly across the region where the Moho shallows is 1.6

mGal/km with a modelled Moho gradient of 0.22 (Fig 4.2.4). This increased extension in the easternmost Betic Cordillera has been related to stretching in the Valencia trough (Van der Beek & Cloetingh 1992). Gravity modelling in the western and central Betic Cordillera reveals a more abrupt steepening of the Moho gradient towards the Alboran Sea. Watts et al. (submitted) account for this steepening as being due to a narrow transition from stretched to unstretched crust. Torné & Banda (in press) postulate that this steep gradient may be accounted for by the presence of a previous transform type margin.

4.4. Interpretation of the upper crustal structure

Analysis of the upper crustal i.e. the shorter wavelength phenomena such as the basement/wedge interface and the geometries of the Tertiary basins, in the External Zones of the eastern Betic Cordillera contributes much to our understanding of the tectonics of this area. Fig 4.4.1. shows a contour plot of the basement elevation compiled from the five modelled sections with BP well data included to provide an additional constraint. A decreasing basement gradient is exhibited from west to east in the Prebetic Zone which may be due to the local loading affects of the Prebetic/Subbetic thrust pile which appears to be generally thicker in the west (Fig 4.4.2.) and to have undergone a greater amount of shortening (section 5.3). The gravitational effect of altering the thickness of the thrust pile and hence the basement gradient is shown for the Cazorla section in Fig 4.2.6. Decreasing or increasing the thickness of the thrust pile causes a related decrease or increase respectively in the value of the gravity minimum but no significant change in its wavelength. This may be

enhanced by an increased evaporitic content in the décollement horizon to the east, causing a lower angle of critical taper to develop (section 3.3). The initial crustal section compiled from geological and geophysical data incorporated the backthrust nature of the Internal/External Zone boundary and therefore the presence of a wedge of Internal Zone nappes beneath the southern part of the Subbetic Zone (Lonergan et al. in press). Matching the calculated gravity anomalies to those observed for each profile allowed this model to be refined. The frontal nose of the wedge and hence the greatest thickness of the relatively low density Prebetic/Subbetic thrust pile was located at the point of the gravity minima. Fig 4.4.3. shows the gravitational effects of displacing the frontal nose of the Internal Zone wedge. (The co-ordinates of the alterations to the gravity model are shown in Appendix 2). If the frontal nose is displaced towards the foreland or the hinterland, the gravity minimum is consequently also displaced towards the foreland or the hinterland respectively. Fig 4.4.1. shows the positive gradient of this basement wedge. This feature becomes less well defined and more complex towards the east (Figs 4.2.3/4). Other models in which the Internal/External Zone boundary is inferred to be only a NW directed thrust contact show a calculated gravity anomaly over the boundary which appears to be too large in magnitude compared to the observed gravity anomaly (Van der Beek & Cloetingh 1992).

From the non-alignment of the contours on the map of the basement elevation with the Socovos fault, it can be interpreted as a thin-skinned feature across which there is no dramatic change in the basement structure. A depression of the basement and associated thickening of the thrust pile is observed within the NW Trending Limb and the Cenajo Syntaxis. This may result from the increased loading affect produced by the concomitant NE-SW thrusting and backthrusting observed in the NW

Trending Limb (section 2.2.1.3) and the convergent NE-N-NW directed shortening observed in the Cenajo Syntaxis (section 2.2.1.4).

A large, short wavelength perturbation in the Bouger anomaly (Fig 4.1.2.) and hence the regional ENE-WSW trend of the basement/wedge interface, is displayed in the Orcera section (Fig 4.2.2). This large positive gravity anomaly can be accounted for by the emplacement of metasomatic adamellite from remobilised Hercynian granites into the upper basement and Triassic in this part of the Betic Cordillera during the Tertiary deformation (IGME Memoir no. 865 Siles) (section 2.2.1.1).

The very short wavelength negative anomalies e.g. located at 150-165 km on the Cazorla section (Fig 4.2.1), are due to the presence of low density Tertiary and Quaternary basins, both onshore and offshore, which have also been described by Casas & Carbo (1990). Fig 4.4.4. shows the effect of varying the basin geometries on the calculated gravity anomalies. (The co-ordinates of the alterations to the gravity model are shown in Appendix 2). A deeper basin would cause a decrease in the value of the short wavelength anomaly minimum and therefore an increase in the amplitude of the anomaly but no alteration of the wavelength. Displacement of the deepest part of the basin towards the hinterland causes the short wavelength anomaly to be displaced towards the hinterland.

To help elucidate the 3-D upper crustal structure in addition to a basement elevation map compiled from the five modelled sections with all their inherent interpretive bias, the complete Bouger gravity anomaly set for the area of study was filtered to remove the longer wavelength, regional structure (Fig 4.4.5). A 2-D band-pass filter was used to remove all gravity anomalies with wavelengths greater than 80 km. Features

previously described for the upper crust from the results of the gravity modelling such as the adamellite perturbation, the decreasing gradient of the basement slope from SW to NE, the NW dip of the Internal Zone (basement)/Subbetic Zone contact and the increased loading in the NW Trending Limb, Cenajo Syntaxis and to the SW of the area, are also indicated from the filtered gravity data. Moho structures such as the crustal root inferred in the western region are not observed in the filtered gravity data.

4.5. Summary of results

Five profiles across the eastern Betic Cordillera which sub-parallel the tectonic transport direction were chosen for gravity modelling to elucidate the subsurface structure and increase our understanding of the Betic Cordillera. The gravity anomalies over hypothetical, but well constrained, 2-D crustal cross-sections were calculated based on line-integral methods and altered, iteratively, until a best fit with the observed gravity anomaly measured along each section was obtained.

Analysis of the regional structure shows a marked lateral change across the eastern Betic Cordillera. The most westerly section indicates the presence of a small crustal root under the Internal Zones which becomes reduced in the profiles to the east where the Moho becomes shallower and its gradient decreases. This occurs landward of the coast indicating that the transition between stretched and unstretched crust is narrow and located beneath onshore regions. The most easterly section shows an increase in Moho gradient and thinning of the Iberian crust which may be related to stretching in the Valencia trough.

Analysis of the upper crustal shows a decreasing gradient of the basement/Prebetic-Subbetic thrust pile interface from west to east in the Prebetic Zone which may be due to the local loading affects of the thrust pile which appears to be thicker and to have undergone a greater amount of shortening in the west. The frontal nose of the Internal Zone wedge beneath the Subbetic Zone was located at the point of the gravity minima. This feature becomes less well defined and more complex towards the east. The non-alignment of the contours on the map of the basement elevation with the Socovos fault indicate that this is a thin-skinned feature across which there is no significant change in the basement structure. The very short wavelength negative anomalies are due to the presence of low density Tertiary and Quaternary basins.

The Bouger gravity anomaly set for the area was filtered by using a 2-D band pass to remove the longer wavelength (>80 km), regional structure. Features previously described for the upper crust from the results of the gravity modelling are also indicated from the filtered gravity data. Moho structures such as the crustal root inferred in the western region are not observed in the filtered gravity data.

CHAPTER 4

FIGURES

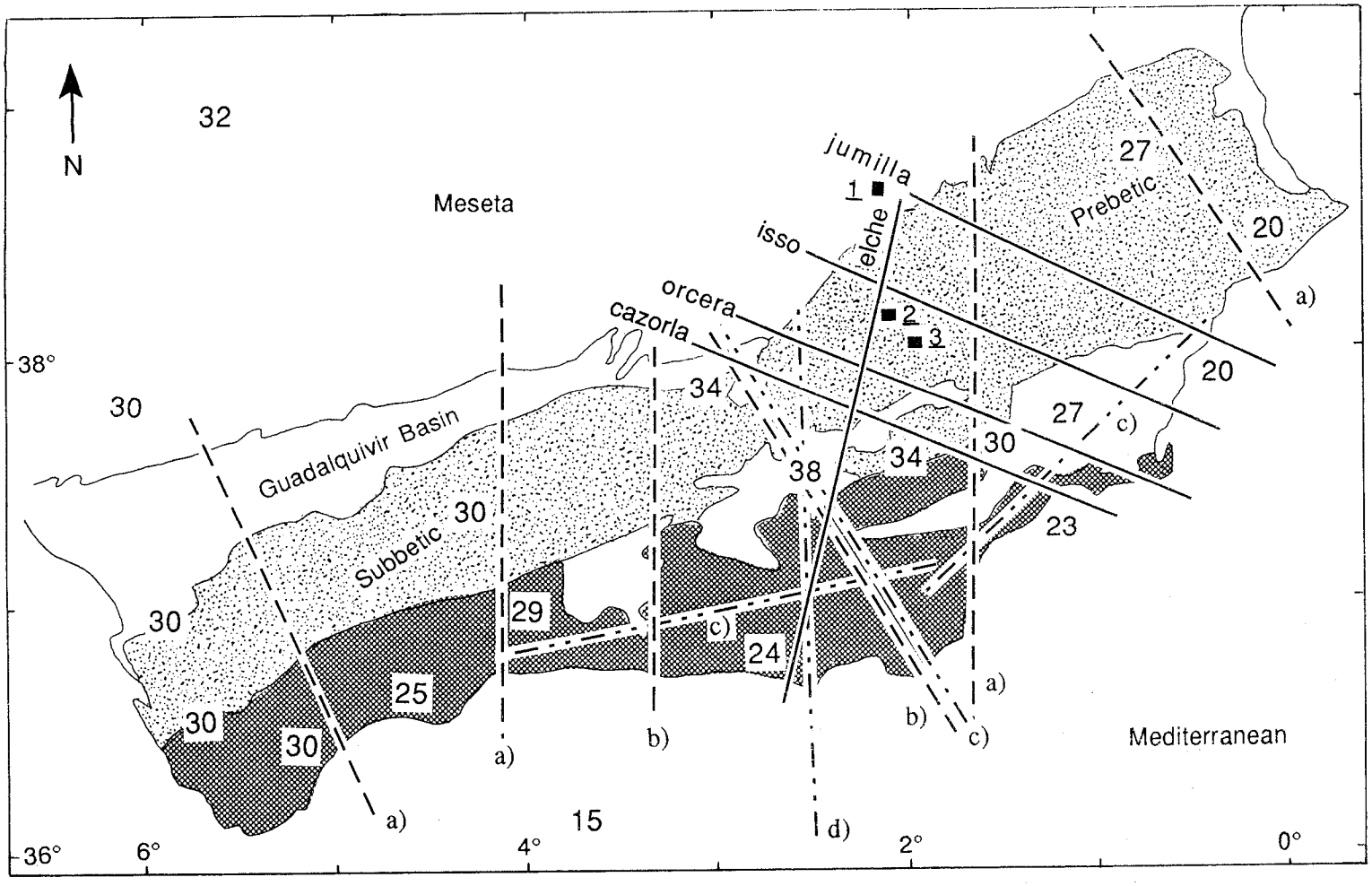


Fig 4.1.1. Summary map of the Betic Cordillera showing the locations of profiles along which gravity models and/or seismic interpretation, referenced in this work, have been constructed. The regional variation in Moho depths is shown (after Van der Beek & Cloetingh 1992 and Banda et al. in press). Solid line - gravity model included in this study. Dashed line - gravity model from other workers (a) Van der Beek & Cloetingh 1992, b) Torné & Banda in press. Dot/dashed line - interpretation of seismic refraction or reflection. (c) Banda et al. in press, d) Hatzfeld 1976. Black squares - B.P. wells, 1-Salobral, 2-Socovos 2, 3-Rio Segura.

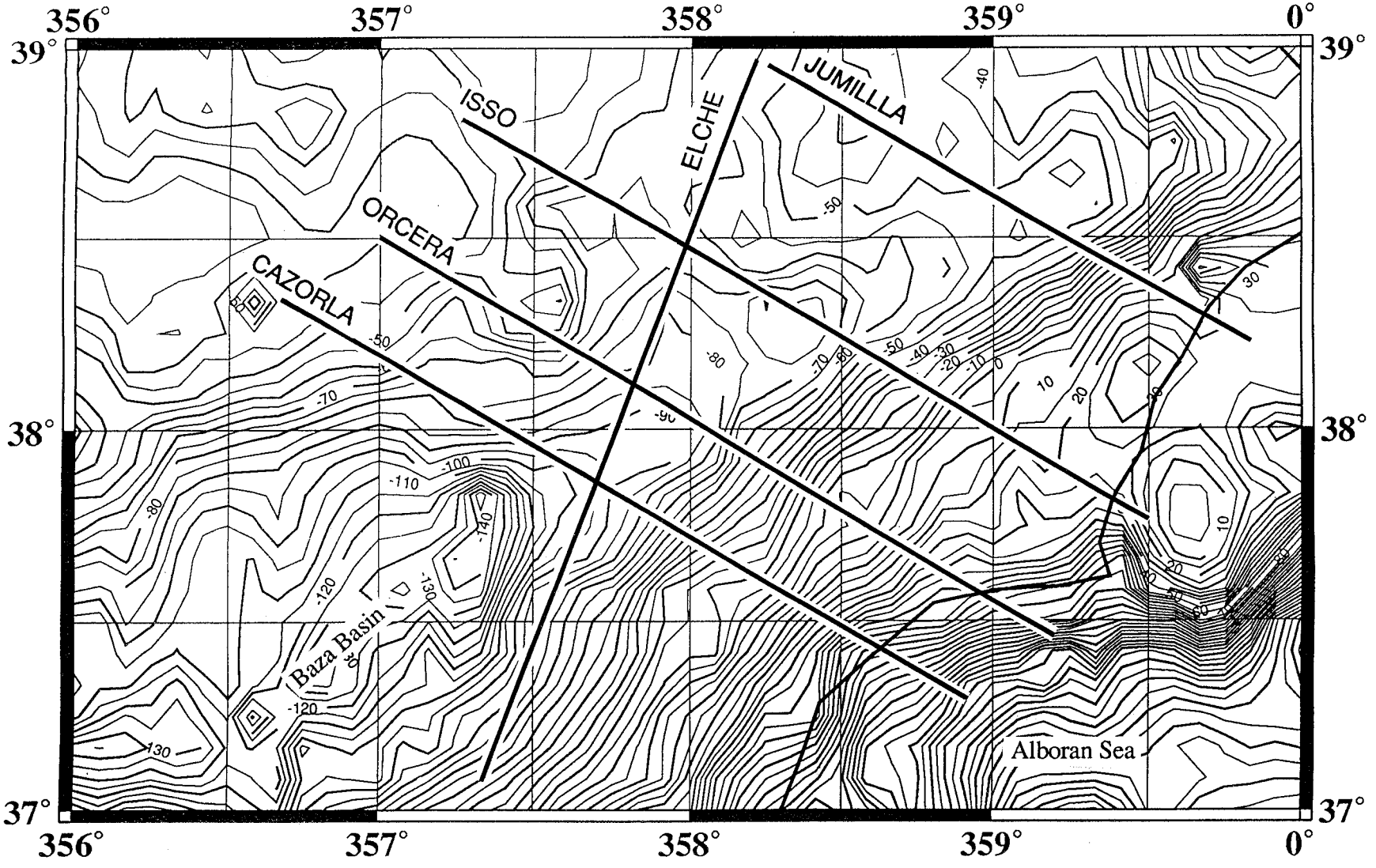


Fig 4.1.2. Contour map of the Bouger gravity anomaly for the eastern Betic Cordillera showing the strong NE-SW regional trend. A steep positive gradient is shown to the SE of the area and a gravity minimum occurs to the SW of the area. Locations of the five profiles which have been modelled for gravity in this study. The Cazorla, Orcera, Isso and Jumilla profiles are parallel and oriented at 120° whereas the Elche profile is oriented at 200°.

Unit	Density (Kgm^{-3})	References	Probable lithology	Source
Neogene/Quaternary sediments	2300	Torné & Banda, in press Docherty & Banda, in press	Clastics and shallow marine carbonates	Well log velocity data Seismic data I.G.M.E. published data
Undeformed Meseta and External Zones	2450	Torné & Banda, in press Docherty & Banda, in press	Shallow to deep marine carbonates	Well log velocity data and empirical relationship between P-wave velocity and density (Nafe & Drake 1961)
Internal Zones	2750	Torné & Banda, in press	Low to high pressure metamorphics	Seismic velocity studies and empirical relationship between P-wave velocity and density (Nafe & Drake 1961)
Iberian upper crust	2750	Torné & Banda, in press Banda et al., in press Banda & Ansorge (1980)	Deformed Hercynian Palaeozoic sediments and intrusives	Seismic velocity studies and empirical relationship between P-wave velocity and density (Nafe & Drake 1961)
Alboran upper crust	2750	Torné & Banda, in press Banda et al., in press Banda & Ansorge (1980)	Low to high pressure metamorphics similar to those of the Internal Zones	Seismic velocity studies and empirical relationship between P-wave velocity and density (Nafe & Drake 1961)
Lower crust	2900	Torné & Banda, in press Banda et al., in press Banda & Ansorge (1980)	Unsure as not incorporated into upper thrust sheets. Undifferentiated lower crust (Banda et al., in press)	Seismic velocity studies and empirical relationship between P-wave velocity and density (Nafe & Drake 1961)
Iberian upper mantle	3330	Torné & Banda, in press Banda et al., in press Banda & Ansorge (1980) Hatzfeld (1976)	'Normal' mantle (Torné & Banda, in press)	Seismic velocity studies and empirical relationship between P-wave velocity and density (Nafe & Drake 1961)

Table 4.2 Summary of density values used in modelling and the sources of the data.

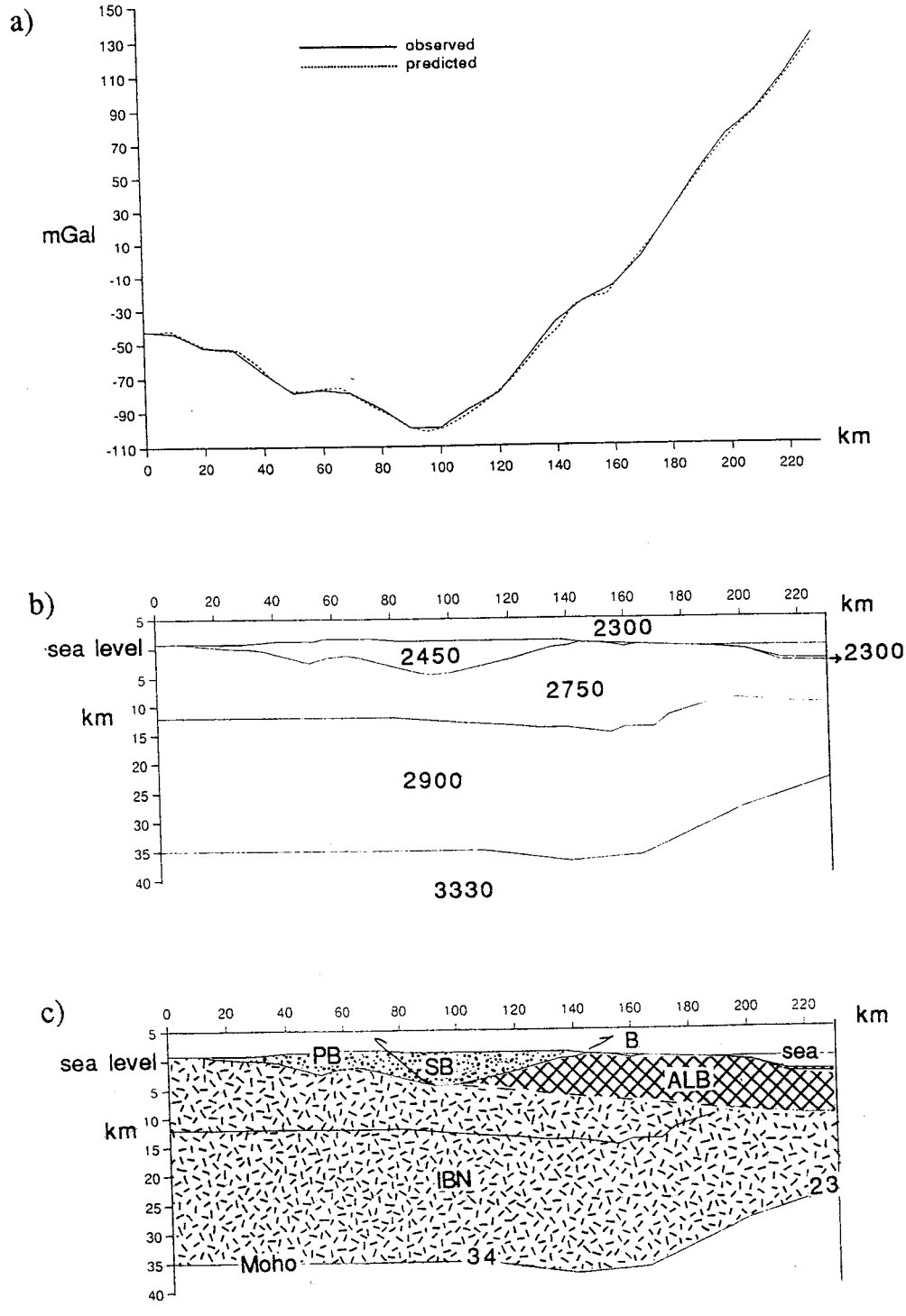


Fig 4.2.1. a) Comparison of the observed and predicted Bouger gravity anomalies for the Cazorla section.
b) Density distribution model for the Cazorla section used to generate the predicted gravity anomaly shown in a). The densities shown are in Kg /m^3.
c) Geological model for the Cazorla section. PB - Prebetic Zone, SB - Subbetic Zone, B - Tertiary/Quaternary basin, ALB - Alboran crust, IBN - Iberian crust. Values on Moho from Fig 4.1.1.

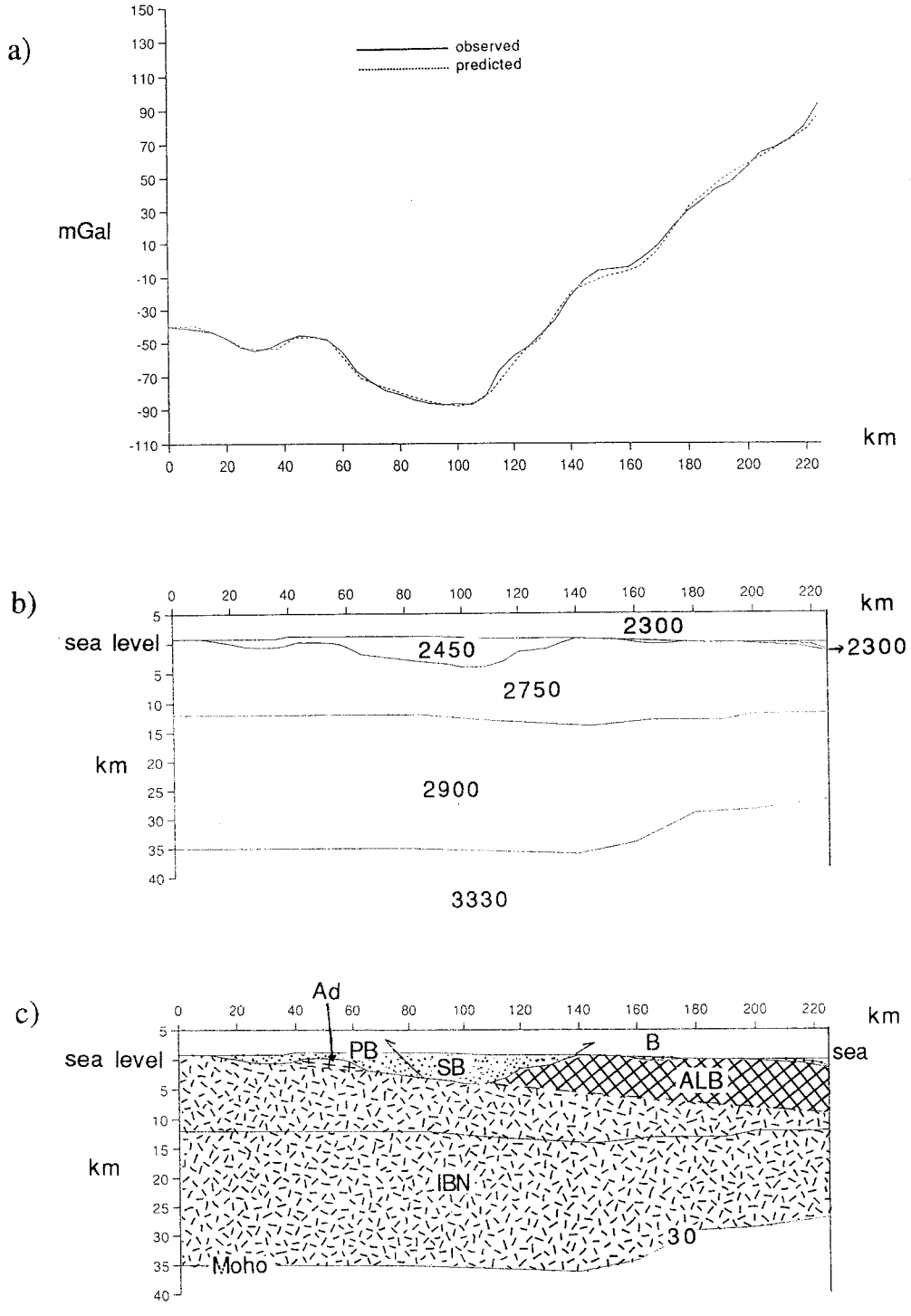


Fig 4.2.2. a) Comparison of the observed and predicted Bouger gravity anomalies for the Orcera section.
b) Density distribution model for the Orcera section used to generate the predicted gravity anomaly shown in a). The densities shown are in Kg /m^3.
c) Geological model for the Orcera section. PB - Prebetic Zone, SB - Subbetic Zone, B - Tertiary/Quaternary basin, ALB - Alboran crust, IBN - Iberian crust, Ad - Adamellite. Value on Moho from Fig 4.1.1.

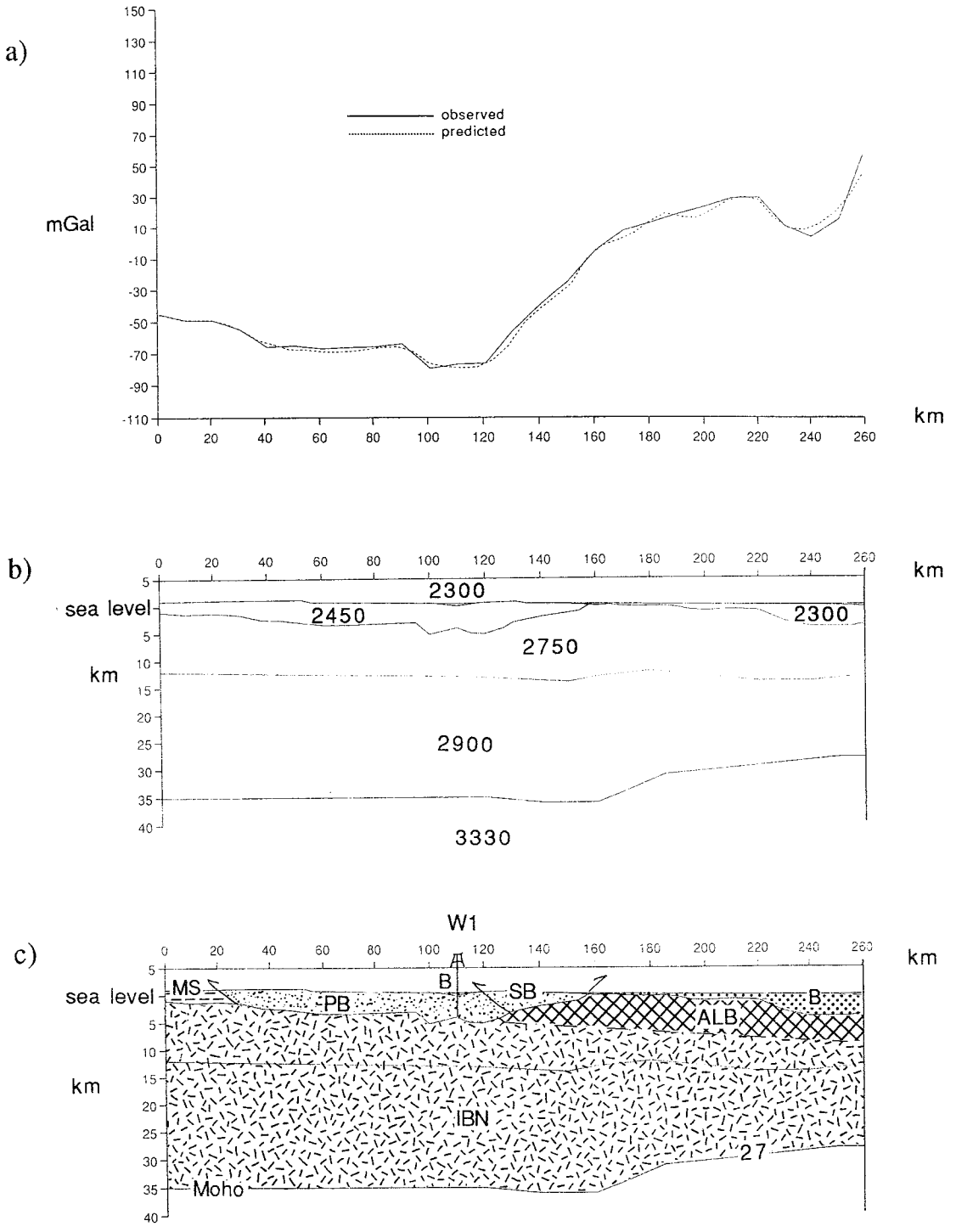


Fig 4.2.3. a) Comparison of the observed and predicted Bouger gravity anomalies for the Isso section.
b) Density distribution model for the Isso section used to generate the predicted gravity anomaly shown in a). The densities shown are in Kg /m^3.
c) Geological model for the Isso section. MS - Undeformed Mesozoic of the Meseta, PB - Prebetic Zone, SB - Subbetic Zone, B - Tertiary/Quaternary basin, ALB - Alboran crust, IBN - Iberian crust. Value on Moho from Fig 4.1.1. W1 - B.P. Rio Segura well.

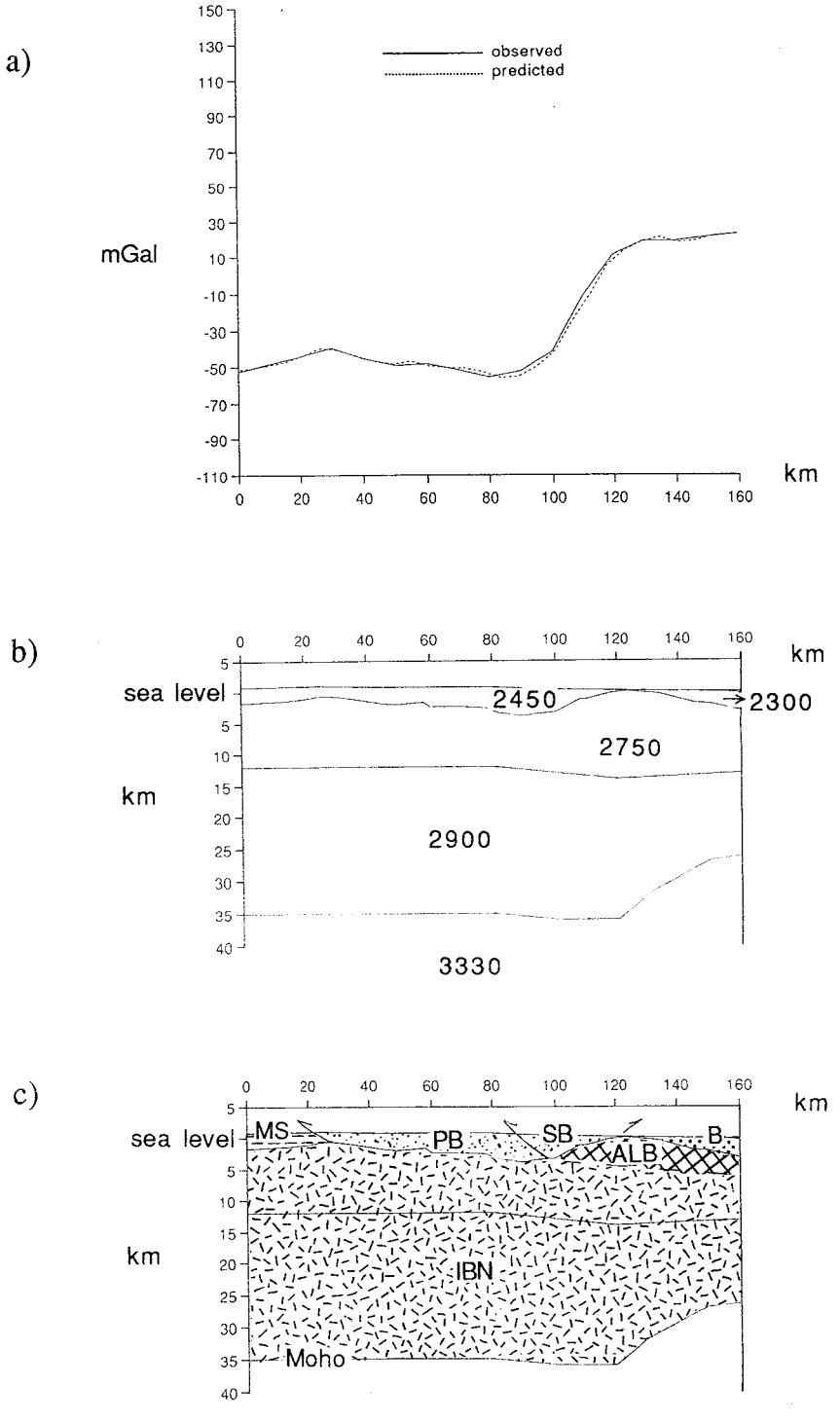


Fig 4.2.4. a) Comparison of the observed and predicted Bouger gravity anomalies for the Jumilla section.
b) Density distribution model for the Jumilla section used to generate the predicted gravity anomaly shown in a). The densities shown are in Kg /m^3.
c) Geological model for the Jumilla section. MS - Undeformed Mesozoic of the Meseta, PB - Prebetic Zone, SB - Subbetic Zone, B - Tertiary/Quaternary basin, ALB - Alboran crust, IBN - Iberian crust.

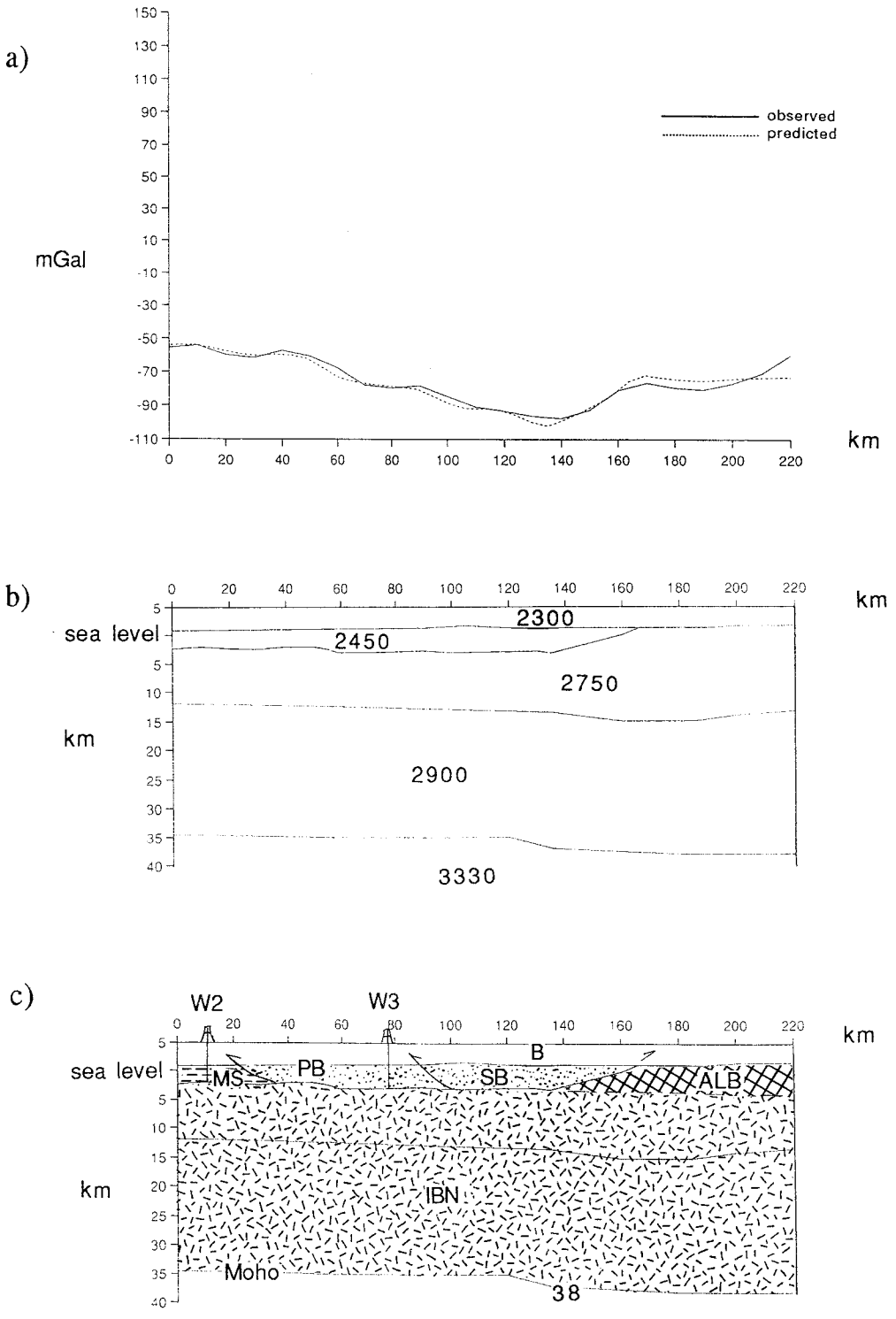


Fig 4.2.5. a) Comparison of the observed and predicted Bouger gravity anomalies for the Elche section.
b) Density distribution model for the Elche section used to generate the predicted gravity anomaly shown in a). The densities shown are in Kg /m^3.
c) Geological model for the Elche section. MS - Undeformed Mesozoic of the Meseta, PB - Prebetic Zone, SB - Subbetic Zone, B - Tertiary/Quaternary basin, ALB - Alboran crust, IBN - Iberian crust. Value on Moho from Fig 4.1.1. W2 - B.P. Salobral well, W3 - B.P. Segura 2 well.

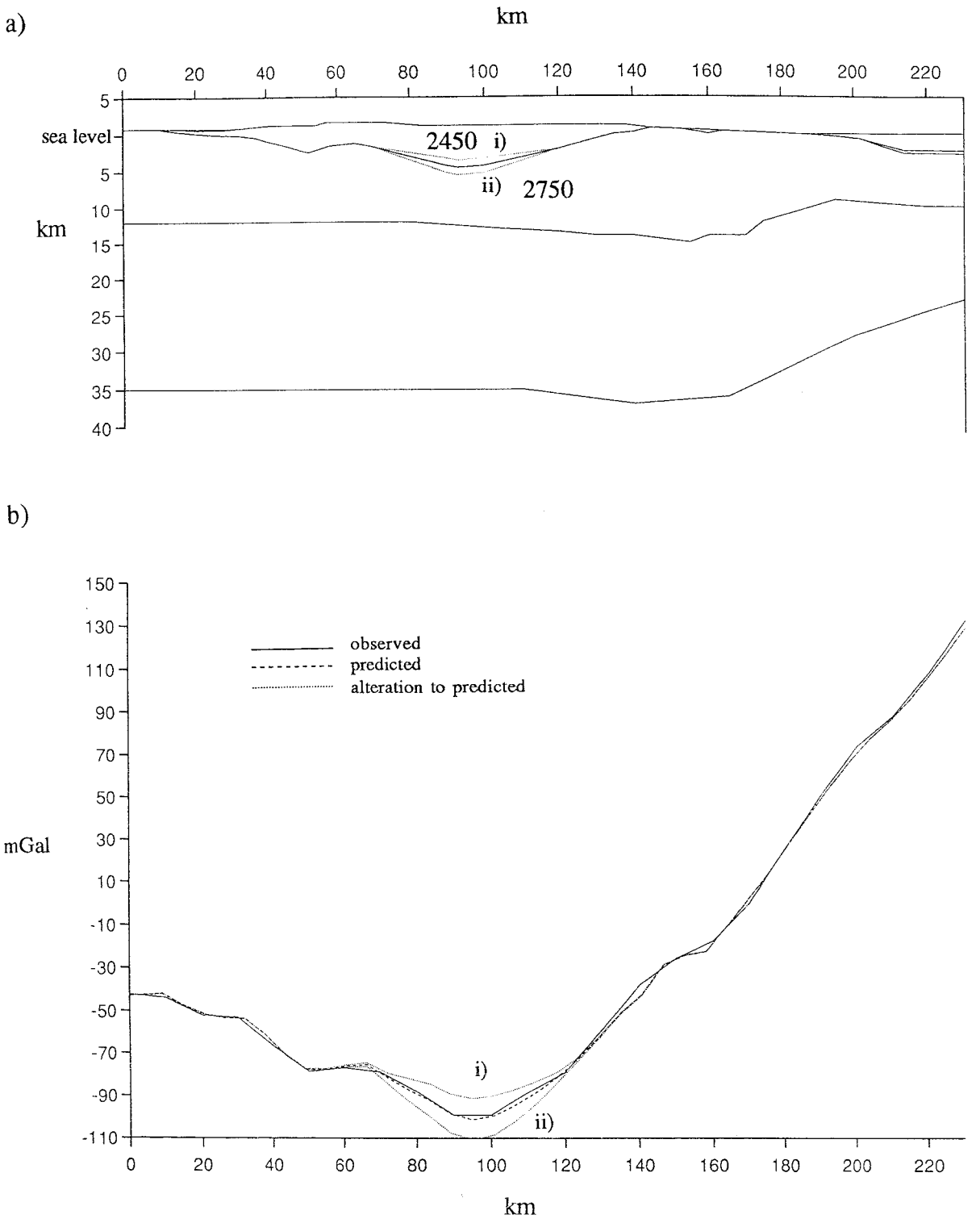


Fig 4.2.6. a) Density distribution model for the Cazorla section showing the alterations in the thickness of the Prebetic/Subbetic nappe pile. The gravity anomalies predicted from these alterations are shown in b). Densities shown are in Kg /m^3.
b) Observed and predicted Bouger gravity anomalies for the density distribution model shown in a). A decrease in the thickness of the Prebetic/Subbetic nappe pile, i), causes a decrease in the minimum value of the gravity anomaly whereas an increase in the thickness of the Prebetic/Subbetic nappe pile, ii), causes an increase in the minimum value of the gravity anomaly.

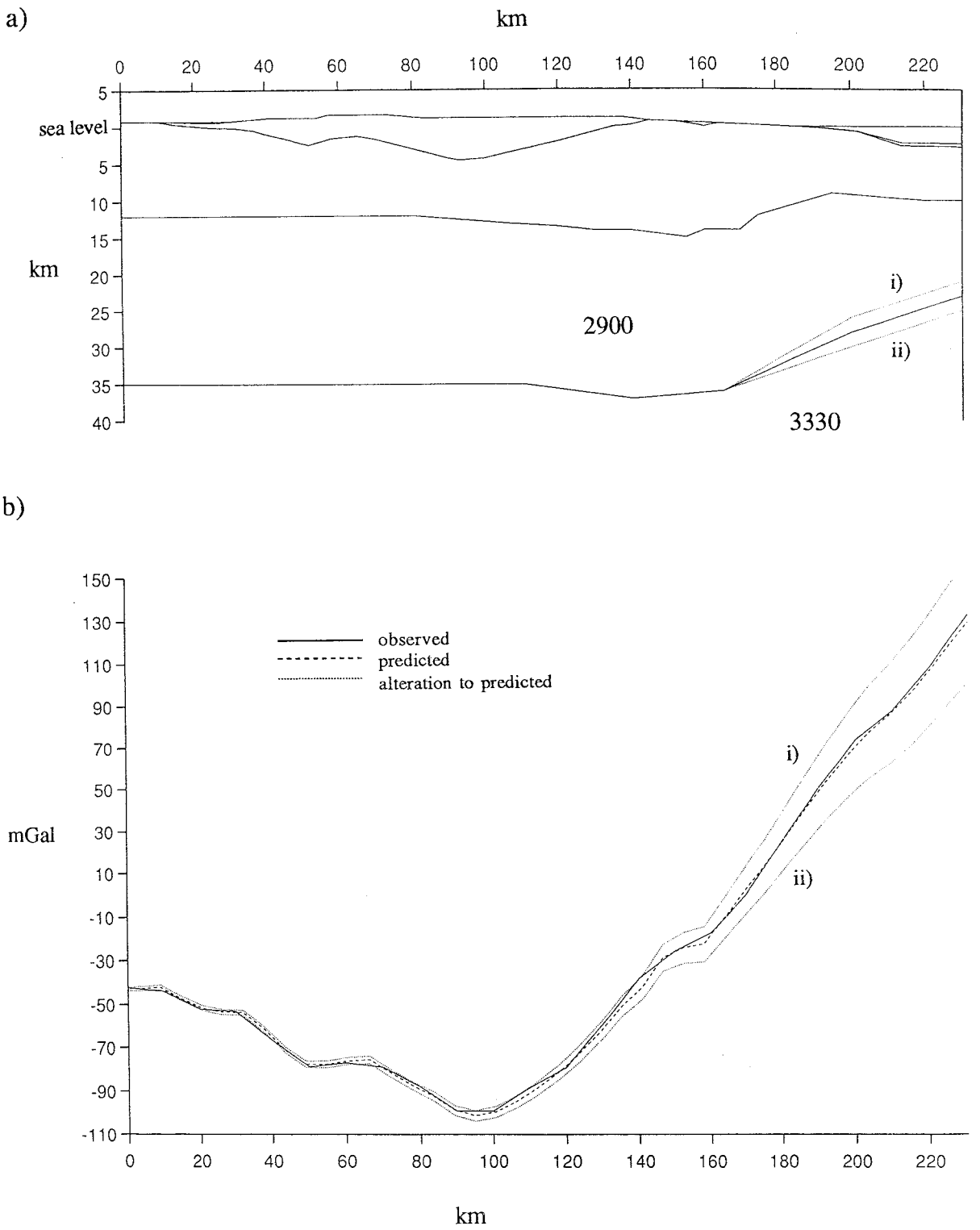


Fig 4.2.7. a) Density distribution model for the Cazorla section showing the alterations in the gradient of the Moho as it shallows to the SE. The gravity anomalies predicted from these alterations are shown in b). Densities shown are in Kg /m^3.
b) Observed and predicted Bouger gravity anomalies for the density distribution model shown in a). An increase in the gradient of the Moho, i), causes an increase in the value of the positive gradient of the gravity anomaly whereas a decrease in the gradient of the Moho, ii), causes a decrease in the value of the positive gradient of the gravity anomaly. Alteration of this long wavelength feature effects a larger portion of the predicted anomaly than that part directly above it.

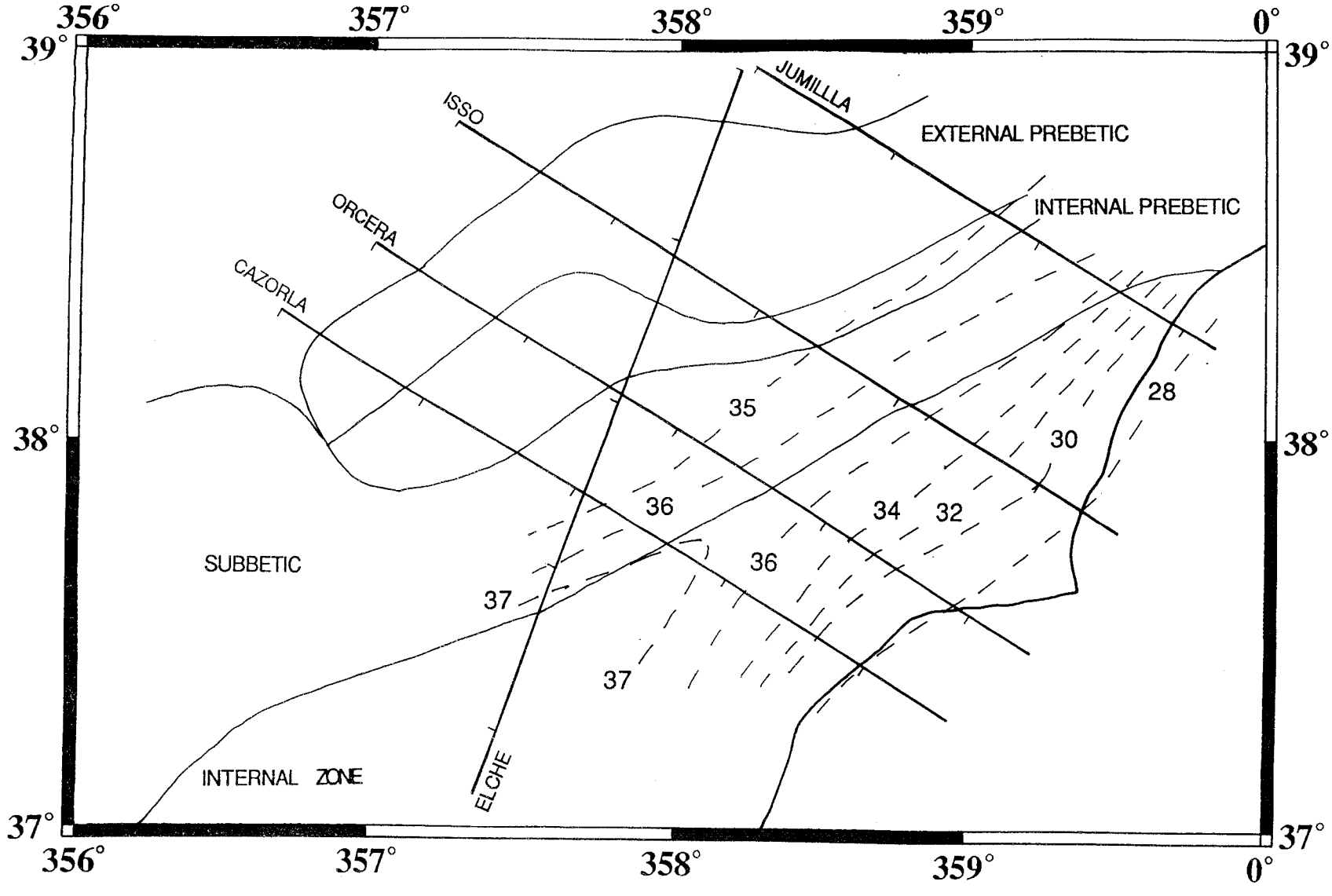


Fig 4.3.1. Contour plot of the depth of the Moho obtained from gravity modelling across the five profiles shown in Figs 4.2.1c)-5c). Values are in kilometres.

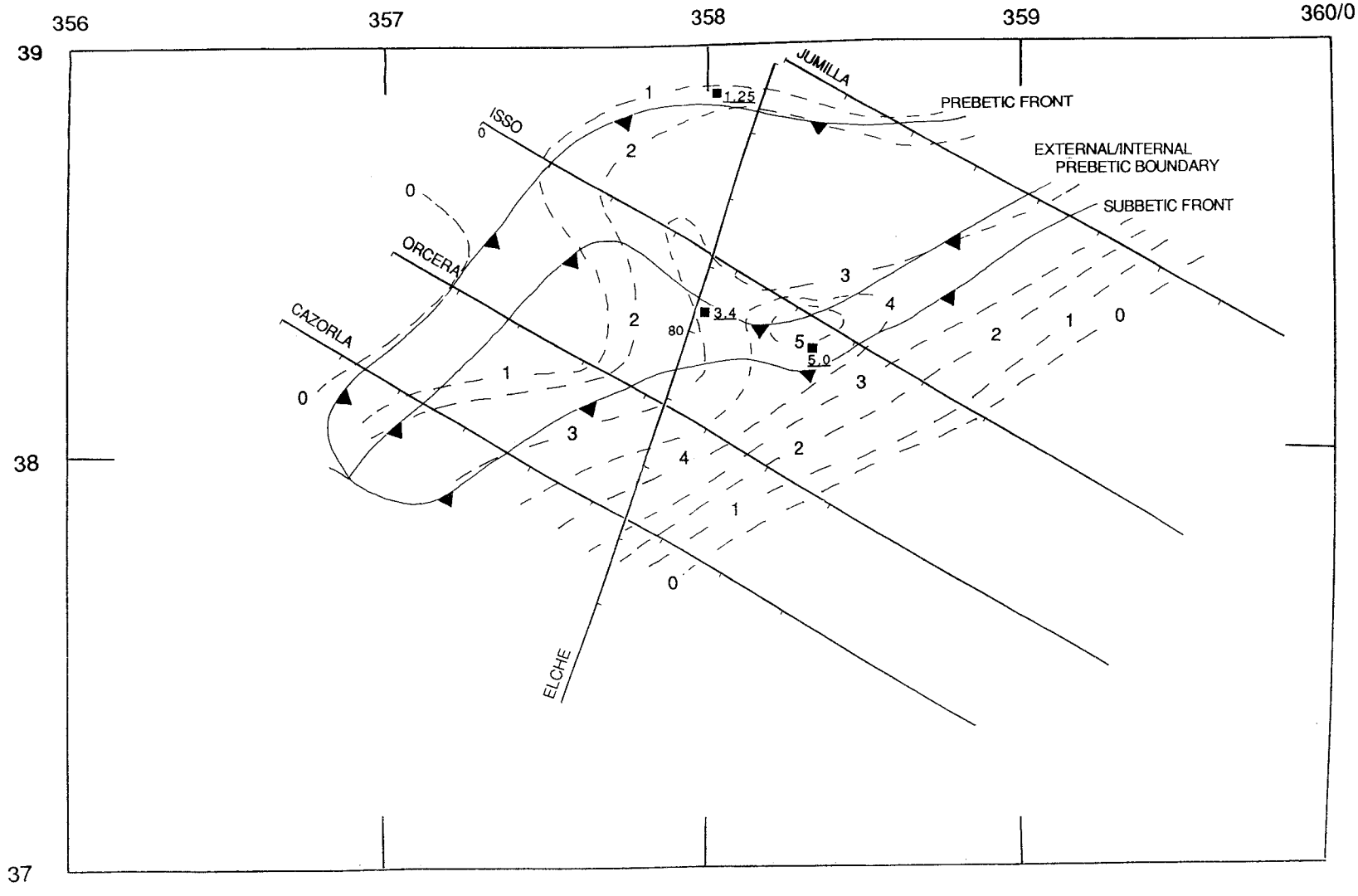


Fig 4.4.1. Contour plot of the basement elevation obtained from gravity modelling across the five profiles shown in Figs 4.2.1c)-5c). Values are in kilometres. Black squares represent the localities of B.P. wells and the actual basement elevation or that predicted from well-logs.

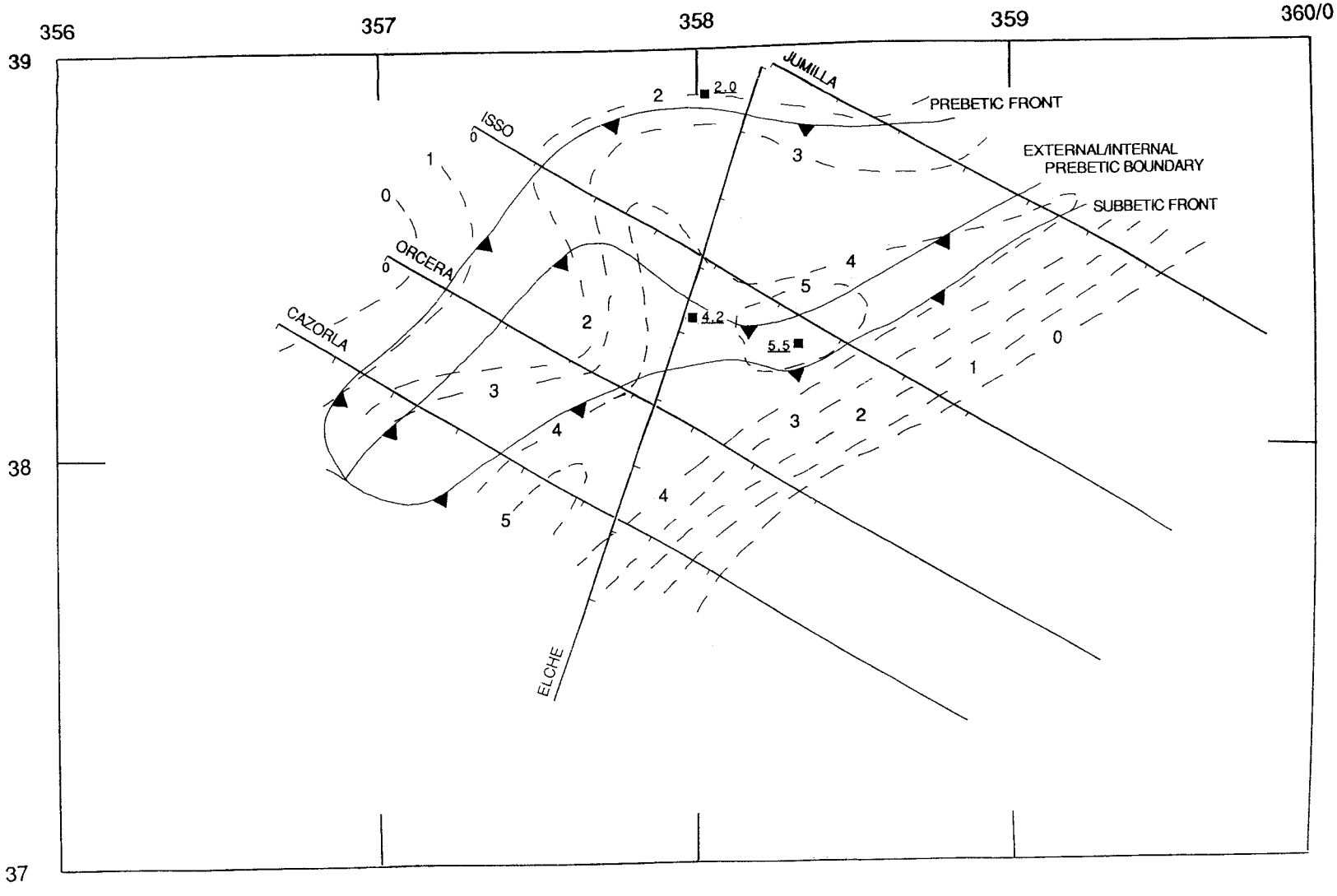


Fig 4.4.2. Contour plot of the thickness of the Prebetic/Subbetic nappe pile obtained from gravity modelling across the five profiles shown in Figs 4.2.1c)-5c). Values are in kilometres. Black squares represent the localities of B.P. wells and the actual thickness or that predicted from well-logs.

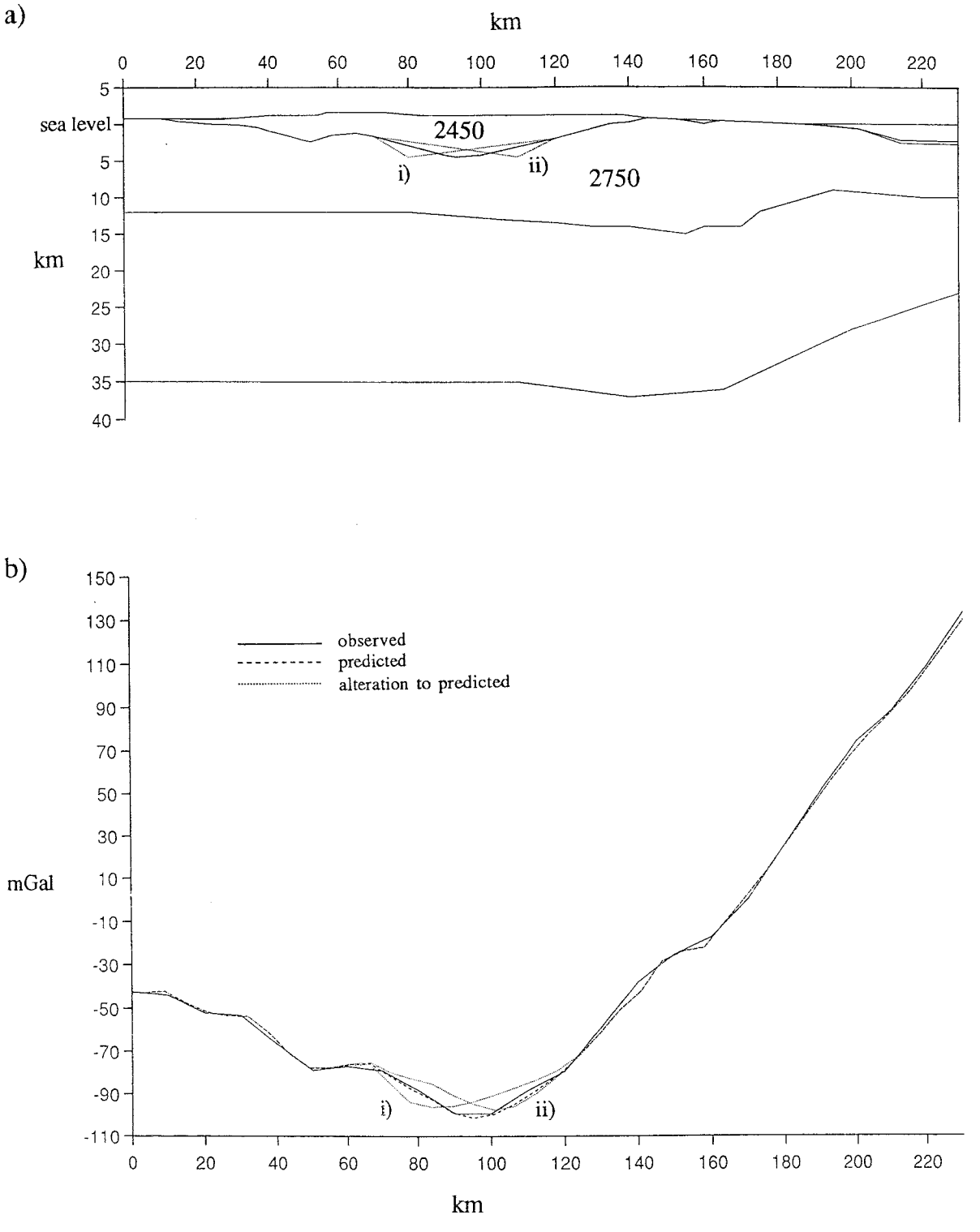


Fig 4.4.3. a) Density distribution model for the Cazorla section showing the alterations in the position of the nose of the Internal Zone wedge. The gravity anomalies predicted from these alterations are shown in b). Densities shown are in Kg /m^3.
b) Observed and predicted Bouger gravity anomalies for the density distribution model shown in a). Translation of the nose of the Internal Zone wedge towards the foreland, i), causes a corresponding shift in the minimum value of the gravity anomaly towards the foreland whereas translation of the nose of the Internal Zone wedge towards the hinterland, ii), causes a corresponding shift in the minimum value of the gravity anomaly towards the hinterland.

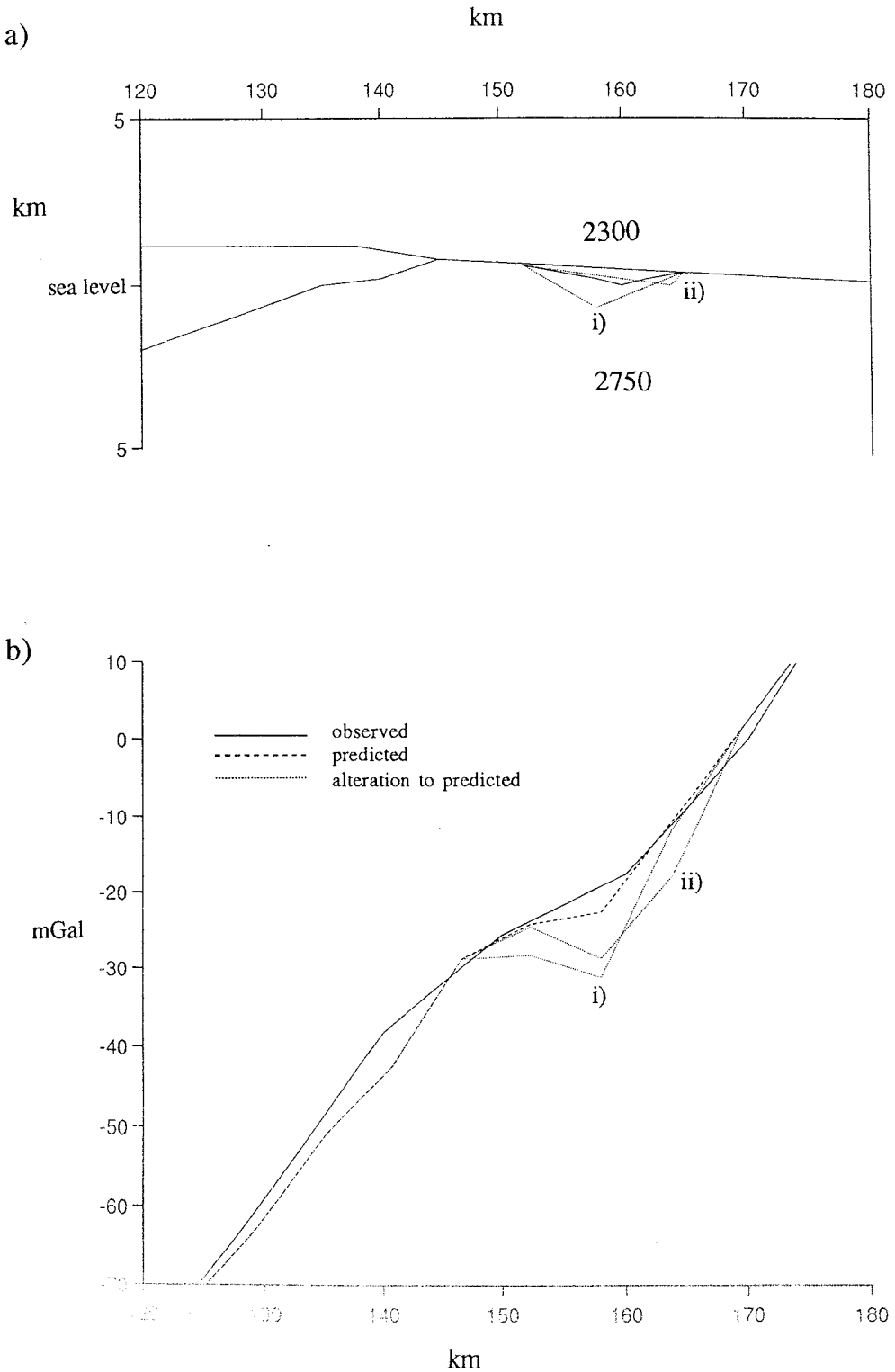


Fig 4.4.4. a) Density distribution model for the Cazoria section showing the alterations in the depth and geometry of a Tertiary basin. The gravity anomalies predicted from these alterations are shown in b). Densities shown are in Kg /m^3.
b) Observed and predicted Bouger gravity anomalies for the density distribution model shown in a). An alteration which increases the depth of the Tertiary basin, i), causes a corresponding decrease in the value of the gravity anomaly for this feature whereas displacement of the deepest part of the basin towards the hinterland, ii), causes a corresponding displacement of the gravity anomaly for this feature towards the hinterland.

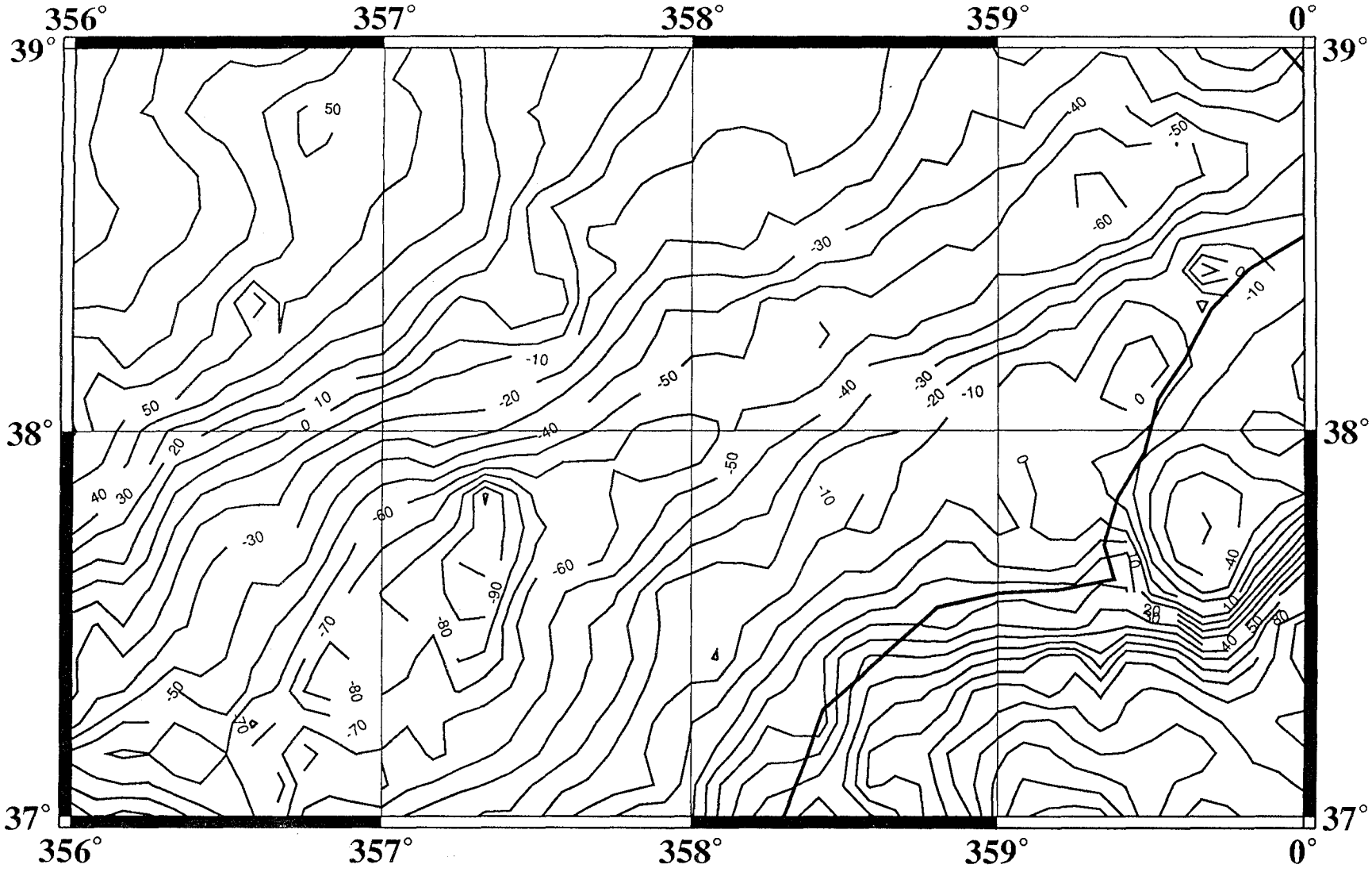


Fig 4.4.5. Contour map of the Bouger gravity anomaly for the eastern Betic Cordillera after filtering of the longer wavelength (>80km) features. Features previously described for the upper crust from the results of the gravity modelling are also indicated from this filtered gravity data. E.g. the adamellite perturbation (357.5°,38.4°), the decreasing gradient of the basement slope from SW to NE (widening of contours to NE) and the NW dip of the Internal Zone (basement) /Subbetic Zone contact (e.g. positive filtered gravity gradient between 358° 38° and 358.5° 37.5°)

Chapter 5

CHAPTER 5

ESTIMATES OF SHORTENING ACROSS THE PREBETIC OROGEN

5.1. Introduction

Reconstruction of the initial geometry of the Prebetic Arc is necessary to increase our understanding of its structural history and to ascertain why it deformed in the particular manner described in the previous chapters. The Prebetic Zone has been hypothesized to have an originally arcuate geometry in the Mesozoic (Garcia-Hernandez et al. 1980). This geometry, however, is based on the facies distribution in the Prebetic Zone and may be biased by its present shape. Hence, a method of reconstructing this region quantitatively is required to produce a more detailed and accurate original geometry. Restoration of a series of balanced cross-sections, located at intervals from west to east, constructed parallel to the observed tectonic transport directions may produce a fairly well constrained reconstruction of the Prebetic Arc. The construction of balanced sections allows the amount of shortening across an orogen to be estimated whilst also providing useful controls on the structure at depth.

A balanced section must satisfactorily incorporate all geophysical, borehole and surface data. This information may be extrapolated from locations off the line of section down-plunge on to the section (Elliott 1983). A number of basic concepts for the structural evolution and predicted thrust geometries within a orogenic belt have been compiled after analysis of several orogens, predominantly the Canadian Rockies, the Appalachians, the Alps and the Moine thrust belt of Scotland, which have then been used to constrain the structural geometries allowable in a balanced section (e.g.s Dahlstrom 1969,1970, Boyer & Elliott 1982, Butler 1987). Production of a valid cross-section relies on the fulfilment of a number of conditions:

i) The section must be constructed parallel to the tectonic transport.

ii) Only 2-D plane strain affected the section and no strain occurred normal to it. The direction of tectonic transport may be ascertained from analysis of kinematic vectors. This becomes more complicated if the transport direction varies through time.

iii) A pin line must be constructed at a point where there is a known amount of strain or displacement. Construction of a pin line where there is an unknown amount of strain or displacement may produce a viable but not necessarily correct section which is useful for minimum displacement calculations.

iv) The sequence of the thrusting must be known i.e. by foreland and/or hinterland propagation, together with out-of-sequence deformation (Butler 1987).

v) The area of the section must remain constant at all stages of restoration and balancing as plane strain is assumed.

There are two methods by which balanced sections may be produced:

a) Bed-length balancing assumes the conservation of the lengths and thicknesses of the beds during deformation.

b) Area balancing assumes the conservation of the cross-sectional area during deformation.

It is important to remember that a balanced section, although a viable interpretation of the subsurface structure, is a non-unique solution. Errors are inherent in the calculation of the degree of shortening experienced along the section due to the partial fulfilment in practice of the five conditions listed above. Initial uncertainties in the thickness of the stratigraphic sequence cause inaccuracies in the structure and

calculated shortening of a section. Hossack (1979) calculated that a 50% underestimate of the thickness of the undeformed sequence of the Etnedal nappes of the southern Norwegian Calidonides caused only a 10% increase in the amount of shortening. Also, construction of a section using an inexact sequence of thrusting may give rise to invalid geometries and hence an erroneous calculation of the amount of shortening (Butler 1987). The post deformation cross-sectional area may be reduced with respect to the initial cross-sectional area by compaction or pressure solution. For example slates may decrease in volume by 10-20% during finite strain (Ramsey & Wood 1973). Compaction may occur during lithification, although this also occurs in the measured sequences used to compile the stratigraphic thicknesses, or during the deformation event itself, in which case a volume decrease of less than 10% has been predicted from various studies (Hossack 1979). Development of a pressure solution cleavage may cause a 20-30% contraction normal to the cleavage. However, if the dissolved material is redeposited locally, the overall volume will remain approximately constant. Variation in the orientation of the strain, both spatially and temporally, is typical of non-linear orogenic belts and results in material moving in and out of the plane of section, thereby causing a increase or decrease in the cross-sectional area of the section.

In the Prebetic Zone, the existence of a component of non-plane strain is probably the most important source of error. Around the Alcaraz Antitaxis there is a component of strike-parallel extension resulting from the divergence in transport directions; the NW Trending Limb and Cenajo Syntaxis both show temporal overprinting of tectonic transport vectors due to strain partitioning across the Socovos Fault and convergent deformation and the NE Trending Limb shows a anticlockwise swing in its tectonic transport direction towards the foreland.

Previous workers in the Prebetic Zone have attempted to balance structural sections drawn from the stable Iberian margin to the Internal Prebetics and further into the Subbetic Zone (Fig 5.1.1.). Guezou et al. (1991) present two "semi-balanced" sections, orientated at 100° and 110/115°, across the NE Trending Limb. These sections are arbitrarily cut-off at sea-level and hence the validity of the more complicated duplex structures within the sections e.g. the Embalse del Guadalquivir duplex, cannot be tested rigourously. Banks & Warburton (1991) present a structural cross-section, oriented at 135°-150°, which cuts across the Alcaraz Antitaxis and extends through the Internal Prebetics and into the Subbetic Zone. This section, although it is sub-parallel to the tectonic transport direction, may exhibit inaccuracies in its geometry and shortening as it crosses the complex hinge area of the antitaxis in which there is a component of strike-parallel extension and small block rotation and oblique backthrusting have been described (section 2.2.1.2).

5.2. Balanced sections in 2-D

Three sections, at various locations across the External Prebetics, were balanced and restored to provide a more detailed insight into the subsurface structure and to allow a comparison of the shortening around the Prebetic Arc. Bed-length balancing, as opposed to area balancing, was chosen as the most appropriate method in this region of brittle deformation. After analysis of the pattern of tectonic transport around the arc, three sections were chosen that were oriented parallel to the local transport direction. Two sections, oriented at 120°, were located to the west and to the east of the main Socovos Fault, whilst the third section,

oriented at 200°, was located in the NW Trending Limb where there is local shortening approximately normal to the overall northwestward tectonic transport direction (Fig 5.1.1). These sections lie along three of the profiles which have undergone detailed gravity modelling thus providing a constraint on the depth to the basement in areas were there is a paucity of seismic and well-log data (chapter 4).

The original stratigraphic sequence and thicknesses were compiled from data published by I.G.M.E., the Instituto Geologica y Minero de España, combined with field observations. The balanced sections themselves, were constructed using the thrust geometries, branch-line patterns and thrust sequences observed and deduced from field work and published geological maps, both along the section and from localities off-section (Hossack 1983). These were then extrapolated onto the section to provide extra information, especially in the parts of the sections covered by Tertiary or Quaternary basins. The pin lines for the Cazorla and Jumilla sections were located on the undeformed or displaced Meseta. The short Elche section is located within the NW Trending Limb, which has undergone later shortening approximately normal to the earlier more hinterland transport direction seen in the Elche section. The Elche section does not fulfil the condition 5.1.ii) in that there is some component of non-plane strain but construction of this section is useful to provide a minimum shortening estimate. Therefore a `pseudo´ pin line, which has undergone later displacement itself, is invoked to allow reconstruction of the section. It was not considered applicable to extend this section northeastwards to the stable Meseta as there is a marked change in the tectonic transport direction towards the foreland, causing complex patterns of 3-D strain (Fig 2.2).

5.2.1. The Cazorla section

The Cazorla balanced section, drawn between GR 66224017 and GR 68523888 and oriented at 120°, traverses the External Prebetics and the more foreland section of the Internal Prebetics of the NE Trending Limb and is shown in Fig 5.2.1.1. The initial stratigraphic sequence in the External Prebetics is dominated by Middle Jurassic dolomite capped by a thin sequence of Upper Jurassic limestone and Barremian marl (Fig 5.2.1.2). These show lateral discontinuities and gaps in stratigraphy, which may be due to deposition in shallow grabens formed during Mesozoic continental rifting. The Upper Jurassic units appear to be present in four locations regularly spaced at 12-15 km intervals along the section which indicates a regular spacing of the graben extensional faults. Although these original faults have now been overprinted to some extent by the Miocene compressive deformation, evidence of previous extensional faulting remains. The Internal Prebetics of this section shows a thicker and more complete Mesozoic sequence and thin early-middle Miocene units (Fig 5.2.1.2).

The deformational style displayed in this section is predominantly that of a foreland verging imbricate stack with a majority of the branch lines within the sole thrust. This section has undergone sequential thrusting to the NW and also minor backthrusting to the SE. Existing discontinuities such as the External/Internal Prebetic boundary may have been reused. The backthrusting is associated with backsteepening of the hinterland thrust slices as deformation continued towards the foreland. Due to the significant relief exhibited along road sections in this area, it is possible to constrain to some extent the dip of the thrust planes at depth.

The Prebetic Front is weakly emergent with only small amounts of displacement occurring on the frontal thrusts, and the Messinian marl of the easternmost part of the Guadalquivir basin is incorporated into these frontal thrust sheets. The frontal imbricate thrust slices show a gradual shortening of their length towards the foreland coincident with the thinning of the stratigraphic sequence and the absence of the incompetent Barremian marl which greatly facilitated overthrusting (Goff & Wiltschko 1992). A passive-roof duplex developed within the section, possibly initiated due to a temporary sticking of the orogenic front in an area in which the Barremian marl was absent (Figs 2.2.1.8/9). The deformational sequence involved in the formation of this passive-roof duplex is shown in Fig 5.2.1.3.

The main décollement horizon of the Cazorla section is located within the evaporite-rich Triassic unit to the SE of the section and is deduced to ramp upwards to the Triassic/Jurassic boundary which became the main décollement horizon for the thrust slices in the NW of the section. Minor décollements develop at the base of the Oxfordian limestone and at the base of, and within, the Barremian marl. These minor décollements are displayed in the roof thrust and higher thrust sheets of the passive-roof duplex and in the backthrusting across the External/Internal Prebetic boundary. The décollement horizon used is strongly dependent on the highly variable Upper Jurassic and Lower Cretaceous stratigraphy. A middle Miocene (Seravallian?) minor décollement horizon is present in the hinterland part of the section within the Internal Prebetics.

5.2.2. The Elche section

The Elche balanced section, drawn between GR 74984430 and GR 74104214 and oriented at 200° only traverses the part of the External Prebetics of the NW Trending Limb where the tectonic transport direction is to the NNE (Fig 5.2.2.1.). Changes in the thrust transport direction further to the foreland and hinterland, prevent the extension of this balanced section to the stable Meseta or to include part of the Internal Prebetics as the cross-sectional area would not be preserved and the fundamental assumption of plane strain in a balanced section would be unfulfilled. The more northern part of the Elche section consists predominantly of Jurassic shelf deposits with discontinuous deposits of the Barremian/Aptian Weald Facies (Garcia-Hernandez et al. 1980). The discontinuous nature of the Albian deposits is supported by Miocene sediments shown to be lying unconformably on Jurassic units. The southern part of the section comprises a thicker and more complete Cretaceous sequence from the Albian onwards (Fig 5.2.2.2.). This coincides with the development of listric extensional faults in the more basinward parts of the Prebetic Zone and this increase in stretching is shown in some of the tectonic subsidence profiles from the Internal Prebetics (section 3.2.2). Intramontane Tertiary basins are ubiquitous throughout this section. The Post-deformational Tertiary deposits, however, are only shown in the balanced section and have been removed from the restored section to aid clarity.

The sequence of thrusting in this section is predominantly to the NNE with episodes of foreland propagating backthrusting (Fig 5.2.2.3). The backthrusts, formed at the thrust front, cause the development of a blind

front geometry (Price 1981, Vann et al. 1986) and the formation of a passive-roof duplex (Banks & Warburton 1986). Where there is convergence of the differing polarities of thrusting a triangle zone is formed, between two thrusts with the same basal detachment and with opposing vergence (McClay 1991) (stage 9 of Fig 5.2.2.3.) and where there is a divergence of the thrusting directions, there is a jacking-up of a thrust slice (stage 13). In this case a branch line that was initially within the sole thrust has been displaced upwards along a new thrust and the thrust slice has an overall synclinal form. Within both the hinterland and foreland dipping thrust slices small duplexes are formed with branching at high structural levels, predominantly within the footwall of previous thrusts. These still show foreland progression of deformation and are facilitated by the development of minor décollement horizons, also observed in the Jumilla section. The Socovos wrench fault is located at the very SSW of the Elche section. The detailed structure of this feature and the juxtaposed Internal Prebetics, however, cannot be included in, or ascertained from, this section as the major movement along the Socovos fault and within the Internal Prebetics in this area is approximately normal to the plane of the Elche section.

The Elche section also exhibits a main décollement horizon located within the Triassic, with lesser amounts of displacement locally along the Triassic/Jurassic interface. Other important décollement horizons have developed at the base of the Middle Jurassic and the Barremian/Aptian Weald facies. Minor décollement horizons are present locally within the Weald facies and at the base of, and within, the lower to middle Seravallian. Some individual thrusts have well developed staircase geometry with flats present in several décollement horizons.

5.2.3. The Jumilla section

The Jumilla balanced section, drawn between GR 79434663 and GR 83884432 and oriented at 120°, traverses the External Prebetics and the most foreland part of the Internal Prebetics to the east of the arc and is shown in Fig 5.2.3.1. The External Prebetics of the Jumilla section consist of a thicker and more complete Mesozoic sequence than that of the Cazorla or Elche sections (Fig 5.2.3.2.). The discontinuous lateral deposition of the upper Jurassic and lower Cretaceous in the Cazorla area is not exhibited within this section. The Jumilla stratigraphic sequence also consists of basinal Tertiary deposits which are preferentially preserved within the footwall of thrusts. Both pre-deformational Oligocene and early Miocene, and syn- to post-deformational middle-late Miocene are present. The stratigraphic sequence does not vary dramatically across the Internal and External Prebetic boundary in this section as it does in the Cazorla section. This may be due to more uniform subsidence occurring in the area of the Jumilla section. The SE of the Jumilla section, however, shows a thicker Cretaceous sequence from the Albian onwards associated with the development of listric faults in the more basinward parts of the External Prebetics.

The structure of this section is more difficult to interpret than the Cazorla and Elche sections due to the lower relief of the area and the presence of large intramontane Neogene and Quaternary basins which cause discontinuous exposure of the deformed sequence, especially to the SE of the section. Structural details, such as the location of branch points and minor décollement horizons and fold axes, have been extrapolated onto the section from adjacent exposures of the deformed Mesozoic

sequence (Elliott 1983, Hossack 1983). The post-deformational deposits have been removed from the section to aid clarity.

The sequence of thrusting in this section is predominantly foreland propagating with occasional development of backthrusting as the mode of frontal accretion and out-of-sequence thrusting. The out-of-sequence thrusting, causes a thickening of the orogenic wedge and may occur as the wedge deforms internally to stabilise itself with concurrent rapid frontal accretion. To the foreland of this section is a Mesozoic shelf sequence with relatively thick, evaporite-rich Triassic, which lacks shallow or exposed basement, thereby facilitating rapid frontal accretion. Fig 5.2.3.2 shows the sequence of thrusting/backthrusting (no.s 10-14) between kilometre 40 and kilometre 50 of the section which cause the formation of a blind front geometry (Price 1981, Vann et al. 1986), a passive-roof duplex (Banks & Warburton 1986) and a triangle zone (McClay 1991), bounded by oppositely verging thrusts, in which the Mesozoic stratigraphy is at regional elevation although it has undergone significant displacement to the NW. The deformation in the Jumilla region shows a greater complexity, both within the plane of the section and in 3-D, than the Cazorla section. The Jumilla section shows more folding within the thrust sheets and closely associated with the thrust faults themselves, which is facilitated by the increased component of incompetent mud and marl in this section compared to the Cazorla section. There is increased branching of the thrusts at high structural levels giving rise to small duplexes of thrust slices with an incomplete stratigraphic sequence due to the development of minor décollement horizons within the more muddy and marly units. There appears to be greater displacement along the individual thrust faults to the NW of the section and hence a repetition of more stratigraphic units. The Prebetic Front in this part of the Prebetic Zone is buried and

transfers its displacement to the foreland out of the Prebetic Zone s.s. into a broad zone of low strain exhibited as gentle folding of the Jurassic and Cretaceous sequence.

Within the Jumilla Section the main décollement horizon is, again, located within the evaporite-rich Triassic. At the blind Prebetic Front, the main décollement horizon ramps up to the Triassic/Jurassic interface, although there is a lesser amount of subsequent displacement. An important décollement horizon is developed higher up the stratigraphic sequence in the Albian Utrillas Facies. Other minor décollement horizons developed locally at the base of the Oxfordian and the Barremian/Aptian Weald Facies and at the base of and within the Seravallian/Tortonian.

5.2.4. Correlation of décollement horizons

Due to the wide range in lithology and thickness across the Prebetic Zone many décollement horizons are exploited during compression and examples of these have been described in 5.2.1-3 for the three balanced sections. Fig 5.2.4.1. shows the correlation between five representative stratigraphic sections which have been compiled from the balanced sections. Sections **Cazorla 1** and **Cazorla 2** represent the Internal and External Prebetics of the NE Trending Limb respectively; the section **Elche** represents the NW Trending Limb, whilst the sections **Jumilla 1** and **Jumilla 2** represent the more foreland and hinterland External Prebetics respectively, to the east of the Cenajo Syntaxis. The locations of these stratigraphic sections are shown in Fig 5.2.4.2. The main sole thrust is located within the Triassic, possibly in the Keuper facies with its high evaporite and shale content. The more foreland Cazorla 2 and Jumilla 1

sections show the final ramping of this sole thrust through the Triassic onto the the Triassic/Jurassic interface. The timing and location of this ramping may be ascertained from field evidence and may be correlated with the propagation of the main wave of deformation (section 2.3.). In both the Cazorla and Jumilla balanced sections the ramping is inferred to be Tortonian-Early Messinian in age and appears to have occurred simultaneously. The presence of ramping may also be inferred along a line of synchronous deformation between these two sections and situated to the foreland of the zone where Triassic rocks are exposed at the surface (the Tranco Zone) (Fig. 5.2.4.3.). This highlights the linked, 3-D nature of the propagating sole thrust (Prebetic Front) and again indicates the thin-skinned nature of the intervening Socovos Fault. Correlation with the location of the wave of deformation (section 2.3) indicates that the probable timing of this deformation was Late Tortonian/Messinian. The ramping up to a higher décollement horizon may be due to a decrease in the thickness or evaporite content of the Triassic in the area adjacent to the emergent Palaeozoic massif. This decrease in the thickness of the thrust slices may facilitate the greater amount of shortening exhibited in the NE Trending Limb (section 5.3).

Within the Jurassic sequence, décollements are developed in the Middle and Upper Jurassic of the more easterly Elche and Jumilla sections as they contain an increasing ratio of limestone to recrystallised dolomite. The base of the Cretaceous sequence is consistently exploited as a décollement horizon across both the External and Internal Prebetics. After the break in sedimentation in the uppermost Jurassic, initial deposition in the Cretaceous shows an increased component of marl to the west and conglomerate, sandstone and mud of the Weald facies to the east which would favour the development of décollement horizons. Within the

Cretaceous sequence, décollements are present in the continentally-derived Weald and Utrillas facies which are well-developed in the more easterly Elche and Jumilla sections.

Minor décollement horizons develop locally within the predominantly marl/limestone intramontane basin deposits of the middle to upper Miocene, where it is present.

5.3. Estimates of shortening

5.3.1. Method

5.3.1.1. Bed length balancing

The orogenic contraction and absolute shortening experienced by each of the three sections may be quantified using the standard equation for strain, ε, (Boyer & Elliott 1982):

$$\varepsilon=(l_1-l_0)/l_0$$

where l_1 is the final length of the section and l_0 is the original length of the section i.e. the restored length. This calculation, based on the construction of a non-unique balanced section, assumes that only plane strain occurs along the section. However carefully the position of the section to balance is chosen, the 3-D nature of interlinked thrust belts usually causes a certain amount of movement in and out of the plane of section producing inaccuracies in the estimation of orogenic contraction (section 5.1). Strain calculated along a line of section with a known deviation away from the tectonic transport direction may be corrected to a strain parallel to the tectonic transport. Deviations of 10° or less produce very small errors in the estimate of strain (Cooper 1983). Equally valid

sections drawn in the same location, but displaying different thrust geometries, may indicate slightly differing amounts of shortening.

5.3.1.2. Cumulative displacement-distance diagram

The cumulative displacement-distance diagram of Chapman & Williams (1984) can also be used, as an additional method to bed-length balancing, in estimating the orogenic contraction of a foreland thrust belt where all the contraction is accommodated above a single décollement horizon. The reference point is taken as the branch point of the first imbricate thrust to the foreland and the individual fault displacements are measured and then added progressively for each imbricate fault to calculate the cumulative displacement. The structurally lowest stratigraphic horizon, closest to the décollement, is used if possible to record the displacement as this records the total displacement across that fault even if splaying occurred at a higher structural level. Layer-parallel shortening cannot be accounted for by this method.

The cumulative displacement, Σd, is plotted against the distance from the reference point, l, using the same scale (Fig 5.3.1.1.). The strain, ε, is given by:

$$\varepsilon = \Sigma d/(l+\Sigma d)$$

and from the relationship between the strain and the gradient, $\Sigma d/l$ or $\tan \vartheta$, where ϑ is the angle between the plotted line and the distance axis.

$$\varepsilon = \tan \vartheta/(1+ \tan \vartheta)$$

The amount of contraction obtained from this method parallels the décollement horizon and hence may be slightly greater than the amount of shortening calculated along the horizontal by bed length balancing.

5.3.1.3. Errors in calculation.

In the Prebetic Zone, the locations of the sections to be balanced were specifically chosen away from the Alcaraz Antitaxis and Cenajo syntaxis where there is a component of non-plane strain to minimise any errors inherent in construction of a section which underwent non-plane strain.

The main source of error in the three sections presented is the basement elevation. There is a sparsity of available seismic reflection and well-log data for the western External Prebetics. The depth to basement around the Prebetic Arc was ascertained using the gravity modelling techniques described in Chapter 4 and shown in Fig 4.4.1. As this technique relies on the construction of a non-unique physical model for the section across the Betic Cordillera using available geophysical and geological data, significant errors are unavoidably introduced. The effects of alteration of the basement elevation on the Cazorla gravity section are shown in Fig 4.2.6. From this it is estimated that the greatest amount of error produced in the three balanced sections, which only involve the more foreland parts of the gravity modelled sections where the complicated effects of the crustal thinning is reduced, is a value of $\pm$ 500m at the most hinterland part of the balanced sections.

The balanced sections include regions, especially at depth, where there is insufficient data to be confident of the geometries and thrust sequences presented. The final construction of the sections involve the simplest interpretation possible from the available data for these regions from which a minimum amount of shortening can be estimated. The original lengths of individual thrust slices may be difficult to determine if no cut-offs are identified due to lack of preservation during erosion or difficulty in identifying internal cut-offs if the slice consists entirely of one

lithology e.g. the frontal slices of the Cazorla section. Again, the minimum feasible horse length is included in the construction and hence allows a minimum shortening estimate.

The stratigraphic sequences used to construct these balanced sections are fairly well constrained by well-log data and field logging and only introduce a very small error compared to the errors inherent in the calculation of the basement elevation.

5.3.2. The Cazorla section

The Cazorla section shows a progressive change in its tectonic transport direction, from northwesterly to more north-northwesterly, towards the foreland, and therefore, in these localities, the section deviates sightly from the tectonic transport direction. Calculation along the straight section produces a minimum value for the strain or shortening. The errors in the estimates of this shortening vary with the cosine of the angle between the line of section and the direction of net tectonic displacement. If this angle is less than 30°, the error introduced in this way is normally less than 15% (Price 1981). The effect of this swing in tectonic transport direction may be quantified by incorporating into the calculation a division of the section into three segments, by analysis of strain and kinematic data, which shows the progressive deviation from the line of section (Fig 5.3.2.1.). The strain exhibited by each segment may be individually corrected to parallel the transport direction and then combined to produce an overall shortening across the NE Trending Limb. This method can only incorporate the effect of plane-strain within each segment rather than the non-planar strain indicated by the gradual swing in transport direction and hence errors are introduced. However, the

results of strain calculation for these three segments may produce a more accurate value for overall shortening than that resulting from calculation of the whole straight section drawn at 120°.

a) Bed length balancing

The initial and final bed length of the ubiquitous Jurassic of the External Prebetics was measured in the restored and balanced sections respectively, from the most foreland hangingwall cut-off to the most hinterland footwall cut-off. Using $\varepsilon=(l_1-l_0)/l_0$:

For the Cazorla section,

$l_0 = 69.6km$ $l_1 = 21.4km$ (shortening = 48.2km)

$\therefore \varepsilon = -48.2/69.6 = -0.69 = 69\%$ shortening

It is estimated that the greatest amount of error produced in the balanced sections is the depth to basement calculated from gravity modelling techniques (chapter 4). This gives rise to a possible ± 500m error in the value of this figure, at the most hinterland part of the balanced sections, petering off to zero at the foreland part of the section where the Prebetic Front is emergent. Inclusion of a shallower basement (i.e. an error of maximum -500m) gave a l_0 value of 58km and hence, $\varepsilon = 36.6/58 = -0.63$ or 63% shortening. Therefore a value of ±6% would give a fairly accurate estimation of the errors involved in the shortening estimate.

b) Cumulative displacement-distance diagram

The cumulative displacement and distance from the reference point of 26 thrust slices was measured; Fig 5.3.2.2. shows the resulting plot. The overall shortening for the External Prebetics is calculated from the

gradient of the line interpolated between the origin and the final cumulative displacement-distance value for the External Prebetics. Using $\varepsilon = -\Sigma d/(1+\Sigma d)$:

For the Cazorla section,

$\Sigma d = 44.2 \quad l = 21.8 \quad \therefore \varepsilon = -0.67 \quad = 67\%$ shortening

The variation in strain i.e. the gradient of the curve, can be seen to vary markedly along the section. Hence, the strain for individual segments may be calculated and the first increasing and then decreasing nature of the strain rate, from hinterland to foreland, can be ascertained.

For Segment 1,

$\Sigma d = 6.2 \quad l = 3.2 \quad \therefore \varepsilon = -0.66 \quad = 66\%$ shortening

For Segment 2,

$\Sigma d = 24.0 \quad l = 7.0 \quad \therefore \varepsilon = -0.77 \quad = 77\%$ shortening

For Segment 3,

$\Sigma d = 14.0 \quad l = 11.6 \quad \therefore \varepsilon = -0.55 \quad = 55\%$ shortening

The strain is shown to be inconstant in distribution and vary from -0.55 to-0.77 along the Cazorla section. This may result from the variations in geometry and composition of the thrust slices at different locations along the section. The more hinterland segments, 1 and 2, display duplex geometries which can accommodate a large amount of shortening compared to the more simple, imbricate stacking in the most foreland segment 3. Segment 2 shows a greater amount of shortening than the

average calculated for the whole section. This may be due to the presence of Barremian marl at the top of the sequence allowing greater displacement along overthrusts. Segment 3, in contrast, shows a lesser amount of shortening compared to the average shortening calculated which may be due to the difficulty in overthrusting sequences dominated by competent recrystallised dolomite.

The bulk strain may also be calculated parallel to the tectonic transport direction across the NE Trending Limb incorporating the deviations of the tectonic transport direction in segments 2 and 3. From Cooper (1983), l_0, l_0'; l_1, l_1' represent the initial and final lengths of the normal section i.e. that which parallels the transport direction, and the oblique section. α and α' represent the angle of obliquity of the undeformed and deformed sections respectively and ε and ε' represent the bulk strain for the oblique and normal section. The values for the normal section are calculated from the following:

$$l_1 = l_1' \cdot \cos \alpha'$$

$$\sin \alpha = \frac{\tan \alpha' \, (\cos \alpha' \cdot l_1')}{l_0'}$$

$$l_0 = l_0' \cdot \cos \alpha$$

For segment 1,

$l_0 = 9.4$ $l_1 = 3$ No deviation

For segment 2,

$l_0' = 31.0$ $l_1' = 7.0$ $\alpha' = 10°$ $\varepsilon' = -0.77$ = 77% shortening

Incorporating a 10° deviation from the tectonic transport direction,

l_0 = 31.0 l_1 = 6.9 ε = -0.78 = 78% shortening

For segment 3,

l_0' = 25.6 l_1' = 11.6 α' = 20° ε' = -0.55 = 55% shortening

Incorporating a 20° deviation from the tectonic transport direction,

l_0 = 25.3 l_1 = 10.9 ε = -0.57 = 57% shortening

For the whole Cazorla section,

l_0 = 25.3+31+9.4=65.7 l_1 = 10.9+6.9+3=20.8 ε = -0.68

= 68% shortening

5.3.3. The Elche section

The Elche section, oriented at 200°, parallels the tectonic transport direction in the NW Trending Limb but does not include the most frontal thrust slices where there is a change in tectonic transport direction or the details of the Socovos Fault at depth where material is transported perpendicular to the section. Unavoidably in this complex area, there are effects of later deformation in and out of the plane of section which are very hard to quantify. If a greater amount of material is added to the section than is removed by the non-coaxial deformation, as may be the case in this area of converging shortening, a slight overestimate of the amount of shortening may result. Calculation of the strain exhibited in

this section may greatly improve the understanding of the nature of the change in strain across the Socovos Fault.

a) Bed length balancing

The initial and final bed length of the Jurassic of the External Prebetics was measured in the restored and balanced sections respectively, from the hangingwall cut-off of the most foreland thrust slice to the most hinterland footwall cut-off included in this incomplete section.

For the Elche section,

l_0 = 45.6km l_1= 20.9km (shortening = 24.7 km)

$\therefore \varepsilon$ = -24.7/45.6 = -0.54 = 54% shortening

Inclusion of a shallower basement in the hinterland (i.e. an error of maximum -500m) (section 5.3.2.a), gave a l_0 value of 39.5km and hence, ε = -18.6/39.5 = -0.47 or 47% shortening. Therefore a value of ±7% would give a fairly accurate estimation of the errors involved in the shortening estimate.

b) Cumulative displacement-distance diagram

Fig 5.3.3.1. shows the cumulative displacement and distance from the reference point of the 9 thrust slices of the External Prebetics included in the Elche section. The overall shortening calculated from the gradient of the line interpolated between the origin and the final cumulative displacement-distance value is,

For the whole section,

Σd = 24.7 l = 18.4 $\therefore \varepsilon$ = -0.57 = 57% shortening

The gradient of the curve, and hence the strain rate, can be seen to increase slightly along the section from the hinterland to the foreland with a noticeable break between the two segments arising as a result of a triangle zone caused by converging thrusting and backthrusting. There is no in-sequence displacement of this triangle zone but later displacement occurs along the sole thrust flooring it with continued deformation to the foreland. The variation in strain between the more hinterland and more foreland segments may be calculated.

For Segment 1,

$\Sigma d = 10.9 \quad l = 9.1 \quad \therefore \varepsilon = -0.55 \quad = 55\%$ shortening

For Segment 2,

$\Sigma d = 13.8 \quad l = 5.5 \quad \therefore \varepsilon = -0.72 \quad = 72\%$ shortening

The strain in the Elche section is shown to vary from-0.55 in the hinterland to-0.72 in the foreland (with 0 for the intermediate triangle zone). This overall increase in strain towards the foreland arises due to the interaction of thrusting and backthrusting causing a jacking up of some of the thrust slices and hence a large amount of displacement over a small area of the section.

5.3.4. The Jumilla section

To the foreland of the Jumilla section is an area of very low strain exhibited as gentle folds which is outside the length of section. The displacement along the décollement flooring these folds is contained

within the displacement measured across the Triassic ramp of the buried Prebetic Front.

a) Bed length balancing

The initial and final bed length of the Jurassic of the External Prebetics was measured in the restored and balanced sections respectively, from the foreland hangingwall cut-off of the buried Prebetic Front to the most hinterland footwall cut-off against the Internal Prebetics.

For the Jumilla section,

$l_0 = 58.7\text{km}$ $l_1 = 46.3\text{km}$ (shortening = 12.4 km)

$\therefore \varepsilon = -12.4/58.7 = -0.21$ = 21% shortening

Inclusion of a shallower basement (i.e. an error of maximum -500m) (section 5.3.2.a) gave a l_0 value of 53.8 km and hence, $\varepsilon = -4.9/53.8 = -0.14$ or 47% shortening. Therefore a value of ±7% would give a fairly accurate estimation of the errors involved in the shortening estimate.

b) Cumulative displacement-distance diagram

Fig 5.3.4.1. shows the cumulative displacement and distance from the reference point of the 15 thrust slices of the External Prebetics of the Jumilla section. The overall shortening calculated from the gradient of the line interpolated between the origin and the final cumulative displacement-distance value is,

For the whole section,

$\Sigma d = 13.6$ $l = 45.8$ $\therefore \varepsilon = -0.23$ = 23% shortening

The gradient of the curve, and hence the strain rate, can be seen to increase along the section from the hinterland to the foreland. The variation in strain between the more hinterland and more foreland segments may be calculated.

For Segment 1,

$\Sigma d = 3.3 \qquad l = 25.3 \qquad \therefore \varepsilon = -0.16 \quad = 16\%$ shortening

For Segment 2,

$\Sigma d = 10.3 \qquad l = 20.5 \qquad \therefore \varepsilon = -0.33 \quad = 33\%$ shortening

The strain in the Jumilla section is shown to vary from -0.16 in the hinterland to -0.33 in the foreland. The main controls on the shortening are the initial thickness, the amount of thickening required to produce a critically tapered geometry and the total shortening in the wedge as a whole. The increase in strain towards the foreland in the Jumilla section may be due to the presence of a thinner initial stratigraphy and the development of more décollement horizons within the Mesozoic.

5.4. Discussion of results

There appears to be a slight discrepancy in the results obtained for each section when applying the two different techniques. The bulk strain estimated from analysis of the cumulative displacement-distance diagram varies slightly from that obtained from comparing the balanced and restored sections produced by bed length balancing but this difference is slight compared to the errors produced in the calculation of the depth to

basement i.e. ±6-7%. An increasing amount of measurement error is introduced as the displacement across each successive thrust slice is added to the cumulative value. The value of the strain obtained by the cumulative displacement-distance diagram is that which parallels the décollement horizon and hence greater than the amount of shortening calculated along the horizontal as on bed length balancing depending on the dip of the décollement.

Although the overall shortening calculated from the balanced and restored section is probably more accurate, the cumulative displacement - distance diagram reveals more about the strain distribution within the section and the variation of this strain with time.

The above results, which show a west to east variation from -0.69 to -0.54 to -0.21 in bulk strain, indicate that there is no dramatic decrease in the amount of deformation to the east of the major Socovos wrench fault. The component of deformation to the NW (sub-parallel to the movement along the Socovos Fault), however, does decrease significantly across the Socovos Fault with most deformation occurring in the orientation of the other component of partitioned deformation, i.e. approximately perpendicular to the Socovos Fault. The amount of NW strain exhibited in the Elche section can be attained by the graphical method applied to oblique sections in Cooper (1983) (Fig 5.4.1.). The value of ε' for an oblique section oriented at 120-130° varies between -0.05 and -0.18. This result is comparable to the Jumilla section (bulk strain = -0.21), which is also sited to the east of the Socovos Fault.

Previous workers have estimated the amount of contraction across the NE Trending Limb and the Alcaraz Antitaxis. Banks and Warburton

(1991) calculate that a bulk strain of -0.73 occurred across the External Prebetics to the foreland of the Tranco Zone i.e. where Triassic units outcrop which corresponds the combined segments 2 and 3 of the Cazorla section. Guezou et al. (1991) calculate, for their semi-balanced sections, a bulk strain of -0.55 or greater for the *Beas de Segura unit* which is equivalent to segment 3 and a bulk strain of -0.70 for the *Cazorla unit* which is equivalent to segment 2.

The most foreland segment of the Cazorla section shows a decrease in bulk strain to below the average for that section. This may be due to the influence of the Palaeozoic Massif which is present in the undeformed foreland. The Triassic units were deposited up against this massif and hence thin towards it. An increased continental component to this Triassic, which is preferentially used as a décollement horizon, may cause a decrease in the rate of propagation of deformation.

The greater amount of backthrusting exhibited in the Jumilla and Elche sections has been explained as a method of increasing the thickness of the thrust wedge during frontal accretion. The results shown in Fig 5.3.3.1 and Fig 5.3.4.1 verify the existence of increased strain towards the foreland in the segments where both polarities of deformation occur. The strain rates for the Jumilla and Elche sections show an increase towards the foreland where there is a basin of Mesozoic sediments compared to the Palaeozoic Massif which is located to the foreland of the Cazorla section.

The areas which have undergone the greatest amount of shortening during the Tertiary deformation and therefore probably the greatest amount of tectonic thickening, usually correspond to the areas of greatest present-day elevation and do not appear to have suffered greatly differing

amount of subsidence in the Mesozoic rifting than the areas which underwent lesser shortening (section 3.2.1). The amount of shortening exhibited in an area of the Prebetic Zone is a result of its position relative to main the Socovos wrench fault with its strain partitioning into strike-parallel dextral slip and perpendicular thrust/backthrust movement. Within an area the variation in the distribution of the shortening results from the differing composition and thicknesses within the stratigraphic sequence.

CHAPTER 5

FIGURES

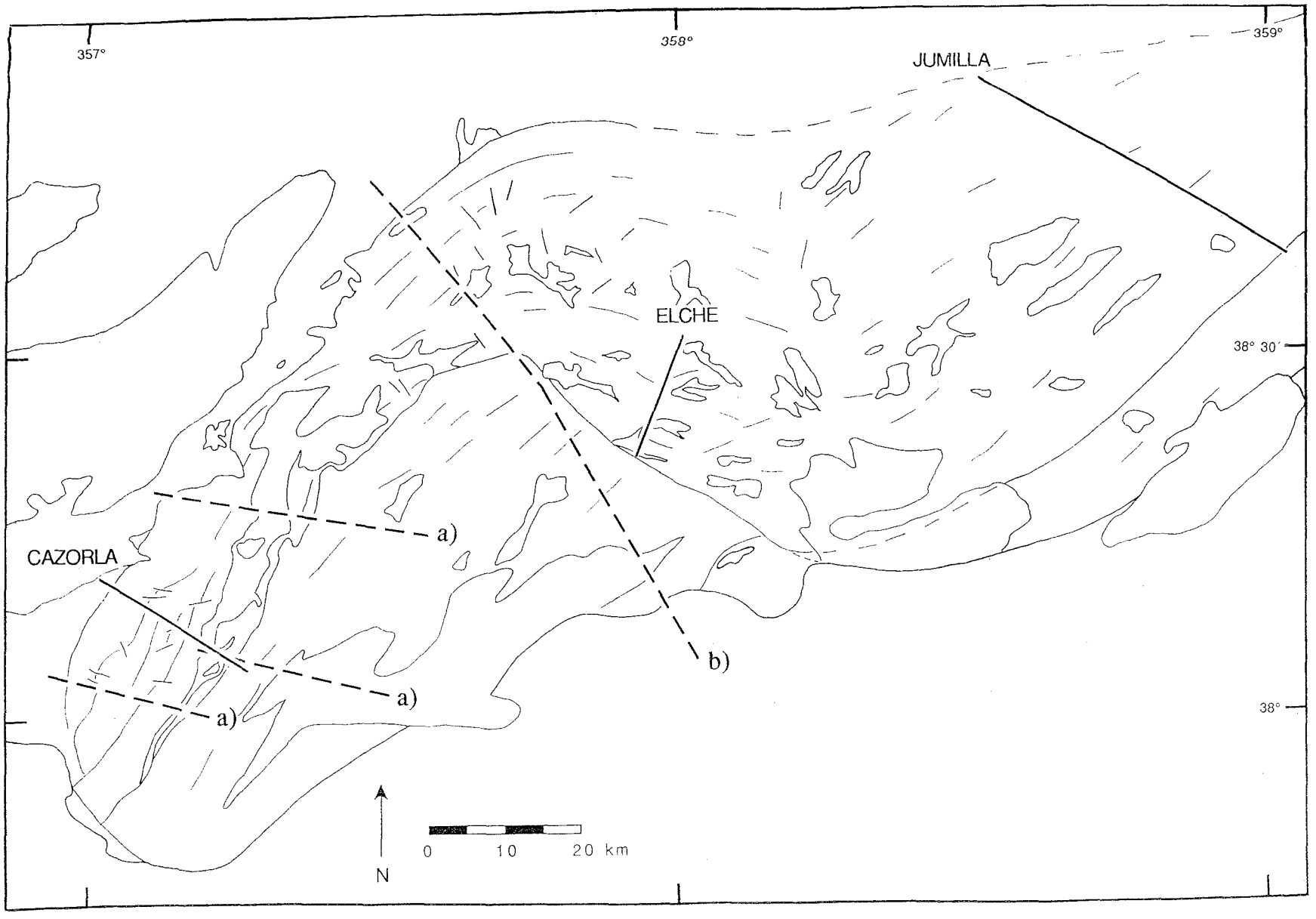
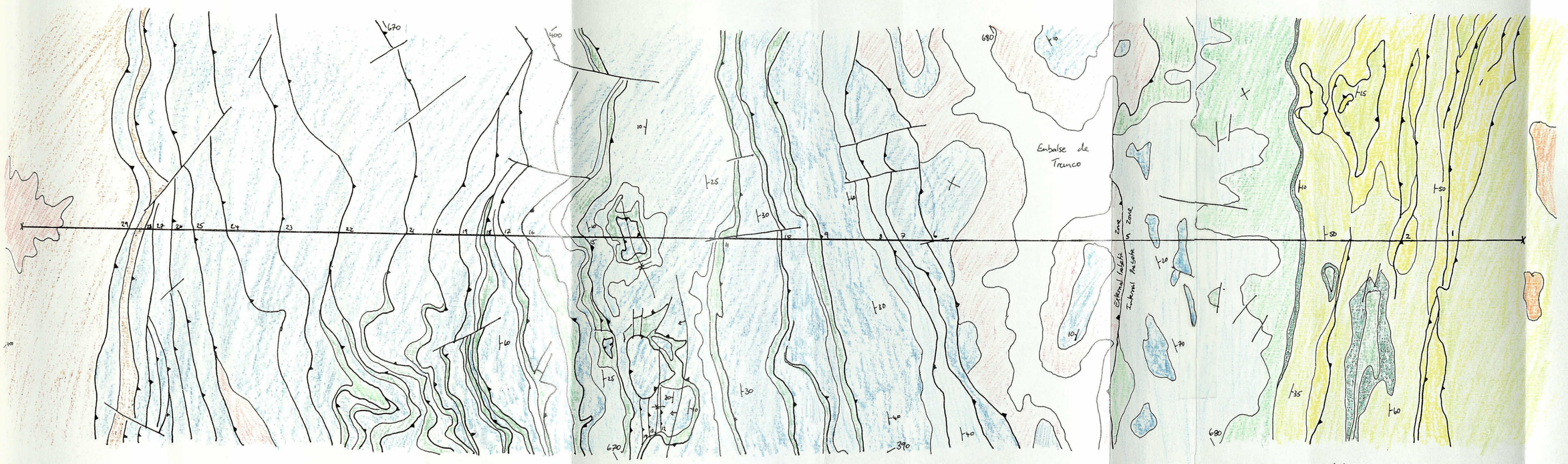


Fig 5.1.1. Locations of previously balanced or 'semi-balanced' cross-sections in the western Prebetics shown by dashed lines. a) Guezou et al. 1991, b) Banks & Warburton 1991. The locations of the three balanced cross-sections presented in this study, the Cazorla, Elche and Jumilla sections are shown as solid lines.



Compiled from I.G.M.E. 1:50,000 Geological maps and field mapping 1989-92.

Map for Fig 5.2.1.1.
Cazorla Section

Key

- Late Miocene marl
- Middle Miocene marl
- Early Miocene limestone
- Cenomanian/Turonian dolomite
- Albian sandstone, marl and mud
- Barremian marl
- Malm limestone
- Lias/Dogger dolomite
- Triassic sandstone
- Palaeozoic basement

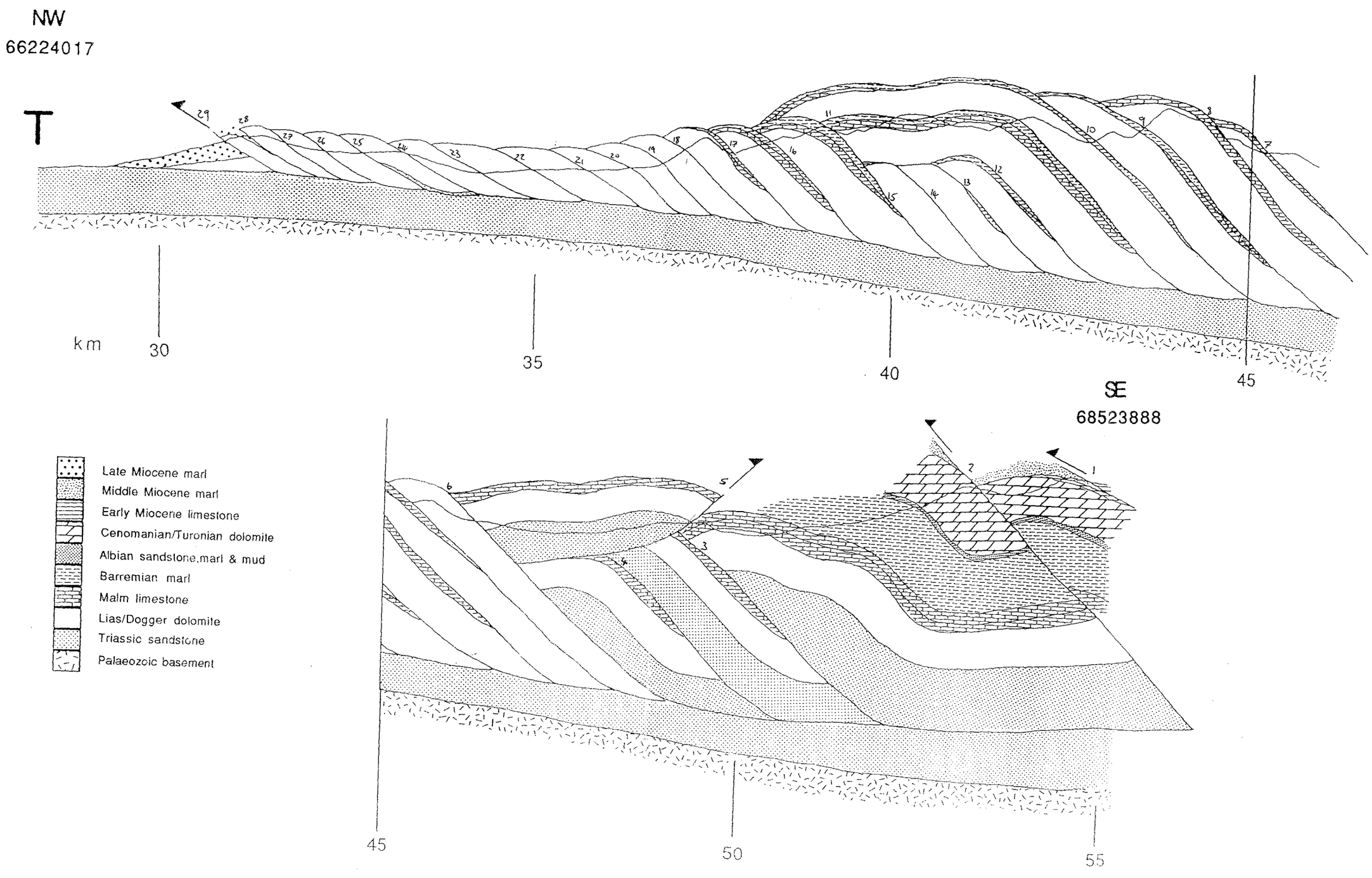


Fig 5.2.1.1. The Cazorla balanced section. The deformational style is predominantly that of a foreland verging imbricate stack showing later backthrusting in the more hinterland region associated with backsteepening. A passive-roof duplex developed between kms 40-43 and its formation is shown in detail in Fig 5.2.1.3. The Prebetic Front is emergent and Late Miocene marl is incorporated into the frontal thrust. Area of greatest uncertainty of structure at depth in this section is the geometry between 47-52 km. Total shortening = 69% (48.2 km)

T

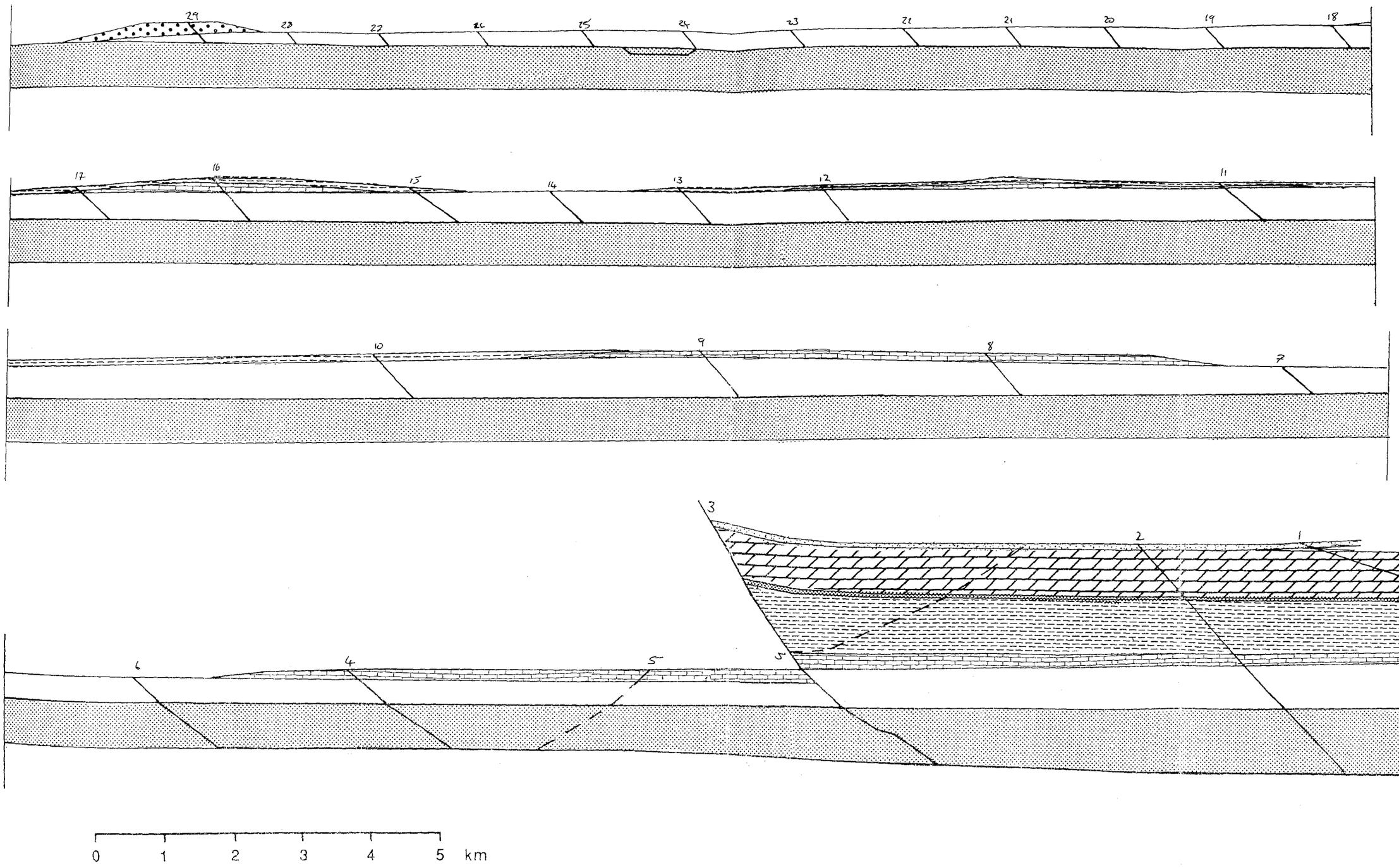


Fig 5.2.1.2. The Cazorla restored section. There are significant gaps in the stratigraphic sequence of the External Prebetics. The Internal Prebetics, the most hinterland 10 km of the restored section, shows a thicker and more complete sequence.

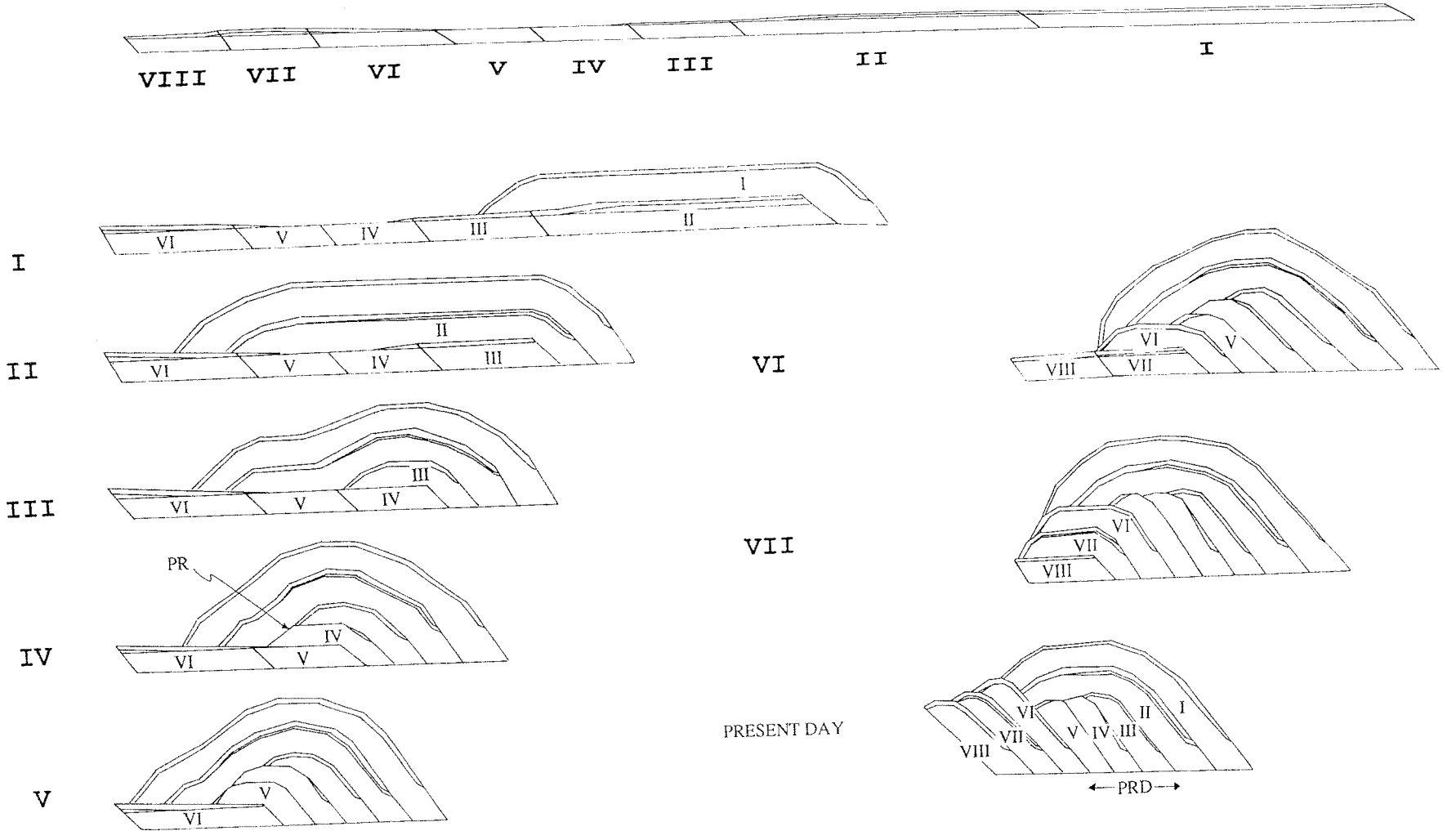
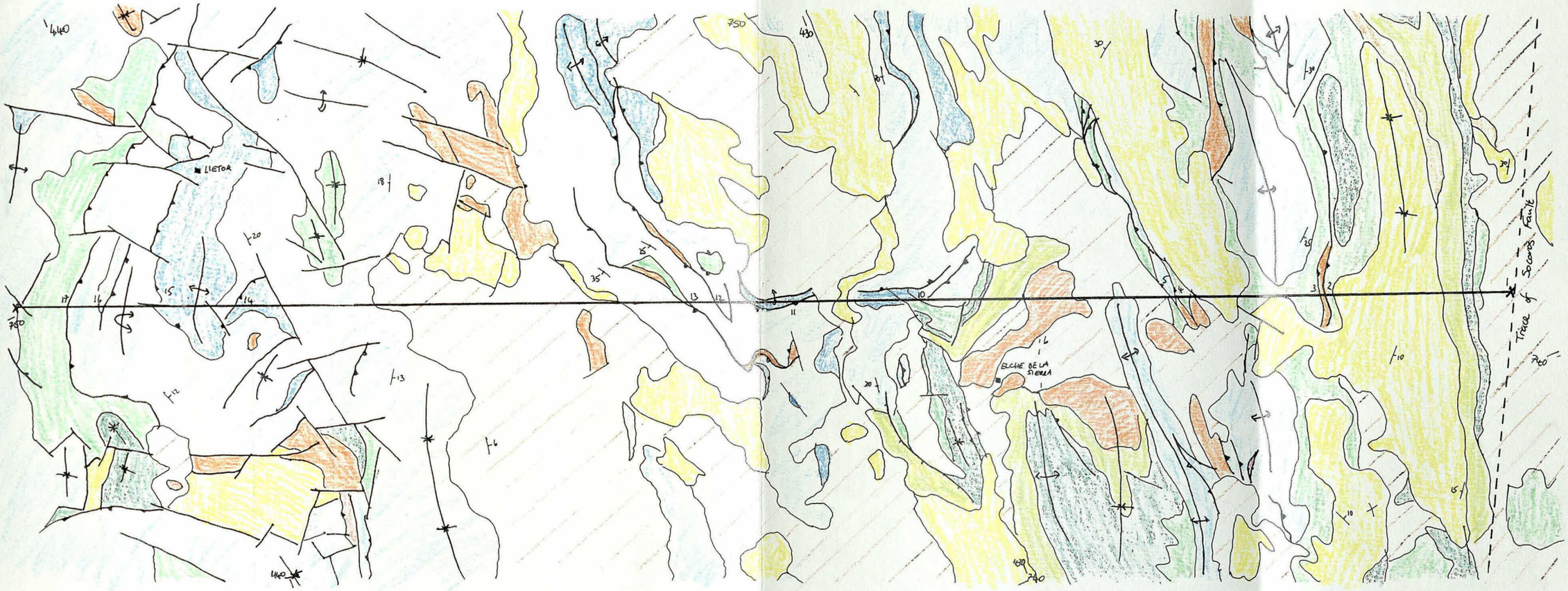


Fig 5.2.1.3. Cartoon of the sequence of deformation (I to VIII) resulting in the formation of the Cazorla passive-roof duplex (PRD). The stratigraphic units are shown in Fig 5.2.1.2. Stages I and II show sequential overthrusting of relatively long thrust slices. Stages III-V show the formation of the hinterland-dipping duplex by in sequence thrusting with ramps developed beneath existing overthrust slices causing an antiformal geometry of the roof slices to develop. The roof thrust, although originally a forethrust in stage II, becomes a passive backthrust (PR) and the roof slices are not significantly transported towards the hinterland but undergo some internal deformation. Later foreland vergent thrusting, stages VI-VII, causes the development of the passive-roof duplex (PRD) geometry seen at the present day.



Key

- Pliocene / Quaternary
- Late Seravallian - Messinian limestone and marl
- Aquitanian - Mid Seravallian limestone
- Conacian / Maastrichtian limestone
- Cenomanian / Turonian dolomite
- Barremian / Aptian marl
- Dogger / Malm limestone
- Lrassic dolomite
- Triassic sandstone

Compiled from I.G.M.E 1:50,000 geological maps and field mapping 1989-92

Map for Fig 5.2.2.1.
Elche Section

NNE

74984430

SSW

74104214

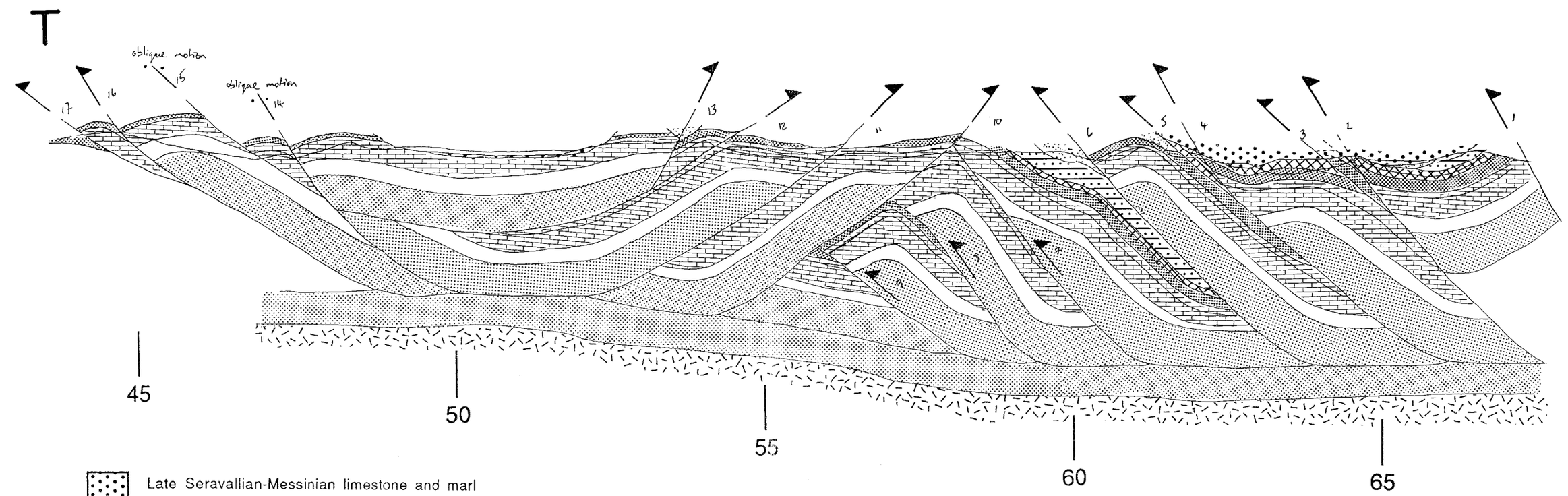


Fig 5.2.2.1. The Elche balanced section. The sequence of thrusting is predominantly to the foreland with episodes of foreland propagating backthrusting. The backthrusts, formed at the thrust front, cause the development of a blind front geometry at km 55, the formation of a passive-roof duplex, kms 56-58 (Fig 5.2.2.3). Where there is convergence of the differing polarities of thrusting a triangle zone is formed between two thrusts with the same basal detachment and with opposing vergence, kms 54-58, and where there is a divergence of the thrusting directions, there is a jacking-up of a thrust slice, kms 47-56. Greatest uncertainty of structure at depth in this section is the geometry of the passive-roof duplex and the jacked up zone of diverging polarity of thrusting. Total shortening = 54% (24.7 km)

T

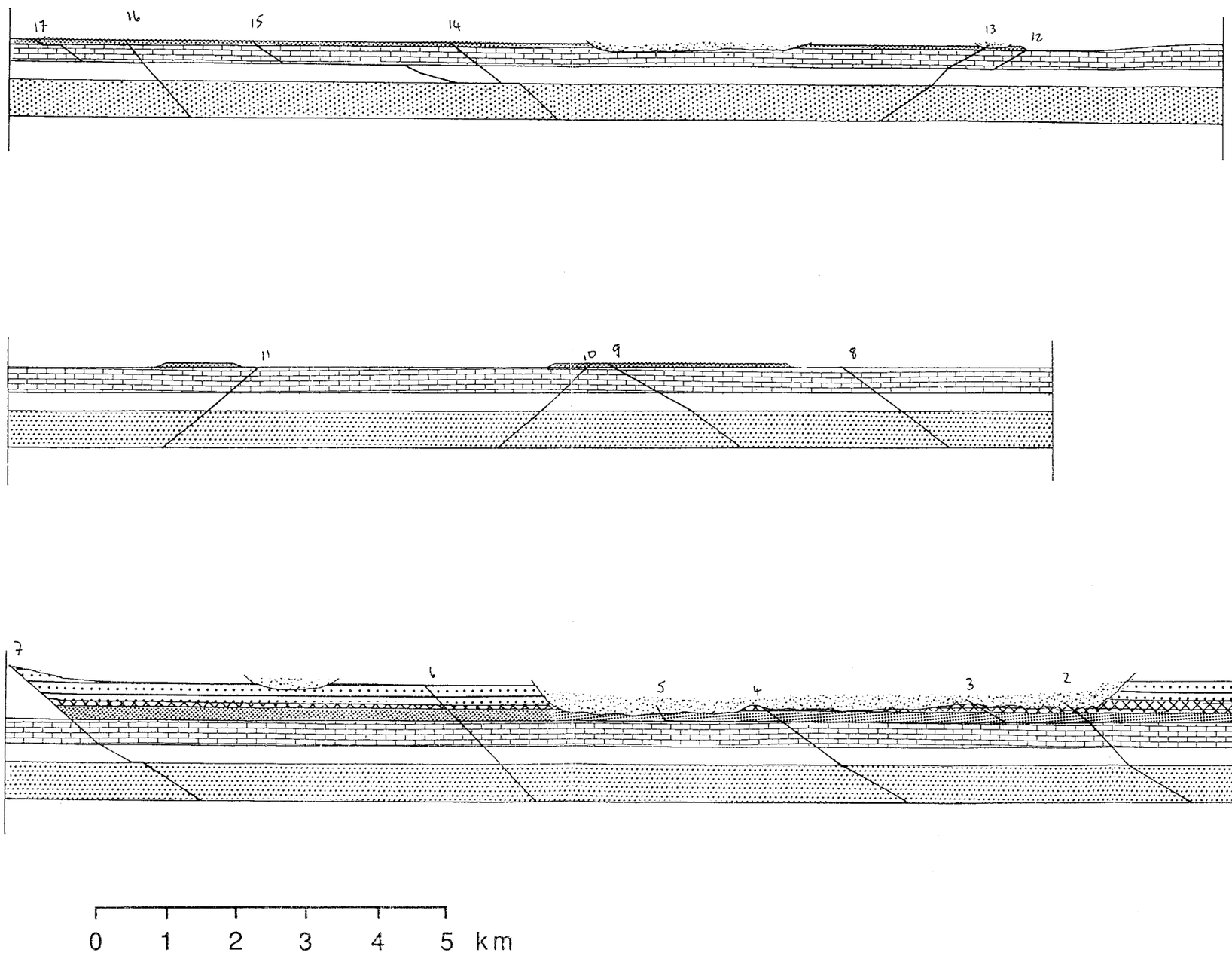


Fig 5.2.2.2. The Elche restored section. The northern part of the section shows a discontinuous Barremian/Aptian Weald Facies. There is an increase in the thickness of the stratigraphic sequence to the hinterland of the section. Post deformational Tertiary deposits are not shown for clarity.

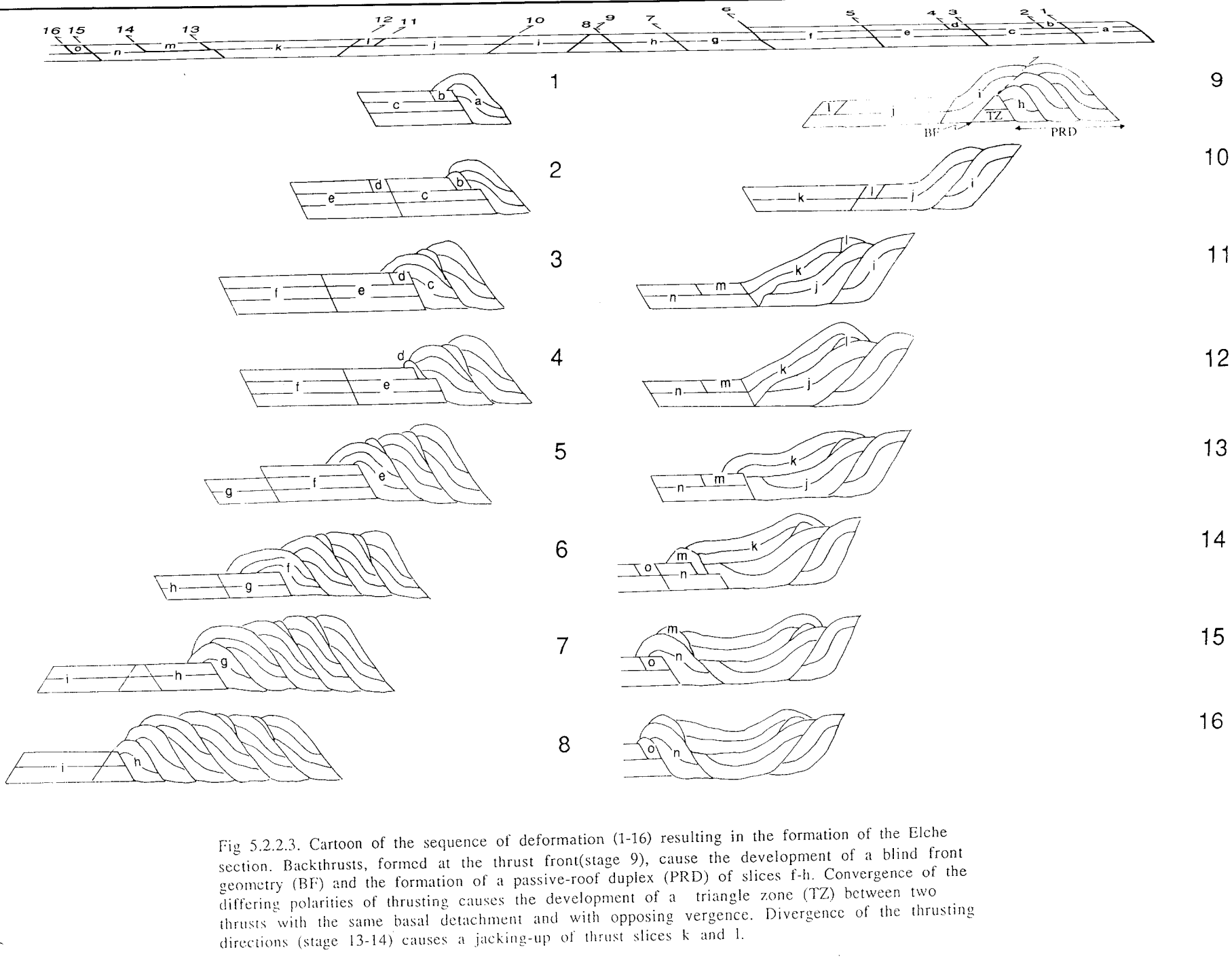
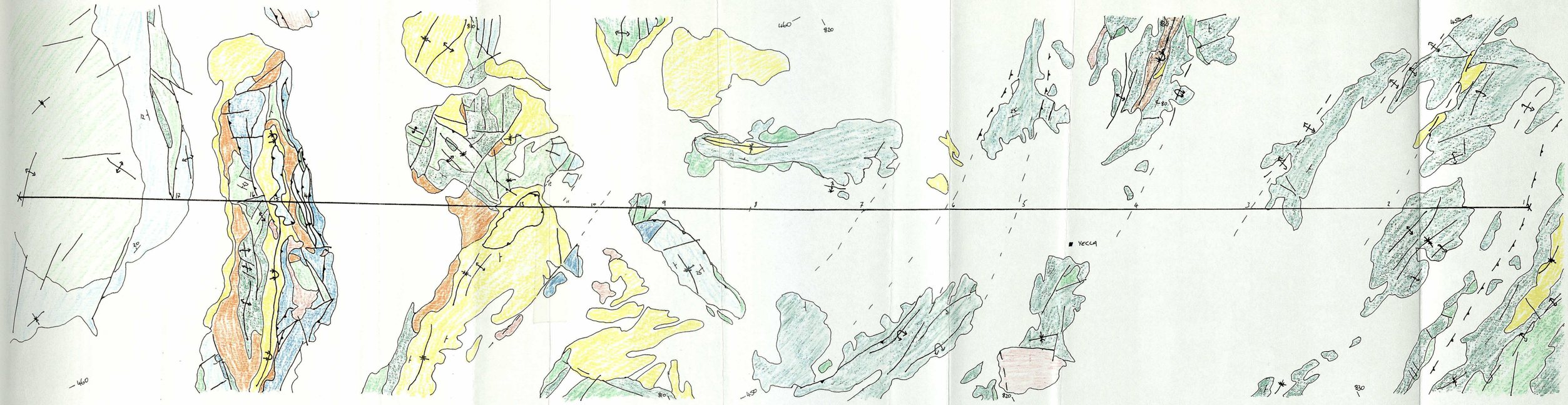


Fig 5.2.2.3. Cartoon of the sequence of deformation (1-16) resulting in the formation of the Elche section. Backthrusts, formed at the thrust front(stage 9), cause the development of a blind front geometry (BF) and the formation of a passive-roof duplex (PRD) of slices f-h. Convergence of the differing polarities of thrusting causes the development of a triangle zone (TZ) between two thrusts with the same basal detachment and with opposing vergence. Divergence of the thrusting directions (stage 13-14) causes a jacking-up of thrust slices k and l.



Key

- unconformity
- Pliocene and Quaternary
- Serravallian / Tortonian
- Langhian
- Oligocene
- Upper Cretaceous
- Lower Cretaceous
- Oxfordian / Kimmeridgian
- Lias / Dogger
- Triassic

Map for Fig 5.2.3.1.
Jumilla Section

Compiled from I.G.M.E 1:50,000 geological maps and field mapping 1989-92.

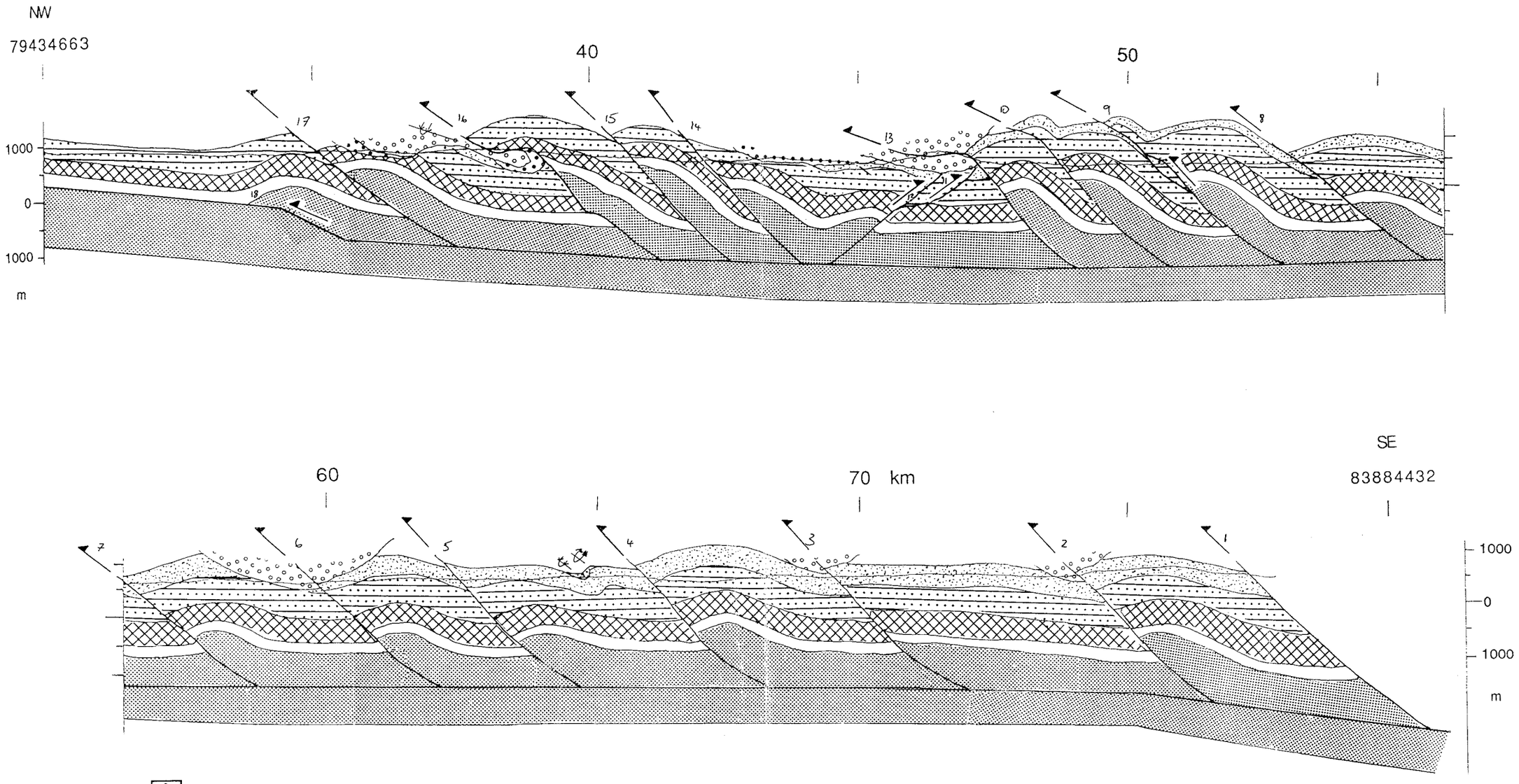


Fig 5.2.3.1. The Jumilla balanced section. The deformation style is characterised by the development of foreland verging thrust slices with occasional development of backthrusting and associated formation of a triangle zone, kms 45-47, and out-of-sequence thrusting (no. 13 of Fig 5.2.3.2). The Prebetic Front is buried and transfers its displacement to the foreland in a broad zone of low strain. Area of greatest uncertainty of structure at depth in this section is the geometry between 42-47 km. Total shortening = 21% (12.4 km)

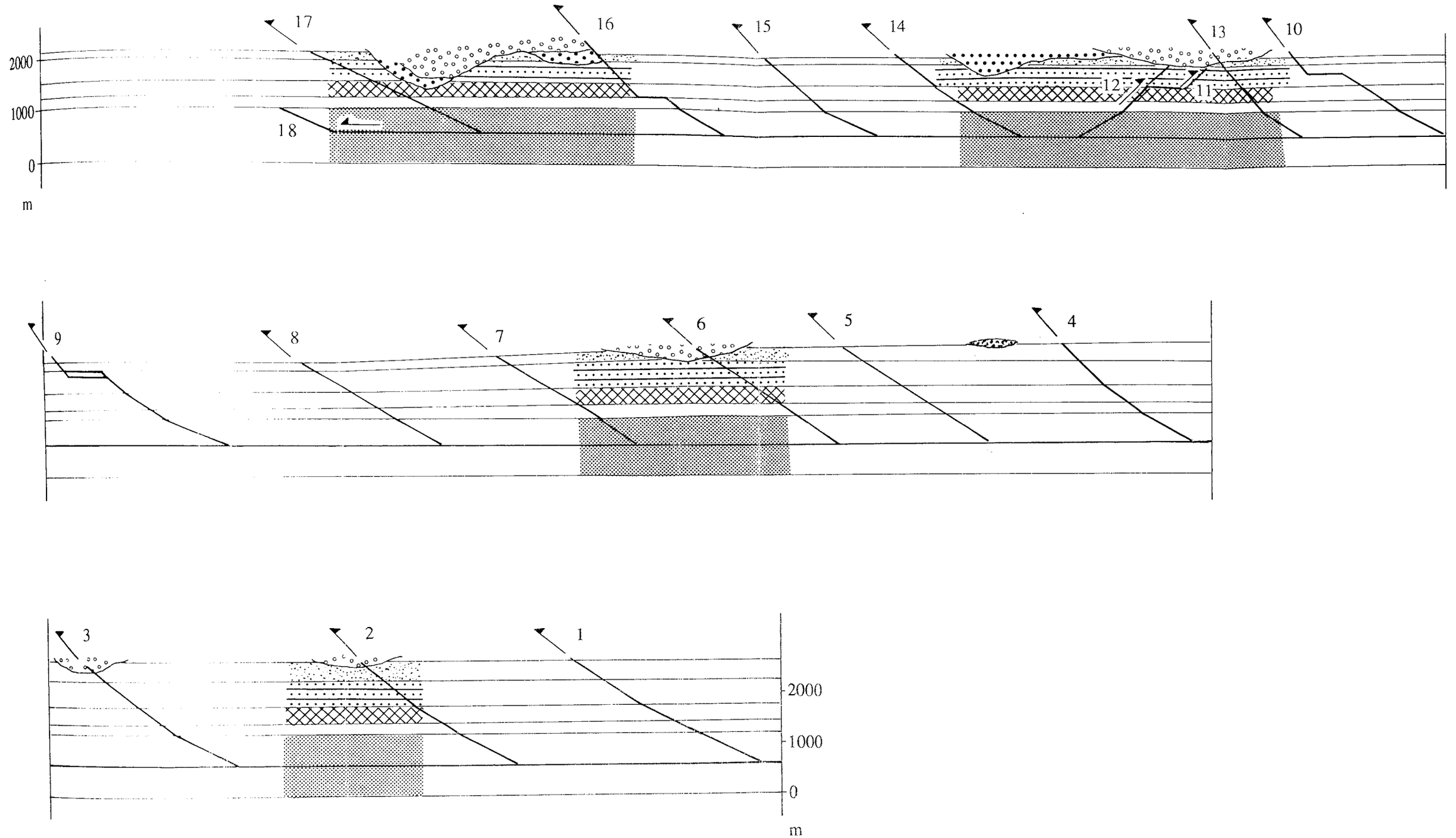


Fig 5.2.3.2. The Jumilla restored section. The stratigraphic sequence for the foreland and hinterland parts of this section are relativcly consistent with an increase in thickness toward the hinterland. The no.s, 1-18, show the sequence of the deformation including the development of frontal backthrusting, 11 and 12 and the out-of-sequence thrust, 13.

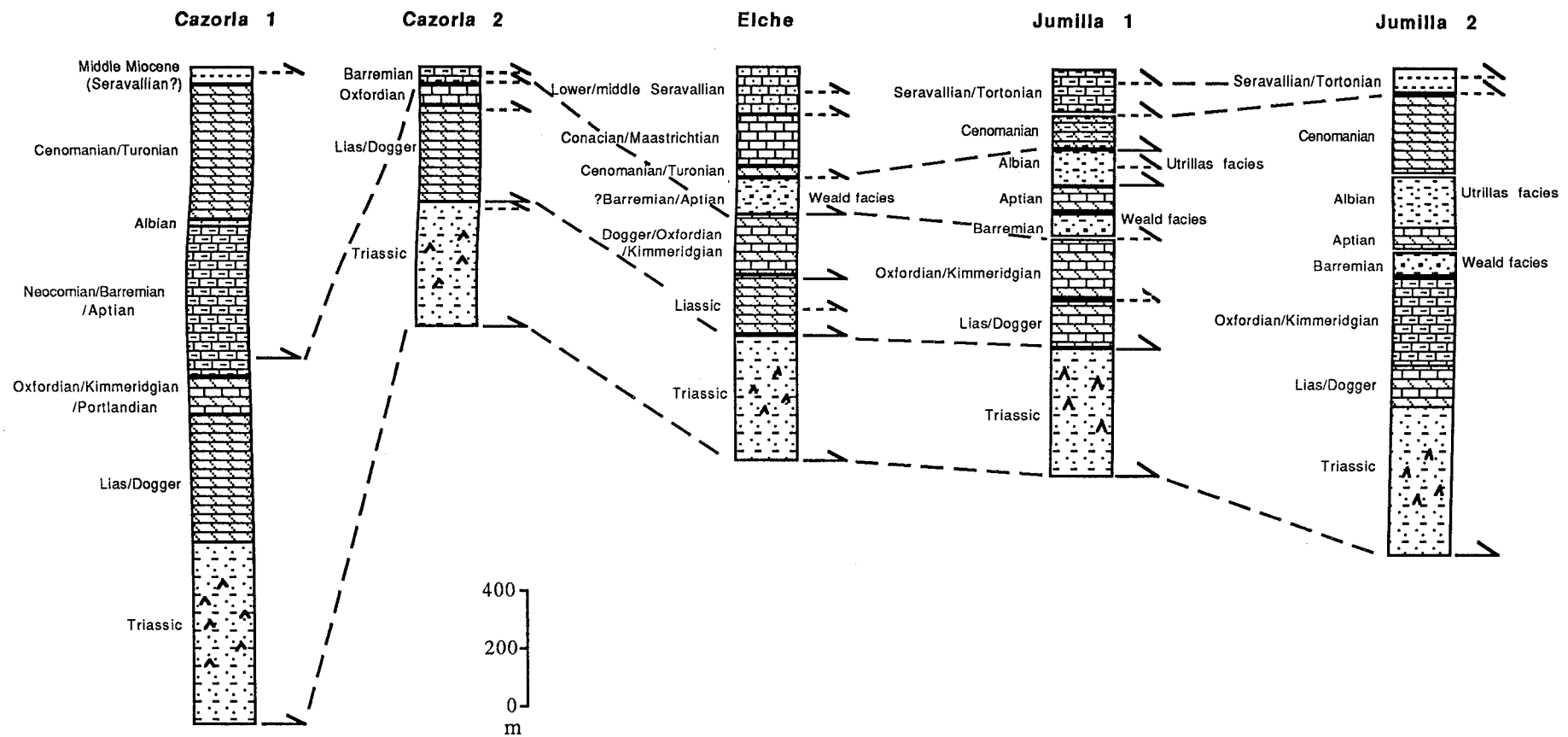


Fig 5.2.4.1a). The correlation of décollement horizons for five representative stratigraphic sections for the three balanced sections. Solid arrows-major detachments. Dashed arrows-minor detachments. Key for stratigraphic columns shown in Fig 5.2.4.1b).

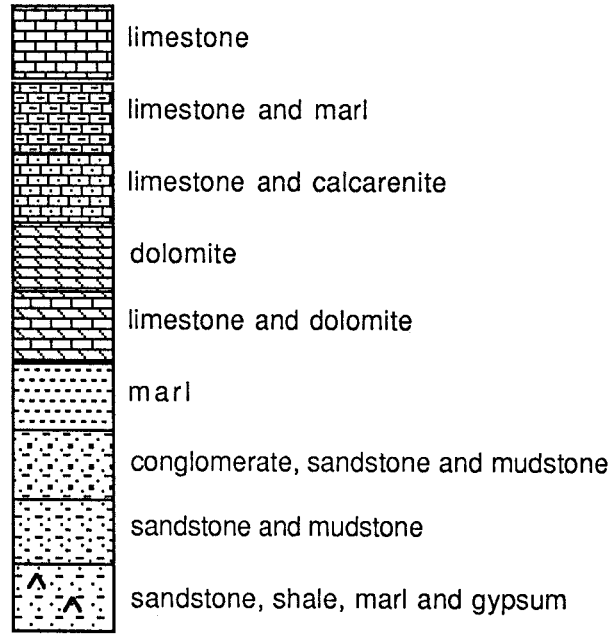


Fig 5.2.4.1.b). Key for stratigraphic columns shown in Fig 5.2.4.1.a).

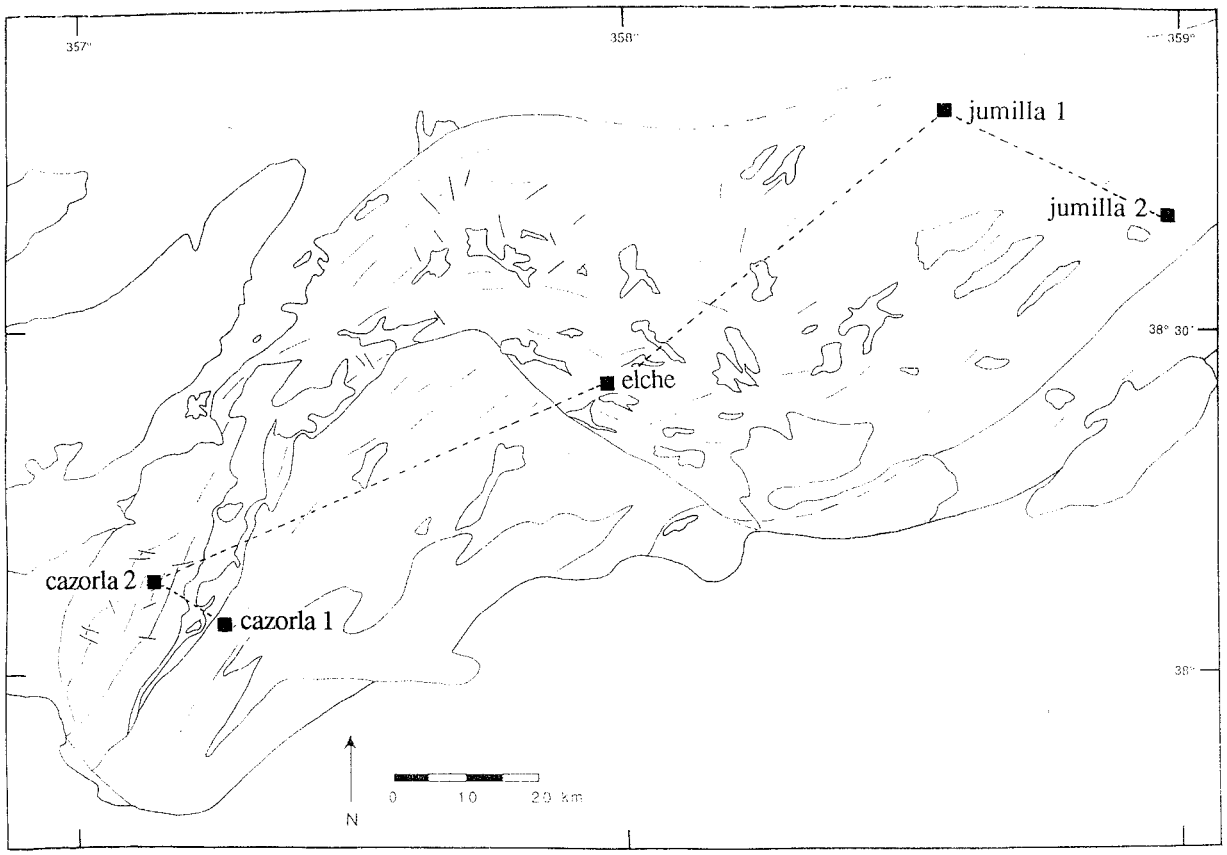


Fig 5.2.4.2. Locations of the five stratigraphic sections shown in Fig 5.2.4.1.

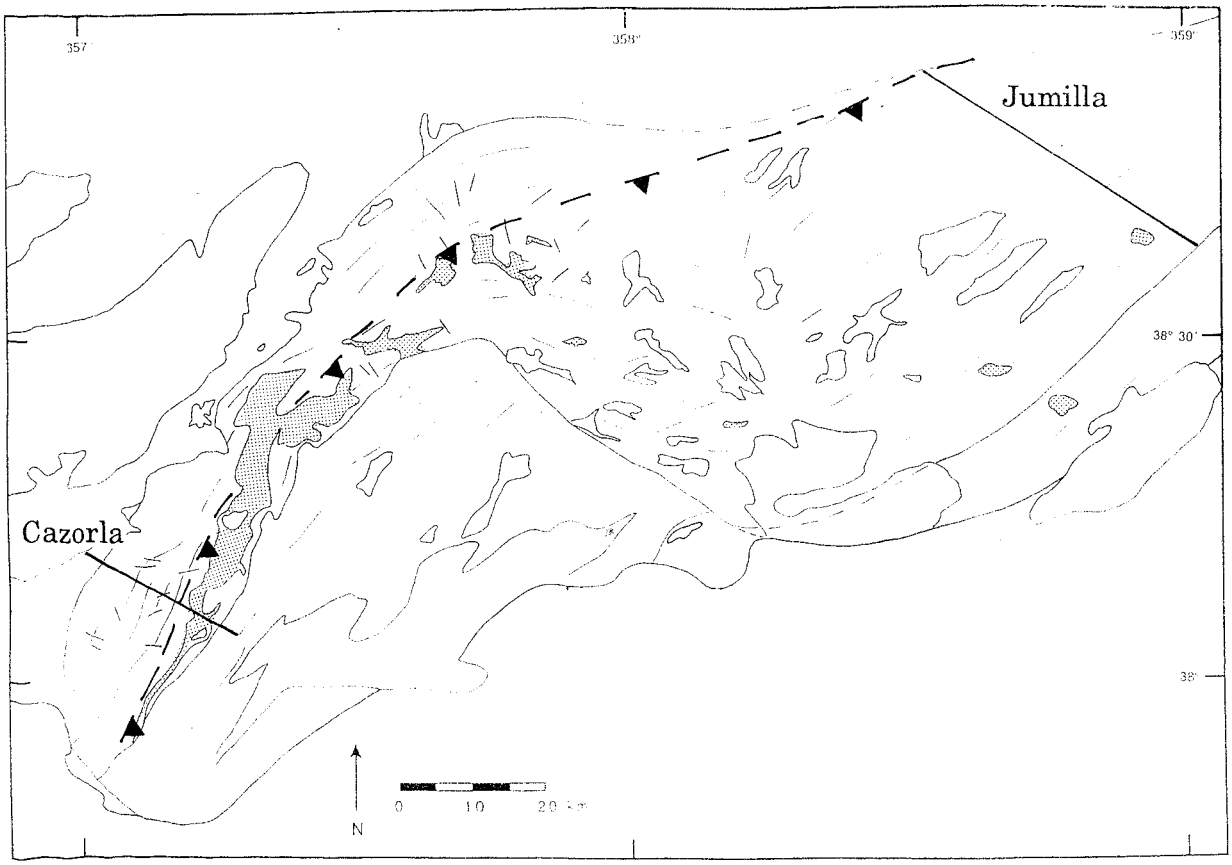


Fig 5.2.4.3. Possible linking of the last ramping of the basal décollement through the Triassic. This deformation is located to the foreland of the Tranco Zone i.e. the zone where Triassic, involved in thrust slices, is present at the surface. Correlation with the location of the wave of deformation (section 2.3) indicates that the probable timing of this deformation was Late Tortonian/Messinian. Pale stipple-Triassic within Prebetic Zone.

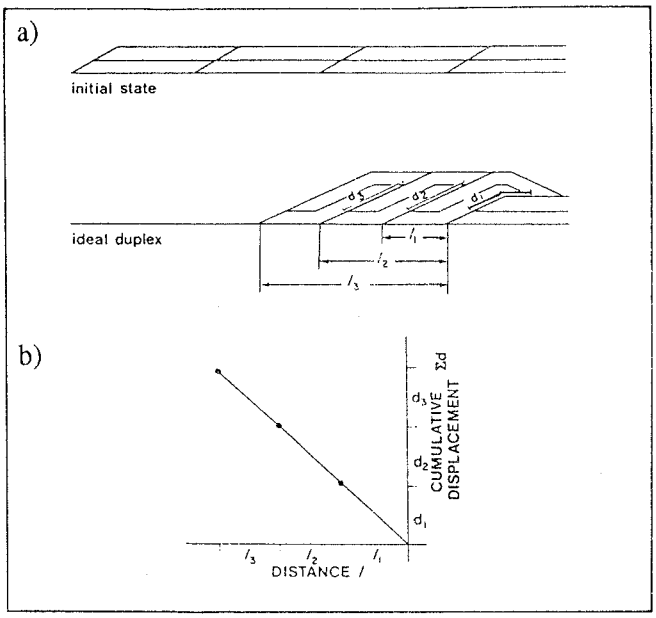


Fig 5.3.1.1. Diagram of the cumulative displacement-distance method of analysis after Chapman & Williams (1984).

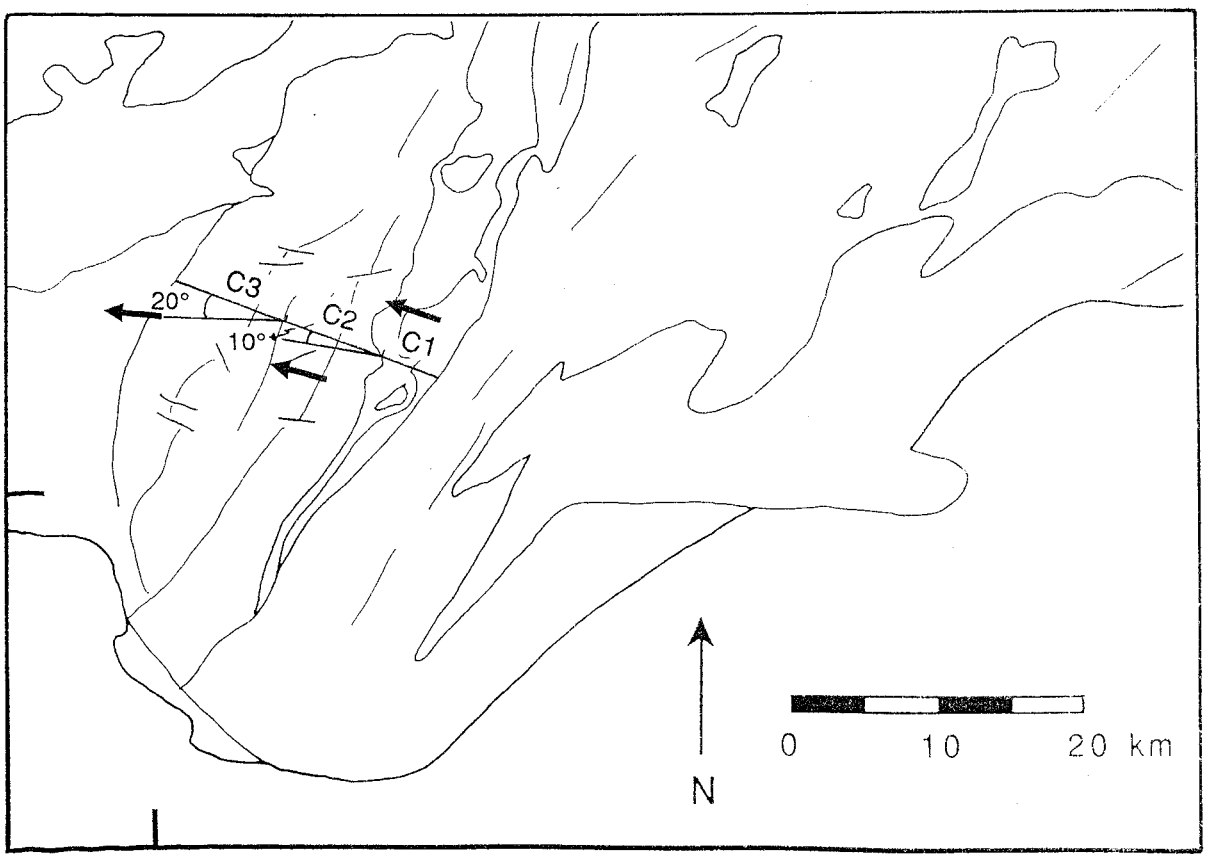


Fig 5.3.2.1. Division of the Cazorla section into three segments (C1-C3) which have experienced slightly different trends of deformation i.e. C2 at 10° to the main section and C3 at 20° to the main section. Solid arrows-thrust transport directions (section 2.2).

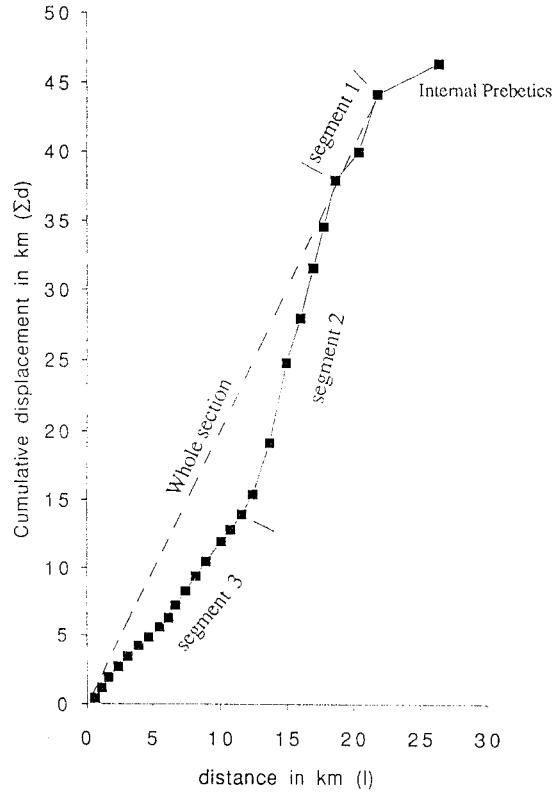


Fig 5.3.2.2. The cumulative displacement-distance diagram for the Cazorla section. The section is subdivided into three segments which exhibit different amounts of shortening. Overall there is a decrease in the amount of strain towards the foreland. The cumulative displacement-distance for the whole section is shown as a dashed line.

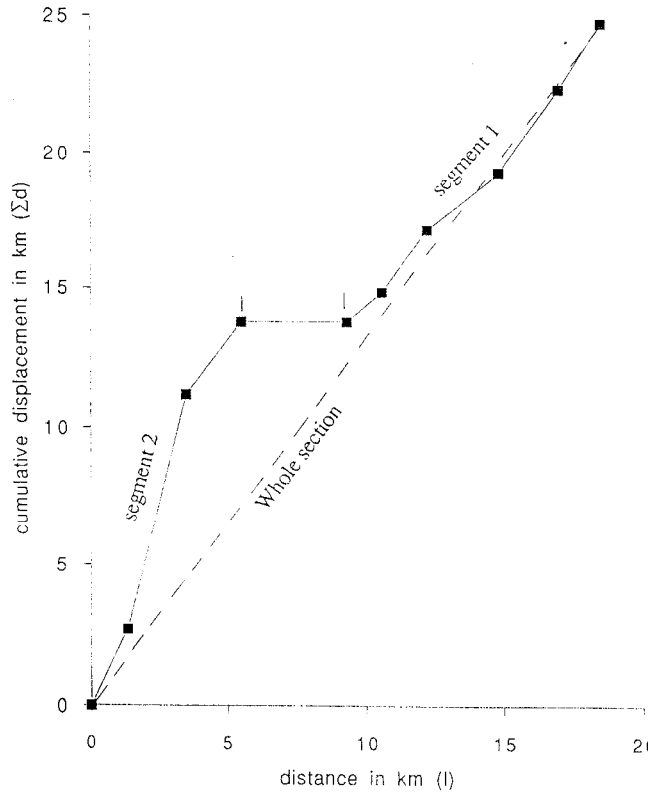


Fig 5.3.3.1. The cumulative displacement-distance diagram for the Elche section. The section is subdivided into two segments, separated by a segment of zero shortening representing the triangle zone, which exhibit different amounts of shortening. Overall there is an increase in the amount of strain towards the foreland. The cumulative displacement-distance for the whole section is shown as a dashed line.

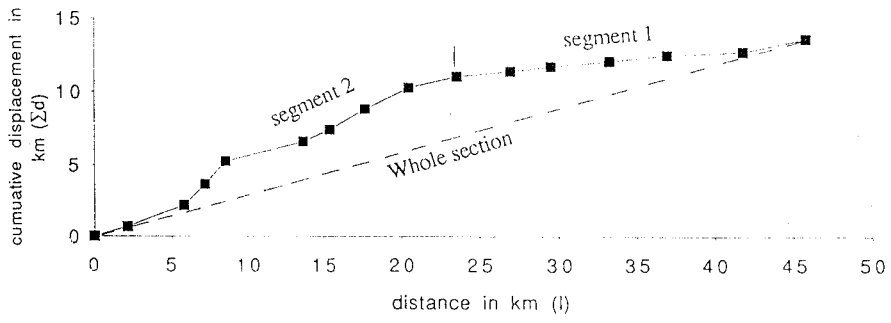


Fig 5.3.4.1. The cumulative displacement-distance diagram for the Jumilla section. The section is subdivided into two segments which exhibit different amounts of shortening. Overall there is an increase in the amount of strain towards the foreland. The cumulative displacement-distance for the whole section is shown as a dashed line.

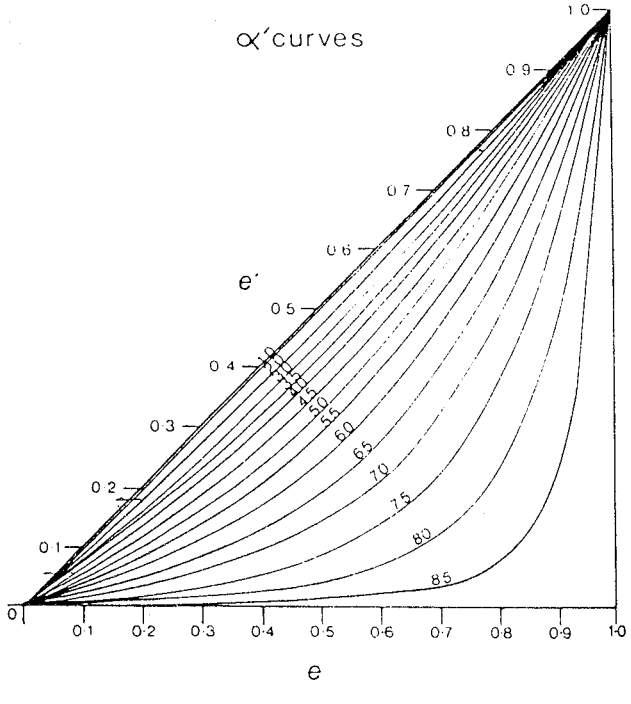


Fig 5.4.1. Graphical method to attain ε' from ε for obliquely oriented sections after Cooper (1983). The figures at the edges of the triangle are values of strain, the figures on the contours within the triangle are the degrees of obliquity.

Chapter 6

CHAPTER 6

3-D RECONSTRUCTION OF THE PREBETIC ARC

6.1. Introduction

Restoration of 2-D balanced sections, such as those described in Chapter 5, is a well-accepted and routine way of calculating the bulk strain experienced across a specific area. To investigate the initial geometry of an orogenic belt and the intermediate stages of its deformation, restoration of the whole orogenic belt in 3-D is required. Orogenic belts, formed by complex 3-D networks of interlinked faults, may show marked lateral variations in structural geometry and the amount and direction of tectonic displacement. In the case of a linear orogenic belt which exhibits only plane strain perpendicular to strike, a series of well-constrained, parallel 2-D sections should produce a reasonably accurate reconstruction of the initial geometry. However, in orogenic belts which are arcuate in plan view and show converging and/or diverging tectonic transport directions, a more thorough method is needed to produce a step-wise reconstruction of the deformation, an acceptable initial geometry and an estimate of bulk areal reduction in the horizontal plane. An 'areal balancing' or reconstruction in 3-D, in which a number of non-parallel (but each perpendicular to the transport direction of that area) balanced sections are sequentially restored in a reverse order to that of their formation, will produce a fair representation of the initial geometry and a minimum estimate of the shortening in the horizontal plane i.e. in plan view.

There has been very little work published on areal balancing of thin-skinned arcuate thrust belts. Julivert & Arboleya (1986) restore the Cantabrian Zone of NW Spain in a step-wise manner to its pre-deformational state by:

1) defining the true present-day shape of the arc.

2) unfolding the radial sets of folds.

3) translating the thrust sheets according to the shortening produced by the folds.

4) rotating the thrust sheets according to field evidence concerning the motion direction and the overlapping amplitude.

Hirt et al. (1992) attempt to further constrain the reconstruction of the Cantabrian Arc by defining more accurately its original shape and whether it possessed any primary curvature. Palaeomagnetic data from around the Cantabrian Arc was corrected for local tectonics and rotation around a vertical axis to allow for the superimposed radial folding on earlier structures. The corrected palaeomagnetic declinations were found to vary systematically along the arc of the fold belt indicating that it possessed a original curvature which may have mirrored the depositional margin.

The example of the Cantabrian Arc is relatively complex due to the important rotational component of the thrust sheets. The translational and rotational components have been evaluated separately using field evidence such as the direction of displacement vectors of thrust sheets and the overlapping amplitudes (Julivert & Arboleya 1984). The Prebetic Arc, which experiences a more localised rotation of thrust sheets with a lesser magnitude, allows a more accurate attempt at areal balancing.

Representative stratigraphic sections can be compiled for various sub-areas within an orogenic belt and reconstruction of these using approximate vector paths established by the 3-D reconstruction may allow the initial distribution of the undeformed stratigraphic sequence to be established.

Within the boundaries of the reconstructed region the volume pre- and post-deformation should remain constant. Simplified calculation and comparison of these volumes can provide a strong control on the reliability of the reconstructed initial geometry.

6.2. Restoring the Prebetic Arc

A scaled drawing of the arc of the External Prebetics including the location of the three balanced sections, the Cazorla, Jumilla and Elche sections, was constructed. The balanced sections were divided into segments using the variance of the amount of strain experienced along the section and the timing of deformation as selection criteria. The segments used in this reconstruction correspond to those determined using the cumulative displacement-distance method of Chapman & Williams (1984). The original lengths of the segments were also calculated by this method of analysis (section 5.2.). The restoration was carried out over four discrete time periods to elucidate the intermediate stages of deformation and the varying translation paths for material from different areas of the arc. The transport directions for the Cazorla and Elche balanced sections are well constrained due to kinematic data collection presented in this study (section 2.2). The transport direction of the Jumilla section is less well constrained in this study. The orientation of the section, 120° and parallel to the Cazorla section, is approximately perpendicular to the strike of the deformation. Results of palaeostress analysis of fault-slip data and stylolites for the eastern Prebetic Zone in the Early-Mid Miocene by De Ruig (1990) indicate a maximum compression direction in the area of the Jumilla section at approximately 110°-140 °.

The division of the deformation into four discrete time periods (late Burdigalian-early Seravallian, mid-late Seravallian, Tortonian and Messinian) is based on timing evidence from field studies and literature reviews which is summarised and illustrated in section 2.3. The Cazorla and Jumilla sections are pinned onto the stable Meseta, whereas the Elche section contains a pseudo pin-line and therefore undergoes translation other than that calculated in its 2-D restoration.

Figs 6.2.1.a)-d). show the successive restoration of the External Prebetics between the Cazorla and Jumilla sections using the External/Internal Prebetic boundary as a convenient marker to illustrate the successive stages of areal reduction.

In the Messinian, deformation occurred predominantly in the NE Trending Limb and the Alcaraz Antitaxis. Fig 6.2.1.a) illustrates the restoration of the most foreland segments of the Cazorla section, C3 and C2.

In the Tortonian, deformation occurred predominantly in the hinterland parts of NE Trending Limb and the Alcaraz Antitaxis and the foreland parts of the NW Trending Limb and the area further to the east. Fig 6.2.1.b) illustrates the restoration of the most hinterland segment of the Cazorla section, C1, and the foreland segment of the Jumilla section, J2. The Elche segment which has not been pinned to the stable foreland, has undergone a certain amount of later northwesterly translation which needs to be restored prior to the restoration of the Elche section itself. Although it is difficult to quantify this translation exactly, an average figure of 23% total shortening along 120°, comparable to that experienced by the Jumilla

section which is also located to the NE of the Socovos Fault, is a reasonable first estimate. Therefore, the Elche section is displaced to the SE by an amount comparable to the shortening shown in segment J2 of the Jumilla section.

In the Mid-Late Seravallian, deformation occurred predominantly in both the middle part of the NW Trending Limb and along the Socovos Fault, due to strain partitioning, and in the hinterland part of the area to the east. Fig 6.2.1.c) illustrates the restoration of the hinterland segment of the Jumilla section, J1, and the foreland segment of the Elche segment, E2. The Elche section is displaced to the SE by an amount comparable to the shortening shown in segment J1 of the Jumilla section, giving a total shortening of 23% along 120° due to the dextral strike-slip motion exhibited along the Socovos Fault. The overall transport direction for the NW Trending Limb during this time period was, therefore, to the NNW. The deformation in the NW Trending limb has been divided into its strike parallel (strike-slip along the Socovos Fault) and strike perpendicular (NE thrusting) components for ease of reconstruction. It must be emphasised that these deformational components occurred due to strain partitioning and show synchronous activity.

In the late Burdigalian-early Seravallian, deformation occurred predominantly in the NW Trending Limb and was centred about the Socovos Fault due to the partitioning of strain both parallel and perpendicular to it. The overall transport direction for the area around the Socovos Fault which includes part of the NW Trending Limb and the Internal Prebetics was to the NNW as in Fig 6.2.1.c). At this early time, much of the NW directed motion of the block to the SW of the Socovos Fault occurred within the foreland part of the Internal Prebetics and

therefore is not incorporated into this reconstruction of the External Prebetics. Fig 6.2.1.d) illustrates the restoration of the hinterland segment of the Elche segment, E1. The Cenajo Syntaxis cannot be accurately reconstructed due to the convergent transport directions giving rise to non-planar strain. An approximate reconstruction is obtained from interpolation between the locations of the External/Internal Prebetic Zone boundary derived from the reconstructions of the Elche and Jumilla sections. The initial location of the External/Internal Prebetic boundary and the original geometry of the External Prebetics in plan view are shown.

The dextral strike-slip of the Socovos Fault is sequentially restored as the Cazorla and Jumilla sections, which are sub-parallel to this strike-slip motion, are reconstructed. This results in a graphical estimation of a minimum displacement along the Socovos Fault in the External Prebetics of 45-53 km. This value is in the same order as the 35-40 km calculated for the Linea Electrica Fault, the eastward transfer of the Socovos motion onto the Subbetic/Internal Prebetic boundary, by Baena Perez & Jerez Mir (1982). The initial geometry of the External Prebetics can be shown to be arcuate in plan view. Strike-slip motion was probably initiated preferentially in the area where the boundary is oriented approximately NW-SE. With continued differential deformation across the Socovos Fault, the arcuate feature becomes exaggerated and the hinge angles of the antitaxis and syntaxis decrease. The orientation of the Socovos Fault appears to undergo a slight clockwise rotation with time until it becomes sub-parallel to the overall tectonic displacement vector of the hinterland Subbetic Zone and Internal Prebetic Zone. After this occurs during the Late Seravallian/Early Tortonian, a large amount of NW displacement is facilitated in the NE

Trending Limb. A cartoon of the variation of the approximate location of the deformation front through time is shown in Fig 2.3.5.

6.3. Calculation of the deformation

The overall reduction, in the horizontal plane, of the area of the External Prebetics between the Cazorla and Jumilla sections may be determined graphically from scaled drawings of the post-deformation geometry and reconstructed original geometry.

In the specified region:

The post-deformational horizontal area is 4,850 km^2.

The original horizontal area is 8,825 km^2.

$\therefore$ the overall reduction in horizontal area is 3,975 km^2

i.e. 45% reduction

This magnitude of areal reduction calculated for the Prebetic Arc is very close in value to the 50% calculated for the Cantabrian Arc by Julivert & Arboleya (1986).

The amount of areal reduction can also be calculated for each of the four stages of the reconstruction.

Stage	Reduction in area (km^2)	Cumulative reduction in area (km^2)
Late Burdigalian-early Seravallian	375	375
Mid-late Seravallian	750	1125
Tortonian	1200	2325
Messinian	1650	3975

Fig 6.3.1. shows a plot of the amount of areal reduction through time, from the late Burdigalian to the end of the Messinian. This emphasises the steady increase in the area involved in the deformation per unit time. The rate of areal reduction can be calculated for each deformational stage.

Stage	Rate (km^2/Ma)
Late Burdigalian - early Seravallian	197
Mid-late Seravallian	395
Tortonian	324
Messinian	1100

Fig 6.3.2. shows the variation of the rate of deformation during the four stages. The results of this plot indicate that the rate of deformation in the External Prebetics did not remain constant over the 9 Ma in which deformation occurred. In the Seravallian there was a gradual increase in the rate of deformation in the External Prebetics. This is explained by the gradual increase in deformation as material is added to the toe of the orogenic wedge, formed in the hinterland, and which includes the Subbetic and Internal Prebetic thrust sheets. There is a slight decrease in the rate of deformation in the Tortonian which may be related to the formation of the `Tranco zone', where deformed Triassic is exposed at the erosional surface i.e. above regional. This zone was formed by the overthrusting of a thrust slice whose sole thrust lay within the Triassic and which was subsequently uplifted by underthrusting and duplex formation. There is a two-fold increase in the rate of deformation in the Messinian where the deformation is located predominantly in the NE

Trending Limb. This increase coincides with the final ramping up of the basal décollement from within the Triassic to the Triassic/Jurassic interface. This facilitates a greater amount and rate of shortening within the sequence of relatively thin shallow shelf carbonates and marls which comprise the NE Trending Limb and the Alcaraz Antitaxis.

Propagation rate of the Prebetic Front is 2.5 times greater for the Cazorla section than the Jumilla section.
Cazorla section 9.06 km Ma^{-1}
Jumilla section 3.57 km Ma^{-1}

6.4. Original shelf geometry

Representative post-Triassic stratigraphic sections for various locations around the present-day Prebetic Arc have been compiled from field and published data. The initial position of these sequences within the area of the undeformed shallow shelf can be reconstructed using the material translation paths for different parts of the External Prebetic Arc produced from the 3-D reconstruction (Fig 6.4.1). Fig 6.4.2. shows a post-Triassic contour plot of the reconstructed shelf geometry. A marked increase in the thickness of the sequence from the west to the east is illustrated. This increase, which becomes greater basinward, appears to be fairly abrupt in nature and the presence of a pre-existing heterogeneity may be invoked. Strike-slip motion may initiate preferentially in the location of this NW-SE heterogeneity and its associated area of sub-parallel strike. This indication of a greater degree of subsidence occurring in the east of the area is also indicated from the results of analysis of the variations in basement and tectonic subsidence around the Prebetic Arc (section 3.2.1). The shallower nature of the westerly area is also indicated by the presence of localised stratigraphic gaps representing periods of temporary emergence and hence a large increase or decrease in

Post deformational volume does not include a calculation of the volume of material eroded as most of the material was trapped in the syn/post deformational basins, within the Preberth Zone, which are included in the calculation.

stratigraphic thickness over a small area (comparison of stratigraphic sections shown in Fig 2.1.4).

Inclusion in Fig 6.4.2. of the thickness of the most foreland sequences of the deeper shelf Internal Prebetics indicates a more dramatic increase in the thickness of the sequence across the External/Internal Prebetic boundary in the west than in the east.

On completion of the reconstruction of the initial shelf geometry, a comparison of the approximate initial and post-deformational volume of the External Prebetics enclosed between the Cazorla and Jumilla sections is possible. For the reconstruction to be valid the post-deformational volume must not be significantly different from that calculated for the initial undeformed External Prebetic sequence.

Fig 6.4.3. shows the geometrical division of the pre- and post-deformational External Prebetics used to calculate the approximate volumes. The Mesozoic thicknesses used in the volume calculation for the pre-deformational reconstruction are obtained by combining the post-Triassic thicknesses shown in Fig 6.4.1. with the Triassic thickness obtained from literature and bore-hole data (e.g. Garcia-Hernandez et al. 1980, Banks 1985, Banks & Warburton 1991). The volume of the post-deformational thrust pile is obtained from the contour plot of thrust pile thickness calculated from gravity modelling techniques (Fig 4.4.2). For each small area the vertical cross-section is approximated to a upper rectangle and a lower triangle, where the gradient of the basement is assumed to be planar (Fig 6.4.4).

Volume = (volume of upper box) + (volume of lower wedge)

Volume = (length × width× [max elevation–min contour]) + (length × width × [max–min contour] × 0.5)

Post-deformational geometry	Volume (in km^3)	Pre-deformational geometry	Volume (in km^3)
a	120	a	2844
b	600	b	7560
c	750	c	2460
d	882	d	6188
e	750		
f	2,508		
g	924		
h	5,880		
i	2,240		
j	1,848		
k	2,250		
l	2,048		
TOTAL	20,800 km^3	TOTAL	19,052 km^3

The results of these calculations show that, within the errors of the approximation, the volume of the area of the External Prebetics between the Cazorla and Jumilla sections remains constant during deformation i.e. there is no significant loss or gain of material. This constancy of volume indicates, in a similar manner to that involved in balancing 2-D cross-sections, that the reconstruction is viable but non-unique.

At a more detailed scale this volume balance would probably break down due to the local variations in transport directions.

6.5. Summary of results and comparison with previous reconstruction

An 'areal balancing' or reconstruction in 3-D of the External Prebetics was constructed by restoring the known amounts of deformation obtained by the construction of three balanced cross-sections at various locations around the Prebetic Arc (chapter 5). The resulting pre-deformational 3-D reconstruction was attained by restoring the segments of the balanced sections in reverse order of formation in four discrete time steps. The initial geometry of the External Prebetics can then be shown to be arcuate in plan view. The dextral strike-slip of the Socovos Fault is sequentially restored as the Cazorla and Jumilla sections, which are sub-parallel to this strike-slip motion, are reconstructed. This results in a graphical estimation of a minimum displacement along the Socovos Fault in the External Prebetics of 45-53 km. Strike-slip motion was probably initiated preferentially in the area where the boundary is oriented approximately NW-SE. With continued differential deformation across the Socovos Fault, the initial arcuate feature becomes exaggerated and the hinge angles of the antitaxis and syntaxis decrease.

The overall reduction, in the horizontal plane, of the area of the External Prebetics between the Cazorla and Jumilla sections was determined graphically from scaled drawings and a value of 45% was indicated. The rate of the deformation varied during this Miocene deformation. In the Seravallian there was a gradual increase in the rate of

deformation, then a decrease in the Tortonian, possibly associated with the formation of the 'Tranco Zone' and then a two-fold increase in the rate of deformation in the Messinian when the final ramping up of the basal décollement from within the Triassic to the Triassic/Jurassic interface occurs.

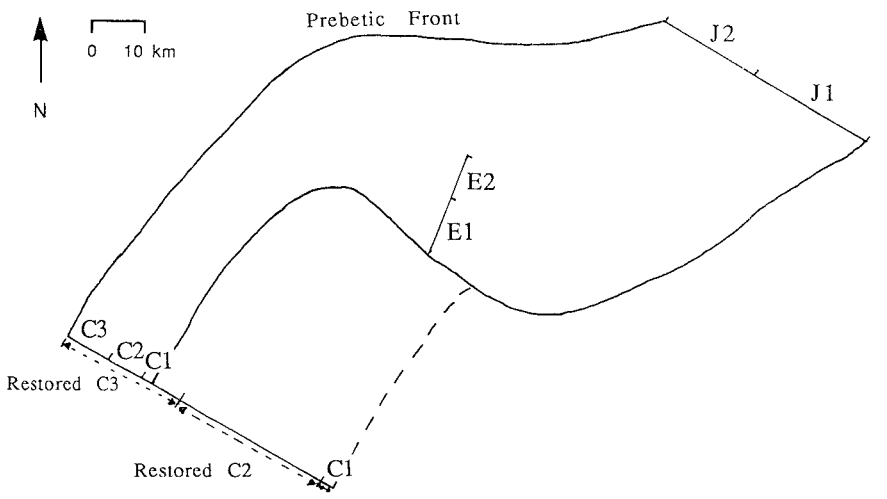
The original shelf geometry shows a marked increase in the thickness of the stratigraphic sequence from west to east. This increase, which becomes greater basinward, appears to be fairly abrupt in nature and the presence of a pre-existing heterogeneity is invoked. Calculation of the pre- and post-deformation volumes of the area indicate that they are not significantly different and the 3-D reconstruction is valid.

The main reconstruction of the Prebetic Arc which exists in the literature is that of Garcia-Hernandez et al. (1980) and is displayed in Fig 6.5.1. There are several drawbacks with this reconstruction based on stratigraphic and tectonic data rather than a graphical reconstruction along known translation paths. The existence of a significant amount of NE-SW shortening in the NW Trending Limb is ignored and only NW displacement is inferred. The amount of shortening, both to the west and to the east of the Socovos Fault, does not agree with that obtained from the construction of balanced sections. To the west of the Socovos Fault the shortening is estimated at about 15 km (after Dabrio & Lopez-Garrido 1970) compared to the 48.2 km calculated along the Cazorla section. To the east of the Socovos fault, there appears to be no significant shortening in the External Prebetics of the Garcia-Hernandez et al. (1980) reconstruction compared to the 12.4 km calculated along the Jumilla section.

CHAPTER 6

FIGURES

a)



b)

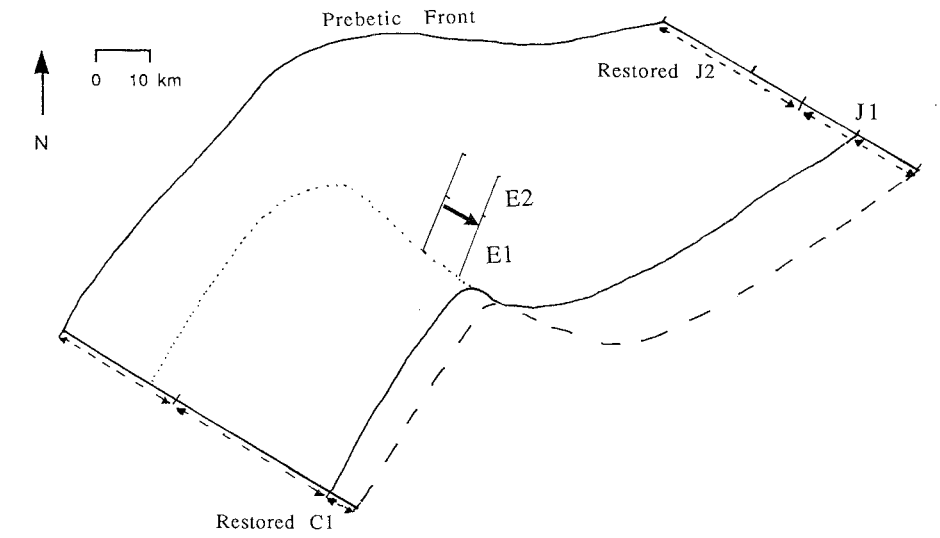
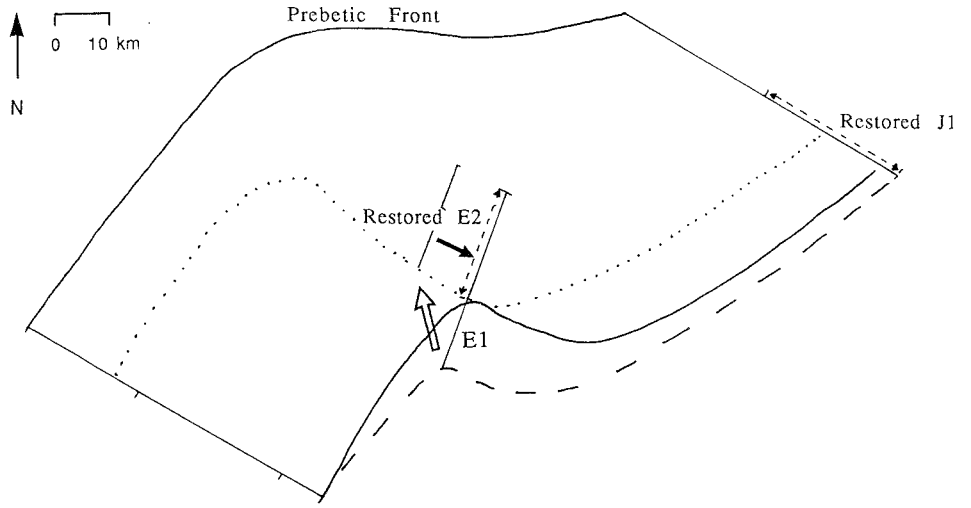


Fig 6.2.1.a) Reconstruction of Messinian deformation. Segments C3 and C2 of the Cazorla section are restored to their original lengths. The thick line is the present day External/Internal Prebetic Zone Boundary (EIPZB). The dashed line represents the position of the pre-Messinian EIPZB.

Fig 6.2.1.b) Reconstruction of Tortonian deformation. Segments C1 of the Cazorla section and J2 of the Jumilla section are restored to their original lengths. The dotted line is the present day EIPZB. The dotted line is the present day EIPZB, the thick line is the pre-Messinian EIPZB and the dashed line is the position of the pre-Tortonian EIPZB. The Elche section itself is passively restored to a position to the southeast using an amount of shortening comparable to that experienced by the Jumilla J2 segment.

c)



d)

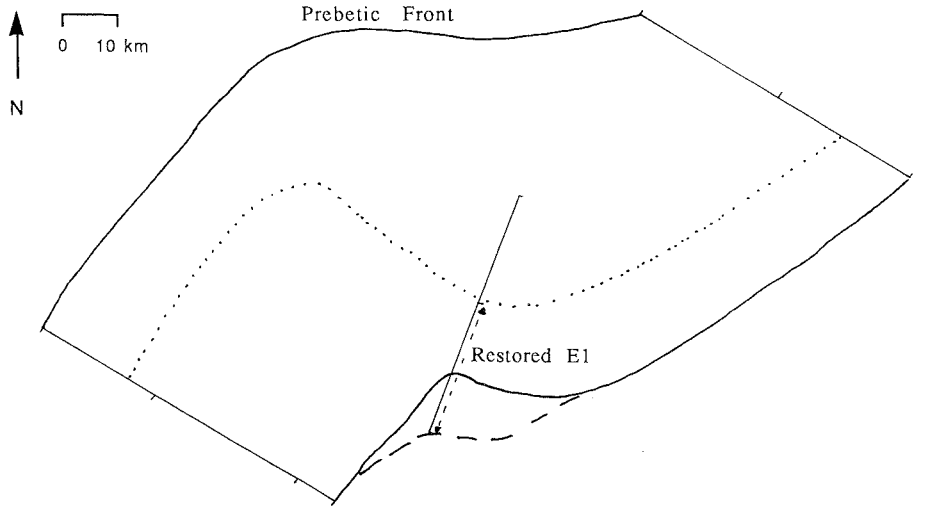


Fig 6.2.1.c) Reconstruction of Mid-late Seravallian deformation. The Elche section is again restored to a position to the southeast using an amount of shortening comparable to that experienced by the Jumilla J1 segment. Segments J2 of the Jumilla section and E2 of the Elche section are then restored to their original lengths. The dotted line is the present day EIPZB, the thick line is the pre-Tortonian EIPZB and the dashed line is the position of the pre-Mid-Late Seravallian EIPZB. Open arrow-overall transport direction for the NW Trending Limb.

Fig 6.2.1.d) Reconstruction of late Burdigalian-early Seravallian deformation. Segment E1 of the Elche section is restored to its original length. The dotted line is the present day EIPZB, the thick line is the pre-Mid-Late Seravallian EIPZB and the dashed line is the position of the pre-upper Burdigalian-lower Seravallian EIPZB.

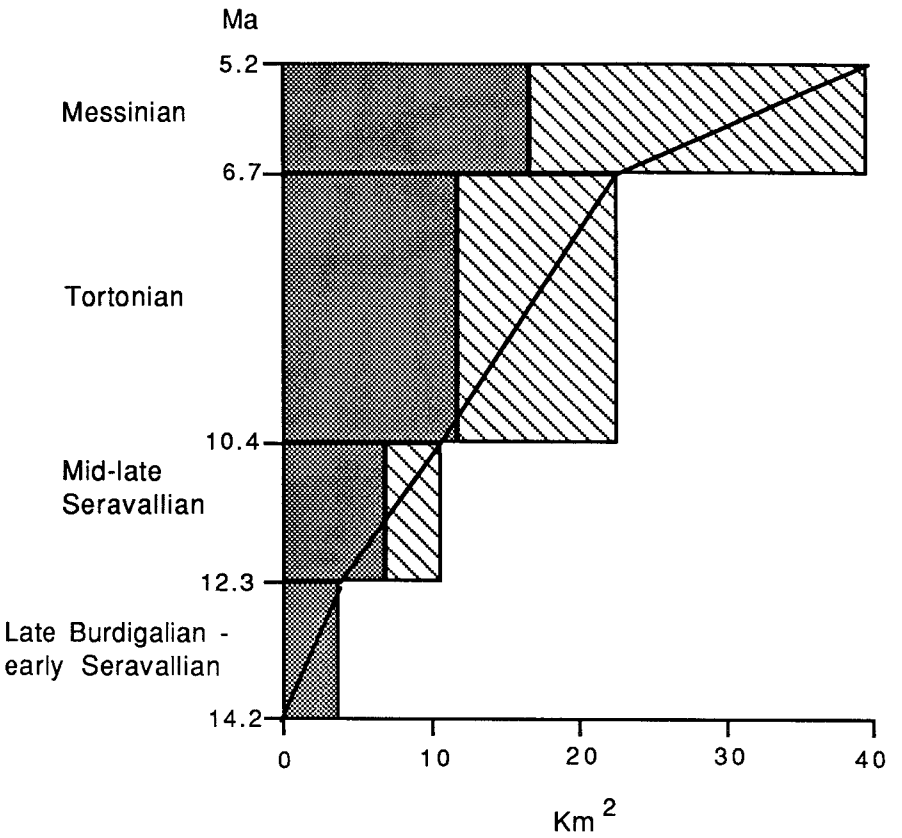


Fig 6.3.1. The amount of areal reduction of the External Prebetics through time. Dark stipple-amount of areal reduction for each time division, diagonal stripes-cumulative areal reduction for each time division, solid line-cumulative areal reduction through time.

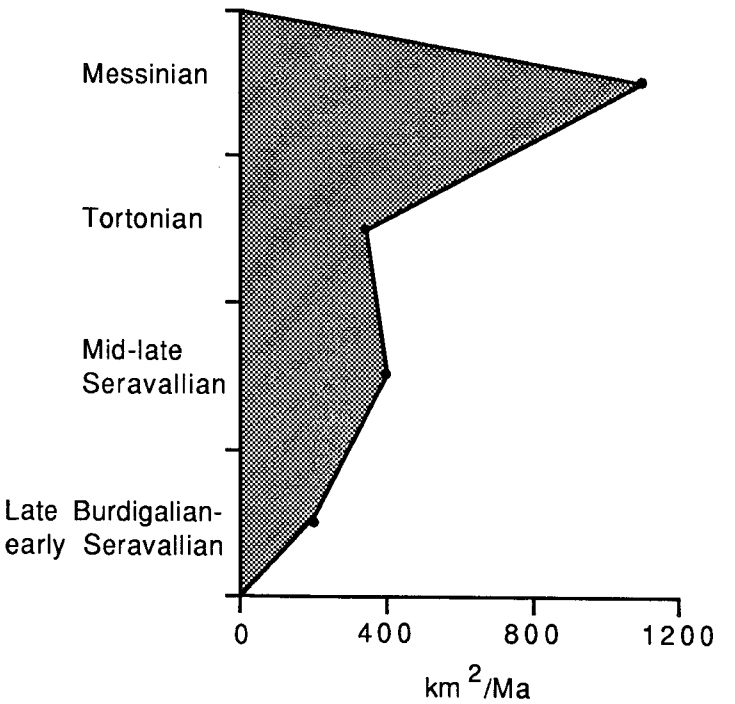


Fig 6.3.2. Variation in rate of deformation during the four time divisions. See text for more details.

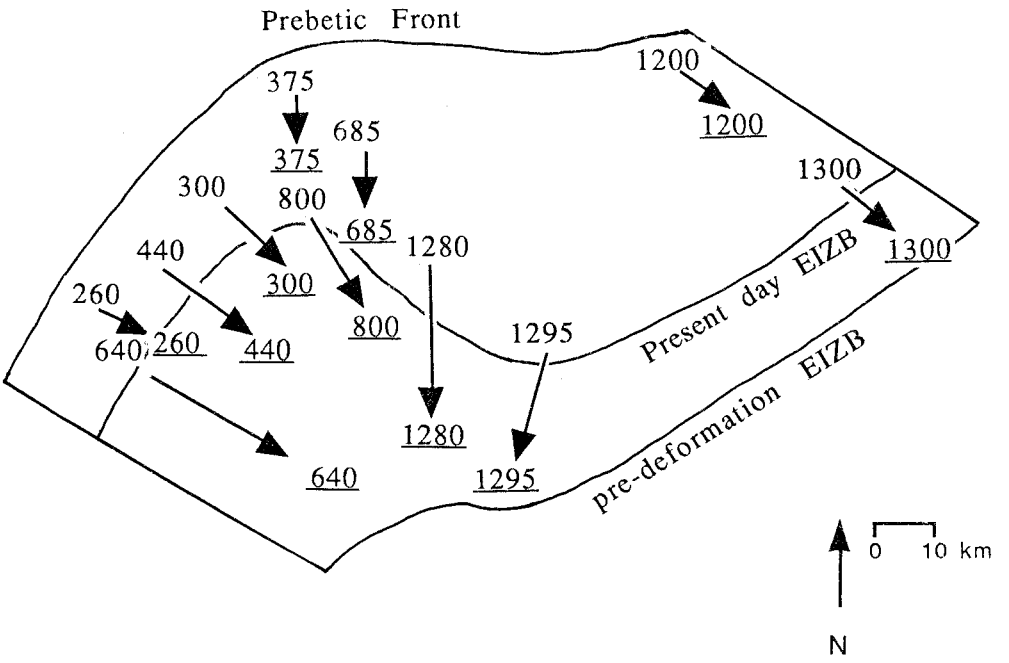


Fig 6.4.1. Restoration of representative post-Triassic stratigraphic sequences to their original pre-deformational locations along translation paths obtained from the area restoration. The thicknesses shown are in metres.

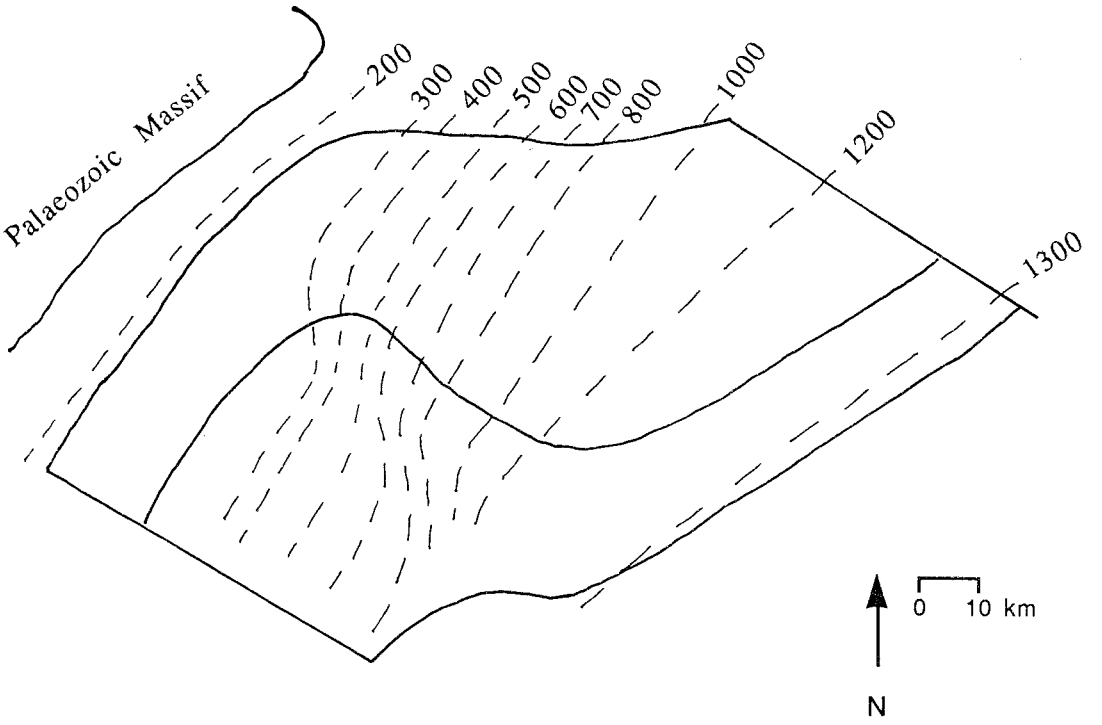


Fig 6.4.2. Contour plot of the post-Triassic thickness of the original shelf sequence of the External Prebetics. The contours are in metres.

The deformation to the east propagated onto a deep Mesozoic sequence whereas the deformation to the west propagated onto the Meseta. This may influence the formation of a foreland basin.

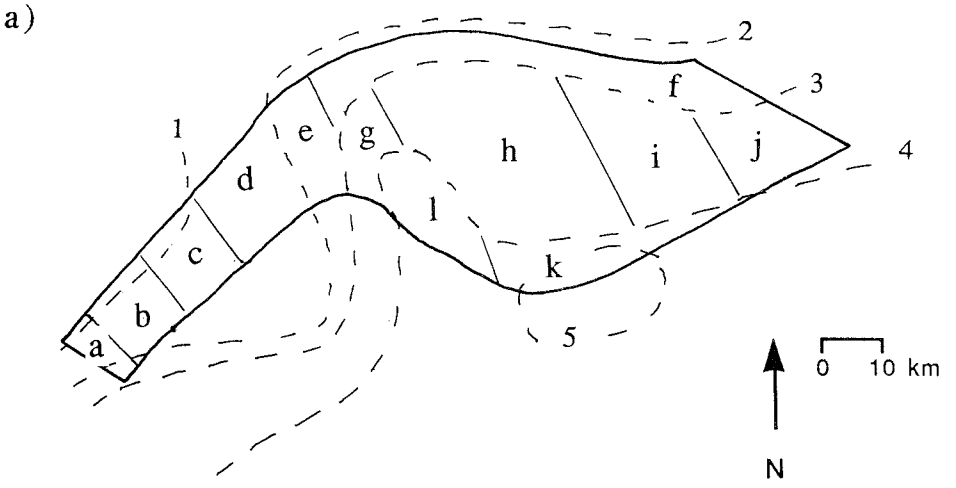


Fig 6.4.3.a) Geometrical division of the External Prebetics used to calculate the post-deformational volume. The contours are in kilometres and refer to those calculated from gravity modelling and are shown in Fig 4.4.2.

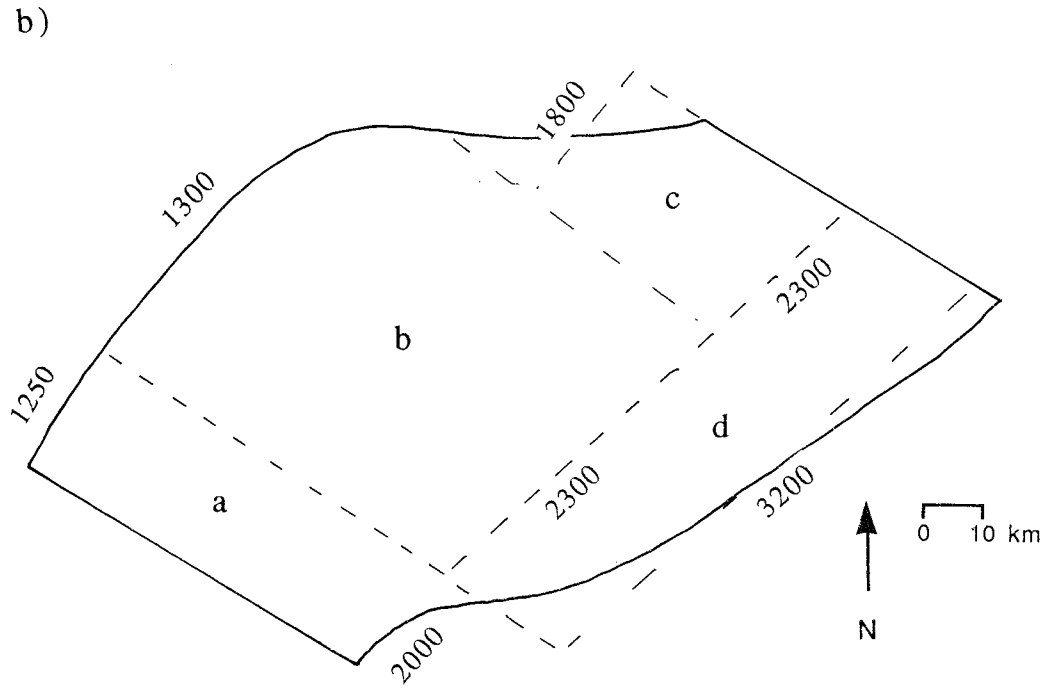


Fig 6.4.3.b) Geometrical division of the External Prebetics used to calculate the pre-deformational volume. The values shown are in metres and represent the thickness of the Mesozoic section.

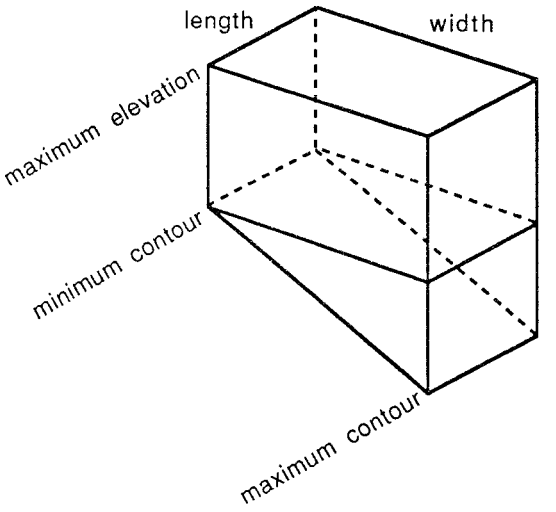


Fig 6.4.4. Geometrical approximation for volume calculations

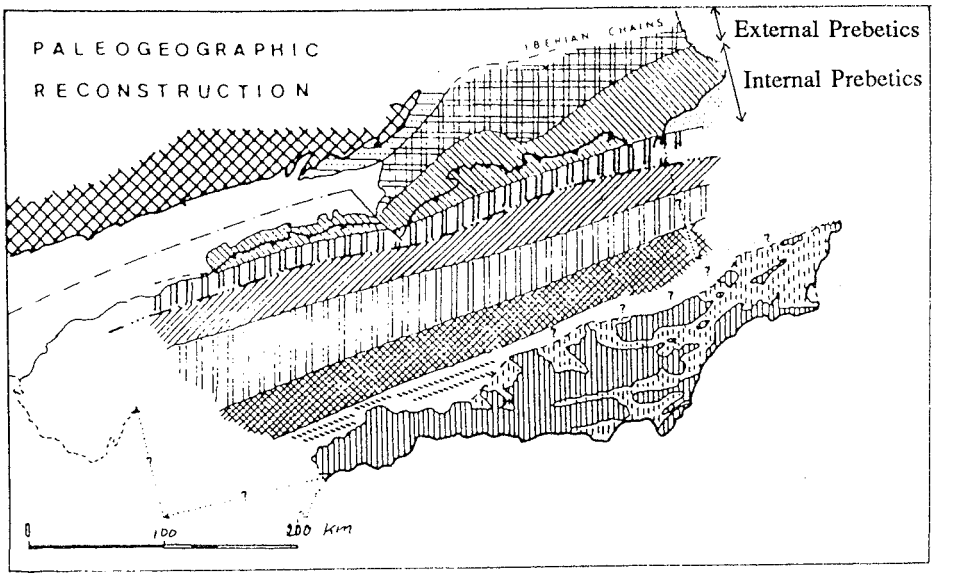


Fig 6.5.1. Previous reconstruction of Garcia-Hernandez et al. (1980).

Chapter 7

CHAPTER 7

INTEGRATED SYNTHESIS AND CONCLUSIONS

7.1. Summary of results of the structural study of the Prebetic Arc

The Prebetic Arc poses many interesting problems for an inquiring structural geologist. How does the style of deformation, both at the surface and at depth, vary around the arc? What is the detail of its deformational history through time? When and why has it experienced episodes of both extension and compression? Can a valid reconstruction of the original 3-D geometry be produced from the available structural data?

These problems have been addressed in the previous chapters by using a variety of structural and geophysical techniques which included field mapping and kinematic data analysis (chapter 2), preliminary palaeomagnetic studies (chapter 2), backstripping of stratigraphic sections to produce tectonic subsidence curves (chapter 3), gravity profiling and modelling (chapter 4), construction of balanced cross-sections (chapter 5) and 3-D areal balancing (chapter 6). A summary of the results of these analyses is shown in Table 7.1 and described below.

The deformation in the Prebetic Zone was initiated during the late Burdigalian-early Seravallian and propagated towards the foreland from the Subbetic Front to the NNW/NW by frontal accretion of new material onto a deforming thrust wedge in a wave of deformation that became more WNW directed with time. Deformation also nucleated around, and propagated outwards from, the dextral Socovos wrench fault. The differential displacement and the partitioning of strain across the Socovos fault, into strike-slip motion parallel to the fault and orthogonal NE-SW thrusting/backthrusting, caused the formation of firstly, the Cenajo Syntaxis and NW Trending Limb and with progressive deformation the Alcaraz Antitaxis and the NE Trending Limb. The Cenajo Syntaxis

underwent convergent displacement with NW thrusting in the east and NE thrusting in the west arising as a result of strain partitioning across the Socovos Fault. Superposition of these trends of deformation was due to the tightening of the hinge area with time. The Alcaraz Antitaxis underwent divergent displacement as extension in the outer arc was accommodated The hinge angle was tightened as deformation continued and interference with obstacles in the foreland occurred. The anticlockwise swing in the displacement trend of the NE Trending Limb, from NW to WNW, was facilitated by movement along WNW-ESE oriented tear faults.

In the Internal Prebetics, deformation occurred from the upper Burdigalian to the Tortonian.

For the External Prebetics, in the late Burdigalian-early Seravallian, deformation occurred predominantly in the NW Trending Limb and the Socovos Fault due to the partitioning of strain both parallel and perpendicular to it. In the mid-late Seravallian, deformation occurred in both the middle part of the NW Trending Limb and the Socovos Fault and in the hinterland part of the area to the east. In the Tortonian, deformation occurred predominantly in the hinterland region of the NE Trending Limb and the Alcaraz Antitaxis, and the foreland region of the NW Trending Limb. In the Messinian, deformation occurred in the NE Trending Limb and the Alcaraz Antitaxis.

The models which have been proposed in recent literature to account for the formation of arcuate orogens may be divided into the following seven different mechanisms: i) later noncoaxial deformation, ii) movement along wrench faults and within shear zones, iii) the

generation of local body forces, iv) the presence of an originally irregular continental margin and hence facies distribution, v) the action of a rigid indentor against the deforming margin, vi) the presence of one or several obstacles in the foreland, vii) formation of independent thrust corridors.

The mechanism for the formation of the Prebetic Arc may be obtained from analysis of this detailed structural study of the variation of the style of deformation, both spatially and temporally. Hence, the formation of the arc was found to be predominantly due to movement along, and the differential shortening across, a wrench fault i.e. the Socovos Fault (model ii). The presence of obstacles in the foreland had a minor affect on tightening the hinge of the Alcaraz Antitaxis (model vi). The External Prebetics possessed a slightly arcuate original form due to the strong control of an irregular continental margin on deposition of sedimentary facies which had a minor contributory role in the formation of the arc and may have had an influence on the location of the Socovos Fault (model iv).

The style of deformation exhibited in the Prebetic Arc and the mechanism for its formation cannot be predicted from relative plate motion vectors (Shackleton & Ries 1984, Baird & Dewey 1986) or previous models for the formation of the Betic-Rif Orogen. Local body forces associated with shear faults and obstacles, and the partitioning of strain all exert a strong influence on the strain pattern. The change in the overall tectonic transport direction from NNW to NW to WNW may have resulted from changes in the relative plate motions. A change to a more WNW direction in the relative motion vector of Africa with respect to Europe at 9 Ma is documented by Helman (1989) and Dewey et al. (1989).

Backstripping of a series of stratigraphic sections compiled from different locations around the arc produced a set of basement and tectonic subsidence curves, which allowed a more detailed study of the timing and duration of the different extensional and compressional events that occurred in the Prebetic area.

The tectonic subsidence curves indicate an initial subsidence in the Triassic, which then decayed exponentially in the Jurassic, Cretaceous and early Tertiary which is indicative of a stretched continental margin exhibiting a phase of gentle subsidence followed by thermal relaxation. Theoretical subsidence curves, generated by the uniform stretching model, were fitted to these tectonic subsidence curves allowing the stretching factor, ß, to be estimated. There is a gradual increase in ß from the western to the eastern External Prebetics, which may have given rise to an irregular continental margin and associated distribution of the sedimentary facies. There is also a notable increase in ß, basinward, from the External Prebetics through the Internal Prebetics to the Subbetic Zone. There is a greater contrast in the amount of subsidence occurring between the External and Internal Prebetics in the west than in the east. Extension was accommodated differently in the western and eastern Prebetic Zone; in the west, deformation was concentrated on a few, large-displacement faults; whereas in the east, it was more pervasive and accommodated by many small-displacement faults.

Some of the more internal sections show a marked increase in subsidence within the Cretaceous, which was probably due to local pulses of extension. In the Internal Prebetics two exclusive periods of increased subsidence are observed, at the Jurassic/Cretaceous boundary and within the Albian, but not within every section.

Tertiary deposits, which are absent in the NE trending limb, increase in distribution around the arc and into the Internal Prebetics and the Subbetic Zone. The sections from the Alcaraz Antitaxis and the NW Trending Limb show only very minor amounts of subsidence in the Miocene whereas the section from the Cenajo Syntaxis shows a marked increase in subsidence rate during this time. The four sections in the Internal Prebetics all show a certain amount of rapid subsidence in the Miocene. More detailed investigation of the eastern and western regions, separated due to the presence of the dextral Socovos Fault, shows that there is a variation in the timing of the onset of the main deformation. The subsidence curves show the variation in the timing of the initial deviation from the exponentially decreasing subsidence path to that of increased subsidence in both the east and the west. In the east, initial basin formation varies from 30-25 Ma (Oligo-Aquitanian) for the Internal Prebetics to about 20-15 Ma (Burdigalian/Langhian/early Seravallian) for the Cenajo Syntaxis to 15-10 Ma (mid-late Seravallian/early Tortonian) for the area located close to the undeformed foreland. Whereas, in the west, the initial basin formation varies from 23-20 Ma (Aquitanian/Burdigalian) in the Internal Prebetics close to the present Subbetic Front to about 15-10 Ma (mid-late Seravallian/early Tortonian). This compares well with the timing of the initiation of deformation around the arc, compiled from structural and sedimentological data, rather than that of the main deformation.

This deviation in Miocene subsidence rates from the theoretical curve and does not represent a Mesozoic rift-related phenomena nor a new phase of rifting as the subsidence rate appears to increase in time i.e. is convex in shape, and no thermal relaxation phase is present. The areas which show this rapid Miocene subsidence were probably subject to a

greater amount of loading locally, due to the emplacement of relatively thick Internal Prebetic/Subbetic thrust piles from the SE. The basins formed by a local flexural response to this loading are not foreland basins sensu stricto, as with continued deformation towards the foreland they were carried towards the foreland in a passive, piggy-back style and received a sediment supply from both hinterland and foreland thrust slices.

Five profiles across the eastern Betic Cordillera, which sub-parallel the tectonic transport direction, were chosen for gravity modelling to elucidate the subsurface structure. The gravity anomalies over hypothetical, but well constrained, 2-D crustal cross-sections were calculated based on line-integral methods and altered, iteratively, until a best fit with the observed gravity anomaly measured along each section was obtained.

Analysis of the regional structure shows a marked lateral change across the eastern Betic Cordillera. The most westerly section indicates the presence of a small crustal root under the Internal Zones which becomes reduced in the profiles to the east where the Moho becomes shallower and its gradient decreases. This occurs landward of the coast indicating that the transition between stretched and unstretched crust is narrow and located beneath onshore regions. The most easterly section shows an increase in Moho gradient and thinning of the Iberian crust which may be related to stretching in the Valencia trough.

Analysis of the upper crustal shows a decreasing gradient of the basement/Prebetic-Subbetic thrust pile interface from west to east in the Prebetic Zone, which may be due to the local loading affects of the thrust

pile which appears to be thicker and to have undergone a greater amount of shortening in the west. The frontal nose of the Internal Zone which wedges beneath the Subbetic Zone, was located at the point of the gravity minima. This feature becomes less well defined and more complex towards the east. The non-alignment of the contours on the map of the basement elevation with the Socovos fault indicate that this is a thin-skinned feature across which there is no significant change in the basement structure. The very short wavelength negative anomalies are due to the presence of low density Tertiary and Quaternary basins.

The Bouger gravity anomaly set for the area was filtered by using a 2-D band pass to remove the longer wavelength (>80 km), regional structure. Features previously described for the upper crust from the results of the gravity modelling are also indicated from the filtered gravity data. Moho structures such as the crustal root inferred in the western region are not observed in the filtered gravity data.

Construction of a series of three balanced cross-sections, located at intervals from west to east, parallel to the observed tectonic transport directions allowed the amount of shortening across the Prebetic orogen to be estimated whilst also providing useful controls on the structure at depth and the correlation of décollement horizons. Two methods for calculating the amount of shortening of section, both bed length balancing and cumulative displacement-distance analysis, were applied to the three balanced sections. The results of these calculations show a west to east decrease in shortening strain from 69% to 54% to 21% ±6% calculated error. The decrease from 69% to 54% across the major Socovos wrench fault indicates that there is no dramatic decrease in the amount of

deformation to the east of this fault. The component of deformation to the NW (sub-parallel to the movement along the Socovos Fault), however, does decrease significantly across the Socovos Fault with most deformation occurring in the orientation of the other component of partitioned deformation, i.e. approximately perpendicular to the Socovos Fault. The amount of NW strain exhibited in the Elche section was obtained using the graphical method of Cooper (1983) applied to an oblique section oriented at 120-130° and gave values for an oblique section which varied between 5% and 18% shortening.

The most north-westerly segment of the Cazorla section shows a decrease in bulk strain to below the average for that section due to the influence of the Palaeozoic Massif, present in the undeformed foreland which gives rise to an increased continental component to the Triassic, preferentially used as a décollement horizon. The strain for the Jumilla and Elche sections show an increase towards the foreland where there is a basin of Mesozoic sediments compared to the Palaeozoic Massif which is located to the foreland of the Cazorla section. The greater amount of backthrusting exhibited in the Jumilla and Elche sections has been explained as a method of increasing the thickness of the thrust wedge during frontal accretion.

The amount of shortening exhibited in an area is a result of its position relative to main the Socovos wrench fault and the variation in the distribution of the shortening results from the differing composition and thicknesses of the stratigraphic sequence.

'Areal balancing' of the External Prebetics was attempted to provide a viable 3-D reconstruction This was completed by restoring the known

amounts of deformation obtained by the construction of three balanced cross-sections at various locations around the Prebetic Arc over four discrete time steps. Calculation of the pre- and post-deformation volumes of the area indicated that they were not significantly different and therefore 3-D reconstruction is valid. The initial geometry of the External Prebetics can then be shown to be arcuate in plan view with a marked increase in the thickness of the stratigraphic sequence from west to east. This increase, which becomes greater basinward, appears to be fairly abrupt in nature and the presence of a pre-existing heterogeneity is invoked.

Sequential restoration of the dextral strike-slip of the Socovos Fault results in a graphical estimation of a minimum displacement along the Socovos Fault in the External Prebetics of 45-53 km. Strike-slip motion was probably initiated preferentially in the area where the boundary is oriented approximately NW-SE. With continued differential deformation across the Socovos Fault, the initial arcuate feature became exaggerated and the hinge angles of the antitaxis and syntaxis decreased.

An overall reduction in the horizontal plane of 45% was determined graphically from scaled drawings of the area of the External Prebetics between the Cazorla and Jumilla sections. The rate of deformation varied during this Miocene deformation. In the Seravallian there was a gradual increase in the rate of deformation, which decreased in the Tortonian, possibly associated with the formation of the 'Tranco Zone' where deformed Triassic is exposed at the erosional surface. A two-fold increase in the rate of deformation occurred in the Messinian, where the deformation was located predominantly in the NE Trending Limb and the Alcaraz Antitaxis, and coincided with the final ramping up of the basal décollement from within the Triassic to the Triassic/Jurassic interface.

The results of the structural analysis, the predicted model of formation of the Prebetic Arc and the 3-D reconstruction cannot be wholly applied to any other arcuate orogen at whatever scale although aspects may apply in some cases. Each arcuate orogen needs to be analysed systematically using every structural and geophysical tool available to provide a unique and detailed model for its formation and viable reconstructions in both 2-D and 3-D.

7.2. The model of the formation of the Prebetic Arc in regional context

The results of the structural study of the most External Zone of the Betic Cordillera, the Prebetic Zone, allow localised models to be produced for the formation of the Prebetic Arc and a detailed history and description of the deformation experienced by both the External and Internal Prebetics to be compiled. The model of formation of the Prebetic Arc and the overall tectonic transport directions and style of deformation documented for the Prebetic Zone cannot be extended to apply to the more hinterland parts of the orogen i.e. the Subbetic Zone and the Internal Zones. These results, which are from an important area at the boundary of the region of intracontinental deformation between Europe and Africa and the stable Iberian margin, can provide new evidence to support or discount existing models for the evolution of the Betic-Rif orogen.

There have been numerous models proposed for the tectonic evolution of the Betic-Rif orogen, with special reference to the formation

of the Gibraltar Arc. These models, which are more fully described in section 1.2, may be sub-divided into five main categories:

1) Gravitational sliding of nappes from a high located in the Alboran Sea.
2) Oroclinal bending of an initially linear orogenic belt.
3) Westward emplacement of a Alboran microplate with associated zones of dextral and sinistral strike slip to the north and south respectively.
4) Formation of a broad zone of dextral transpression between the Iberian and African plates.
5) Syn- or post-orogenic extensional collapse of an overthickened collisional ridge in the Alboran region.

These models of formation for the Betic-Rif orogen can be reassessed using the results of the structural study of the Prebetic Zone, which are presented in this thesis and summarized in section 7.1.

Table 7.2. evaluates the new evidence produced by this study in relation to the five main Betic evolutionary models.

1) Gravitational sliding of nappes from a high located in the Alboran Sea.

The development of large nappes which were emplaced to the north in the Betic Cordillera by gravitational sliding due to either crustal thickening or doming due to a thermal anomaly or diapir has been postulated by (Van Bemmelen 1969, Loomis 1975, Mäkel 1985, Weijermars 1985, Torres-Roldan 1979). This mechanism for orogenic formation is not currently considered viable.

2) Oroclinal bending of an initially linear orogenic belt.

Oroclinal bending of an originally linear mountain belt, formed earlier in the Betic-Rif deformation, has been postulated for the Betic-Rif orogen (Carey 1958, Didon 1969, Tubía & Cuevas 1987). The late stage oroclinal bending would have to occur after the latest stage of deformation of a 'linear' or less arcuate Betic Cordillera. As the latest deformation documented on the Prebetic Boundary Fault is of Messinian age, this would place the oroclinal bending stage post-Messinian when there is no evidence and probably an insufficient time for a significant amount of deformation. Also, results of preliminary palaeomagnetic studies in the Prebetic Zone indicate sites in Messinian marl in the NW Trending Limb which have been unrotated. If late, oroclinal bending of the Betic Cordillera did occur, approximately NW-SE wrench faults may have developed in the more foreland region of the Betic Cordillera i.e. the External Prebetics or the Tertiary foreland basin, where present, but there is no evidence for existence of these type of structures.

3) Westward emplacement of an Alboran microplate with associated zones of dextral and sinistral strike slip to the north and south respectively.

The westward displacement of an independent Alboran microplate, comprising the Internal Zones of the Betic and Rif and the Alboran Basin has been proposed by Andrieux et al. (1971), de Smet (1984), LeBlanc & Olivier (1984), Boullin et al. (1986) and Sanz de Galdeano (1990). This model fails to account for the non-rigid behaviour i.e. pervasive compressional and extensional deformation, within the Internal Zones. However, Frizon de Lamotte et al. (1989) regard the Internal Zones as a double pile of nappes which have undergone significant deformation.

Guezou et al (1991) present results of kinematic analysis in the NE Trending Limb of the Prebetic Zone and the Guadalquivir Basin, which indicate a bulk translation to the WNW. They cite this as evidence to support the model of Betic-Rif formation of Frizon De Lamotte et al. (1989) in which there is westward translation of the Alboran Domain with displacement trajectories which are independent of strike and subparallel all along the belt. Detailed study of kinematic and timing relations of the Prebetic Zone shows an anticlockwise swing in the overall tectonic transport direction from NNW to NW to WNW from the upper Burdigalian to the Messinian. Hence, it is clear that the WNW translation identified by Guezou et al. (1991) in the NE Trending Limb of the Prebetic Zone and the Guadalquivir Basin does not apply to all sub-areas of the Prebetic Zone, nor is it consistent through time.

If overall westward displacement had occurred in the External Zones of the Betic Cordillera, approximately NE-SW to E-W shear zones should have developed, especially in the Prebetic Zone due to the interference of the Palaeozoic massif located to its west. The tectonic subsidence curves compiled for various locations around the Prebetic Zone show a marked increase in subsidence rate in the Miocene due to the development of small, intramontane basins. The mechanism of formation of these basins cannot be wholly established from analysis of the tectonic subsidence curves and the possibility of the basins being formed in a transtensional strike-slip regime cannot be ruled out. The lack of basin margin strike slip faults observable in the field does not lend support to this hypothesis.

The results of gravity studies across the eastern Betic Cordillera indicate that the External/Internal Zone boundary may not be represented by the sub-vertical shear zone which is implied in the model of westward

emplacement of an Alboran microplate. A gently, foreland-dipping External/Internal Zone boundary was incorporated into the gravity models as the frontal nose of the Internal Zone can be shown to wedge beneath the Subbetic Zone.

4) Formation of a broad zone of dextral transpression between the Iberian and African plates.

Osete (1989) has interpreted the Betic-Rif orogen to have developed under the influence of a broad zone of distributed dextral strike slip. This model, however, predicts only clockwise rotations about a vertical axis in the Betic Cordillera. Preliminary palaeomagnetic studies indicate the presence of possible anticlockwise rotations in the Alcaraz Antitaxis and areas of non-rotation relative to stable Iberia in the Internal Prebetics. These results show that rotations about a vertical axis may be present within the Prebetic Zone but these are neither directionally nor spatially consistent.

5) Syn- or post-orogenic extensional collapse of an overthickened collisional ridge in the Alboran region.

Radial syn- or post-orogenic collapse of an overthickened collisional ridge situated in the Alboran region has been invoked to account for the presence of the Alboran Basin and the underlying thinned crust, and low velocity mantle (Banda et al. 1983) and provide a viable mechanism for exhuming the high P/T rocks of the metamorphic core complexes (Doblas & Oyarzun 1989, Platt & Vissers 1989). Doblas & Oyarzun (1989) propose a regional post-orogenic extensional collapse model in which they believe compressional and extensional events to be well-differentiated whereas the model of Platt & Vissers (1989) implies delamination of cold and

gravitationally unstable lithosphere from beneath the collisional ridge, giving rise to an increase in the surface elevation and gravitational potential energy of the ridge. Extension would then occur in the centre of the orogen which would drive concomitant compression in the External Zones.

Field relationships documented from the Prebetic Zone indicate that compression occurred from the upper Burdigalian to the Messinian i.e. synchronously with the extension in the Internal Zones and the Alboran Basin, which has been recorded from earliest Miocene to late Miocene times. The lack of evidence for regional extension occurring during the Tertiary in the Prebetic Zone and the presence of compression occurring up to and including the Messinian does not support the model of Doblas & Oyarzun (1989) who advocate a regional, post-orogenic extensional collapse event in the eastern Betic Cordillera from the Seravallian to the Tortonian.

During the extensional event, and up to the present day, there has been only slow relative movement between Africa and Europe. However, in the Tortonian and Messinian a significant amount of rapid shortening has been observed in the External Prebetics which then died out in the latest Messinian/Pliocene. This lack of correlation between the rate and temporal extent of relative plate movement and Prebetic Zone deformation indicates that a significant amount of the compressive deformation documented in the Prebetic Zone may have been driven by locally-induced body forces, such as the collapse of an orogenic ridge.

Therefore, no conclusive evidence for the westward emplacement of a Alboran microplate or the formation of a broad zone of dextral

transpression between the Iberian and African plates has resulted from this study and the details of structural analysis, timing, palaeomagnetic and kinematic analysis all contradict the predictions of these models. Extensional collapse of an overthickened collisional ridge in the Alboran region is, however, consistent with the results of this study (Fig 7.2.1). Syn-orogenic rather than post-orogenic extensional collapse is the mechanism indicated by the detailed analysis of timing relationships.

7.3. Future work to extend this study of the Prebetic Arc

This structural study of the Prebetic Arc has been as comprehensive as is possible considering the time and funds allotted to it. However, there are areas of study which would benefit from more extensive or more detailed analysis.

An increased kinematic data set, including more localities to the east and west and the infilling of some key areas e.g. the Alcaraz Antitaxis and the Cenajo Syntaxis, would provide tighter controls on the styles and extent of deformation across the whole Prebetic Zone. Although palaeomagnetic data proved difficult to obtain in the western External Prebetics, further exploratory studies could be made in the more easterly External Prebetics and the Internal Prebetics where there are more complete Mesozoic and Tertiary sequences and hence more lithologies which may provide a stable magnetic signal. The accuracy of the evidence for the timing of the deformation may be improved if further work into the subdivision of the Miocene is undertaken. Some units have been assigned a very broad age range e.g. upper Burdigalian-mid Seravallian or upper Miocene, and more detailed and probably specialised

palaeontological analysis is required to further define these units. Further compilation and backstripping of stratigraphic sequences in previous less studied parts of the Prebetic Zone may help to date more accurately the initiation of episodes of both extensional and compressional deformation. The results of the gravity modelling in this study may be enhanced by further profiling to the east and west in areas where there is more sub-surface coverage which can then be compared with the profiling across the Prebetic Zone to assess the validity of their proposed sub-surface structures. The balanced cross-sections and hence the 3-D reconstruction presented in this study could be extended to include the Internal Prebetics and possibly the more frontal region of the Subbetic Zone, depending on the presence or absence of significant rotations around vertical axes.

CHAPTER 7

FIGURES

	NE Trending Limb	Alcaraz Antitaxis	NW Trending Limb	Cenajo Syntaxis	Internal Prebetics
Chapter 2 Deformational variation around arc - Structure	NE-SW trending thrust faults-laterally continuous. Dextral tear faults.	Trend varies from NE-SW to E-W to NW-SE. Conjugate strike-slip faults.	NW-SE thrusts and backthrusts. Greater folding. Major NW-SE dextral Socovos Fault.	Trend varies from NW-SE to NE-SW with both intermediate E-W and N-S.	NW-SE thrusting. Greater folding. Original listric extensional faults.
- Tectonic transport direction	Gradual change from NW to NNW towards foreland. Later ESE backthrusting.	Divergent NW-N-NE transport. Later oblique backthrusting in the hinge area.	Strain partitioned into NE-SW thrusting/ backthrusting and dextral movement on Socovos wrench fault.	Convergent NE-N-NW transport. Later ESE directed deformation related to diapirism.	NW-SE thrusting and backthrusting becoming more WNW-ESE towards the foreland.
- Timing of main deformation	Tortonian-Messinian.	Tortonian-Messinian.	Upper Burdigalian - Tortonian.	Hinterland - Upper Burdigalian-Upper Seravallian. Foreland - Tortonian.	Upper Burdigalian - Tortonian.
Chapter 3 Backstripping - Mesozoic extension	? Increase in ß from W to E.	→	→	→	?? Increase in ß from ext to int PB.
- Tertiary deformation	Minor subsidence.	→	→	Increase in subsidence rate Hinterland 20-15 Ma Foreland 15-10 Ma	More rapid subsidence Hinterland 30-20 Ma Foreland 15-10 Ma
Chapter 4 Gravity modelling -Results	Decreasing gradient from west to east.	→ Intruded Adamellite anomaly.	→ Socovos Fault a thin-skinned feature.	→	Increasing influence of small Tertiary basins.
Chapter 5 Balanced sections - Structure at depth	Cazorla section. Foreland verging imbricate stack. Later backsteepening.	N/A	Elche section. Stack of thrusts and backthrusts. Development of blind-front geometries and triangle zones.	Jumilla section. (E of Cenajo Syntaxis). Similar to NW Trending Limb.	N/A
- Percentage shortening	69% shortening along 120°		54% shortening along 200°	21% shortening along 120°	
Chapter 6 3-D reconstruction - Original shelf geometry	Increase in stratigraphic thickness from west to east.	→	Marked increase in thickness.	→	Stratigraphic thickness shows a greater increase basinward.

Table 7.1. Summary of results of the structural study of the Prebetic Arc

	New evidence from the Prebetic Zone FOR:	New evidence from the Prebetic Zone AGAINST:
Oroclinal bending	No evidence	i) No evidence and an insufficient time for post-orogenic (post-Messinian) deformation. ii) Palaeomagnetic results indicate sites in Messinian marl which have been unrotated. iii) No evidence of late wrench faults developed in the more foreland region of the Betic Cordillera.
Westward emplacement of an Alboran microplate	i) One interpretation of the mechanism for the evolution of the Tertiary basins, from the tectonic subsidence curves, is that they were formed in a region influenced by a transtensional strike-slip regime.	i) Anticlockwise swing in tectonic transport direction NNW→NW→WNW from late Burdigalian→Messinian. Westward translation therefore, does not apply to all sub-areas nor is it consistent through time. ii) No development of E-W shear zones due to interference of the Palaeozoic massif located to the west. iii) No evidence for basin margin strike slip faults. iv) Wider gravity studies indicate that the External/Internal Zone boundary is not a sub-vertical shear zone but a gently, foreland-dipping backthrust.
Broad zone of dextral shear	No evidence	i) Palaeomagnetic studies do not indicate anticlockwise rotations in the Alcaraz Antitaxis and non-rotation of the Internal Prebetics rather than consistent clockwise rotations.
Extensional collapse	i) Field relationships indicate that compression from the late Burdigalian to the Messinian synchronously with extension in the Internal Zones and the Alboran Basin (earliest-late Miocene). ii) Rapid shortening in the Tortonian and Messinian which halted in the Messinian/Pliocene during slow relative movement between Africa and Europe indicates that the compressive deformation in the Prebetic Zone may have been driven by locally-induced body forces e.g. the collapse of an orogenic ridge.	i) No evidence for regional extension occurring during the Tertiary and the presence of compression up to and including the Messinian does not support the model of Doblas & Oyarzun (1989) who advocate a regional, post-orogenic extensional collapse event in the eastern Betic Cordillera from the Seravallian to the Tortonian.

Table 7.2. Summary of new evidence from this study towards the existing models of formation of the Betic-Rif orogen.

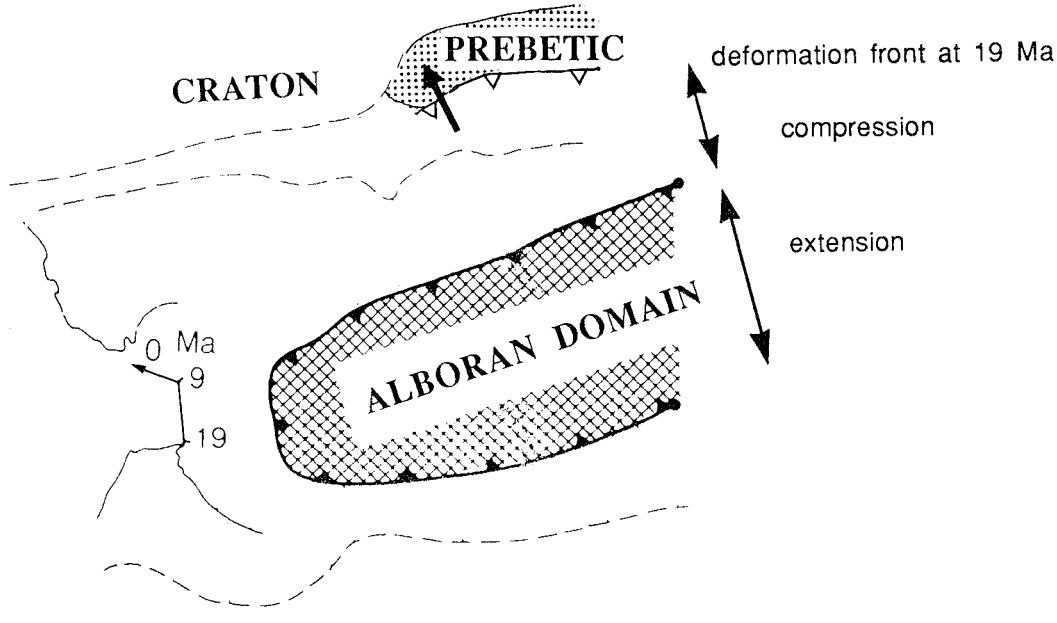


Fig. 7.2.1. Cartoon of the tectonic setting of the Prebetic Zone with respect to the extending Alboran Domain at 19 Ma. The present day coastline of Gibraltar and Morocco, and the relative plate motion vector of Africa with respect to Iberia, from 19 Ma, are also shown. Arrow-direction of compression in Prebetic Zone.

References

Allen, P. A. &. Allen, J. R. 1990. Basin analysis: principles and applications. *Blackwell*, p.451.

Allerton, S., Platt, J. P., Platzman, E.S., Lonergan, L.& McClelland, E. submitted. Palaeomagnetic evidence for a complex pattern of rotations in the eastern Subbetic Zones, S. Spain. *Earth and Planetary Science Letters.*

Alterman, I. B. 1984. The orocline hypothesis versus thin skin rotation in the central and southern Appalachians. *Geophysical Research Letters*, **11**, p.88-89.

Andrieux, J., Fontbote, J.-M., & Mattauer, M. 1971. Sur un modele explicatif de l'arc de Gibraltar. *Earth and Planetary Science Letters*, **12**, p.191-198.

Baby, P., Herail, G., Salinas, R. & Sempere, T. 1992. Geometry and kinematic evolution of passive roof duplexes deduced from cross section balancing: example from the foreland thrust system of the southern Bolivian subandean zone. *Tectonics*, **11**, p.523-536.

Baena Perez, J. &. J. M., L. 1982. Síntesis para un esayo palaeogeográfico entre la Meseta y la Zona Bética. *Inst. Geol. y Min. de España, Madrid, Colleccíon-Informe*, 256 pp.

Baird, A. W., & Dewey, J. F. 1986. Structural evolution in thrust belts and relative plate motion: the upper pennine piemont zone of the internal Alps, southwest Switzerland and northwest Italy. *Tectonics*, **5**, p.375-387.

Balanyá, J. C., & García-Dueñas, V. 1987. Les directions structurales dans le Domaine d'Alboran de part et d'outre du Détroit de Gibraltar. *C. R. Acad. Sci. Paris Ser II*, **304**, p.929-933.

Balanyá, J. C., & García-Dueñas, V. 1988. El cabalgamiento cortical de Gibraltar y la tectonica de Béticas y Rif. *II Congreso Geol. España (Simposios)*, p.35-44.

Banda, E., & Ansorge, J. 1980. Crustal structure under the central and eastern part of the Betic Cordillera. *Geophysical Journal Royal Astronomical Society*, **63**, p.515-532.

Banda, E., Udias, A., Mueller, St., Mezcua, J., Boloix, M., Gallart, J. & Aparicio, A. 1983. Crustal structure beneath Spain from deep seismic experiments. *Physics of Earth and Planetary Interior*, **31**, p.277-280.

Banda, E., Gallart, J., Garcia-Duenas, V., Danobeitia, J. J. & Makris, J. in press Lateral variation of the crust in the Iberian Peninsula. New evidence from the Betic Cordillera. *Tectonophysics.*

Banks, C. B. 1985. Internal B.P. Report.

Banks, C. B., & Warburton, J. 1986. "Passive-roof" duplex geometry in the frontal structures of the Kirthar and Sulaiman mountain belts, Pakistan. *Journal Structural Geology*, **8**, p.229-237.

Banks, C. B., & Warburton, J. 1991. Mid-crustal detachment in the Betic system of southeast Spain. *Tectonophysics*, **191**, p.275-289.

Barton, P., & Wood, R. 1984. Tectonic evolution of the North Sea basin: crustal stretching and subsidence. *Geophysical Journal Royal Astronomical Society*, **79**, p.987-1022.

Beaumont, C. 1981. Foreland basins. *Geophysical Journal Royal Astronomical Society* , **65**, p.291-329.

Bertram, G. T., & Milton, N. J. 1989. Reconstructing basin evolution from sedimentary thickness; the importance of palaeobathymetric control, with reference to the North Sea. *Basin Research*, **1**, p.247-257.

Blanco, M. J., & Spakman, W. in press. The P-wave velocity structure of the mantle below the Iberian Peninsula: evidence for subduction lithosphere below southern Spain. *Tectonophysics*.

Blumenthal, M. M. 1927. Versuch einer tektonischen Gliederung der betischen Cordilleren von Central und Südwest (Andalusien). *Eclogæ Geologicæ Helvetiæ*, **20**, p.487-532.

Boullin, J.-P., Durand-Delga, M. & Oliver, Ph. 1986. Betic-Rifian and Tyrrhenian arcs: Distinctive features, genesis and development stages. *The Origin of Arcs, edited by Wezel, F.-C.*, p.281-304.

Boyer, S. E., & Elliott, D. 1982. Thrust systems. *American Association of Petroleum Geology Bulletin*, **66**, p.1196-1230.

Brunet, M. F. 1986. The influence of the evolution of the Pyrenees on adjacent basins. *Tectonophysics*, **129**, p.343-354.

Butler, R. W. H. 1987. Thrust sequences. *Journal Geological Society of London*, **144**, p.619-634.

Carey, S. W. 1955. The orocline concept in geotectonics. *Proceedings of Royal Society of Tasmania*, **89**, p.255-288.

Carey, S. W. 1958. A tectonic approach to continental drift. *In Continental drift-A symposium: Hobart, University of Tasmania edited by Carey, S. W.*, p.177-355.

Casas, A., & Carbó, A. 1990. Deep structure of the Betic Cordillera derived from the interpretation of a complete Bouger anomaly map. *Journal of Geodynamics*, **12**, p.137-147.

Chapman, T. J., & Williams, G. D. 1984. Displacement-distance methods in the analysis of fold-thrust structures and linked-fault systems. *Journal Geological Society of London*, **141**, p.121-128.

Cobbold, P. R., Marqure, D. & Davy, P. 1985. Continental thrust corridors in nature and experiment. *TSG Abstract, University of Southampton.*

Cooper, M. A. 1983. The calculation of bulk strain in oblique and inclined balanced sections. *Journal of Structural Geology*, **5**, p.161-165.

Dabrio, J. C., & Lopez-Garrido, A. C. 1970. Estructura en escamas del sector noroccidental de la Sierra de Cazorla (Zona Prébetica) y del borde de la Depressión del Guadalquivir (Prov. de Jáen). *Cuad. Geol. Univ. Granada*, **1**, p.149-157.

Dahlstrom, C. D. A. 1969. Balanced cross sections. *Canadian Journal of Earth Sciences*, **6**, p.743-757.

Dahlstrom, C. D. A. 1970. Structural geology in the eastern margin of the Canadian Rocky Mountains. *Bulletin of Canadian Petroleum Geology*, **18**, p.332-406.

Davis, D., Suppe, J. & Dahlen, F. A. 1983. Mechanics of Fold-and-Thrust Belts and Accretionary Wedges. *Journal of Geophysical Research*, **88 no. B2**, p.1153-1172.

Davis, D. M., & Engelder, T. 1985. The role of salt in fold-and-thrust belts. *Tectonophysics*, **119**, p.67-88.

De Ruig, M. J. 1990. Fold trends and stress deviation in the Alicante fold belt, southeastern Spain. *Tectonophysics*, **184**, p.393-403.

De Ruig, M. J., Smit, J., Geel, T. & Kooi, H. 1991. Effects of the Pyrenean collision on the Paleocene stratigraphic evolution of the southern Iberian margin (southeast Spain). *Geological Society of America Bulletin*, **103**, p.1504-1512.

De Smet, M. E. M. 1984. Wrenching in the external zone of the Betic Cordilleras, southern Spain. *Tectonophysics*, **107**, p.57-79.

Dercourt, J., Zonenshain, L. P., Ricou, L. -E., Kazmin, V. G., Le Pichon, X., Knipper,A. L., Grandjacquet, C., Sbortshikov, I. M., Geyssant, J., Lepvrier, C., Pechersky, D. H., Boulin, J., Sibuet, J. -C., Savostin, L. A., Sorokhin, O., Westphal, M., Bazhe 1986. Geological evolution of the Tethys Belt from the Atlantic to the Pamirs since the lias. *Tectonophysics*, **123**, p.241-315.

Dewey, J. F., Pitman, W. C., Ryan, W. B. F. & Bonnin, J. 1973. Plate tectonics and the evolution of the Alpine System. *Association of Petroleum Geology Bulletin*, **84**, p.3137-3180.

Dewey, J. F., Helman, M. L., Turco, E., Hutton, D. H. W. & Knott, S. D. 1989. Kinematics of the western Mediterranean. *Alpine Tectonics, edited by Coward, M. P., Dietrich, D. & Park, R. G., Geological Society of London Special Publication*, **45**, p.265-283.

Dickinson, W. R., Armin, R. A., Beckvar, N., Goodin, T. C., Janecke, S.U., Mark, R. A. Norris, R.D., Radel, G. & Wortman, A.A. 1987. Geohistory analysis of rates of sediment accumulation and subsidence from selected California Basins. *in Ingersoll, R. V., & Ernst, W.G. (eds) Cenozoic basin development of coastal California (Rubey Volume VI) Prentice-Hall*, p.1-23.

Didon, J. 1969. Étude géologique du Campo de Gibraltar (Espagne méridionale) *Unpublished Ph.D. Thesis, University of Paris*, 539 pp.

Dillon, W. P., Robb, J. M., Greene, M. G. & Luucena, J. C. 1980. Evolution of the continental margin of southern Spain and the Alboran Sea. *Marine Geology*, **36**, p.205-226.

Doblas, M., & Oyarzun, R. 1989. Neogene extensional collapse in the western Mediterranean (Betic-Rif Alpine orogenic belt): Implications for the genesis of the Gibraltar Arc and magmatic activity. *Geology*, **17**, p.430-433.

Durand-Delga, M. 1966. Titres et travaux scientifiques. *Im. Priester, Paris*, 43 pp.

Egeler, C. G., & Simon, O. J. 1969. Orogenic evolution of the Betic Zone (Betic Cordilleras, Spain), with emphasis on the nappe structures. *Geologie en Mijnbouw*, **48(3)**, p.296-305.

Eldredge, S., Bachtadse, V. & Van der Voo, R. 1985. Palaeomagnetism and the orocline hypothesis. *Tectonophysics*, **119**, p.153-179.

Elliott, D. 1983. The construction of balanced cross-sections. *Journal of Structural Geology*, **8**, p.101.

England, P., & Jackson, J. 1989. Active deformation of the continents. *Annual Review of Earth and Planetary Science*, **17**, p.197-226.

England, P. C., & Houseman, G. A. 1988. The mechanics of the Tibetan plateau. *Royal Society of London Philosophical Transactions*, **326**, p.301-320.

Fallot, P. 1948. Les Cordillères bétiques. *Estud. Geol.*, **8**, p.83-172.

Frizon de Lamotte, D. 1987. La structure du Rif externe (Maroc): mise au point sur le rôle des décrochements, des chevauchements et des glissements gravitaires. *Journal of African Earth Sciences*, **6/5**, p.755-766.

Frizon de Lamotte, D., Guezou, J-C. & Albertini, M.-A. 1989. Deformation related to Miocene westward translation in the core of the Betic zone. Implications on the tectonic interpretation of the Betic orogen (Spain). *Geodinamica Acta*, **3**, p.267-281.

Galdeano, A., Courtillot, V., Le Borgne, E., Le Mouel, J-L. & Rossignol, J-C. 1974. An aeromagnetic survey of the southwest of the Mediterranean: description and tectonic implications. *Earth and Planetary Science Letters*, **23**, p.323-336.

García-Dueñas, V., & Balanyá, J. C. 1991. Fallas normales de bajo ángulo a gran escala en las Béticas occidentales. *Geogaceta*, **9**, p.29-33.

Garcia-Hernandez, M., Lopez-Garrido, A. C., Rivas, P., Sanz de Galdeano, C. & Vera, J. A. 1980. Mesozoic palaeogeographic evolution of the external zones of the Betic Cordillera. *Geologie en Mijnbouw*, **59**, p.155-168.

Goff, D., & Wiltschko, D. V. 1992. Stresses beneath a ramping thrust sheet. *Journal of Structural Geology*, **14**, p.437-449.

Graham, R. H. 1978. Wrench faults, arcuate fold patterns and deformation in the southern French Alps. *Proceedings of the Geological Association*, **89**, p.125-142.

Grubbs, K. L., & Van der Voo, R. 1976. Structural deformation of the Idaho-Wyoming overthrust belt (U.S.A.), as determined by Triassic palaeomagnetism. *Tectonophysics*, **33**, p.321-336.

Guezou, J. C., Frizon de Lamotte, D., Coulon, M. & Morel, J. L. 1991. Structure and kinematics of the Prebetic nappe complex (southern Spain): definition of a

«Betic Floor Thrust» and implications in the Betic-Rif orocline. *Annales Tectonicæ*, **1**, p.32-48.

Hancock, P. L. 1985. Brittle microtectonics: principles and practice. *Journal of Structural Geology*, **7**, p.437-457.

Haq, B. U., Hardenbol, J. & Vail, P. R. 1987. Chronology of fluctuating sea-levels since the Triassic. *Science*, **235**, p.1156-1167.

Hatzfeld, D. 1976. Étude sismologique et gravimétrique de la structure profonde de la mer d'Alboran: mise en évidence d'un manteau anormal. *C. R. Acad. Sc. Paris*, **283**, p.1021-1024.

Helman, M. 1989. Tectonics of the western Mediterranean. *Unpublished D.Phil. Thesis, University of Oxford.*

Hermes, J. J. 1978. The Prebetic zone, the Guadalquivir basin and the Balearic promontory. *C. R. somm. Soc. Geol. France*, **4**, p.187-190.

Hirt, A. M., Lowrie, W., Julivert, M. & Arboleya, M. L. 1992. Palaeomagnetic results in support of a model for the origin of the Asturian arc. *Tectonophysics*, **213**, p.321-339.

Homewood, P., Allen, P. A. & Williams, G. D. 1986. Dynamics of the Molasse Basin of western Switzerland. *In: Allen, P. A. & Homewood, P., Foreland Basins. Special Publication of the International Association of Sedimentologists*, **8**, p.199-217.

Hossack, J. R. 1979. The use of balanced cross-sections in the calculation of orogenic contraction. *Journal Geological Society of London*, **136**, p.705-711.

Hossack, J. R. 1983. A cross-section through the Scandinavian Caledonides constructed with the aid of branch-line maps. *Journal of Structural Geology*, **5**, p.103-111.

Howard, C., & Kusznir, N. 1991. A rheological, thermal and flexural isostatic model of lithospheric shortening, thrust sheet emplacement and foreland basin formation. *Terra abstracts*, **3 no. 1**, p.134.

Jarvis, G. T., & McKenzie, D. P. 1980. Sedimentary basin formation with finite extension rates. *Earth and Planetary Science Letters*, **48**, p.42-52.

Jaume, S. C., & Lille, R. J. 1988. Mechanics of the Salt Range-Potwar Plateau, Pakistan: a fold-and-thrust belt underlain by evaporites. *Tectonics*, **7**, p.57-71.

Jerez Mir, F. 1973. Geologia de la zone Prebetica en la Transversal de Elche de la Sierra y sectores adyacents (Provincia de Albacete y Murcia), *Ph.D. thesis, University of Granada* .

Jerez Mir, F. 1981. Propuesta de un nuevo modelo tectonico general para las Cordilleras Beticas. *Bol. Geol. Miner.*, **42**, p.1-18.

Julivert, M. &. Arboleya, M. L. 1984. A geometrical and kinematic approach to the nappe structure in an arcuate foldbelt: the Cantabrian nappes (Hercynian chain, NW Spain). *Journal of Structural Geology*, **6**, p.499-519.

Julivert, M. &. Arboleya, M. L. 1986. Areal balancing and estimate of areal reduction in a thin-skinned fold-and-thrust belt (Cantabrian zone, NW Spain): constraints on its emplacement mechanism. *Journal of Structural Geology*, **8**, p.407-414.

Karner, G. D., & Watts, A. B. 1983. Gravity anomalies and flexure of the lithosphere at mountain ranges. *Journal of Geophysical Research*, **88**, p.10,449-10,477.

Kenter, J. A. M., Reymer, J. J. G., van der Straaten, H. C. & Peper, T. 1990. Facies patterns and subsidence history of the Jumilla-Cieza region (southeastern Spain). *Sedimentary Geology*, **67**, p.263-280.

Leblanc, D., & Oliver, Ph. 1984. Role of strike-slip faults in the Betic-Rifian orogeny. *Tectonophysics*, **101**, p.345-355.

Lonergan, L., & Mange, M. submitted. Internal Zone unroofing and foreland basin sediments in the Betic Cordillera, SE Spain. *Journal Geological Society of London.*

Lonergan, L., Platt, J.P. & Gallagher, L. in press. The Internal/External Zone Boundary in the eastern Betic Cordillera, SE Spain. *Journal of Structural Geology.*

Loomis, T. P. 1975. Tertiary mantle diapirism, orogeny, and plate tectonics east of the Strait of Gibraltar. *American Journal of Science*, **275**, p.1-30.

Mäkel, G. H. 1985. The geology of the Malaguide complex and its bearing on the geodynamic evolution of the Betic-Rif orogen (southern Spain and northern Morocco). *GUA Papers in Geology*, **Ser. 1, 22**, 263 pp.

Marshak, S., Geiser, P. A., Alvaraz, W. & Engelder T. 1985. Structural geometry of the "orocline" in the Appalachian foreland, near Kingston, New York. *Geological Society of America Abstract Programme*, **17**, p.53.

Marshak, S. 1988. Kinematics of orocline and arc formation in thin-skinned orogens. *Tectonics*, **7.1**, p.73-86.

McClay, K. R. 1991. Glossary of thrust tectonics terms. *Thrust Tectonics, edited by McClay, K. R.*, p.419-433.

McKenzie, D. P. 1978. Some remarks on the development of sedimentary basins. *Earth and Planetary Science Letters*, **40**, p.25-32.

McNutt, M., Diament, M. & Kogan, M. G. 1988. Variations of elastic plate thicknesses at continental thrust belts. *Journal of Geophysical Research*, **93**, p.8825-8838.

Molnar, P., & Tapponier, P. 1975. Cenozoic tectonics of Asia: effects of a continental collision. *Science*, **189**, p.419-426.

Morley, C. K. 1986. A classification of thrust fronts. *American Association of Petroleum Geology Bulletin*, **70**, p.12-25.

Oldow, J. S. 1984. Spatial variability in the structure of the Roberts Mountains allochthon, western Nevada. *Geological Society of America Bulletin*, **95**, p.174-185.

Ori, G. G. &. F., P. F. 1984. Sedimentary basins, formed and carried piggyback on active thrust sheets. *Geology*, **12**, p.475-478.

Osete, M. L., Freeman, R. & Vegas, R. 1989. Palaeomagnetic evidence for block rotations and distributed deformation of the Iberian-African plate boundary. *Palaeomagnetic Rotations and Continental Deformation, edited by Kissel, C. & Laj, C.*, p.381-391.

Paquet, J. 1969. Etude géologique de l'Oest de la Province de Murcie (Espagne). *Mem. Soc. Géol. Fr.*, **11**, p.1-270.

Peper, T., & Cloetingh, S. 1992. Lithospheric dynamics and tectono-stratigraphic evolution of the Mesozoic Betic rifted margin (southeastern Spain). *Tectonophysics*, **203**, p.345-361.

Petit, J. P. 1987. Criteria for the sense of movement on fault surfaces in brittle rocks. *Journal of Structural Geology*, **9**, p.597-608.

Pitman, W. C. 1978. Relationship between eustasy and stratigraphic sequences of passive margins. *Geological Society of America Bulletin*, **89**, p.1389-1403.

Platt, J. P. 1986. Dynamics of orogenic wedges and uplift of high-pressure metamorphic rocks. *Geological Society of America Bulletin*, **97**, p.1037-1053.

Platt, J. P., Leggett, J. K. & Alam, S. 1988. Slip vectors and fault mechanics in the Makran accretionary wedge, southwest Pakistan. *Journal of Geophysical Research*, **93 no. B7**, p.7955-7973.

Platt, J. P., & Vissers, R. L. M. 1989. Extensional collapse of thickened continental lithosphere: A working hypothesis for the Alboran Sea and Gibraltar arc. *Geology*, **17**, p.540-543.

Platt, J. P., Behrmann, J. H., Cunningham, P. C., Dewey, J. F., Helman, M., Parish, M., Shepley, M. G., Wallis, S. & Weston, P. J. 1989a. Kinematics of the Alpine arc and the motion history of Adria. *Nature*, **337**, p.158-161.

Platt, J. P., Lister, G. S., Cunningham, P., Weston, P., Peel, F., Baudin, T. & Dondey, H. 1989b. Thrusting and backthrusting in the Briançonnais domain of the western Alps. *Alpine Tectonics, edited by Coward, M. P., Dietrich, D. & Park, R. G., Geological Society of London Special Publication* , **45**, p.135-152.

Platzman, E. S. 1992. Palaeomagnetic rotations and the kinematics of the Gibraltar arc. *Geology*, **20**, p.311-314.

Price, R. A. 1981. The Cordilleran foreland thrust and fold belt in the southern Canadian Rocky Mountains. *Thrust and Nappe Tectonics, edited by McClay, K. R. & Price, N. J., Geological Society of London Special Publication*, **9**, p.427-448.

Puga, E., Diaz de Federico, A., Bargossi, G. M., Bodinier, J. L., Desmons, J. & Morten, L. 1991. Rodingites in serpentinized wehrlites and protogranular and spinifex harzburgites in the Betic ophiolite association (BOA), southern Spain. *Terra abstracts*, **3**, p.98.

Ramsay, J. G., & Wood, D. S. 1973. The geometric effect of volume change during deformation process. *Tectonophysics*, **16**, p.263-277.

Ricou, L. E., & Siddans, A. W. B. 1985. Collision tectonics in the western Alps. *In: Collision Tectonics, edited by Coward, M. P. & Ries, A., Geological Society of London Special Publication*, **19**, p.229-260.

Ries, A. C., & Shackleton, R. M. 1976. Patterns of strain variation in arcuate fold belts. *Philosophical Transactions of the Royal Society of London*, **A. 283**, p.281-288.

Rutter, E. H., Maddock, R. H., Hall, S. H. & White, S. H 1986. Comparative microstructures of natural and experimentally produced clay-bearing fault-gouges. *PAGEOPH*, **124**, p.3-30.

Sanz de Galdeano, C. 1990. Geologic evolution of the Betic Cordilleras in the Western Mediterranean, Miocene to the present. *Tectonophysics*, **172**, p.107-119.

Sarwar, G., & De Jong, K. A. 1979. Arcs, oroclines, syntaxes: the curvatures of mountain belts in Pakistan. *Geodynamics of Pakistan, edited by Farah, A. & De Jong, K. A. Geol. Survey of Pakistan*, p.341-349.

Schwartz, S. Y., & Van der Voo, R. 1983. Palaeomagnetic evaluation of the orocline hypothesis in the central and southern Appalachians. *Geophysical Research Letters*, **10, no.7**, p.505-508.

Sclater, J. G., & Christie, P. A. F. 1980. Continental stretching: an explanation of the post-Mid-Cretaceous subsidence of the central North Sea Basin. *Journal of Geophysical Research*, **85**, p.3711-3739.

Shackleton, R. M., & Ries, A. C. 1984. The relation between regionally consistent stretching lineations and plate motions. *Journal of Structural Geology*, **6**, p.111-117.

Spakman, W. 1986. Subduction beneath Eurasia in connection with the Mesozoic Tethys. *Geologie en Mijnbouw*, **65**, p.145-153.

Steckler, M. S., & Watts, A. B. 1978. Subsidence of the Atlantic-type continental margin off New York. *Earth and Planetary Science Letters*, **41**, p.1-13.

Stockmal, G. S., Beaumont, C. & Boutilier, R. 1980. Geodynamic models of convergent margin tectonics: transition from rifted margin to overthrust belt and consequences for foreland basin development. *Bulletin of American Association of Petroleum Geology*, **70**, p.181-190.

Talwani, M. J., Worzel, J. L. & Landesman, L. 1959. Rapid gravity computation for the two-dimensional bodies with application to the Mendocino submarine fracture zone. *Journal o Geophysical Research*, **64**, p.49-59.

Tapponier, P., & Molnar, P. 1977. Rigid plastic indentation: The origin of syntaxis in the Himalayan belt. *Coll. Int. Cent. Nat. Rech. Sci.*, **81**, p.431-432.

Torné, M., & Banda, E. in press. Crustal thinning from the Betic Cordillera to the Alboran Sea. *GeoMarine Letters*.

Tomé, M. G., Pascal, G., Buhl, P., Watts, A. B. & Mauffret, A. 1992. Crustal and Velocity Structure of the Valencia Trough (Western Mediterranean) Part 1: A combined refraction/wide angle reflection and near vertical reflection study. *In The Valencia Trough: Geology and Geophysics, edited by E. Banda & P. Santanach, Tectonophysics*, **203**, p.1-20.

Torres-Roldán, R. L. 1979. The tectonic subdivision of the Betic Zone (Betic Cordilleras, southern Spain): its significance and one possible geotectonic scenario for the westernmost Alpine belt. *American Journal of Science*, **279**, p.19-51.

Tubia, J. M., & Cuevas, J. 1987. Structures et cinématiques liées à la mise en place des péridotites de Ronda (Cordillères Bétiques, Espagne). *Geodinamica Acta*, **1**, p.59-69.

Van Bemmelen, R. W. 1969. Origin of the western Mediterranean Sea. *Geologie en Mijnbouw*, **26**, p.13-52.

Van der Beek, P. A., & Cloetingh, S. 1992. Lithospheric flexure and the tectonic evolution of the Betic Cordilleras (SE Spain). *Tectonophysics*, **203**, p.325-344.

Van der Straaten, H. C. 1990. The Abaran Basin - A Neogene pull-apart basin in SE Spain. *Unpublished Ph.D. thesis, University of Amsterdam*

Van der Voo, R., & Zijderveld, J. D. A 1969. Palaeomagnetism in the western Mediterranean area. *Verh. K. Ned. Geol. Mijnbouwk. Genoot.*, **26**, p.121-138.

Van der Voo, R., & Channell, J. E. T. 1980. Palaeomagnetism in orogenic belts. *Review of Geophysics and Space Physics*, **18**, p.455-481.

Vann, I. R., Graham, R. H. & Haywood, A. B. 1986. The structure of mountain fronts. *Journal of Structural Geology*, **8**, p.215-227.

Vialon, P. 1987. The interaction of rotation-indentation in the evolution of the western Alpine arc. *Abstract submitted to Alpine Tectonics meeting.*

Watts, A. B., & Steckler, M. S. 1979. Subsidence and eustasy at the continental margin of eastern North America. *American Geophysical Union Series*, **3**, p.218-234.

Watts, A. B. &. Thorne, J, 1984. Tectonics, global changes in sea-level and their relationship to stratigraphic sequences at the US Atlantic continental margin. *Marine Petroleum Geology*, **1**, p.319-339.

Watts, A. B. submitted. The effective elastic thickness of the lithosphere and the evolution of foreland basins. *Basin Research.*

Watts, A. B., Platt, J. P. & Buhl, P. submitted. Tectonic evolution of the Alboran Sea Basin. *Basin Research.*

Weijermars, R. 1985. Uplift and subsidence history of the Alboran Basin and a profile of the Alboran diapir. *Geologie en Mijnbouw*, **64**, p.349-356.

Weston, P. J. 1989. The origin and kinematics of the Alpine Arc. *Unpublished Ph.D.Thesis, University of Oxford.*

Woodcock, N. H., & Fischer, M. 1986. Strike-slip duplexes. *Journal of Structural Geology*, **8**, p.725-735.

Wooler, D., Smith, A. & White, N. 1992. Measuring lithospheric stretching on Tethyan passive margins. *Journal of the Geological Society of London*, **149**, p.517-532.

Wortel, M. J. R. &. Spakman, W. 1991. Dynamic evolution of convergent plate boundaries in the Mediterranean region. *Terra abstracts*, **3**, p.135.

Zoetemeijer, R., Desegaulx, P., Cloetingh, S., Roure, F. & Moretti, I. 1990. Lithospheric dynamics ann tectono-stratigraphic evolution of the Ebro basin. *Journal of Geophysical Research*, **95**, p.2701-2711.

Appendices

APPENDIX 1

KINEMATIC DATA

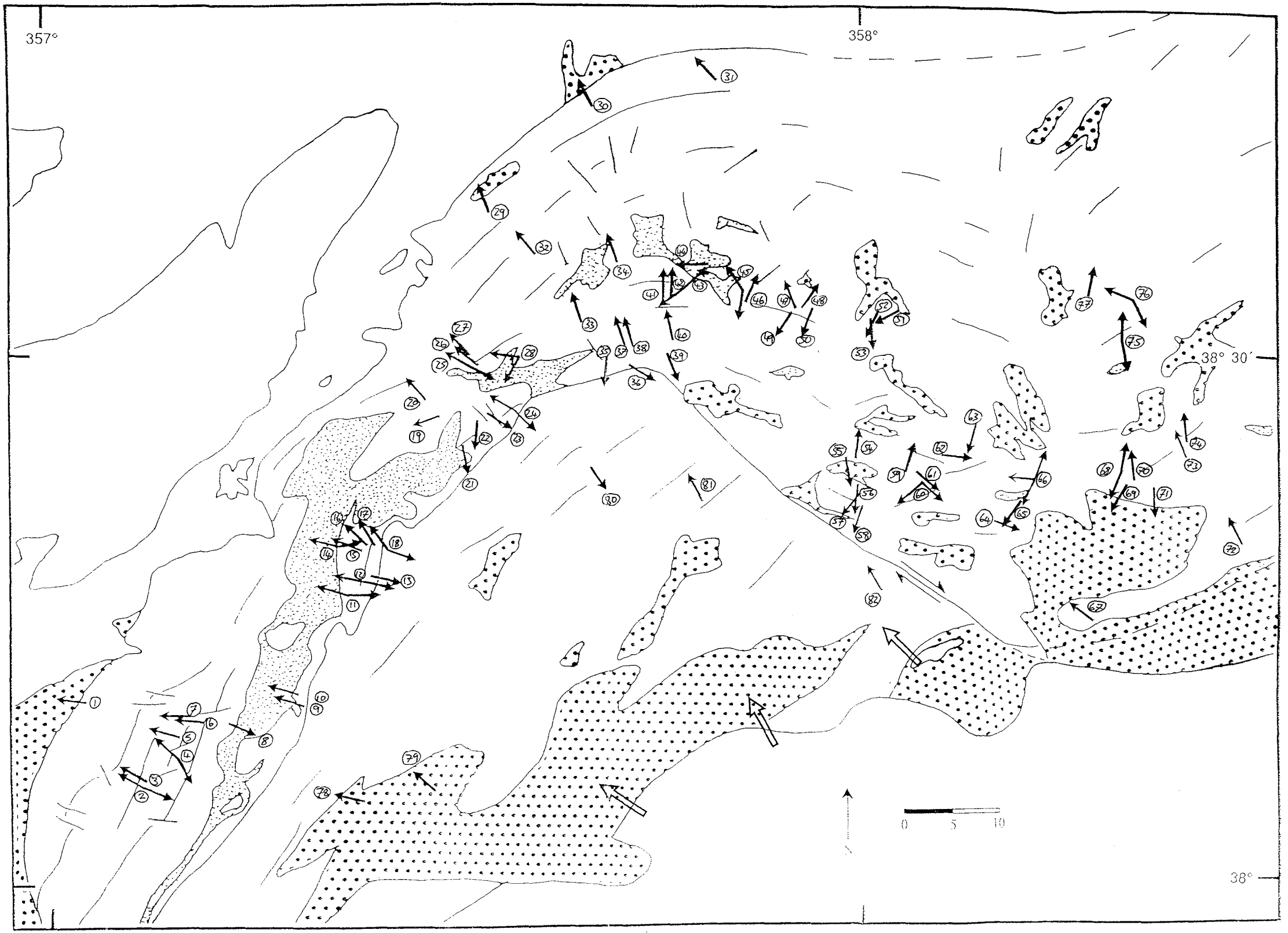


Fig 2.2. Summary map of the variation in tectonic transport directions around the Prebetic Arc. Closed arrows-this study, open arrows-Platt & Allerton, pers. comm. Numbers-see Appendix 1.

Compilation of kinematic data for the Prebetic Zone shown in Fig. 2.2.

No.	Grid ref.	Mean vector/s
The NE Trending Limb		
1.	66263972	58/098
2.	67103927	25/122 54/294
3.	67093937	48/117
4.	67353955	38/139 39/331
5.	67433972	32/110
6.	67673990	38/095
7.	67623991	59/092
8.	67883975	50/293
9.	68744016	43/122
10.	68534017	61/112
11.	69054115	46/107 40/267
12.	69154120	60/102 60/282
13.	69164119	29/283
14.	68954144	55/106 62/247
15.	69054145	59/110
16.	69154151	53/143
17.	69234149	41/129
18.	69424151	65/139 29/289
The Alcaraz Antitaxis		
19.	69924320	44/070
20.	69864337	33/139
21.	70074262	43/355
22.	70634292	30/010
23.	70724309	36/306
24.	70864300	54/119 43/317
25.	70334355	40/118 26/298
26.	70404355	50/133
27.	70274362	52/134
28.	70934356	54/034 41/097
29.	70344447	16/162
30.	71944588	19/155
31.	72764592	44/144
32.	71044437	41/136
33.	71294391	48/166
34.	71944475	13/163
35.	71764330	19/006
36.	71964338	40/295
37.	72184367	31/163
38.	72164370	28/169
39.	72604353	35/343
40.	72524358	34/148
41.	72474428	39/182
42.	72494427	24/189
43.	72604438	37/042 36/243
44.	72384478	43/084

No.	Grid ref.	Mean vector/s		
45.	73134419	34/007	53/150	
46.	73154410	36/193		
The NW Trending Limb				
47.	73734402	37/157		
48.	73764405	33/219		
49.	73654399	46/038		
50.	73864407	42/024		
51.	75184397	34/068		
52.	75114399	23/058		
53.	74914396	46/354		
54.	74554267	70/208		
55.	74504264	26/353		
56.	74704250	31/007		
57.	74694246	23/047		
58.	74724231	62/028		
59.	75074248	29/202		
60.	75284238	61/053	45/309	
61.	75184247	45/313		
62.	75284246	18/277		
63.	75754264	41/021		
The Cenajo Syntaxis				
64.	76514223	41/290		
65.	76614218	41/042		
66.	76754243	25/026	21/094	28/205
67.	77524105	14/126		
68.	77414239	41/020	46/192	
69.	77434236	31/030		
70.	77444237	35/175		
71.	77874237	24/357		
72.	789420*	32/153		
73.	78354297	27/155		
74.	78354292	50/175		
75.	775437*	26/182	26/354	
76.	777443*	24/114	20/334	
77.	771443*	13/200		
Internal Prebetic Zone				
78.	69063911	38/103		
79.	69743918	33/137		
80.	71764261	55/326		
81.	729424*	39/154		
82.	74914095	59/149		

* From 1:200,000 geological map: other grid references from 1:50,000 geological maps

APPENDIX 2

GRAVITY MODELS

Co-ordinates of the gravity models used in Chapter 4

The models are constructed by defining a set of quadrilaterals and their density contrasts. Each model is constructed from 1 to 2000km, with the length of the section to be compared with the observed gravity anomaly drawn from 1000km. This is to eliminate from the key area the end effects which arise as the predicted gravity anomaly is calculated using the GBOTT program. The formula for inputing the data is,

a
b c
d
x y
x y
etc

where
a=total number of quadrilaterals
b=number of the quadrilateral to be defined
c=total number of co-ordinates in this particular quadrilateral
d=gravity contrast of this quadrilateral
x, y=co-ordinates of the quadrilateral

The quadrilaterals represent different geological phenomena. For example, for the Cazorla section:
Quadrilateral 1 - the Prebetic/Subbetic thrust pile below sea level
Quadrilateral 2 - the Prebetic/Subbetic thrust pile above sea level
Quadrilateral 3 - upper/lower crust boundary
Quadrilateral 4 - variation in Moho depth
Quadrilateral 5 - the topography which was inaccurately compensated for (in this case under compensated) when the predicted Bouger anomaly was calculated.
Quadrilateral 6 and 7 - Tertiary/Quaternary basins
Quadrilateral 8 - boundary of sea-floor sediments with respect to the Internal Zones
Quadrilateral 9 - boundary of sea-floor sediments with respect to seawater

The gravity models for the five profiles described in chapter 4: the Cazorla, Orcera, Isso, Jumilla and Elche sections, and the alterations to the Cazorla section shown in Figs 4.2.6./4.2.7. and Figs 4.4.3./4.4.4., are presented in this appendix.

Co-ordinates of the gravity model for the Cazorla section

```
9
1       21
-.3
1010    -.8
1015    -.4
1020    -.2
1025    0
1032    .1
1037    .4
1040    .9
1046    1.6
1050    2.2
1052    2.4
1058    1.5
1065    1.2
1070    1.6
1090    4.2
1093    4.5
1100    4.2
1120    2
1135    0
1140    -.2
1145    -.8
1010    -.8
2       10
-.22
1010    -.8
1145    -.8
1138    -1.2
1083    -1.2
1073    -1.6
1057    -1.6
1054    -1.2
1041    -1.2
1030    -.8
1010    -.8
3       18
-.15
1       -2
1       12
1000    12
1080    12
1105    13
1120    13.5
1130    14
1140    14
1155    15
1160    14
1170    14
1175    12
1195    9
1220    10
1250    10
2000    10
2000    -2
1       -2
4       10
.43
1       35
1       37
2000    37
2000    15
1280    15
1200    28
```

```
1165    36
1140    37
1110    35
1       35
5       5
.08
1       -.8
1       0
1185    0
1145    -.8
1       -.8
6       6
-.37
1152    -.6
1158    -.2
1160    -0
1162    -.2
1165    -.4
1152    -.6
7       5
-.22
1015    -.8
1022    -.6
1028    -.7
1030    -.8
1015    -.8
8       8
-.45
1185    0
1193    .25
1202    .7
1214    2.6
1263    3
2000    3
2000    0
1185    0
9       8
.37
1185    0
1193    .2
1202    .6
1214    2.2
1263    2.6
2000    2.6
2000    0
1185    0
```

Co-ordinates of the gravity model for the Orcera section

```
8
1        9
-.22
1010     -.8
1020     0
1135     0
1140     -.8
1110     -.8
1090     -1.2
1040     -1.2
1035     -.8
1010     -.8
2        20
-.3
1020     0
1025     .5
1030     .7
1035     .6
1038     .5
1043     -.2
1050     -.2
1055     -.1
1058     .2
1060     .6
1065     1.9
1085     3
1095     3.5
1100     4
1108     4
1115     3
1120     1.5
1130     1
1135     0
1020     0
3        14
-.15
1        0
1000     12
1085     12
1110     13
1145     14
1165     13
1185     13
1190     13
1200     12
1220     12
1300     10
2000     10
2000     0
1        0
4        13
.43
1        35
1        37
2000     37
2000     15
1300     15
1250     25
1200     28.5
1180     29
1160     34
1140     36
```

```
1080    35
1000    35
1       35
5       10
.37
1195    0
1215    .1
1217    .4
1220    .4
1225    1.2
1230    2
1260    2.6
2000    2.6
2000    0
1195    0
6       8
-.45
1195    0
1200    .2
1215    .6
1233    2.2
1260    3.2
2000    3.2
2000    0
1195    0
7       5
-.45
1150    -.7
1165    .2
1170    .2
1180    -.2
1150    -.7
8       6
-.08
1140    -.8
1185    0
1195    0
2000    0
2000    -.8
1140    -.8
```

Co-ordinates of the gravity model for the Isso section

```
8
1        13
-.22
1        -1
1        0
1157.4   0
1159.5   -.1
1144     -.4
1135     -.4
1131     -.8
1110     -.4
1056     -.8
1053     -1.2
1035     -1.2
1000     -1
1        -1
2        24
-.3
1        0
1        1
1000     1
1010     1.4
1020     1.2
1030     1.5
1038     2.4
1040     2.4
1042     2.5
1045     2.5
1050     2.8
1060     3.4
1070     3.4
1095     3
1100     5.2
1110     4.
1115     5
1120     5.1
1127     4
1130     3
1140     2
1154     1
1157.4   0
1        0
3        13
-.15
1        0
1        12
1000     12
1115     13
1150     14
1160     13
1180     12
1220     14
1240     14
1320     10
2000     10
2000     0
1        0
4        13
.43
1        35
1        37
2000     37
2000     18
```

```
1320    18
1260    28
1250    28
1185    31
1160    36
1140    36
1120    35
1000    35
1       35
5       9
.37
1215    0
1251    .2
1283    .8
1292    1.2
1301    2.4
1320    2.6
2000    2.6
2000    0
1215    0
6       23
-.45
1144    -.4
1160    0
1165    -.1
1170    .1
1175    .2
1185    .1
1190    .35
1195    .9
1200    1
1210    .8
1220    1
1230    3
1240    4
1245    4
1250    4
1255    4
1283    1.1
1292    1.6
1301    2.7
1320    2.7
2000    2.7
2000    -.4
1144    -.4
7       5
-.08
1144    -.4
1215    0
2000    0
2000    -.4
1144    -.4
8       5
-.22
1100    -.5
1110    0
1120    -.6
1110    -.4
1100    -.5
```

Co-ordinates of the gravity model for the Jumilla section

```
7
1       9
-.22
1       -.8
1       0
1140    0
1095    -.4
1080    -.8
1045    -.8
1025    -1
1000    -.8
1       -.8
2       24
-.3
1       0
1       1.7
1000    1.7
1014    1.4
1020    1.1
1024    .8
1027    .6
1033    .9
1045    1.8
1049    2
1058    1.6
1060    2.3
1070    2.3
1073    2.4
1078    2.5
1082    3.3
1090    3.8
1093    3.5
1100    3.2
1108    1.2
1110    1.2
1118    .2
1123    0
1       0
3       9
-.15
1       0
1       12
1000    12
1080    12
1120    14
1300    10
2000    10
2000    0
1       0
4       16
.43
1       35
1       37
2000    37
2000    15
1300    15
1260    24
1250    25
1200    25
1180    25
1150    27
1130    32
1120    36
```

```
1100    36
1080    35
1000    35
1       35
5       9
.37
1145    0
1205    .2
1211    .6
1237    1
1257    2.4
1282    2.6
2000    2.6
2000    0
1145    0
6       18
-.45
1119    -.2
1125    0
1130    .2
1133    .3
1135    .5
1140    1.2
1145    1.8
1150    2
1160    3
1170    4
1205    3.5
1211    2.5
1237    2
1257    3.2
1282    3.2
2000    3.2
2000    -.2
1119    -.2
7       5
-.08
1119    -.2
1145    0
2000    0
2000    -.2
1119    -.2
```

Co-ordinates of the gravity model for the Elche section

```
6
1       9
-.22
1       -.8
1       0
1160    0
1166    -1.2
1120    -1.2
1105    -1.6
1090    -1.2
1000    -.8
1       -.8
2       17
-.3
1       0
1       2.3
1000    2.3
1010    2
1020    2.3
1030    2.4
1040    2
1050    2
1055    2.4
1059    3
1070    3
1090    2.7
1100    3
1130    2.8
1135    3.1
1160    0
1       0
3       13
-.15
1       0
1       12
1000    12
1059    12.5
1100    13
1135    13.5
1160    15
1185    15
1200    14
1230    13
2000    13
2000    0
1       0
4       12
.43
1       34.5
1       39
2000    39
2000    38
1230    38
1180    38
1135    37
1120    35
1100    35
1059    35
1000    34.5
1       34.5
5       5
-.22
1120    -1.2
```

```
1128    -1
1133    -1
1140    -1.2
1120    -1.2
6       7
-.08
1166    -1.2
1190    -1.2
1202    -1.6
1230    -1.6
2000    -1.6
2000    -1.2
1166    -1.2
```

Altered co-ordinates of the gravity model for the Cazorla section showing the affect of:

i) decreasing the thickness of the Prebetic/Subbetic nappe pile. Fig 4.2.6.
(Only the first quadrilateral altered)

1	21
-.3	
1010	-.8
1020	-.2
1025	0
1032	.1
1037	.4
1040	.9
1046	1.6
1050	2.2
1052	2.4
1058	1.5
1065	1.2
1070	1.6
1090	3.2*
1093	3.5*
1100	3.2*
1120	2
1135	0
1140	-.2
1145	-.8
1010	-.8

ii) increasing the thickness of the Prebetic/Subbetic nappe pile. Fig 4.2.6.
(Only the first quadrilateral altered)

1	19*
-.3	
1010	-.8
1020	-.2
1025	0
1032	.1
1037	.4
1040	.9
1046	1.6
1050	2.2
1052	2.4
1058	1.5
1065	1.2
1070	1.6
1080	4.5*
1120	2
1135	0
1140	-.2
1145	-.8
1010	-.8

iii) increasing the Moho gradient. Fig 4.2.7. (Only the fourth quadrilateral altered)

4	10
.43	
1	35
1	37
2000	37
2000	13*
1280	13*
1200	26*
1165	36
1140	37
1110	35
1	35

iv) decreasing the Moho gradient. Fig 4.2.7. (Only the fourth quadrilateral altered)

4	10
.43	
1	35
1	37
2000	37
2000	17*
1280	17*
1200	30*
1165	36
1140	37
1110	35
1	35

v) a more north-westerly position for the nose of the Internal Zone wedge. Fig 4.4.3. (Only the first quadrilateral altered)

1	19*
-.3	
1010	-.8
1020	-.2
1025	0
1032	.1
1037	.4
1040	.9
1046	1.6
1050	2.2
1052	2.4
1058	1.5
1065	1.2
1070	1.6
1080	4.5*
1120	2
1135	0
1140	-.2
1145	-.8
1010	-.8

vi) a more south-easterly position for the nose of the Internal Zone wedge. Fig 4.4.3. (Only the first quadrilateral altered)

1	19*
-.3	
1010	-.8
1020	-.2
1025	0
1032	.1
1037	.4
1040	.9
1046	1.6
1050	2.2
1052	2.4
1058	1.5
1065	1.2
1070	1.6
1110	4.5*
1120	2
1135	0
1140	-.2
1145	-.8
1010	-.8

vii) deepening of a Tertiary basin. Fig. 4.4.4. (Only the sixth quadrilateral altered)

6	4*
-.37	
1152	-.6
1158	.7*
1165	-.4
1152	-.6

viii) offsetting the deepest part of a Tertiary basin. Fig. 4.4.4. (Only the sixth quadrilateral altered)

6	4*
-.37	
1152	-.6
1164	0*
1165	-.4
1152	-.6

* denotes a line which has been changed from the original Cazorla gravity model.